TUM School of Engineering and Design

Analysis of the Carbon Nanotube Solid-Liquid Interface for Designing a Preparative Potential-Controlled Chromatography

Tatjana Trunzer

Vollständiger Abdruck der von der TUM School of Engineering and Design
der Technischen Universität München zur Erlangung des akademischen Grades
einer Doktorin der Ingenieurwissenschaften genehmigten Dissertation.

Vorsitz: Prof. Dr.-Ing. Andreas Kremling

Prüfer*innen der Dissertation:

1. Prof. Dr. rer. nat. Sonja Berensmeier

2. Prof. Dr.-Ing. Matthias Franzreb

Die Dissertation wurde am 20.04.2021 bei der Technischen Universität München eingereicht
und durch die Fakultät für Maschinenwesen am 28.09.2021 angenommen.

Life is a path with many junctions, new doors that open
and old doors that close.

To decide means to go my own way,
as I can only go once.

Acknowledgements

First of all, I am deeply grateful to Prof. Sonja Berensmeier, who gave me the chance to pursue a Ph.D. and to let me be part of her research family. I thank her from my heart for her supervision, encouragement, and all the freedom she gave me to challenge myself with this fascinating project. It was a pleasure to learn and work in this interdisciplinary field.

I thank Prof. Matthias Franzreb for his agreement to examine my work and express my gratitude to him and Robin Wagner, as well as Prof. Wolfgang Wenzel, and Dr. Christian Schrader for all the exciting discussions as S3kapel project partners.

I give my special gratitude to Dr. Paula Fraga-Garcia for taking over my mentorship and guide me in my scientific development. With all your passion for expressing interfacial effects, you showed me new directions in formulating and answering research questions.

Thanks to the many students involved and contributed to my research significantly through excellent discussions and constantly testing new approaches to fix the numerous challenges. Thank you for your creative and refreshing ideas, efforts, and support I experienced. I enjoyed working with you together. Among all of you I supervised, I want to highlight my gratitude to Melanie Porzenheim, Timothy Stummvoll, Dominik Voltmer, Marc Tschuschner, Melanie Gerigk, and Andreas Will for your decisive contributions to my dissertation.

It was a pleasure to work with all my colleagues in a pleasant atmosphere. The fruitful discussions and the time around always motivated me to get forward. I want to take the opportunity to thank my office mate Stefan Rauwolf, as well as Lea Martin and Michael Schobesberger, for their consistent motivation and being there when needed.

I thank my family, who always supported me and had my back when there was a fork in the road or when there were obstacles in the way.

Thanks to all those who have accompanied and shaped me through the years of my studies and doctorate. I will keep this time with all its joyous and turbulent moments in my heart.

Table of Contents

Nomenclature

Abbreviations

Abbreviation	Description
3D	Three dimensional
Abbr.	Abbreviation
AC	Activated carbon
CE	Counter electrode
CEX	Cation exchange
CDI	Capacitive deionization
CNT	Carbon nanotubes
CV	Cyclic voltammetry, Cyclic voltammogram
DI-water	Deionized water
EDX	Energy-dispersive X-ray spectroscopy
EIS	Electrochemical impedance spectroscopy
El.	Electric
EST	Estimated
EMLC	Electrochemically modulated liquid chromatography
GC	Glassy carbon
GCS	Gouy-Chapman-Stern
HT	Hypothesis
IEP	Isoelectric point

Abbreviation	**Description**
K	Coefficient
MWCNT	Multi-walled carbon nanotubes
OCP	Open circuit potential
PBS	Phosphate buffer solution
PCC	Potential-controlled chromatography
PGC	Porous graphitic carbon
pzc	Point of zero charge
R	Place-holder parameter
RE	Reference electrode
RQ	Research question
SBC	Static binding capacity
SEM	Scanning electron microscopy
SMA	Steric mass action
SSA	Specific surface area
SWCNT	Single-walled carbon nanotubes
TEM	Transmission electron microscopy
TGA	Thermogravimetric analysis
VdW	Van-der-Waals forces
WE	Working electrode
XPS	X-ray photoelectron spectroscopy

Latin Symbols

Symbol	Description	Unit
I	Electrical current	A
c	Concentration	mol/L
C	Conductivity	mS/cm
C	Electric capacity	F
$HETP$	Height equivalent of theoretical plates	cm
N	Number of theoretical plates	˘
q	Adsorption amount/Load	mol/g
Q	Electric charge	C
R	Resistance	Ω
t	Time	min
T	Temperature	°C
U	Voltage	V
V	Volume	mL
$\dot{V}$	Volumetric flow rate	mL/min
w	Width	cm

Greek Symbols

Symbol	Description	Unit
η	Dynamic viscosity	Pa s
ϕ	Electric potential	V
ρ	Density	kg/m^3
τ_{Rel}	Residence time	s

Subscripts

Symbol	Description
0	Initial
ads	Adsorption
ax	Axial
$break$	Breakthrough
col	Column
eff	Effective
eq	Equilibrium
exp	Experiment/experimental
F	Freundlich
in	Inlet/initial
H	Henry
max	Maximum
neg	Negative/negative region
pos	Positive/positive region
R	Retention
sup	Supernatant
sim	Simulation/simulative
tot	Total

1 Introduction

The continually growing social prosperity increases the energy demand, and people aspire to a long, healthy life. While the production of the required fine and specialty chemicals as well as pharmaceutical products has been in the hands of the chemical industry for the past decades, biotechnological production is now the upcoming industrial sector that aims to make energy, packaging materials, food supplements, cosmetics, and pharmaceuticals 'greener' [1, 2].

The biotechnological synthesis route is divided into a biomass growth and product production step (*upstream*), followed by a product recovery and purification step (*downstream*). The cost balance depends on the process objective. Thus, the percentage costs for the downstream part dominate the more separation, purification, and concentration steps are required to gain highly pure products, which is why optimization of the single process steps is needed [3, 4].

This thesis focuses on chromatography, which is an established concentration and purification module of the downstream cascade. Different chromatography methods exist for analytical or preparative processing. The working principle is based on the different interaction kinds formed between the target species dissolved in the mobile phase (fluid) and the stationary phase (solid or fluid). A commercially wide-spread application is solid-liquid ion-exchange chromatography (IEX), already realizable as an inexpensive, large-scale production unit. Nevertheless, IEX is limited in its operation range separating either cations or anions and can require specifically functionalized stationary phase materials (resin) to separate the desired target species from bulk mixtures. In addition, the batch process requires large amounts of elution media necessary to regenerate the column, resulting in dilute product fractions and a large amount of unwanted waste.

An exciting alternative for IEX is potential-controlled chromatography (PCC), also called electrochemically modulated liquid chromatography (EMLC) for analytical applications. The use of the extended amount of 'green' power to control the surface charge and binding character electrochemically offers an inexpensive and multi-applicable system that can either act as an anion or cation exchanger for all kinds of polarized or charged ions and molecules. Moreover, no additional elution medium is necessary, as the column regeneration can be

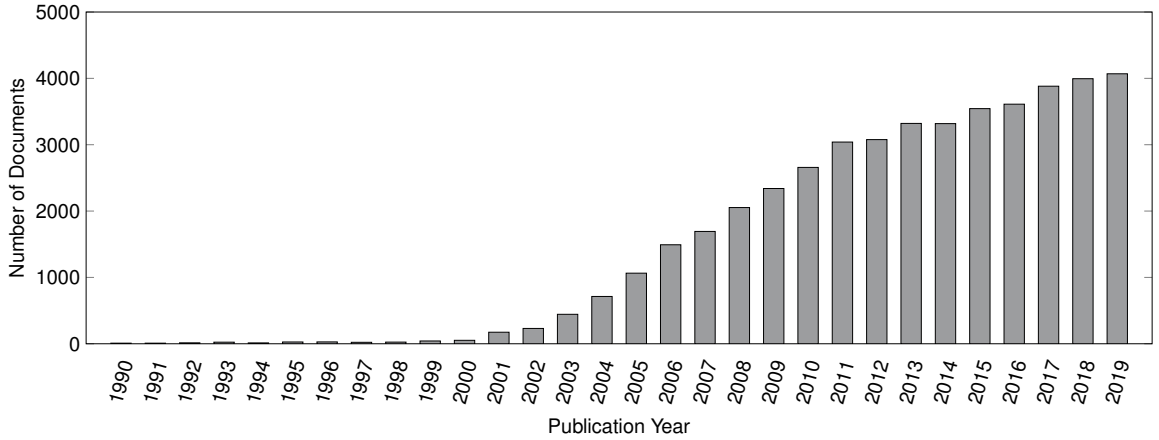

Figure 1.1: Relevance of CNT in the research illustrated as the amount of publications including 'CNT' from the end of the 20^{th} century until today (data taken from scopus.com [5]).

triggered by inverting the potential applied. The only requirements left are installing a conductive resin and a setup designed as an electrochemical flow-through cell.

A commercially applied system close to PCC is capacitive deionization (CDI), which has been successfully developed from a laboratory to an industrially used technology in the last decades. Meanwhile, it is not only used for desalination but also for continuous purification of industrial waste-water and is continually being expanded [6]. Today, CDI electrodes mainly consist of carbon-based nanoparticles or carbon fleet plates, which fabrication and application are among the most recent and popular research topics.

The further development and specialization of promising carbonaceous materials with their extraordinary (surface) properties aroused interest not only in CDI but also in many other capacitive disciplines [7, 8]. The most exciting ones are carbon nanotubes (CNT) [7], which own extraordinary thermal and electric conductivities due to the distinctive delocalized electron system. Thus, the heat transmission is larger than that of diamond, and the electric current carrying capacity is larger than copper [9]. Moreover, the tubes own an extremely high tensile strength and Young modulus, which also explains the growing research interest from the end of the 20^{th} century until today as illustrated in Figure 1.1.

1.1 Background and Motivation

The idea of capacitive separation using carbonaceous materials motivates to develop a preparative potential-controlled chromatographic application to separate organic molecules by merely applying an electrical potential. However, triggering electrostatic interactions of charged species via electric potential came up in the 1960ies [10, 11]. Some decades, the focus was set on designing analytical applications, when the transfer to the preparative scale began in 2003. The group of Sell *et al.* [12, 13] were among the first who published a preparative setup using a nonporous and expensive glassy carbon packed bed electrode to separate carboxylic and amino acids (SSA $<10\,m^2/g$, 1.74 €/g [14]). Afterwards, PCC has been marginally explored further until Brammen *et al.* [15] revolutionized the technology by installing *Baytubes C 150 P* MWCNT as a suitable, inexpensive, and commercially available conductive resin (SSA $220\,m^2/g$).

As PCC can undoubtedly be seen as a promising alternative to elaborate IEX, it absolutely must be developed further. However, since the Baytubes C 150 P disappeared from the market, related materials such as *CNT-K* (0.90 €/g [16]) and *IoLiTec-CNT* (0.45 €/g [17]) have to be screened on their suitability for PCC processing.

The motivation of this work builds on the work of Brammen *et al.* [15], who presented a simple column setup and provided the first proof-of-concept showing that MWCNT can work simultaneously as a chromatographic stationary phase and as a packed electrode. This thesis targets to expand their research and present a universally applicable PCC technology using various MWCNT as an electrode material. Therefore, a precise understanding of the process-operating parameters and their influence on the column response and the electrode performance is necessary to make decisive use of the potential-dependent interactions at the solid-liquid interface, the so-called electrochemical-double layer (EDL). It is essential to understand further that PCC combines two types of separation modes, which both influencing parameters have to be analyzed independently and combined. As the specific EDL formation is the driving force of both technologies, it is particularly focused in this thesis. A multivariant parameter analysis is used to explain the distinct surface effects depending on the operating parameters. The final aim is to deepen the knowledge of potential-dependent surface effects occurring for MWCNT in aqueous systems. In addition, a guide for capacitive process design is developed, taking the PCC prototype a step further for laboratory and industrial applications.

1.2 Fundamental Statements, Hypotheses and Objectives

The fundamentals of the well-established IEX and CDI technologies are used to derive and formulate three general hypotheses (HT), as presented in Table 1.1, on which this thesis' objective of designing a suitable PCC process using a MWCNT matrix is based on.

As capacitive separation technologies already operate with different carbonaceous electrode materials, it is assumed that the application of an electric potential to carbonaceous nanoparticles modifies the surface properties and triggers the interaction mechanism (**HT 1**).

As previous EMLC and PCC studies showed that porous flow-through electrodes are suitable for selective chromatographic separation, it is expected that the MWCNT electrode can be used to separate organic molecules when potential is applied (**HT 2**).

Additionally, it is expected that the formation of the solid-liquid interface depends on several process-operating factors: the setup, the material, and the surrounding environment as well as the target species that affect the cell performance (**HT 3**).

Table 1.1: Fundamental statements the research strategy is based on.

Hypothesis	
HT 1	The application of an electric potential to carbonaceous nanoparticles influences its surface properties.
HT 2	Porous flow-through electrodes are suitable for selective chromatographic separation of organic molecules.
HT 3	The interplay between setup, material, surrounding environment and target species affect the potential-dependent process performance.

1.3 Structure of this Thesis

This thesis's structure correlates to a multi-variant development of a potential-controlled chromatographic process on basis of the process-influencing factors. Figure 1.2 illustrates this thesis's content, divided into the individual chapters, and its classification in the structure.

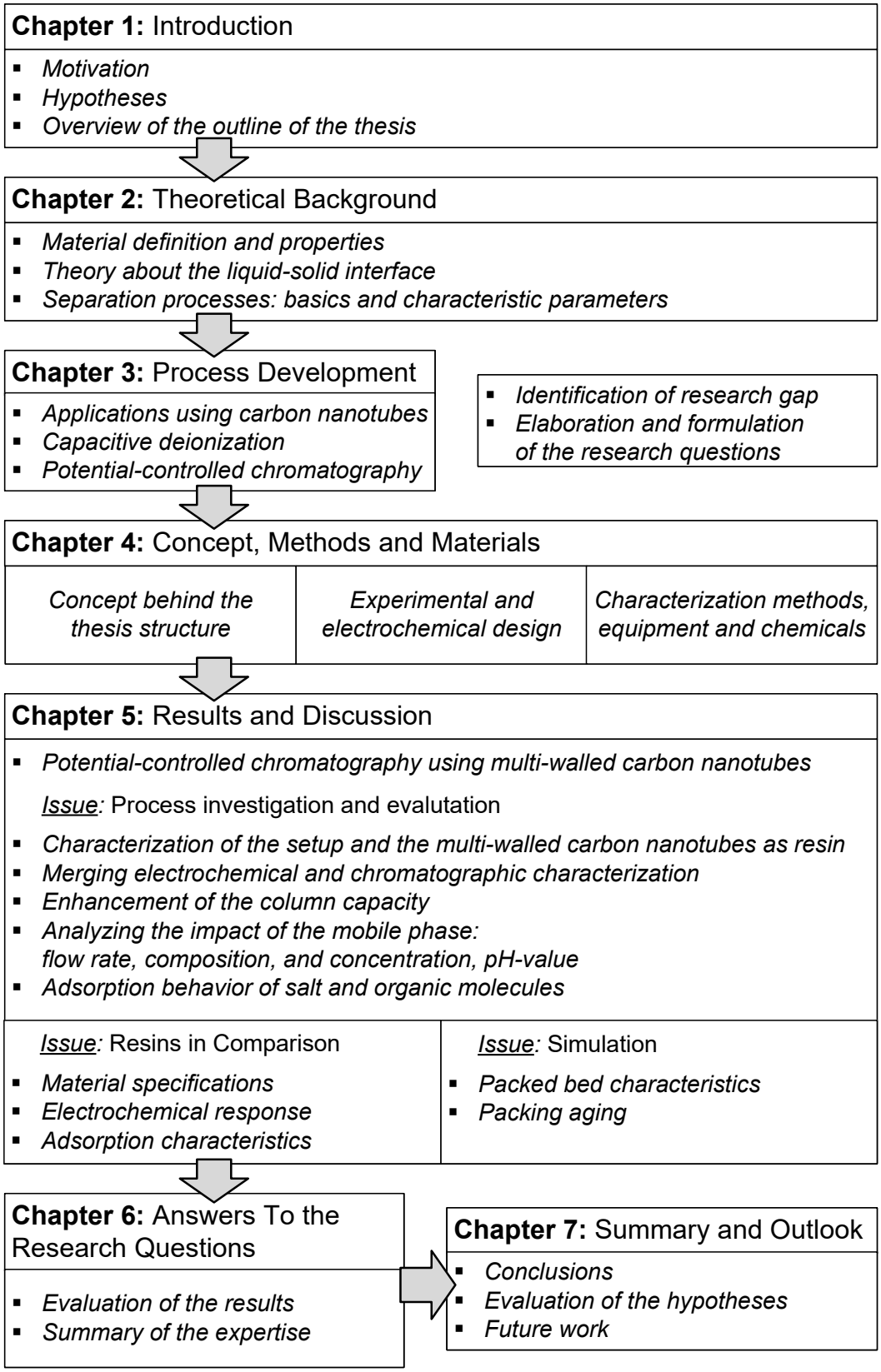

Figure 1.2: Overview of the structure of the thesis.

The contributions and contents presented in publications made during this research project are given in the following:

Trunzer *et al.* [18] – Proof-of-concept for a new CNT-K flow-through cell that functions as a working electrode and a chromatographic fixed bed simultaneously. The combination of chromatographic and electrochemical characterization methods enables evaluating the electrodes' condition and performance over time. Potential-dependent surface effects are visualized, and a competitive character between ions from the mobile phase and the target species for binding sites is presented.

Trunzer *et al.* [19] – Investigation of the influence of the surrounding environment on the column performance. The impact of the fluid flow, as well as the mobile phase's concentration and composition, are investigated chromatographically and electrochemically. The distinct impact of the single parameters on the EDL rearrangement shows that the optimal column performance is always a trade-off. Moreover, a detailed material characterization of the CNT-K is included which ties on the results presented in the previous publication.

Wagner *et al.* [20] – Determination of a simulative model predicting the pH-dependent adsorption of carboxylic and amino acids on different carbonaceous materials. The research about the static binding capacity experiments for CNT-K particles belongs to this thesis. It is highlighted that the adsorption amount of different species to the MWCNT depends on their configuration and their protonation state.

2 Theoretical Background

This Chapter introduces the theoretical background needed to understand PCC processing. Section 2.1 describes the formation of the omnipresent EDL and its role in adsorption processes. Section 2.2 presents general chromatographic characteristics, and Section 2.3 introduces different separation, purification, and concentration methods for polarized or charged ions and molecules. The working principle of capacitive processing is explained in Section 2.4, the specifications of carbon nanotubes are presented in Section 2.5.

2.1 Solid-liquid Interface

The solid-liquid interface formation depends on the interaction mechanism between the solid surface and liquid bulk. The specific concentration gradient formed is called an electrochemical double layer, which is influenced by adsorption (attraction of the species to the surface) and desorption (repulsion of specific species from the surface) processes. The EDL formation is omnipresent and triggered by influencing factors, such as the solid's surface properties, the composition of the liquid (surrounding environment), and the concentration and configuration of the adsorptive species.

2.1.1 Fundamentals of Adsorption

A general three-step adsorption/desorption mechanism is illustrated in Figure 2.1. First, the attracted target species diffuse from the bulk solution (c_{Bulk}) towards the solid surface (**1**). Film diffusion occurs when the natural EDL of the particles has to be passed by the target species (**2**), leading to a linear decline of the species' concentration (c_{film}) towards the solid surface. Here, the target species can adsorb directly on the outer surface (**3a**), or diffuse inside the particle pores (**3b**), which consequences an exponential decrease of the species concentration (c_{pore}). Desorption occurs in the reversed order. The adsorption amount of a target species depends on their concentration in the bulk, the film layer thickness and

permeability, and the accessibility of the pores. The mass transport inside a dynamic system is also limited by convection and dispersion effects. [21]

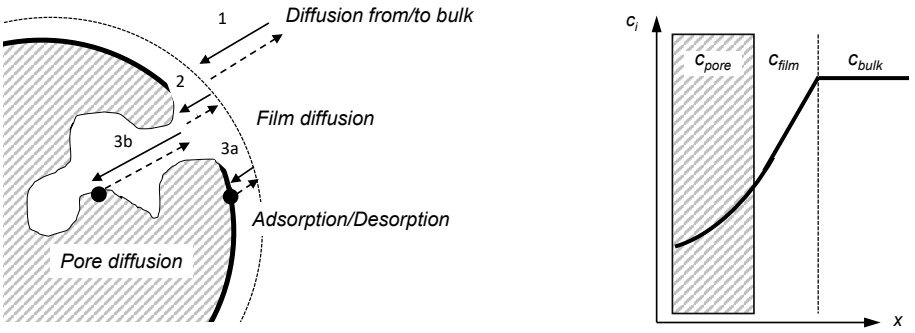

Figure 2.1: Schematic illustration of the adsorption/desorption mechanism.

The adsorption kind and its strength also depend on the characteristics of the specific binding sites (surface properties) and the target species' specification, such as the net charge, the polarization, or the mobility of the species in solution. Here, physisorption appears when the reversible bindings do not affect the surface or species properties, while chemisorption causes irreversible modifications. The interaction forms are divided into electrostatic or covalent bindings. Electrostatic interactions summarize, e.g., strong ionic or atomic bindings, as well as weak hydrogen, dipole-dipole, or Van-der-Waals (VdW) forces. Covalent bindings exist between uncharged species, aromatic ($\pi - \pi$), or coordinated bindings.

Summarizing these fundamentals, a specific material with a specific surface area can bind a specific amount of specific species, defined as load or adsorption amount q. The coverage θ describes the amount of occupied binding sites related to the number of available binding sites. Depending on the adsorption mechanism, the coverage can reach an equilibrium $\theta \leq 1$ when less than or all surface binding places are occupied. Hence, an adsorption maximum q_{max} can exist when the accessible binding sites are blocked. The coverage can also be infinite ($\theta > 1$) when multi-layer adsorption occurs. Different coverage mechanisms at a constant temperature and pressure are theoretically described in so-called adsorption isotherm models, in which the adsorption amount is related to the number of bound ions at equilibrium (equilibrium concentration c_{eq}). The most common adsorption-isotherm models are [3, 22]:

- the *Henry* model, that is often used to determine the relationship between load and equilibrium concentration in lower concentration regions. Its linear equation includes the Henry constant K_H which depicts the slope

$$q = K_H \cdot c_{eq}. \tag{2.1}$$

- the empirical *Freundlich* model, which describes an adsorption amount increasing on basis of a power law. Here, K_F (Freundlich coefficent) and n (Freundlich exponent) presents mathematical parameters

$$q = K_F \cdot {c_{eq}}^{\frac{1}{n}}. \tag{2.2}$$

- the *Langmuir* model, which differs from the others, as it is the simplest model using a physical description based on the assumptions that
  - a homogeneous surface exists at which all binding sites are energetically equal,
  - each binding site can only bind one ion (mono-layer adsorption),
  - no interaction between the binding sites and the ions occurs.

  The mathematical expression

$$q = q_{max} \cdot \frac{K \cdot c_{eq}}{1 + K \cdot c_{eq}} \tag{2.3}$$

  describes a logarithmic increase of the adsorption amount with increasing equilibrium concentration towards a maximal load q_{max} (cf. Figure 2.2). The linear increase of the load in the lower concentration region reflects the Henry isotherm and the slope equals K_H. The Langmuir parameter K depicts the equilibrium concentration at which the load is half, and therewith represents the reaction equilibrium constant between adsorption and desorption mechanism.

The introduced models are only a selection of simplified approaches. As natural systems are more complex, including competing ions or three-dimensional species blocking binding sites, a more complex description of the target's adsorption behavior is necessary. One typical example is the steric mass action model (*SMA* model), which is preferably used to describe

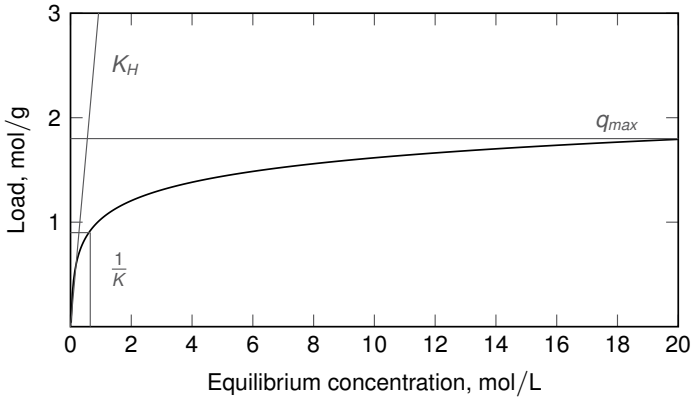

Figure 2.2: Schematic illustration a Langmuir isotherm.

the interaction of proteins on solids. For instance, the model (see Equation 2.4) considers the molecule's effective charge z, its steric hindrance σ, and further information about the influence of counter-ions concentration c_{ion}. [3, 22]

$$q = K \cdot \frac{[q_0 - (z + \sigma)q^z] \cdot c_{eq}}{c_{ion}}. \tag{2.4}$$

2.1.2 Electrochemical Double Layer

How complex the distinct adsorption isotherm models will become, all are based on the same fundamental law: the electrochemical double layer (EDL) theory, defining that each solid surface contacted with a liquid phase is self-charging. Thus, counter-charged ions or molecules are attracted by weak electrosorptive forces, while similarly charged species will be repulsed from the surface. The caused concentration gradient between solid and liquid depends on the characteristic of the material and the surrounding environmental conditions. The EDL's extension and compactness correlate to the surface charge as well as the number of ions and their protonation state in the solution. Moreover, temperature and pressure that triggers the ion mobility and adsorption affinity, influence the EDL. When one of both parameters is modified, a rearrangement of the EDL takes place to restore equilibrium.

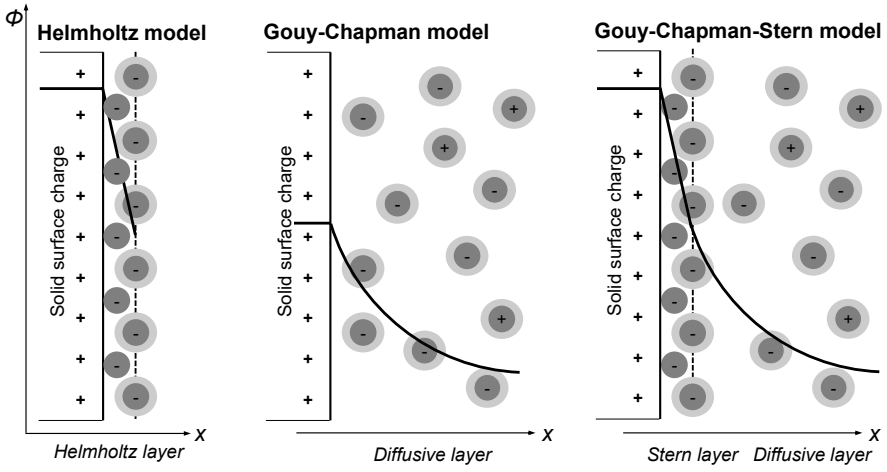

Figure 2.3: Schematic depiction of different electrochemical double layer theories depicting the potential θ decline between charged surface and bulk solution. Non-hydrated ions are printed in dark gray, the hydration shell is illustrated in light gray.

The mathematical description of simplified EDL models (isotherm and isobar conditions) began in the mid of the 19^{th} century: Helmholtz [23, 24] defined that a charged solid surface attracts non-hydrated counter-charged (printed in dark gray) in parallel to the surface and hydrated ions (printed as a light gray shell) in a second layer. The formed, compact layer is illustrated in the left scheme of Figure 2.3 and consequences a linear potential decline between the surface and bulk solution. A complementary theory was formulated by Gouy [25] and Chapman [26] considering the thermal motion of the ions and describing the EDL as a mobile concentration gradient with an exponential potential decline (imprinted in the scheme in the middle). Finally, Stern [27] specified the theory by combining the Helmholtz model with the Gouy-Chapman model to the so-called Gouy-Chapman-Stern (GCS) model in the right picture of Figure 2.3. Today, the model's fundamentals are still valid and are continually being developed further to describe, as the adsorption isotherms, more complex systems properly [28–33].

2.1.3 EDL Formation and Surrounding Environment

Both, the formation of the EDL and the adsorption behavior of a target species to a charged surface depends on the solid's surface properties and the composition and concentration of the surrounding environment (including parts of various species with individual properties). Figure 2.4 illustrates the increasing complexity of the interface formation in multi-component aqueous systems. (**1**) When only water is around, a primary hydration shell of polarized water molecules exists around the solid, correlating to the Helmholtz model. A GCS behavior is expected when an electrolyte or buffer system exists (**2**). Here, the attraction amount and specie's properties define the interfacial properties. Organic broths or wastewater systems

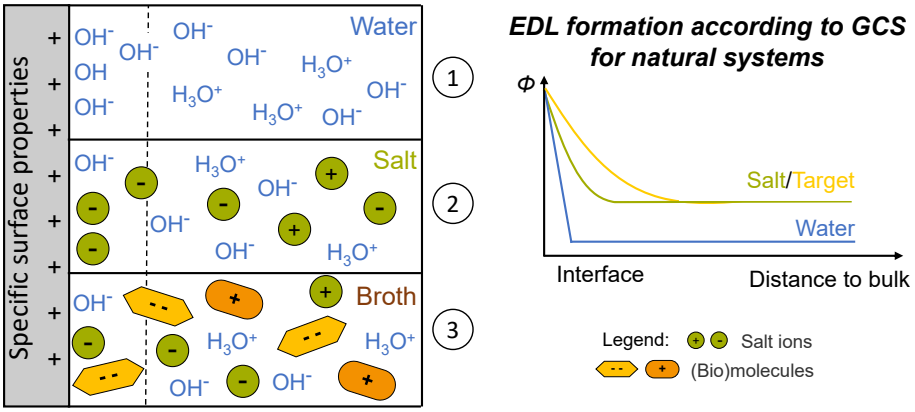

Figure 2.4: Schematic illustration about the complexity of EDL formation in a natural system depending on the ion's and molecule's properties and amount in the surrounding environment.

that contain various salts and organic molecules rise above the simple definition of the GCS model (**3**). The EDL compactness and extension strongly depends on the species' specific properties and their fraction in solution, which is why the surrounding medium determines the binding affinity and amount of a target from the broth to the solid surface.

A key factor influencing a specific formation of the EDL is the acidity or bases of the surrounding medium affecting the solid surface and the molecules' charge. The acidity of a solution is defined over the negative logarithmic concentration of the number of oxonium ions in an aqueous solution, the pH-value. A solution is called acidic when the number of oxonium ions predominates, it is neutral when the amount of oxonium and hydroxyl ions is thermodynamically balanced, and it becomes basic when the amount of hydroxyl ions in the solution rises. Changes of the pH-value directly affect the dissolved molecules' charge and the surface charge of the solid material and reconfigure the EDL.

Chemical species that directly impact the pH-value of a solution being protonated or deprotonated are acids or bases. Their acidic strength (pK_a) depends on their affinity for protolysis and is defined as the logarithm of the relation of protonated state and deprotonated state. Other chemical compounds are affected by the pH-value, which shifts the reaction equilibrium of the oxonium and hydroxyl ions and therewith the charge of the solid surface or the chemical species. A characteristic value to describe the charge of chemical species (e.g., carrying an acid and a basic group) in a specific solution, is the pI-value or isoelectric point (IEP) that describes the pH-value at which the net charge of the molecule is neutral. On the contrary, the net charge of a solid surface is described with the point of zero charge (pzc). When oxonium and hydroxyl ions are the only species in the surrounding liquid, the pH-dependent point of zero charge (pH_{pzc}) equals the IEP.

An overview of common substances' protonation behavior is presented in the Schemes 2.1 for carboxylic acids and 2.2 for amino acids. The protonation behavior of maleic acid and phenylalanine is highlighted as they are used as model adsorbates in this thesis. Further data about specific molecule's protonation can be found in Table A.1 in the supplementary information.

$$\mathrm{R{-}COOH + H_2O \rightleftharpoons R{-}COO^- + H_3O^+}$$

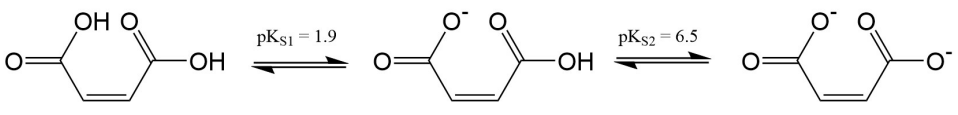

Scheme 2.1: General reaction equilibrium of carboxylic acids and specified for the model analyte maleic acid. *R* reflect various side chains.

$$NH_3{}^+ - CHR - COOH + OH^- \rightleftharpoons NH_2 - CHR - COOH + H_2O$$
$$NH_2 - CHR - COOH + H_2O \rightleftharpoons NH_2 - CHR - COO^- + H_3O^+$$

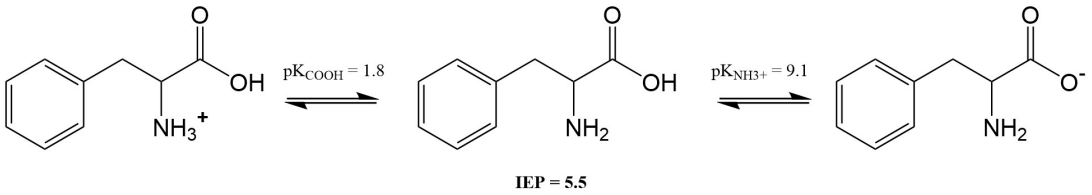

Scheme 2.2: General reaction equilibrium of amino acids and specified for the model analyte phenylalanine. *R* reflect various side chains.

A second EDL influencing factor is the liquid phase's conductivity triggered by the dissolved ions. The small ions have a high charge density, are very mobile in an aqueous solution, and can easily be attracted by an electric field. The dissolution of salt in a solution (electrolyte) can impact the pH-value and trigger molecules' adsorption cooperatively or competitively by promoting the attraction force or blocking binding sites.

For instance, the dissolution of salts from the Hofmeister series in bio-broth (aqueous solution including biomolecules) can, e.g., stabilize the natural structure of the biomolecules (cosmotropic ions) or cause denaturation or precipitation of the enzymes or proteins (chaotropic salts). The phenomenon depends on the hydration degree of the ions. While the cosmotropic ions (left of Cl^-) are well-hydrated and place themselves around the biomolecules, ions with chaotropic character (right of Cl^-) penetrate inside the large molecules and break their tridimensional structure [34].

The chaotrope character of the anions increase in the order:

$$SO_4^{2-} < HPO_4^- < Cl^- < NO_3^- < SCN^-,$$

and the one for cations:

$$H_4^+ < K^+ < Na^+ < Mg^{2+} < Ca^{2+} < \text{Guanidinium}.$$

2.2 The Chromatographic Principle

Chromatography is a commonly used separation or concentration method based on the formation of various interaction forms and strengths of the species and the stationary phase material (resin). The fluid transporting the species through the column is called a mobile phase, not interacting with the solid. Chromatography can be performed two dimensional

(thin-layer chromatography) or three dimensional (column chromatography) and is defined over the combination of the resin state (solid, liquid) and the mobile phase (liquid, gas). Different chromatographic separation methods can be realized depending on the interaction mechanism, like size-exclusion, affinity, hydrophobic or ion-exchange chromatography.

In this thesis, solid-liquid column ion-exchange chromatography is focused only, which exemplary separation process is schematically depicted in Figure 2.5. The interaction kind and affinity of the species controls the adsorption/desorption mechanism at the solid-liquid interface. A high interaction affinity increase the residence time t_R (respectively retention volume V_R) of the species on its way through the column. When the species are retained completely, the bindings are dissolved by changing the mobile phase properties (pH-value, ion concentration, solvent). In addition, t_R depends on the flow rate and the column length L.

The separation efficiency increases the more often the species interacts specifically with the solid phase on their way through the column, and the larger the difference between t_R of the different species. When mass transfer effects are minimal, the fraction purity and yield increase. A control variable describing the separation quality and the peak resolution is the $HETP$ value defining the height equivalent of theoretical plates in dependency of the mass transfer properties (A axial/Eddy-diffusion and B longitudinal dispersion as well as C diffusion kinetics, see Van-Deemter-Equation 2.10) and the flow rate. The smaller the $HETP$ is, the higher is the number of the theoretical plates N (equilibration steps adjusted between the target species and the solid surface) for a defined column length L (see Equation 2.8). [3, 22]

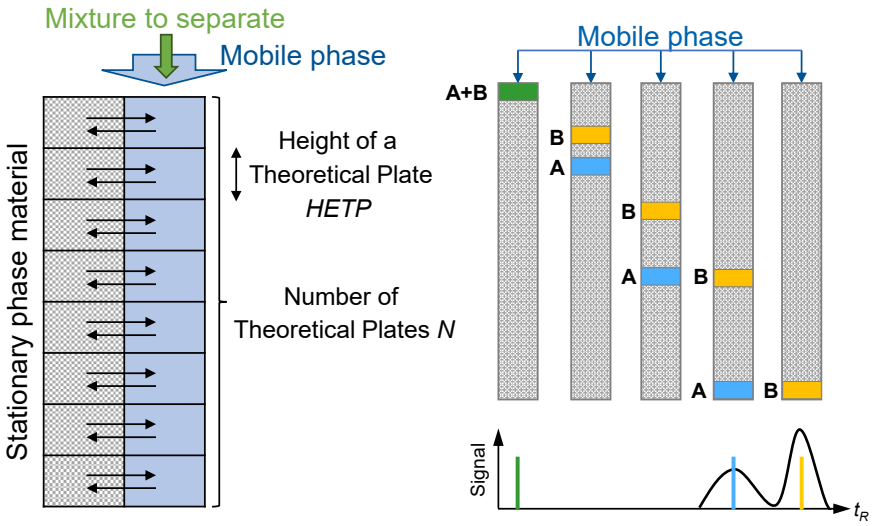

Figure 2.5: General chromatographic separation principle.

Several more characteristic parameters describe the column quality, as summarized below, that can be determined in so-called tracer analysis (see Figure 2.6). Tracers are ions or molecules that do not interact with the stationary phase and give specific information about the species pathway through the porous system. They visualize the accessible column volume or total column volume and highlight the fundamental convection, dispersion, and diffusion effects. Here, convection correlates to the species' longitudinal pathway through the column enforced by the volume flow rate. Dispersion describes the radial distribution of the species when their direct pathway is disturbed by an obstacle. In contrast, diffusion describes the way of a target from bulk to the surface (correlating to the film layer and pore diffusion). The smaller the tracer peak width (fraction) and the more Gaussian it is (asymmetric value), the higher is the column resolution and efficiency [3, 22]:

- the system dead volume V_{dead} represents the plant volume between the injection valve to the UV detector or the conductivity sensor;
- the column volume V_{col} describes the cylindrical volume of the column;
- the retention time t_R or the retention volume V_R is measured in the peak maximum and describes the process time/volume when the eluent reaches its maximum output signal;
- the corrected retention time t'_R or the corrected retention volume V'_R is calculated as the difference of the retention time or retention volume and the dead volume;
- the column porosity, respectively particle bed porosity ϵ_{bed} (inter-particle porosity, see Equation 2.5) is determined using non-pore-penetrating tracer (e.g., dextran; $V_{dextran}$). The peak shape visualizes the pathway of species that do not enter the particle pores and highlights convection and dispersion effects

$$\epsilon_{bed} = \frac{V_{dextran} - V_{dead}}{V_{col}}; \tag{2.5}$$

- the total column porosity ϵ_{tot} is determined with a small pore-penetrating tracer, e.g., NaCl (V_{NaCl}) able to enter the total pore system and equals the sum of inter- and intra-particle porosity (see Equation 2.6)

$$\epsilon_{tot} = \frac{V_{NaCl} - V_{dead}}{V_{col}}; \tag{2.6}$$

- the intra-particle porosity (bead porosity, ϵ_{bead}), which can be calculated as presented in Equation 2.7:

$$\epsilon_{bead} = \frac{V_{NaCl} - V_{dextran}}{V_{col} - V_{dextran}}; \tag{2.7}$$

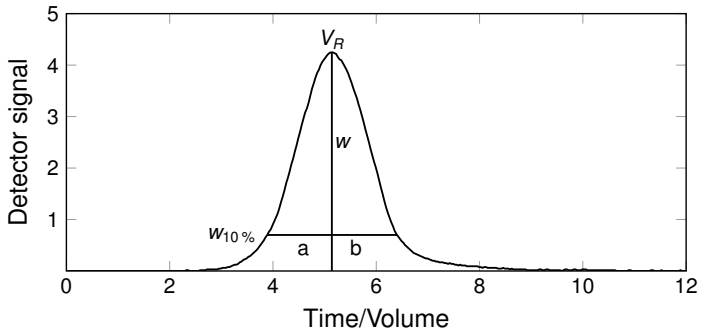

Figure 2.6: Schematic illustration of an ideal shaped (Gaussian) tracer peak to gain characteristic parameters: the retention volume V_R, the peak height w and the peak height at 10 % $w_{10\,\%}$, as well as the distances a and b from the slope of the peak to the perpendicular at the peak maximum to calculate A_s.

- the asymmetric factor $A_s = b/a$ identifies the column's homogeneity, which is ideal when the peak is Gaussian shaped ($A_s = 1$). It is calculated by dividing the distance between the peak maximum perpendicular and the right peak slope b through the distance between the peak maximum and the left peak slope a at 10 % of the peak height ($w_{10\,\%}$). If $A_s < 1$ the tracer peak is *fronting*, while it is *tailing* when $A_s > 1$. Fronting can be induced by channels inside the packed bed or an early saturation of the stationary phase. Tailing is induced when dead zones exist inside the packed bed or overloading of the mobile phase occurs. In real applications, the packing is defined qualitatively valid when $0.8 < A_s < 1.2$; and, as mentioned
- the $HETP$ can be calculated over the number of theoretical plates (Equation 2.8), or from tracer profiles as depicted for the half-peak-height-method in Equation 2.9. Here, $w_{50\,\%}$ depicts the peak width at half of the peak height w and the retention volume V_R. Moreover, it can be calculated with the Van-Deemter Equation (Equation 2.10).

$$HETP = \frac{L}{N} \tag{2.8}$$

$$HETP = \frac{L}{5.54}\left(\frac{w_{50\,\%}}{V_R}\right)^2 \tag{2.9}$$

$$HETP = A + \frac{B}{u} + C \cdot u \tag{2.10}$$

2.3 Separation Processes

A detailed overview of the qualifications of standard liquid-solid separation techniques is given for ion-exchange chromatography (IEX), capacitive deionization (CDI), and potential-controlled chromatography (PCC) shortly. IEX is quite common to separate and concentrate pharmaceuticals or fine chemicals based on the target's ionic adsorption and its replacement when the counter-ion concentration increases in the elution medium. CDI is a capacitive separation method used to purify and concentrate charged ions from wastewater when an electric potential is applied. Today, desalination is the most common application field, but the capacitive technology is also used to capture pharmaceuticals or dyes from wastewater. PCC is a combination of IEX and CDI using the potential-dependent adsorption technology from CDI to separate organic and inorganic molecules in a 3D flow-through cell.

Ion-Exchange Chromatography

Ion-exchange chromatography is a powerful technique to separate and concentrate a broad range of charged molecules in analytic and preparative applications. Depending on the charge of the molecules to be separated, anion and cation exchangers are used, which operate with a counter-charged resin.

The IEX separation process is introduced by loading the column with a sample mixture to separate, as depicted in Figure 2.7 on the left side. Counter-charged target species are adsorbed during the separation phase, while similarly charged molecules are repelled from the resin and flush through the column. Desorption (elution) is induced when salt is used as a counter-ion, replacing the bound molecules. Depending on the interaction strength of the adsorbed molecules, they elute at different salt concentrations. The desorption mechanism is commonly induced by step – immediate change of the mobile phase medium, or gradient – smooth transfer of the mobile phase properties [22].

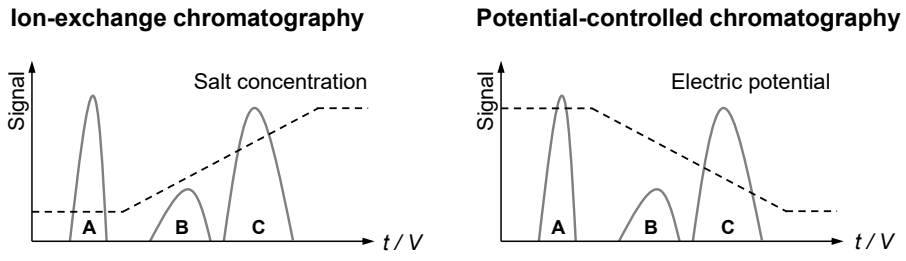

Figure 2.7: Exemplary chromatograms for ion-exchange chromatography (IEX) and potential-controlled chromatography (PCC). The detected fractions represent unbound molecules (fraction **A**), weakly adsorbed molecules (fraction **B**), and strongly bound molecules (fraction **C**).

Potential-Controlled Chromatography

The working principle of PCC is closely related to conventional IEX (see also Figure 2.7). However, a conductive resin is required, which works simultaneously as a chromatographic fixed bed and a working electrode. For instance, suitable PCC resins can be pristine and available carbonaceous particles making the packing inexpensive. The resin is not restricted to specially prepared surfaces, and by controlling the attraction direction via electric potential, PCC can function as an anion and cation exchanger offering a broader field of application than IEX. PCC's key advantage is that no additional elution additives are required to induce desorption, making the technique economically interesting. Thus, scalable PCC can become a cost-effective, fast, and flexible alternative to conventional IEX.

A simplified working principle of a PCC process is illustrated in Figure 2.8. The process is initiated after the potential-controlled surface charge is equilibrated. A positive potential provokes a positive surface charge, while a negative one will enforce negatively charged particles. Potential-controlled separation occurs when controversially charged target species are electrosorbed to the charged surface, while as in IEX, equally charged molecules are repulsed. Afterwards, elution can be induced by inverting the potential direction immediately or via a gradient.

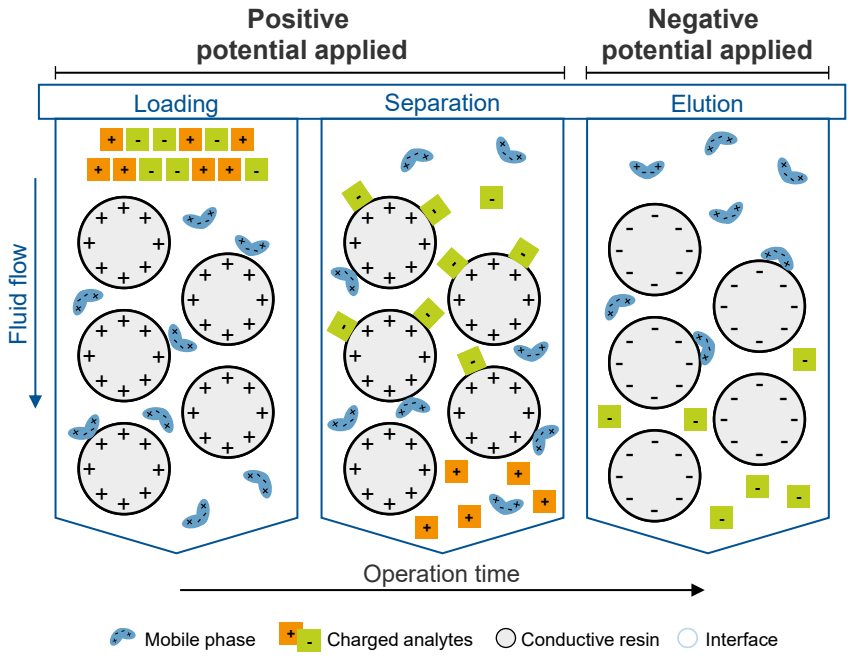

Figure 2.8: Simplified working principle of potential-controlled chromatography. Adapted from Trunzer *et al.* [18].

Capacitive Deionization

While the development of a potential-controlled chromatographic separation process is yet in its infancy, capacitive deionization is a well-established technology in industrial de-salting or wastewater treatment. The scalable parallel-plate device often works with nanoporous electrodes made of porous graphitic carbon or activated carbon electrodes. Controversary to the IEX or PCC columns operating in a batch application, CDI cells exist as flow-by electrodes and can continuously purify or concentrate the mobile phase (working principle in Figure 2.9). The CDI cells can function at high flow rates as chromatographic plants and benefit throughput and yield. Today, several application-dependent improvements of the classical CDI cell, such as membrane CDI or faradaic CDI systems, exist. The advantage of membrane CDI is that the installed ion exchange membranes prevent opposite ion attraction when the electrode direction is shifted. Besides, selective processing can be realized when the electrosorption is triggered via faradaic surface reactions [35–38].

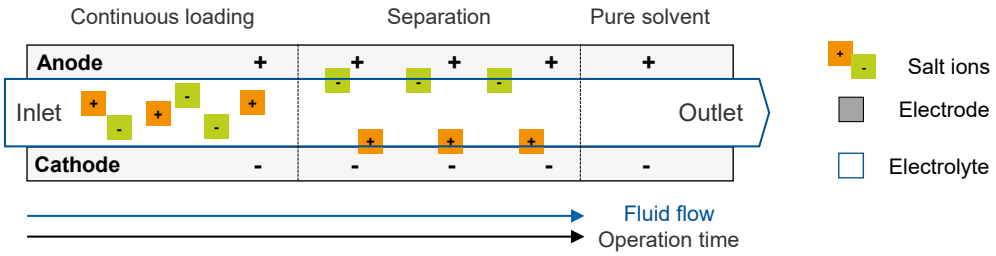

Figure 2.9: Simplified working principle of capacitive deionization.

2.4 Background to Electrochemistry

Fundamental for electrochemical processing is the knowledge about the electrochemical principle and the interplay between electrode resistance, applied potential, and the surrounding environment. Electrochemical applications can differ in their operation conditions, which is why there is a wide range of analysis criteria to gain process-specific information. In the following, the background and the analysis methods relevant to this thesis are presented.

2.4.1 Electrochemical Principle

The electrochemical principle is based on Ohm's law: the amount of electric current I depends on the electric voltage U divided by the resistance R of the conductor. Hence, the fundamental definitions used to describe an electrochemical system are:

- Electric current I, is the amount of electrons that pass through an electric conductor.
- Electric conductor, defines a medium with a high amount of free electrons.
- Electric potential ϕ, is the potential energy in one point which activates charge transport in an electric field.
- Electric voltage U, is the difference of the electric potential between two points.
- Electric charge Q, is the amount of current transported in an electric system over time.
- Electric capacitance C, is the accumulated electric charge divided through the applied voltage.

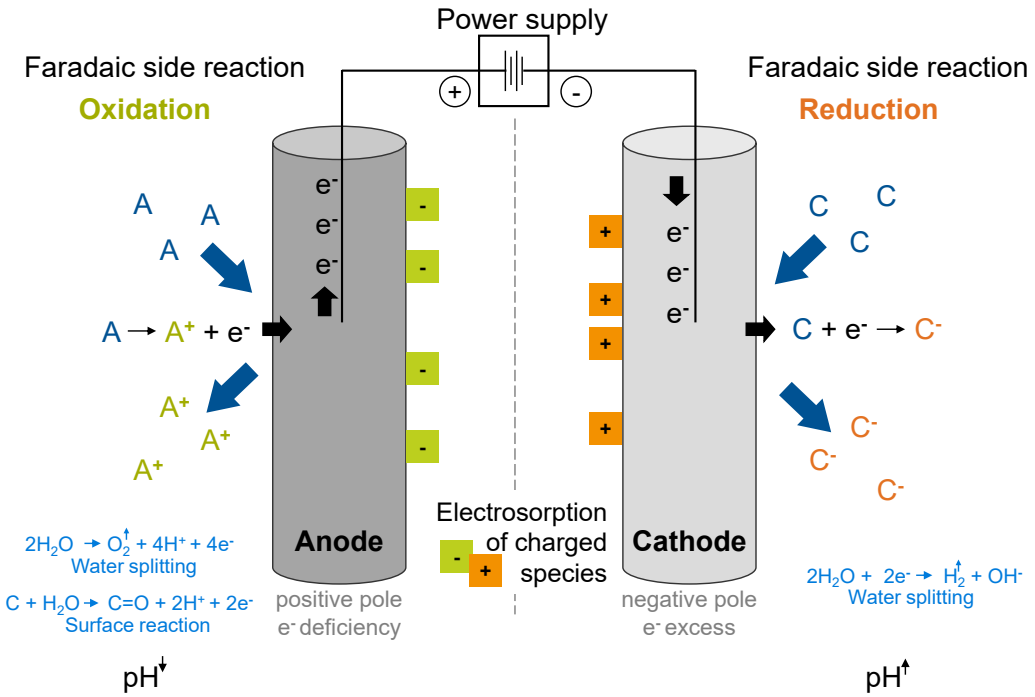

Figure 2.10: Simplified functional principle of an electrolytic cell including charged molecule adsorption and the impact of parasitic side reactions when other species, such as A and C are present.

Operating an electrochemical cell requires energy emission or absorption. Galvanostatic cells provide electric current to the installed system; electrolytic cells require electric current to

induce chemical reactions, and accumulators can provide or adsorb electric current. As electrolytic cells are used in this thesis, Figure 2.10 presents a working scheme to highlight the different electrosorptive and redox-reaction possibilities occurring inside the cell.

Electrolytic cells are built with at least two electrodes working as an electron conductor and placed in an electrolyte solution, which functions as an ion conductor. A power supply forces the current flow from the anode (a positive pole with electron deficiency) to the cathode (a negative pole with electrode excess). Chemical reactions and electrosorption can occur on both electrodes. For instance, the anode is a reduction agent, inducing water splitting by electron adsorption. The free electrons are collected and transported to the cathode, which functions as an oxidation agent and transfers the surplus electrons to the electrolyte.

Electrosorption without releasing electrons occurs on the basis of the EDL theory when the setup is an ideal capacitor. Here, the capacitive current declines to zero when the capacitor is loaded with charged species completely. Faradaic current exists wherever a constant electron uptake or release occurs, providing continuous current flow. Electrolysis and a chemical modification of the surface of the electrode is a consequence. [39]

A natural chemical reaction occurring inside an aqueous electrolytic cell is water splitting:

$$2H_2O \quad \rightarrow \quad 2H_2 + O_2. \tag{2.11}$$

The cathode (surface charge is negative) in particular favors the reduction of water, and a generation of hydroxyl, increasing the pH-value to basic conditions. Besides, dissolved oxygen can also be reduced:

$$2H_3O^+ + 2e^- \quad \rightarrow \quad H_2 + 2H_2O, \tag{2.12}$$

$$2H_2O + 2e^- \quad \rightarrow \quad H_2 + 2OH^-, \tag{2.13}$$

$$O_2 + 2H_2O + 4e^- \quad \rightarrow \quad 4OH^-. \tag{2.14}$$

Water oxidation can occur at the anode (surface charge is positive) favoring the disposal of oxonium ions, which decrease the pH-value to acidic conditions:

$$6H_2O \quad \rightarrow \quad O_2 + 4H_3O^+ + 4e^-, \tag{2.15}$$

$$4OH^- \quad \rightarrow \quad O_2 + 2H_2O + 4e^-. \tag{2.16}$$

Moreover, the surface of carbonaceous electrode can get oxygen-functionalized:

$$C_{surface} + H_2O \rightarrow C = O_{surface} + 2H^+ + 2e^-, \tag{2.17}$$

$$C = O_{surface} + OH^- \rightarrow COOH_{surface}, \tag{2.18}$$

$$COOH_{surface} + OH^- \rightarrow C = OO^-_{surface} + H_2O. \tag{2.19}$$

2.4.2 Electrochemical Characterization Methods

While, in theory, ideal capacitors exist, the reality is more complex. Often porous materials, foams, or particle packed beds are used, guaranteeing a high specific surface area as well as a fast charge and electron transfer. When the cells are built as a series connection of different resistances (contact resistance, electrolyte resistance, and mass transport resistance), a capacitive and a faradaic part exist, which is why the choice of the electrode material, its configuration, and the electrolyte properties are decisive parameters influencing the electrode performance. A selection of standard electrochemical characterization methods to visualize the application differences is introduced in the following. Their results depend on mass transfer effects triggering the formation and rearrangement speed of the solid-liquid interface and can deviate for real systems. [28, 39]

Open circuit potential, point of zero current, and point of zero charge:

The Open circuit potential (OCP) describes the electrode condition, identifying the electrode surface's net charge at rest for an open voltage source when no current flows. Besides, the point of zero current equals the potential applied externally at which no current flows. This potential value is the energetical optimum for capacitive processes. The point of zero charge correlates to the net neutral surface charge density of the electrode.

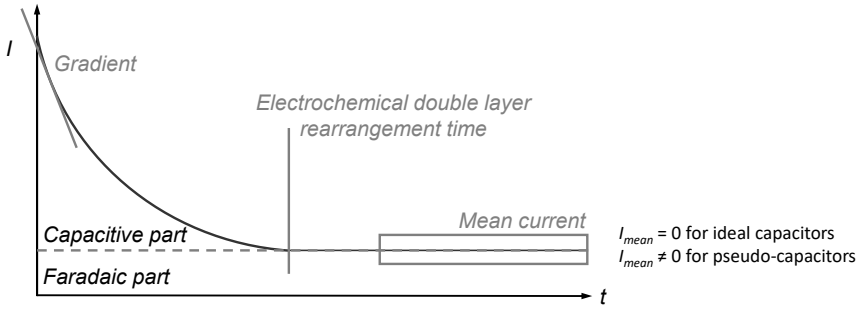

Figure 2.11: Schematic evaluation of a chronoamperogram.

Chronoamperometry:

Chronoamperometry is a method to study the current profile over time when a constant potential is applied. Figure 2.11 depicts an exemplary output signal, illustrating that the current declines until a constant signal is reached. The time necessary to equilibrate the current signal correlates to the EDL's rearrangement time and can be expressed with the gradient calculated immediately at the beginning. When the equilibrium current (mean current, I_{mean}) is zero, the integral area equals the electric charge of an ideal capacitor; when it differs, a pseudo-capacitor exists. Here, I_{mean} correlates to the part of faradaic current and indirectly gives information about the electrode resistance. The total electric charge of the pseudo-capacitor is a sum of the area integral of both capacitive and faradaic current.

Cyclic voltammetry:

Cyclic voltammetry (CV) is used to describe the capacitive and faradaic character of an electrode. The potential applied is continuously modified (increasing and decreasing in the form of a triangle). CV is commonly run for several cycles to determine deviations in the current flow indicating aging due to irreversible changes in the electrode's properties. When the current profile overlaps over the cycles, a reversible, redox-active system is identified. Exemplary current profiles are depicted in Figure 2.12, visualizing that the CV of an ideal capacitor is rectangular, charged and discharged reversibly based on electrosorption. When leakage current or other influencing parameters like convection through fluid flow exist, the rectangular profile is shifted angularly. Faradaic current deforms the current profile. The current peaks correspond to the potential, which induces electron flow on the basis of redox-reactions.

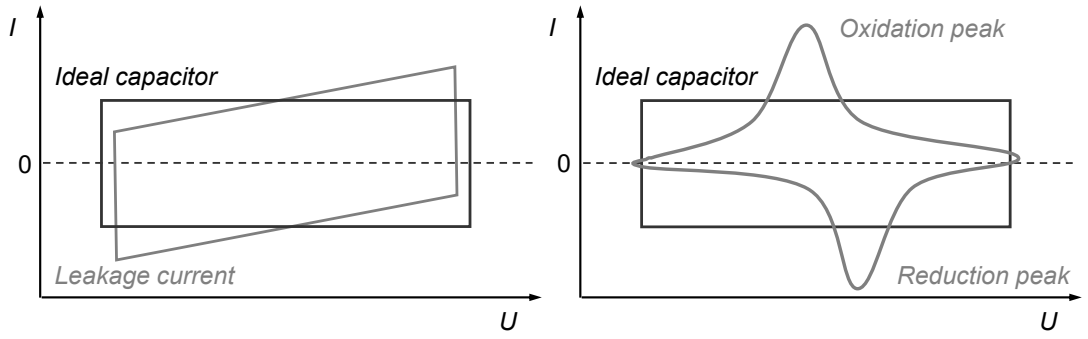

Figure 2.12: Cyclic voltammogram for an ideal capacitor (left) and a redox-active cell (pseudo-capacitor, right).

2.5 Carbon Nanotubes

Carbon nanotubes (CNT) are curled graphene sheets composed of at least one (single-walled, SWCNT) or multiple (multi-walled, MWCNT) tubes. According to the Russian doll model, the MWCNT can be formed as a couple of tubes stacked into each other. On the other hand, they can be wrapped like a parchment. The average outer diameter of a SWCNT is between 0.4 and 2.0 nm, the average of MWCNT is between 2 and 50 nm, but can also increase to 100 nm. The MWCNT are further defined over the numbers of walls that stack into each other, which interlayer spacing is around 0.34 to 0.39 nm. Ideal SWCNT or MWCNT have a smooth sp2-hybridized carbon lattice with open or closed ends. They can grow from less than a hundred nanometers to several centimeters [9, 40, 41]. Schematic drawings and magnifications of a SWCNT and a MWCNT are illustrated in Figure 2.13.

SWCNT exist in three configurations: armchair, zig-zag, and chiral. While the armchair SWCNT are metallic, zig-zag and chiral SWCNT can be metallic or semi-conductive depending on their vector configuration. Rolling the tubes along a graphene sheet related to the chiral vector $c = n \cdot a1 + m \cdot a2$, armchair SWCNT exist when $n = m$, zig-zag SWCNT when $m = 0$, and chiral when $n \neq m$. When $n - m$ is a multiple of 3, the SWCNT is metallic and therewith highly conductive [41]. In comparison to SWCNT, MWCNT are always metallic, as the multiple sheets behave like graphite [42].

There are three main synthesis routes to create carbon nanotubes [41, 43]:

- laser ablation – carbon nanotube growth due to vaporization of a solid carbon source in an inert atmosphere, production temperature ≈ 1500 K, SWCNT and MWCNT;
- electric arc discharge – carbon nanotube growth induced by an electric arc between two graphite electrodes in an inert atmosphere, production temperature ≈ 4000 K, SWCNT and MWCNT; and
- chemical vapor deposition – carbon nanotube growth on metal catalyst particles in a gaseous carbon source, production temperature < 1000 K, mostly MWCNT.

Each method has its advantages and disadvantages. However, to produce CNT in a large series, the chemical vapor deposition (CVD) convince as works at low temperatures and is a simple-to-handle technology. The choice of the catalyst directly controls the nanotube morphology. Thus, it is possible to synthesize high-purity and uniform CNT species, but also inexpensive random bulk mixtures [40, 41].

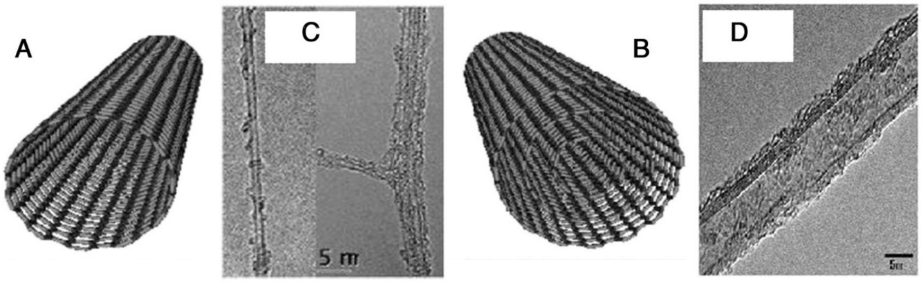

Figure 2.13: Schematic illustrations (A,B) and TEM magnification (C,D) of SWCNT (A,C) and MWCNT (B,D). Adapted from Eatemadi *et al.* [41]. Licensed under CC-BY-4.0 (https://nanoscalereslett.springeropen.com/articles/10.1186/1556-276X-9-393).

Ideally, shaped CNT have a smooth and defect-free hexagon lattice. The sp2-configuration causes a non-polar and hydrophobic behavior, which agglomerate over Van-der-Waals (VdW) forces. These CNT own a extremely high specific surface area (SSA, SWCNT $> 1000\,\mathrm{m^2/g}$) due to their high aspect ratio and low density (SWCNT: $1.4\,\mathrm{g/cm^3}$). Moreover, the tensile strength of CNT is with 11 to 63 GPa around 100 times higher than the one of steel, and the thermal or electric conductivity are similar to copper [9]. However, bulk CNT have often defects, like pentagon or heptagon ring formation, wall flaking, or functionalization of the side-walls, directly impacting and often decreasing the specific material properties. Nevertheless, the conscious changes of the material properties can also be advantageous, e.g., to trigger the dispersion of the CNT in inorganic or organic solvents. For instance, non-covalent functionalization via VdW, hydrophobic, or $\pi - \pi$ binding is preferably used to provide dispersion without damaging the CNT surface structure. Moreover, covalent functionalization directly affects the surface configuration when the desired groups are chemically synthesized to the CNT side walls. [7, 9, 44, 45]

3 Process Development

This Chapter briefly introduces various application fields of CNT in Section 3.1, while Section 3.2 focuses on the development of CDI technology. The fundamentals of potential-controlled chromatography are highlighted in Section 3.3. The Chapter closes by identifying the existing research gap in Section 3.4 that is the origin of this thesis.

3.1 Today's Application Fields of Carbon Nanotubes

For several years, carbonaceous nanoparticles have gained popularity in research and have also aroused industrial interest. Today, the range of applications working with charged carbonaceous surfaces reaches from energy generation, conversion, and storage [46–48], biomedical application and tissue engineering [42, 49], electroanalysis, sensors, and bionic devices [50–52], to wastewater treatment and other separation technologies [53–56]. Notarianni *et al.* [7] highlighted, in particular, the demand for and application of CNT in different disciplines:

Carbon Nanotubes as Supporting Material

The low weight and high SSA, as well as their excellent mechanical stability, chemically inertness and electrically conductive, make CNT an interesting additive or carrier material. For instance, CNT are applied in aerospace to reduce weight or support high tensile strength and thermal stability. They are added in special polymers to be used for radial protection [57], or are implemented as a suitable additive or coating for micro-electrodes and sensors [58]. In research, CNT are investigated for their application in drug delivery and cancer therapy [59–61]. They are also found in sensors for human motion and robotics or are used in tissue engineering [49]. Having a high adsorption capability without the need for ligands or antibodies, MWCNT are further investigated as a universal adsorbent for bacteria or proteins in water purification, food processing, or the purification of implants [62].

Carbon Nanotubes in Separation Technology

The CNT excellent adsorption affinity to organic molecules is caused by various possible interactions [55, 56, 63], which is why they are used, e. g., in solid-phase extraction and micro-extraction. Besides, CNT are applied in chromatography, like gas chromatography, capillary electrochromatography, and liquid chromatography, as well as in electrophoresis [64–66]. For instance, in gas chromatography, CNT benefits with its large number of active sites, binding aromatic or unsaturated organic molecules over $\pi-\pi$ attraction. Moreover, the resin structure enables fast mass transport and a high resolution [64, 67]. Most often, CNT are used as a functionalized or a composite material, gaining an adapted use of the system, promoting simple handling and higher selectivity [67–69]. On the preparative scale, CNT convince as an unspecific or selective functionalized adsorbent to purify water contaminated with toxic organic pollutants, like organic dyes, pharmaceuticals, and pesticides [70, 71].

Carbon Nanotubes in Electrochemical Application

Due to their extraordinary conductivity, CNT are well-established in electrochemical applications, mainly installed as an additive or coating for other carbon-containing, metal, or polymers electrodes [51]. They can be found in analytical electrophoresis technology, e.g., capillary electrochromatography, in which they function as a stationary phase [72–74]. Besides, they are used for electrochemical detection and removal of organic pollutants [50], as well as an additive for fluorescent sensors, calorimetric sensors, electronic and electrochemical sensors [75]. When CNT are functionalized with biomolecules, like proteins, enzymes, or antibodies, they can also be used for biochemical sensing [76–78]. Possibly the largest application field is hydrogen storage, batteries, and super-capacitor technologies [79, 80]. In these applications CNT benefit the electrode performance decisively due to the fast electron transfer inside the delocalized $\pi - \pi$ system [81–83].

3.2 Capacitive Deionization and Related Technologies

Capacitive deionization (CDI) is a electrosorptive separation technique commonly used to separate metal salts or other impurities from low-concentrated saline water. Moreover, CDI technology is today used to remove environmentally harmful organic species from brackish water, such as pharmaceutical residue or dye. In addition, specifically treated electrodes are used for disinfection, e.g., for killing *Escherichia coli* in flowing water [6, 84, 85].

Compared to electrodialysis, in which ion transfer through semi-permeable membranes is triggered, CDI equals a plate capacitor that functions on the basis of the EDL theory. CDI applications have a low energy consumption, and combined with electrodialysis devices an economically, efficient separation and purification method for charged species had been established in the industry.

The development of CDI began in the 1960^{th} when Blair and Murphy [10] were one of the first researchers discussing an electrically induced ionic adsorption on porous electrodes to separate NaCl from saline water. They stated that carbon-based electrodes turn out as the most promising material, with the required properties of electrochemical stability, a large accessible surface area, fast ion mobility within a porous network, high electronic conductivity for a fast electron transfer, and a good wettability [6, 86]. At the turn of the millennium, the research breaks through, and the number of publications exponentially increases to over 250 publications in 2018 [5]. Today, many different carbon-based materials are analyzed and established for CDI, like activated carbon, graphene, carbon nanotubes, carbon aerogels, or carbon-based composite materials. For instance, Farmer *et al.* [87] focused on removing heavy metals using carbon aerogels as a promising alternative to activated carbon electrodes. Other researchers investigated carbon aerogels and CNT-CNF monoliths to deionized groundwater [88–90]. Thereby, it was determined that the use of functionalized CNT with higher hydrophilicity increases the electrode performance and decreases the electrolyte resistance [91]. When the electrodes are designed as meso- or macroporous systems, they achieve a high mass transfer and good electrode performance as no EDL overlapping occurs [92, 93].

Understanding the basic findings of capacitive processing in the simple through-by setup, a competition for the best-operating conditions began with the final goal to enhance the desalination performance and maintain a scalable cell with long-term stability. While the usage of a pristine carbonaceous electrode pairs dominate in the development of CDI [6, 54, 94], some researchers claimed that the upgrade from 2D to 3D electrodes would increase the electrode efficiency due to a higher SSA, lower mass transfer limitations, and shorter processing times [91]. Flow-through, membrane or inverted CDI methods have also been studied with their individual benefits and goals for a specific application. Today, research on capacitive separation is still growing as no optimal and universally applicable process is found yet [6].

3.3 Development of Potential-Controlled Chromatography

Potential-controlled chromatography was initially reported in 1960 when Voorhies and Davis [11] investigated a particulate carbon black electrode for adsorption and electrolysis of organic molecules and inorganic ions. The static process was developed as an analytical method to quantitatively describe the cathodic reduction of the molecules in aqueous systems. Later, Blaedel and Strohl [86] adopted the principle and designed a continuous electrolytic cell for electrolysis and separation of metal ions. The cylindrical three-electrode setup was constructed for dynamic application, using graphite particles packed in a porous glass cylinder. This elaborated setup later proved to be the basis for the subsequent research and can be found similarly in numerous cell types [12, 95–97].

It required some time until the terms *electrolytic chromatography* or *controlled potential electrolysis* were characterized by Fujinaga *et al.* [98] and Okazaki [99], who separated lead and bismuth successfully by potential switch. Even later, the research field was characterized by the well-known terms *electrochemically modulated liquid chromatography* (EMLC) [100] and *potential-controlled chromatography* (PCC) [12].

Although the idea of potential-controlled separation was born early, the development of the challenging process advanced slowly, with its peak in the last decades of the 20^{th} century. Its advancement can be divided into two main and several sub-parts. On the one hand, researchers focus on the macroscopic (hardware) process aspects like the setup, the electrode material, or the molecules to separate. On the other hand, microscopic impact factors are analyzed, such as fluid dynamics, mass transfer properties, and interfacial interactions. There was hardly any research that consistently considered both parts.

Moreover, the process was limited to analytic approaches for a long time only, until Knizia *et al.* [12] and Kocak *et al.* [13] enlarged it to a preparative scale after the turn of the millennium. Most recently, Brammen *et al.* [15] introduced a simple setup filled with low-cost and applicable resin, the MWCNT, and is perhaps the first making PCC interesting for industrial application.

The Hardware Development

Early in the process development, a three-electrode column design with or without an electrolyte reservoir prevailed. However, the working electrode contact was constructed differently, as plates, linear, or coiled wire, which is why longitudinal, semi-radial, or radial potential distribution within the particle fixed bed is possible [96, 101–106].

The most established stationary phase materials are carbonaceous materials like porous graphitic carbon [107, 108] or pristine or polymer-coated glassy carbon (GC) [12, 104, 109]. But also silver powder [110, 111], boron-doped diamond powder [112], or recently multi-walled carbon nanotubes [15].

The various setup were able to successfully separate metal ions [86, 99], quinones [95, 113], benzene derivatives [103, 114], as well as aromatic sulfonates [115–117] and mixtures of corticosteroids [118, 119] on an analytical scale. However, on a preparative scale, the separation of carboxylic or amino acids mixtures were only proven by Sell's group [12, 13]. For this reason, there is a tremendous need for research on the part of preparative process development to understand and build the fundamentals of scalable application.

The Microscopic Investigations

With ongoing research on analytical scale, the microscopic factors gained importance. Therefore, the influence of the material morphology on the column performance as well as the mobile phase composition on the adsorption capacity have been investigated. Furthermore, the impact of the fluid dynamics, the occurring adsorption mechanism, and the effects at the solid-liquid interface were analyzed. A brief overview of the most critical research aspects in the microscale is summarized in Table 3.1 and finally visualized in Figure 3.1.

It were Blaedel and Strohl [86], who determined that the electrode cell performance is limited, when the applied potential rise above a critical value. They further noticed that the pH-value of the liquid phase must be kept in an acceptable range to avoid loss in separation quality. They also recommended the usage of buffers as suitable mobile phase media as their pH-value can be externally adjusted and suppress undesired redox-reactions taking place at the electrode surface. Strohl and Dunlap [95] confirmed a potential-dependency of the column performance, which is restricted when a specific potential break-point is reached. They showed that the column capacity increases with increasing analyte concentration and decreases with increasing flow rate of the mobile phase. They identified an increased molecule's adsorption rate and equilibration time of electrode when the analyte concentration is high. A faster flow rate disturbs the adsorption equilibrium and reduces the column capacity.

Focusing on the fluid dynamical impact, Chu *et al.* [120] discussed mass transfer limitations that occur in dependency on packed bed length and increase with decreasing flow rate. Regarding the impact of the potential on the column efficiency, they observed a decrease of the electrical current inside the electrode cell when the adsorbed amount of target species increases. Tsuda [121] enlarges the study of mass transfer processes and potential impact on the column performance regarding peak broadening effects. He concluded that electrophoretic

mobility and electroosmotic flow, triggered by applied potential, impact the selectivity and purity of the species to separate and should be considered in the process design.

Ge and Wallace [114] studied the interaction kinds of aromatic molecules with polymer-coated reticulated vitreous carbon regarding hydrophobicity, polarity, and ion exchange. Analyzing material properties, they determined that carbon particles without coating do not or only slightly impact the retention of the different molecules even if potential is applied. On the contrary, polymer-coated resin intensifies the retention of molecules with high proton donor capabilities, but only little affects molecules with electron donor capabilities if potential is applied. Furthermore, they found out that the mobile phase composition impacts the retention time. Nagaoka *et al.* [109] studied the interactions of anions with potential-modified polymer-coatings and determined that the anion retention depends strongly on their structure and the preparation of the materials. Hence, polyaniline coated resin guarantees potential-controlled retention of small single-charge carrying anions, while a polypropylene coating interacts with carboxylic anions.

Table 3.1: Overview of the areas examined in the historical development of PCC on analytical scale: resin (Resin); material properties (Mat); fluid dynamics (Flu); mobile phase composition and concentration (Mob); molecule type and adsorption characteristics (Ads); and other distinctive features (Feat). The potential influence is investigated by all authors and is not listed here.

Authors	**Resin**	**Mat**	**Flu**	**Mob**	**Ads**	**Feat**
Blaedel and Strohl [86]	Graphite					pH
Strohl and Dunlap [95]	Graphite		x			
Chu *et al.* [120]	Graphite		x			
Tsuda [121]	Coated silica		x			
Ge and Wallace [114]	Coated GC	x			x	
Nagaoka *et al.* [109]	Coated GC	x			x	
Antrim and Yacynych [122]	–			x	x	EDL
Deinhammer *et al.* [115]	GC, PGC			x	x	EDL
Abdel-Latif and Porter [105, 116, 123]	GC, PGC			x	x	EDL
Ponton and Porter [124, 125]	PGC			x	x	H_2O, T
Keller *et al.* [107]	PGC			x	x	EDL
Yakes *et al.* [108]	PGC			x	x	pH
Ponton *et al.* [126]	GC					T

Antrim and Yacynych [122] introduced the EDL theory in their research and studied the effect of the applied potential and the mobile phase composition on the solid-liquid interface. They discussed different adsorption behaviors of various analytes, identifying that the charge density and the analytes' functional groups impact the column capacity. Besides, they showed that there could be a competition of binding sites between mobile phase ions and the target species reducing the column capacity. Deinhammer *et al.* [115] studied the adsorption of aromatic sulfonates. The interaction between the analyte's electrons and the delocalized $\pi - \pi$ system of the carbonaceous surface is attributed to the donor-acceptor principle and electrostatic interactions. They concluded that the applied potential varies the adsorption type of the aromatic molecules. Thus, if the potential is larger than the point of zero charge, the binding is dominated by aromatic interactions; if it is below, electrostatic interaction predominates.

Abdel-Latif and Porter [105, 116, 123] presented the first multi-variable analysis and defined the column performance as a function of current density caused by the setup, the electrode material, and the material properties. They reported that the mobile phase composition and concentration influence the adsorbate's peak shape, its retention, and the adsorption capability of the electrode. They observed further that high electrolyte concentrations cause higher resolution of the chromatograms, while larger electrolyte molecules reduced the cell constant. Furthermore, they claimed that a cooperative binding effect between specific ion and molecule species could exist and showed that electrolyte ions could induce a shielding effect affecting the retention time. Moreover, they summarized that the molecule size, structure, and functional groups are the leading players of adsorbate/adsorbent interactions, controlled by numerous interaction effects. However, they did not achieve success in defining a universal mechanism to describe the potential-controlled interactions of any molecule with different carbonaceous resins and different electrolyte concentrations.

The works of Ponton and Porter [124, 125] also considered the adsorption mechanism and defined the adsorption behavior of inorganic anions as electrostatic and the one of the aromatic sulfonates as covalent. They reported that the analyte molecules' retention depends strongly on the mobile phase concentration and composition, but contradict Abdel-Latif and Porter [116], by determining a competitive behavior of electrolyte ions and target molecules. They focused on water as the surrounding environment without additives and showed that the retention time increases decisively. Besides, they observed that higher temperatures and higher flow rates decrease the time required for separation.

Keller *et al.* [107] stated in a theoretical approach that the EDL width increases with decreasing electrolyte concentration, and most recently, Yakes *et al.* [108] identified the mobile phase's pH-value as a trigger for the sensitivity towards the electrically charged surface and the

target molecules. Ponton *et al.* [126] resumed the study about the impact of electrosorption thermodynamics and reported the potential-dependent retention of sulfates is reduced with increasing temperature. Finally, Soto *et al.* [127] published a new type of a capillary column for EMLC and provided the associated proof-of-concept for the potential-controlled separation of aromatic sulfonates.

3.4 Formulation of the Research Questions

The numerous publications visualize that several process-operating parameters affect the chromatographic response. However, the publications' content was often one-sided, and the complex relationships between the individual process-influencing parameters and the column performance have not been described for one specific system completely (see classification in Figure 3.1). As the process basics, such as setup and conductive resin, were continuously modified, an overall process description is often missing. Moreover, mainly analytical applications and quantitative separation were investigated, to-date, knowledge is lacking for preparative chromatographic processing in biotechnological applications.

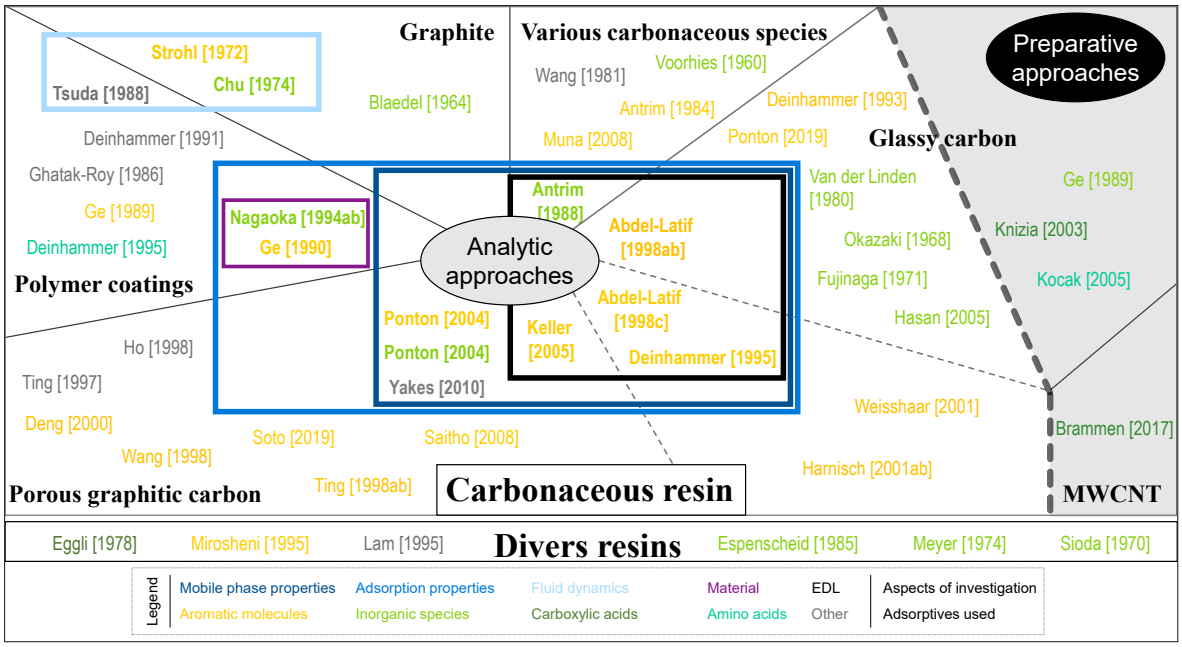

Figure 3.1: Overview of publications containing the process idea of EMLC or PCC. The publications are separated between analytic or preparative approaches and in divers electrode materials (cf. Table 3.1). The analytes investigated and the most relevant research aspects are highlighted in color maps. For visualization, a percental weighting is imprinted in Figure A.1.

Figure 3.1 shows that although all publications succeeded in separating molecule mixtures using electric potential as the trigger, corresponding interfacial effects between a solid material and the bulk solution were often not sufficiently discussed. Thus, only a small number of the publications consider the adsorption properties of the adsorptives and the interaction kind to the solid surface in particular (highlighted by the blue-colored box). Only two of these contributions intensively investigated the material properties (see violet-colored box) but simultaneously failed to capture the impact of the mobile phase properties on the adsorption (dark-blue-colored box). In summary, only five publications, among them four from Porter's group, discussed the EDL development (black box) additionally. However, non of these described the system's fluid dynamic influence particularly (see light-blue-colored box).

Finally, the natural effects inside a PCC system, primarily occurring at the potential-dependent solid-liquid interface, and their impact on the electrode performance is often disregarded. It is recognized that all publications are based on a chromatographic description, while electrochemical characterizations are rare. As PCC is a combination of both techniques, crucial findings to understand the potential-dependent effects properly are lacking, and an overall description of a specific process and its relevant influencing parameters cannot be found in the literature yet.

Being aware of these missing but critical aspects to developing a preparative PCC process suitable for laboratory and industrial applications of separating organic molecules allow the formulation of the following research gap:

Research Gap
A preparative potential-controlled chromatographic application does not exist yet for downstream processing in the domain of biotechnology. None of the published approaches provides a comprehensive chromatographic and electrochemical process description, including the following multi-factorial aspects: material, fluid dynamics, mobile phase properties, adsorption effects of various charged species, and the potential-controlled formation of the interface, in particular, using multi-walled carbon nanotubes as conductive resin.

The final objective of this thesis is to determine the basis for an application design that can simplify downstream processing. Developing a universal separation method for all kinds of charged or polarized ions and molecules can achieve a flexible and easy-to-handle process application for purification and concentration. As the knowledge about the influence of various process parameters on the solid-liquid interface is rare, the PCC process is analyzed on its fundamentals. As Brammen *et al.* [15] presented Baytubes C 150 P as a promising and suitable material for a preparative PCC application, this thesis follows his foot-prints

and MWCNT are selected as an inexpensive conductive resin with extraordinary properties. In this thesis, CNT-K and IoLiTec-CNT are analyzed at their pristine conditions, as both materials are commercially available. DI-water is selected as a standard mobile phase to enhance the visualization of the natural potential-dependent effects inside the column.

The following six research questions (RQ) are derived from the research gap as well as the knowledge from the state-of-the-art. They are summarized in Table 3.2 and built on the process fundamentals (hypotheses) formulated at the beginning of the research and the motivation to understand the newly designed PCC process in its details.

As no proof-of-concept exists for the two selected MWCNT materials, the first research question (**RQ 1**) addresses their feasibility as an electrode material. **RQ 1** arises from the first (**HT 1**) and the second hypothesis (**HT 2**), questioning whether the conductive nanoparticles can be triggered via electric potential and, in addition to that, can be used for selective chromatographic and capacitive processing.

As the MWCNT particles selected are unexplored for PCC application, **RQ 2** is dedicated to the identification of the specific material properties and hence their contribution to the process performance (cf. **HT 1**).

RQ 3 addressees PCC as a combination of chromatographic and electrochemical techniques, questioning if the fundamental potential-dependent effects at the solid-liquid interface can be described in an analysis protocol. **RQ 3** builds on the third hypothesis (**HT 3**), which asserts the interplay of setup, material, and the surrounding environment.

As the success of chromatographic separation depends on different operation conditions, **RQ 4** addresses different impact factors and questions which of these are relevant for optimal processing and column performance (cf. **HT 1** and **HT 3**).

Whether the properties of the surrounding environment, like fluid flow rate, as well as concentration and composition of the mobile phase media, affect the electrochemical response and the formation of the EDL is questioned in **RQ 5** (cf. **HT 3**).

Finally, different interaction mechanisms are presupposed for the qualitative separation of inorganic and organic mixtures and the MWCNT. Therefore **RQ 6** asks whether different interaction mechanisms between various species and the MWCNTs exist (cf. **HT 2**).

Table 3.2: Research questions to develop a preparative PCC process using MWCNT as a particulate fixed bed electrode resulting from the hypotheses and the research gap (cf. Table 1.1).

Research question		**Hypothesis**
RQ 1	Is the setup of the PCC column feasible for a potential-dependent separation process?	**HT 1**: Electric potential triggers the surface properties. **HT 2**: Porous flow-through electrodes are suitable for capacitive processing.
RQ 2	Does the MWCNT materials' specific properties influence the process performance?	**HT 1**: Electric potential triggers the surface properties.
RQ 3	Can a combination of conventional chromatographic and electrochemical analysis methods be employed to describe the potential-dependent effects at the solid-liquid interface?	**HT 3**: Setup, material, surrounding environment and target species affect the process performance.
RQ 4	Does the operation conditions influence the column performance?	**HT 1**: Electric potential triggers the surface properties. **HT 3**: Setup, material, surrounding environment and target species affect the process performance.
RQ 5	Does the surrounding environment impact the chromatographic and electrochemical response of the column?	**HT 3**: Setup, material, surrounding environment and target species affect the process performance.
RQ 6	Do differently charged inorganic and organic species interact differently with an electrically charged MWCNT surface?	**HT 2**: Porous flow-through electrodes are suitable for capacitive processing.

4 Framework, Methods, and Materials

This Chapter introduces this thesis's framework in Section 4.1 and presents the methods and the materials used. Section 4.2 describes the PCC column and its handling. The experimental methods performed are summarized in Section 4.3. Lists of the materials, chemicals, and instruments used are presented in Section 4.5.

4.1 Concept to Address the Research Questions

The process is investigated on the natural influencing parameters to address the research questions of potential-controlled chromatography formulated for this thesis. The focus is on describing the MWCNT material, the column's chromatographic and current response, and the effects at the solid-liquid interface. A shortened guideline of the separate working packages is depicted in Figure 4.1, a detailed description is presented later in the Results and Discussion Chapter, in Chapter 5.

Before starting the overall analyze the native influencing factors of the potential-dependent flow-through setup and MWCNT materials (*CNT-K* and *IoLiTec-CNT*) are screened on their applicability. For this purpose, chromatographic interpretation is used to gain a proof-of-concept and answer **RQ 1**. Moreover, it is analyzed if and how the setup and the MWCNT characteristics contribute to the process performance to answer **RQ 2**. The demand for a universal analysis protocol to describe the PCC column's performance, targeted in **RQ 3**, is investigated by combining chromatographic and electrochemical characterization methods. The same methods are used to identify the impact of the potential applied to the process performance to answer **RQ 4**. The mobile phase's impact on the column response to answer **RQ 5** is investigated by an electrochemical analysis, followed by a chromatographic study of the adsorption behavior to answer **RQ 6**.

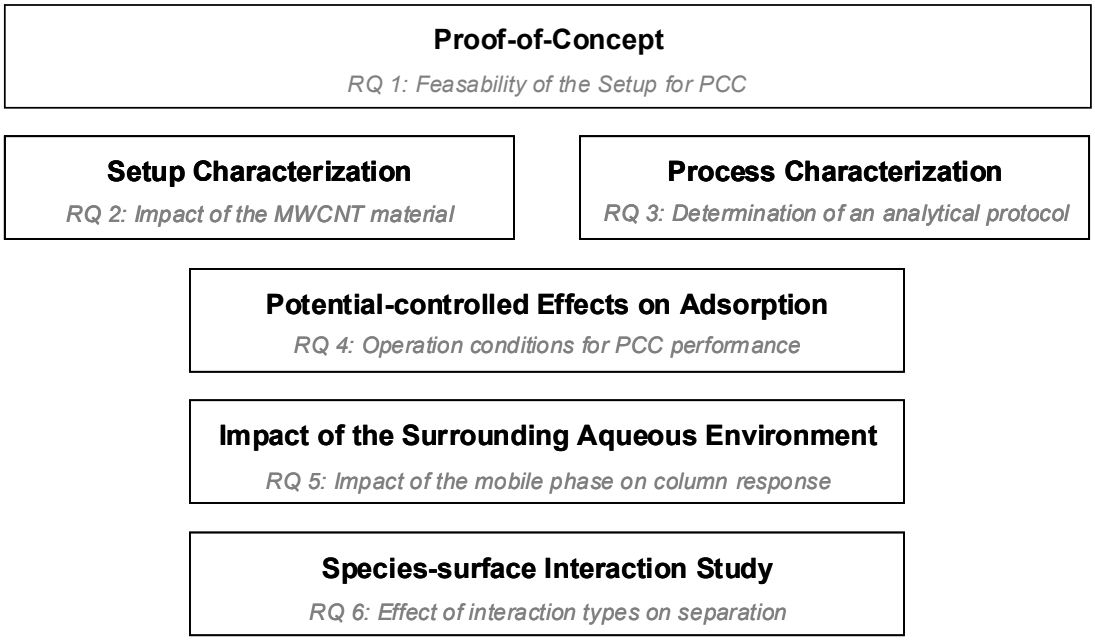

Figure 4.1: Framework of this thesis to address the research questions.

4.2 The Column Setup and Particle Preparation

The column used in this thesis was adapted from Brammen *et al.* [15], who designed it as a three-electrode setup with a packed bed volume of around 7.5 mL. Both the new and the original setups include a stainless steel outer housing in which the counter electrode (CE) is installed, existing as a porous stainless steel inner cylinder (height = 5 cm, inner diameter = 1.5 cm) to offer a large CE surface area. The reference electrode (RE, Ag/AgCl) is screwed through the outer housing and the CE, attaching the ion-exchange membrane to keep the space between the RE and the working electrode (WE) as minimal as possible. The particulate packed bed is contacted by a wire coil and surrounded by a strong cation-exchange membrane, necessary to tight the packing, preventing a direct flow of the current and inhibiting interactions between the CE and the sample molecules, leading to corrosion and a loss of the target species. A schematic illustration is depicted in Figure 4.2, the individual column components are presented additionally in Figure A.4 in the supplementary information. It is highlighted that the fluid flow and the potential flow are perpendiculars.

A MWCNT particle slurry is packed vertically under flow (2.5 mL/min) to guarantee a homogeneous compression and attachment of the particle agglomerates around the wire coil. Around 0.5 g dry CNT-K or 0.7 g IoLiTec-CNT can be installed inside the column. Compared

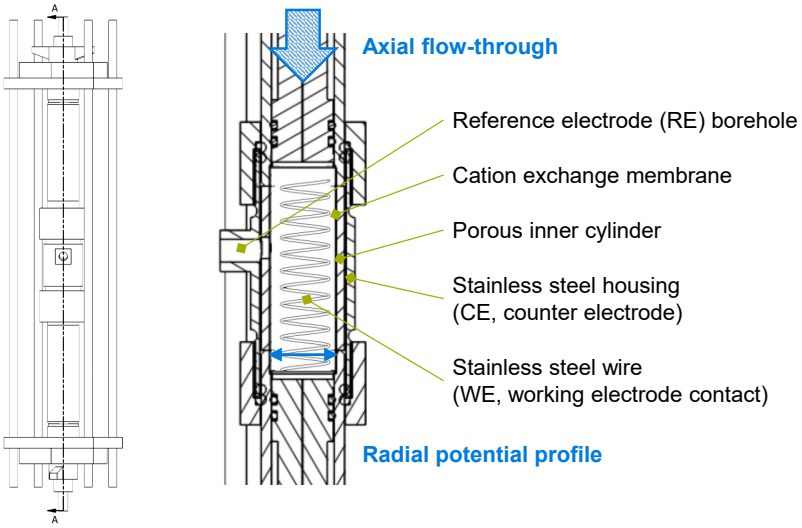

Figure 4.2: Scheme and excerpt of the technical drawing of the PCC column used. Adopted from Trunzer *et al.* [18]. Licensed under CC-BY-4.0 (https://www.mdpi.com/2076-3417/10/3/1133/htm).

to Brammen *et al.* [15], the wire coil is optimized, existing finally as distinct stainless-steel coil with an inner diameter between 0.8 to 1.0 cm including 12 to 15 coils. It enables a homogeneous radial potential distribution and achieves the maximal contact area possible between coil and particles.

Column clamps and membrane caps are installed to facilitate the packing procedure transforming non-spherical nano-powders to a homogeneous packed bed. The column clamps guide the stamps and ensure a centered alignment and a steady force transmission during packing. The membrane clamps fix the membrane ends, circumvents lateral flow, and improve a homogeneous fluid distribution.

The improved PCC column can be run up to 20 bar and with flow rates of up to 10 mL/min. It guarantees a reproducible and easy-to-handle packing mechanism. An ideal packed MWCNT column runs without pressure drop at low flow rates.

Pre-treatment of the Particles

Before the column is packed with the MWCNT, the harmful and highly electrostatic powder must be transformed into a slurry, manageable for further operation. On the CNT-K manufacturer's recommendation [128], a purification step is performed to remove catalyst residues left from the MWCNT bulk synthesis (CVD synthesis route).

Therefore, the dry MWCNT particles are cooked in 1 M hydrochloric acid (80 to 90 °C, > 4 h). Subsequently, the acidic slurry was neutralized and stored in DI-water (called storage-slurry). A defined particle slurry is prepared to work with a reproducible amount of MWCNT in a defined volume. This defined slurry was prepared by centrifuging the storage slurry (3200 xg, 5 min) and discarding the supernatant. The resulting MWCNT pellet, called *wet* MWCNT, was re-suspended in 1.5x weight proportions of DI-water.

4.3 Chromatographic and Electrochemical Characterization Methods

This Section is subdivided in presenting the material characterization techniques for the MWCNT in Section 4.3.1. Different chromatographic analysis methods are summarized in Section 4.3.2, and the methods for electrochemical characterization are introduced in Section 4.3.3. Besides, the background of each experiment is discussed, and the evaluation pathways are presented if necessary.

4.3.1 Material Characterization

The MWCNT materials are characterized concerning structure, surface properties, water content, and static binding capacity. The methods presented are used to identify the particle's advantages or weaknesses.

Catalyst Residue

The recommended purification pre-step is performed always before handling the MWCNT. If this purification succeeds in removing the catalyst is analyzed by burning the particles completely in a muffle furnace at 700 °C. The remaining mass and the ash color are analyzed on possible containing additives, expected to impact the current response of the particles.

Water Content

As the MWCNT are handled in a DI-water slurry, their interaction with water is analyzed, aiming to determine the hydrophilic or hydrophobic character and how strong possible water/surface interactions can be. It is expected that the amount of water kept inside the MWCNT pellets hint at the water affinity of the MWCNT. Known that a fluid film on a solid phase can impact the surface properties and form the three-dimensional agglomerate's structure, the analysis of water effects is particularly focused.

The hydrophilicity/hydrophobicity of the powder is determined with the Washburn tensiometry according to Schwaminger *et al.* [129]. Moreover, the minimum water content of centrifuged MWCNT pellets (3200 *x* g, 5 min) is examined drying different wet MWCNT masses in a drying cabinet at 60 °C. When the MWCNT pellet is completely dried, the water content can be calculated as the mass loss in percent. To investigate the existence of water films on the MWCNT, thermogravimetric analysis is performed with pristine powder and pre-dried MWCNT agglomerates under synthetic air (temperature between 30 and 900 °C, heating rate: 10 K/min). It is expected that the amount of vaporized water and the carbon dioxide content correlates to the existence of free and bound surface water.

Optical Analysis

Different optical analysis methods are used to describe the morphology of the MWCNT agglomerates and the geometry of the single tubes in detail. The MWCNT entanglement and the agglomerate porosity are investigated in light microscopy (MWCNT agglomerates dispersed in DI-water) and in scanning electron microscopy (SEM, dried agglomerates). The agglomerate sizes and forms are analyzed in laser diffraction and image analysis. Transmission electron spectroscopy (TEM, ultrasonicated agglomerates dispersed in DI-water, dried) is used to illustrate the bulk geometry of the single tubes and later transmit their specific properties on the existent shapes.

MWCNT Surface Properties

The specific surface properties affect the suitability of the MWCNT as chromatographic packed-bed material: the more distinct and the larger the number of the binding sites are, the higher is the column capacity. To identify the number of adsorption sites correlating to the material's specific surface area BET measurements using nitrogen as adsorptive ($p/p_0 = 0.05$ to 0.3) is performed. The kind of binding sites that control the distinct interactions and selective adsorption mechanism is examined in X-ray photoelectron spectroscopy (XPS, MgKα X-ray source, $h\nu = 1253.6$ eV).

Determination of the IEP and the pH$_{pzc}$

As functional groups on the MWCNT surface change their protonation states in different environments, the pH-dependent surface charge and the surface charge density of the MWCNT are investigated in two experimental series. Additionally, the pH-transition point is determined.

pH-shift Experiments

A simple method to determine the isoelectric point (IEP) are pH-shift experiments using MWCNT slurries with different masses (ratio of wet MWCNT to volume DI-water: 0.10 and 0.05 g/mL, or 1.00 and 0.05 g/mL when dry MWCNT are used). The initial pH-value pH_{set} is adjusted between 2 and 11 using NaOH or HCl, and measured after an incubation time (pH_{is}) of at least 24 h at room temperature (RT). The IEP of the MWCNT could be identified when pH_{set} equals pH_{is}, or pH_{is} reaches a plateau. These measurements are performed in technical duplicates and triplicates.

Potentiometric Titration

Potentiometric titration is performed according to Lützenkirchen *et al.* [130]. The analyzed pH-range lies between 2 (adjusted with 0.1 M HCl) and 10 (titrated with 0.1 M NaOH). The mass ratios of the slurry are m_{wet} = 5, 10, 15, 20 g per 100 mL. The particle agglomerates are dissolved via sonication to achieve a high surface area and guarantee access to the surface sites. The measurements are performed in technical triplicates, including a blank titration. The surface charge density of the MWCNT particles is calculated from the difference of the titration curves. Plotting the surface charge density over the pH-value, the IEP, respectively, the pH_{pzc} can be determined at the x-axis intersection. Besides the pH-range in which the MWCNT particles are charged positively or negatively, attraction forces between particle and target analytes can be derived.

Static Binding Capacity

The interaction affinity and kind between target species and the solid material is the fundamental criterion for chromatography. Depending on the surface characteristics in different environments, various species will interact differently with the MWCNT.

To examine the primary interaction strength between the analyte and the MWCNT (excluding the impact of flow rate and applied potential), static binding capacity (SBC) experiments are performed. A defined mass of a wet MWCNT pellet (slurry was centrifuged at 3200 xg, 5 min) is incubated with different concentrations of the target analyte. Each experiment is performed at RT for 24 h, stirring the slurry with 500 rpm (Method 1) or 250 rpm (Method 2) to guarantee thorough accessibility for the analyte to the pores of the MWCNT agglomerates. After equilibration, the supernatant is filtrated (0.2 µm) and analyzed using high-performance liquid chromatography (HPLC) at 216, 258 or 280 nm. DI-water is used as mobile phase medium. The samples are measured in technical duplicates or triplicates.

During this thesis, two different methods were developed to determine the SBC:

Method 1: study about the interaction of various analytes with MWCNT

The SBC experiments investigating carboxylic acids (maleic and fumaric acid) are executed with a particle mass to analyte volume ratio of 0.2 g/mL. The interaction of amino acids (alanine, histidine, phenylalanine, tryptophan) with the MWCNT are examined in a ratio of 0.5 g/mL. All analytes are dissolved in DI-water. The carboxylic acids are titrated to pH 7 (pH-adjustment using NaOH), the amino acids solutions are kept at their IEP. The water content of the MWCNT pellets is neglected for calculation. The adsorption amount is directly transferred to the dry mass of the inserted MWCNT (see Equations A.4 to A.8).

Method 2: pH-dependent SBC experiments

As the MWCNT surface charge is expected to change with the surrounding environment, the adsorption capacity of maleic acid and phenylalanine is studied for different pH-values (between 1.5 to 9.5, pH-adjustment using HCl or NaOH). The concentration range is set between 5 to 30 mM and the solvents DI-water, or 0.5, and 5.0 mM phosphate buffer are selected. The MWCNT pellet (mass from 2 mL of a predefined slurry) is incubated in 2 mL of the analyte. To exclude pH-deviations due to contact with the air, a blank of each sample was taken. To precise the calculated adsorption amount, the dilution effect of the solvent kept inside the MWCNT pellets was considered in the calculation (see Equations A.4 to A.13).

4.3.2 Chromatographically Designed Experiments

Using random cotton-ball structured MWCNT agglomerates as a particulate fixed bed, the chromatographic suitability must be examined and guaranteed for the untypical resin. Therefore, the chromatographic characterization of the MWCNT matrix is performed with tracer analysis. Moreover, the binding behavior of different analytes in the dynamic system is analyzed in potential-dependent and potential-independent experiments.

Tracer Experiments

To determine the packed bed structure, tracer analysis is performed at the beginning of each column's life, during its operation time, and after a break-up (1 M NaCl, 50 µL, 1.0 or 1.5 mL/min). For these experiments, DI-water is used as the mobile phase.

The prerequisite for using the column properly is a homogeneous packing with an acceptable asymmetry value ($0.9 < A_s < 3$). It is expected that deviations of the tracer peak shape

occurring during the column's life time identify changes in the matrix structure and give information about the column's long-term stability. Besides, tracer analysis is used to gain information about the mobile phase's convection and dispersion pathway through the column.

Dynamic Adsorption Study for Different Analytes

To investigate the native and potential-dependent adsorption behavior of differently sized or soluble inorganic and organic species on the MWCNT a broad screening is performed using:

- Amino acids: alanine, histidine, lysine, phenylalanine, tryptophan, tyrosine
- Carboxylic acids: ascorbic acid, fumaric acid, maleic acid, salicylic acid
- Metal salts: potassium chloride, sodium chloride, calcium chloride, magnesium chloride, iron chloride, aluminum chloride, sodium phosphate
- Nucleic acid: uracil
- Organic salt: guanidinium thiocyanate
- Proteins: green fluorescent protein, lysozyme
- Polymer: blue dextrane
- Vitamin: riboflavin

The corresponding chemical structures are imprinted in the Figures A.2 and A.3.

Native Adsorption of the Analytes Without Applied Potential

The native interaction of the different molecules and the MWCNT is analyzed at open circuit potential (OCP), when no potential is applied to the column. 50 µL of the analyte solution is injected pulse-wise, the subsequent chromatograms are detected via UV-Vis and conductivity sensor. The adsorption phase is held until the detector signal of a possible breakthrough peak (unbound amount of the analyte) reaches the baseline again, however, at least for three column volumes. Afterward, salt elution (step, 1 M NaCl, one column volume) is induced to regenerate the column. Depending on the breakthrough or elution peak area, the native interaction between the MWCNT and the analytes is calculated over their ratios. The difference between injection and breakthrough amount describes the adsorption amount; the binding kind is analyzed over the molecule structure, and if the analyte's binding is dissolvable by salt replacement. For these experiments, DI-water is used as a mobile phase (adsorption phase: 0.5 mL/min, elution phase 1.5 mL/min).

Potential-step and Potential-gradient Experiments

Potential-dependent adsorption experiments are performed to study how the adsorption amount depends on the applied potential and if potential-induced desorption is possible. DI-water or 10 mM phosphate buffer (pH 7) are selected as the standard mobile phase media. Maleic acid (2 or 5 g/L, respectively 17, 25 or 43 mM) is the model analyte. Its double negatively charged character lets expect a distinct electrostatic interaction behavior with the electrically triggered resin. Since a quantitative analysis of the potential-dependent adsorption and desorption amount of the analytes is not feasible due to the experimental circumstances, balances are calculated from injection, breakthrough and desorption peak areas. The type of correlations compared is noted in the particular results.

The experimental series is enlarged using different metal salts and organic molecules (50 µL) as target species. The different concentrations and pH-values are noted in the appropriate places. Moreover, different potentials (between −500 mV and +800 mV which are the boundaries preventing water decomposition) are applied in the adsorption phase. The desorption is induced via step or gradient (−1 or −5 mV/s) towards −500 mV. The adsorption and desorption phase is held until the conductivity, and respectively the UV-Vis signal reaches its basis again. The flow rate differs between the experimental series (adsorption phase: 0.5, 1.0 or 1.5 mL/min; desorption phase: 1.0 or 1.5 mL/min). In some experiments, the pH-value is detected to study the potential impact on the environmental conditions, or a salt elution step is added in the style of IEX (1 M NaCl, one column volume) to study the binding strength of the targets.

4.3.3 Electrochemically Designed Experiments

The electrochemical suitability of the MWCNT matrix is the second central pillar of PCC processing. Thus, a detailed electrochemical characterization follows the chromatographic tracer analysis at the beginning of each column's life, during operation, and after a break-up. Three main methods are used for electrochemical characterization: open circuit potential measurements, chronoamperometry, and cyclic voltammetry experiments. The potentiostat runs at surface mode, the potential applied is measured against the reference electrode. DI-water, 10 mM electrolytes, or pH-adjusted DI-water are used as mobile phase (1.0 or 1.5 mL/min).

Open Circuit Potential

Open circuit potential (OCP) measurements are performed with the standard protocol installed in the Gamry framework for at least 200 s. It is used to determine the working electrode potential at rest. The knowledge about the electrode matrix's natural surface charge will define the material surface properties and identify the fundamental interaction mechanisms of different analytes with the MWCNT.

Chronoamperometry

The degree of disturbance of the solid-liquid interface (rearrangement of the EDL) can be determined when the column's current response is analyzed over time after immediate potential changes that modify the surface conditions. Therefore, chronoamperometry is performed at various constant potentials applied to the MWCNT electrode. After at least 300 s hold time, the potential value is inverted to its counter value for another 300 s (CNT-K: between ±800 mV; IoLiTec-CNT: between ±1000 mV).

In accordance to Figure 2.11 in the Theory Chapter, the current profile measured over time will give information about the electrochemical double layer's rearrangement time, the electric charge, and the column's resistance. Moreover, information about the capacitive and faradaic current parts can be gained.

Charge-discharge experiments are performed as an alternating series of five chronoamperometry experiments with similar potential switches (+800 to −500 mV). The method is used to regenerate the column matrix structure due to continuous repulsion and attraction of the charged MWCNT tubes. Besides, fluctuations of the conductivity profile of the mobile phase would hint on a continuous adsorption and desorption amount of the species from the surrounding environment.

Cyclic Voltammetry

Cyclic voltammetry (CV) experiments are performed by steadily changing the potential value with a standard rate of 1 mV/s between the positive and negative potential boundaries (+800 to −500 mV). Each measurement was repeated for three cycles. If a constant increase and decrease of the current profiles are determined, the PCC column will be charged capacitive, adsorbing and desorbing a reversible amount of species from the surrounding solvent. However, when the current profile is irregular (peak formation is detected), an electron flow activation is visualized due to faradaic redox-reactions (see also Figure 2.12).

The results of the CV measurements can also be used to predict if the electrode surface is irreversibly damaged over time.

4.4 Simulation with ChromX

To confirm the results of the chromatographic tracer experiments and to investigate characteristic column parameters that could not be determined precisely in the experiments, simulation is performed with ChromX [131]. The simulation works with different mathematical models, pre-installed in the software framework:

- a *column* model is used to implement the column parameters and the mobile phase effects inside the interstitial column volume;
- a *pore* model is used to express mass transfer effects occurring inside the beads; and
- an *isotherm* model is used to specify the adsorption process of an analyte on the solid surface area.

An *ideal* model exists when only convection forces and an adsorption equilibrium are considered. An *equilibrium dispersive* model describes an extended simulation that includes dispersion effects. When the mass transfer cannot be simplified, the *transport dispersive* model is selected including diffusion processes between interstitial and pore volume. This model itself is subdivided into various *lumped rate* models (sub-models only containing a selection of the mathematical models) but entirely summarized in the *general rate* model [132].

The unknown parameters desired to identify the column properties can be gained over estimation using two different algorithms: The complex heuristic algorithm (GAlib) is based on the evolutionary theory and is used to identify primary local and global optima in a broad parameter range. The simple, deterministic algorithm (Levenberg-Marquardt) is based on a gradient-based Newton method and is used to precise the local optima between narrow boundary values. The best estimated parameter set is finally determined when the residue between measurement and simulation curve is minimal.

In this thesis, the column and the total column porosity, as well as the axial dispersion coefficient of a MWCNT matrix are estimated and compared to the experimentally determined results. Therefore, various tracer chromatograms are analyzed on the basis of a fluid dynamic model excluding adsorption effects.

4.5 Materials, Chemicals, and Instrumentation Used

All used materials, chemicals, and instruments are listed in this Section. Table 4.1 summarizes the materials used, Table 4.2 lists the chemicals, and Table 4.3 the employed instruments and software.

Table 4.1: List of materials.

Name	Manufacturer	Specification
CEX membrane	Membranes International Inc. Ringwood, U.S.A	CMI-7000
CNT-K	Future Carbon GmbH, Bayreuth, Germany	308068-56-6
Copper paste	Äronix Spezialschmierstoffe, Walldorf, Germany	Contact mass CU
IoLiTec-CNT	IoLiTec Ionic Liquids Technologies, Heilbronn, Germany	CP-0086-SG-0500
PTFE Frit	Cole-Parmer GmbH, Wertheim, Germany	Omnifit, 15 mm x 20 µm
Membrane glue	Henkel AG & Co. KGaA, Düsseldorf, Germany	Loctite406
Reference electrode	C3 Prozess- und Analysen-technik GmbH, Haar, Germany	RE-3VT (Ag/AgCl)
Stainless steel wire	FilPack, –	FGI08
Stamp	Cole-Parmer GmbH, Wertheim, Germany	Omnifit, 15 x 150 mm, adjustible endpieces
Styringe attachment filter	Macherey und Nagel GmbH & Co.KG, Düren, Germany	CHROMAFIL Xtra 0.2 µm

Table 4.2: List of chemicals.

Name	Manufacturer	Specification
Acetone	Honeywell GmbH Building Solutions, Puchheim, Germany	67-64-1
Aluminium chloride	Sigma-Aldrich Chemie GmbH, Taufkirchen, Germany	7446-70-0
Ascorbic acid	Sigma-Aldrich Chemie GmbH, Taufkirchen, Germany	50-81-7
Blue Dextran	Sigma-Aldrich Chemie GmbH, Taufkirchen, Germany	87917-38-6
Calcium chloride	Sigma-Aldrich Chemie GmbH, Taufkirchen, Germany	10043-52-4
Di-sodium hydrogen phosphate	Carl Roth GmbH & Co. KG, Karlsruhe, Germany	7778-77-0
Ethanol	CLN Freising, Langenbach, Germany	64-17-5
Fumaric acid	AppliChem GmbH, Darmstadt, Germany	110-17-8
Green fluorescent protein	In-house production	–
Guanidium-thiocyanate	Sigma-Aldrich Chemie GmbH, Taufkirchen, Germany	615-030-00-5
Hydrochloric acid	VWR International GmbH, Darmstadt, Germany	7647-01-0
Iron(III) chloride	Sigma-Aldrich Chemie GmbH, Taufkirchen, Germany	10025-77-1
Isopropanol	VWR International GmbH, Darmstadt, Germany	67-63-0
L-Alanine	Serva Electrophoresis GmbH, Heidelberg, Germany	56-41-7
L-Histidine	Carl Roth GmbH & Co. KG, Karlsruhe, Germany	71-00-1
L-Lysine	Sigma-Aldrich Chemie GmbH, Taufkirchen, Germany	56-87-1
L-Phenylalanine	Merck KGaA, Darmstadt, Germany	63-91-2

Name	Manufacturer	Specification
L-Tryptophan	Serva Electrophoresis GmbH, Heidelberg, Germany	73-22-3
L-Tyrosine	Serva Electrophoresis GmbH, Heidelberg, Germany	60-18-4
Lysozyme	Sigma-Aldrich Chemie GmbH, Taufkirchen, Germany	–
Magnesium chloride	Carl Roth GmbH & Co. KG, Karlsruhe, Germany	7791-18-6
Maleic acid	AppliChem GmbH, Darmstadt, Germany	110-16-7
Potassium chloride	Sigma-Aldrich Chemie GmbH, Taufkirchen, Germany	7447-40-7
Riboflavine	Carl Roth GmbH & Co. KG, Karlsruhe, Germany	83-88-5
Salicylic acid	Sigma-Aldrich Chemie GmbH, Taufkirchen, Germany	69-72-7
Sodium chloride	AppliChem GmbH, Darmstadt, Germany	7647-14-5
Sodium dihydrogen phosphate	AppliChem GmbH, Darmstadt, Germany	13472-35-0
Sodium hydroxide	Carl Roth GmbH & Co. KG, Karlsruhe, Germany	1310-73-2
Uracil	AppliChem GmbH, Darmstadt, Germany	66-22-8

Table 4.3: List of instrumentation.

Name	Manufacturer	Specification
Analytical weighing machine	Mettler-Toledo GmbH, Gießen, Germany	XS205 DualRange
Äkta pure	GE Healthcare GmbH, Freiburg, Germany	Äkta^{TM} pure 25 M
Äkta software	GE Healthcare GmbH, Freiburg, Germany	Unicorn 7.3
BET	Micromeritics Instrument Corp., Norcross, U.S.A	Gemini VII system
Bio-Rad	Bio-Rad Laboratories, Inc., Hercules, U.S.A	BioLogic DuoFlow^{TM}
Bio-Rad software	Bio-Rad Laboratories, Inc., Hercules, U.S.A	BioLogic DuoFlow^{TM} Version 5.3
Centrifuge	Thermo Fischer Scientific Inc., Waltham, U.S.A	Megafuge 16R
ChromX	GoSilico GmbH, Karlsruhe, Germany	ChromX Software
Drying cabinet	Thermo Fischer Scientific Inc., Waltham, U.S.A	Hareus Oven
DSC	NETZSCH-Gerätebau GmbH, Selb, Germany	DSC 204 Phoenix
Gamry G750	Gamry Instruments, Warminster, U.S.A	Gamry G750
Gamry I1000	Gamry Instruments, Warminster, U.S.A	Gamry G750
Gamry Software	Gamry Instruments, Warminster, U.S.A	Gamry Framework
HPLC	Agilent Technologies, Inc., Santa Clara, U.S.A	Agilent 1100 Series
Light microscope	Carl Zeiss Microscopy GmbH, Jena, Germany	Axio Observer
Muffle furnace	Nabertherm GmBH, Lilienthal, Germany	Model L9/12
pH-meter	Mettler-Toledo GmbH, Gießen, Germany	FiveEasy pH, FiveEasy Plus pH/mV

Name	Manufacturer	Specification
Photometer	Eppendorf AG, Hamburg, Germany	BioSpectrometer basic
Plate shaker	Eppendorf AG, Hamburg, Germany	Thermomixer comfort
SEM	JEOL GmbH, Freising, Germany	JSM 5900 LV
SEM	Oxford Instruments, Abingdon, U.K.	CamScan 4
STA	NETZSCH-Gerätebau GmbH, Selb, Germany	STA 449 C Jupiter
SYNC	Microtrac Retsch GmbH, Haan, Germany	Microtrac SYNC
Tabletop centrifuge	Eppendorf AG, Hamburg, Germany	Centrifuge 5418
TEM	JEOL GmbH, Freising, Germany	JEM 100-CX
Titrator	Metrohm AG, Herisau, Switzerland	888 Titrando
XPS	Leybold Heraeus GmbH, Cologne, Germany	LHS 10 XPS, MgKα X-ray source

5 Results and Discussion

This Chapter presents the development of a preparative PCC process for MWCNT flow-through electrodes in six Sections, structured accordingly to the building block concept and in concern of the RQ, as depicted in Figure 5.1. The Sections which are extended by a material comparison or simulation are highlighted. Most parts of the presented results are published in Trunzer *et al.* [18], and [19] as well as in Wagner *et al.* [20] cited in the corresponding Figures. Unpublished data include the results on IoLiTec-CNT characterization and electrode performance, the discussion on the comprehensive interaction study of CNT-K, and the simulation results.

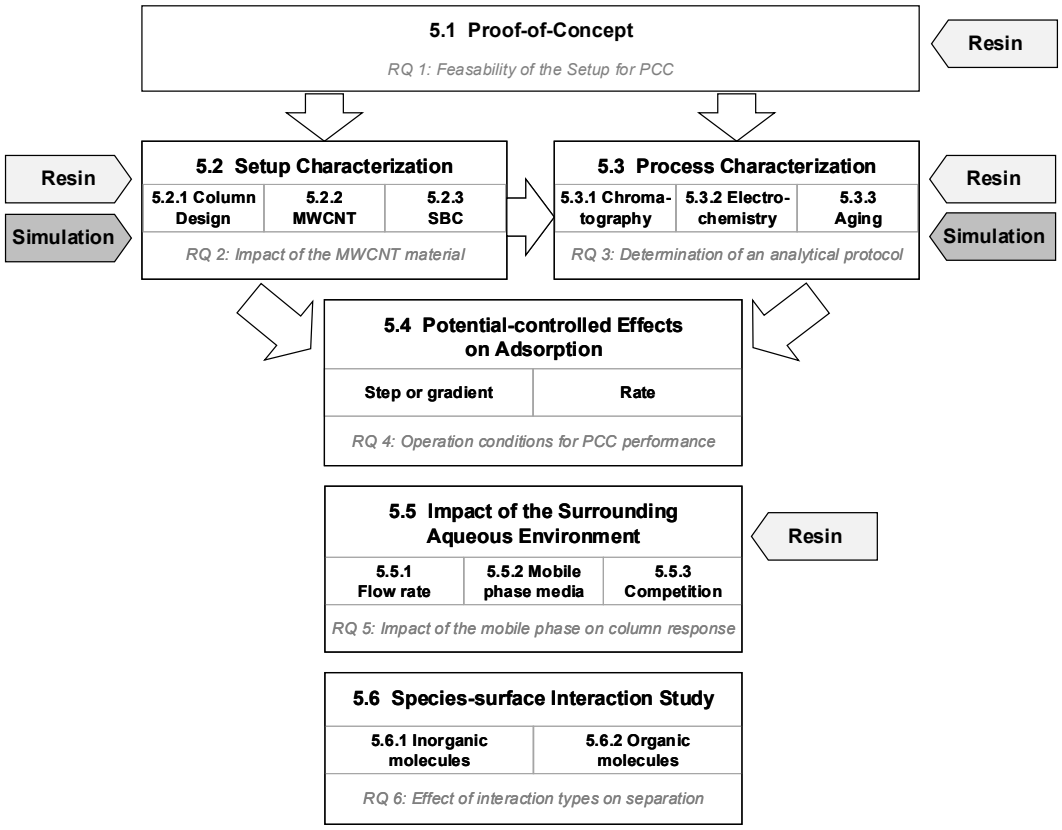

Figure 5.1: Thesis' concept and building blocks of the PCC process development based on the RQ.

A general proof-of-concept in Section 5.1 introduces the research by confirming the suitability of the new MWCNT materials as particulate packed bed electrodes. An analysis of the setup characteristics follows in Section 5.2, investigating the contributions and impacts of the relevant column components on PCC processing in Section 5.2.1. Moreover, the specific properties of MWCNT are highlighted in Section 5.2.2, and their natural interaction behavior is characterized in Section 5.2.3. The fundamental column and current response of the process is examined in Section 5.3, subdivided in chromatographic (see Section 5.3.1) and electrochemical (see Section 5.3.2) analysis methods. An aging study about the electrode performance combining both characterization methods follows in Section 5.3.3. In Section 5.4, optimal processing conditions are analyzed on potential-control and operating conditions. The study about the impact of the surrounding medium in Section 5.5, focuses the fluid flow in Section 5.5.1, as well as the composition and concentration of the mobile phase in Section 5.5.2. On this basis, the impact of the environment on the column capacity is investigated in Section 5.5.3. In the last Section, Section 5.6, results about the interaction study of inorganic metal salts (Section 5.6.1), or organic molecules (Section 5.6.2) and the MWCNT matrix are presented. Here, the natural and potential-dependent adsorption behavior in the dynamic flow-through cell is analyzed.

5.1 Proof-of-Concept

The basic idea of potential-dependent separation relies on the EDL theory, supposing that any solid material surface in contact with a liquid phase is self-charging and triggers specific electrostatic interactions with charged or polarized species in the surrounding environment. Thus, it is expected that the investigated differently charged species do not interact with a similarly charged electrode surface but are adsorbed when the surface is counter-charged.

However, the proof-of-concept for PCC employing MWCNT as an electrode material is given by Brammen *et al.* [15], the used *Baytubes C 150 P* are no longer commercially available. The research presented in this thesis proceeds with another, but comparable, type of MWCNT materials: *CNT-K* as the main resin and *IoLiTec-CNT* as reference material. Knowing from the literature that process performance is sensitive to the material properties [133–135], which is why a proof-of-concept has to be achieved for the newly selected MWCNT first, to confirm that all MWCNT can function as a stationary fixed bed and working electrode simultaneously.

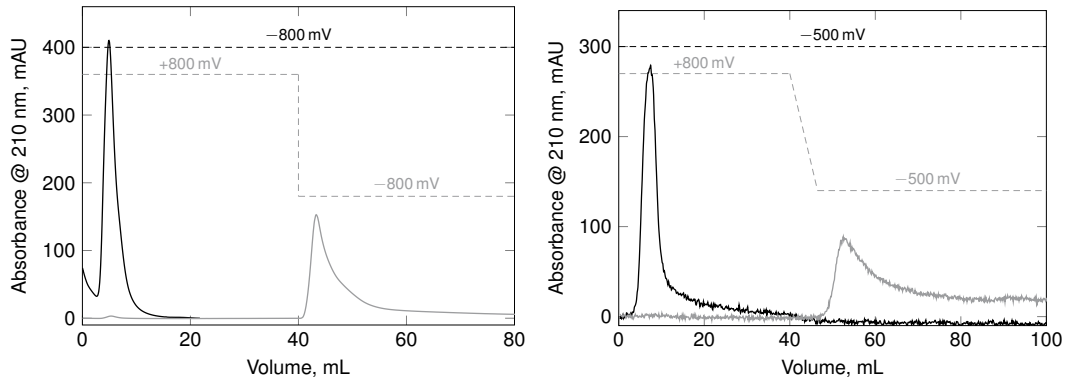

(a) Potential-step. **(b)** Potential-gradient.

Figure 5.2: Proof-of-concept for a CNT-K packed bed electrode. (a) Potential-step experiment: DI-water, adsorption and desorption phase: 1.0 mL/min, 50 µL, 2 g/L maleic acid, pH 7. (b) Potential-gradient experiment: DI-water, adsorption phase: 0.5 mL/min, desorption phase 1.5 mL/min, 50 µL, 25 mM maleic acid, pH 7, gradient −5 mV/s.

According to Brammen *et al.* [15], the proof-of-concept for CNT-K and IoLiTec-CNT is performed with potential-dependent adsorption experiments using maleic acid as a small, double negatively charged molecule. The experiment is subdivided into an *adsorption phase* and a *desorption phase*.

The chromatograms for CNT-K are imprinted in Figure 5.2, showing a *breakthrough* peak for the double negatively charged maleic acid molecules in the adsorption phase when negative potential is applied (−500 mV or −800 mV, black curves). The similarly charged species flush through the column without interacting with the surface. In contrast, when a positive potential is applied to the particles (+800 mV, gray curves), the counter-charged target is attracted and entirely bound (no breakthrough peak is visible). Figure 5.2a illustrates a so-called *potential-step* experiment, in which an immediate potential inversion induces repulsion of adsorbed maleic acid molecules, visible in the *desorption peak*. When desorption is triggered by modifying the potential smoothly over time, a *potential-gradient* experiment is performed as depicted in Figure 5.2b.

Both experiments using CNT-K reflect the expectations and correlate to the EDL theory. The proof-of-concept is also determined for the IoLiTec-CNT, which chromatograms are illustrated in Figure A.5 in the supplementary information. Therewith, CNT-K and IoLiTec-CNT are suitable to be used simultaneously as chromatographic resin and capacitive electrode material. The achieved proof-of-concept characterizing the electrosorptive interaction between any kind of MWCNT and a small organic molecule represents the preliminary stage for further process development and answers RQ 1.

Key findings of Section 5.1 (cf. RQ 1)

⇒ CNT-K and IoLiTec-CNT are suitable for capacitive processing.

⇒ Any kind of MWCNT can function as 3D flow-through electrode.

⇒ Adsorption and elution of a small, compactly charged organic molecule can be triggered via electric potential.

5.2 Evaluation of the 3D Flow-through Cell

While the proof-of-concept showed that the used PCC setup is generally suitable for capacitive processing, further investigations of the specifically designed process are necessary to understand and transfer the knowledge about the influence of the setup configuration and the material properties [6, 134, 135]. This Section addresses RQ 2 and examines the cylindrical flow-through setup with radial potential distribution in its details, including the column framework in Section 5.2.1, and the specific properties of the MWCNT particles in Section 5.2.2. Besides, Section 5.2.3 presents a study about the CNT-K natural interaction with organic molecules in static conditions, aiming to identify whether there is a primary interaction between the MWCNT and the analyte when no electrical potential is applied.

5.2.1 Examination of the Column Components

The PCC column consists of several parts as illustrated in Figure 4.2 and Figure A.4, from which only two are in direct contact with the MWCNT packed bed: the spacer membrane ensures stable particle packing and prevents fluid side flows; the wire coil enables potential transfer from the potentiostat to the particles. Another critical component is the porous inner cylinder, which works as a counter electrode but is not directly in contact with the particle matrix. All three column parts have to be conductive, mechanically stable to function in dynamic applications, and chemically inert in an aqueous environment. Although these components are necessary to run the process, the specific setup should allow the MWCNT packed bed only, to function as a capacitive unit interacting with the liquid environment. To determine if and how the three components contribute to the capacitive process, they are analyzed in the following. The assemble components (such as membrane caps, or the column clamps) are not studied further.

The Impact of the Counter Electrode

In this thesis, two almost identical PCC columns are used, one for CNT-K and another for IoLiTec-CNT. The setup is not interchanged to ensure reproducible processing. However, the custom-made porous inner cylinder of the CNT-K column has a smaller SSA than that of the IoLiTec-CNT column, and both CE cylinders have a smaller SSA than the WE matrix, which causes an unbalanced charge distribution. In contrast, an ideal capacitor works with equivalent electrode properties for achieving an equal charge distribution. As the SSA difference of the CNT-K matrix is larger than the one inside the IoLiTec-CNT column, a more significant radial potential drop is expected for CNT-K than in the IoLiTec-CNT column. However, it is expected that a more balanced potential distribution promotes the process operation, it is yet not confirmed as the CE was no focus of this thesis. For providing a universal setup in the future, further research should be carried out to identify the influence of the CE in a cylindrical setup.

The Role of the Membrane

The spacer membrane function in the first place to seal the CE for electrochemical corrosion, as is expected that redox-reactions can occur between the charged stainless steel surface and the aqueous mobile phase, and that sample molecules could be able to adsorb irreversibly. Thus, it prevents a loss of sample molecules and the mobile phase's escape through the porous structure and the borehole for the reference electrode.

Based on Brammen *et al.* [15], a strong cation exchange membrane is installed, which is woven from polystyrene, cross-linked with divinylbenzene, and functionalized with sulphonic acid [136]. It is deprotonated in the pH-range 1 to 10 and therewith chemically stable in the operating range of PCC. Its function principle in PCC processing is discussed as an excursus in the supplementary information and illustrated in Figure A.53. Although the membrane is permeable for water molecules and small cations, no water permeability is observed at ambient pressure (water column several cm). Osmosis is not expected as the membrane is in direct contact with the CE surface. The SSA of the membrane is around $0.34\,\mathrm{m^2/g}$ and neglectable compared to the WE SSA (approx. $100\,\mathrm{m^2/g}$).

As Su *et al.* [137] reported the application of an electric potential to polymer-functionalized conductive materials can activate the functional groups and induce redox-reactions, the influence of the potential on the membrane is analyzed optically and with energy-dispersive X-ray spectroscopy (EDX) before and after usage.

When the membrane is investigated optically after usage (> 500 working hours), visible changes of the membrane color are detected. The formerly fawn color turned into a spotted surface, and the assumed aging is confirmed. The capacitive operating conditions also seem to affect the SSA, which increases to around $0.5\,m^2/g$ and the chemical composition. The EDX analysis depicts that a new, unused membrane includes carbon, oxygen, fluorine, sodium, and sulfur (see Figure A.6), while iron is also determined on a used membrane. The iron ions could have been adsorbed from the solution (building complexes with the polymer) when $FeCl_3$ was used as an analyte. However, $FeCl_3$ as an analyte is only used in negligible concentrations, strengthening the assumption that the adsorbed iron comes from another source. It might be dissolved electrochemically from the stainless steel CE, the stainless steel wire, or from iron-catalyst residues of the CNT-K particles (details in Section 5.2.2).

The observed changes of the membrane material properties show that the potential-controlled process performance is affected over time. This knowledge can be highly relevant for future process development. When a stable long-term usage is desired, the membrane properties' influence must be examined closer. An alternative is to remove the membrane, which is often done in classical CDI.

The Requirements on the Wire Contact

A conductive wire is required to connect the particulate packed bed to the potentiostat. It should be chemically inert not to cause potential-dependent side reactions, as only the MWCNT matrix should function as an electrode. Last, it should be flexible enough to be formed and installed in the column but simultaneously stable enough to keep its form during the packing procedure.

Examining various stainless steel and gold-coated wires regarding their inertness, a simple, commercially available V4A stainless steel wire with 1 mm diameter fits best. The V4A wire was inert for at least 68 h in a highly concentrated salt solution (1 M NaCl), as no corrosion, brittleness, or optical aging was detected. Furthermore, the V4A wire stands the packing procedure of the column. The selected V4A consists of iron, chromium, and manganese (see EDX analysis in Figure A.6). After use (< 500 working hours), the color did not change, and the detected elements are equal, which confirms an inert behavior. However, the EDX only detects the kind of elements but not their quantitative amount, which is why it cannot be excluded that the stainless steel wire elements are reduced over time, causing, e.g., the surface iron on the membrane.

In chromatography, the best packing is a homogeneous tightest packed bed. In contrast, capacitive applications require a distinctive and homogeneous potential distribution, which can be achieved with hierarchical electrodes, including many particle-particle contacts. Chromatographic and capacitive quality is guaranteed when the maximum number of particles are arranged uniformly inside the column, causing a high number of binding sites and a high column capacity. For that reason, the wire geometry must be well-designed, contacting the maximum possible number of particles but simultaneously not influencing the packing's homogeneity. As a coiled wire is preferably used in the literature, several wire geometries (varying coil diameter and coil number, single-coil, grids, or intertwined wires) are screened in simulations. Finally, a medium coiled wire fits best, with an inner diameter of 8 to 10 mm and 12 to 15 coils per 50 mm, providing enough space for the particles to be homogeneously arranged and a good radial potential distribution for a high current response.

Although the calculated wire configuration is convincing in the experimental application, the wire coil complicates easy handling and will be challenging for process scale-up.

Current Response of Membrane, Wire, and Porous Counter Electrode

However, the PCC setup cannot work without a membrane, a wire, and a porous CE; the MWCNT should function as a key component controlling the capacitive process alone. To confirm this requirement, the influence of the column components on the current response is analyzed with cyclic voltammetry, comparing a packed and an unpacked column.

Figure 5.3 illustrates the CV curves for the column without matrix electrode (black line) and for CNT-K, or IoLiTec-CNT packed bed columns (gray line). No current flows in the empty columns when DI-water is used as a perfect isolator, visualizing that column parts do not actively control the electrochemical process. Comparing the results of the CNT-K packed column in Figure 5.3a with the IoLiTec-CNT packed column in Figure 5.3b, both columns show an elliptic CV. The current increases and decreases steadily and reversibly, indicating smooth EDL formation [138] and confirm the excellent conductivity and the capacitive behavior of the MWCNT. However, the recorded CV shapes match not entirely the rectangular profile of an ideal capacitor, as the recorded shift is caused by the impact of fluid dynamics or the existence of leakage current [134] (discussed in Section 5.3.2).

The measurements show that the current flow of the IoLiTec-CNT column is about two times larger and particularly higher in the negative potential region than the one of the CNT-K electrode. This could be caused when the IoLiTec-CNT column has a better potential distribution. Besides the setup, this can depend on the material properties, such as a higher conductivity of the single tubes or a better matrix architecture formation.

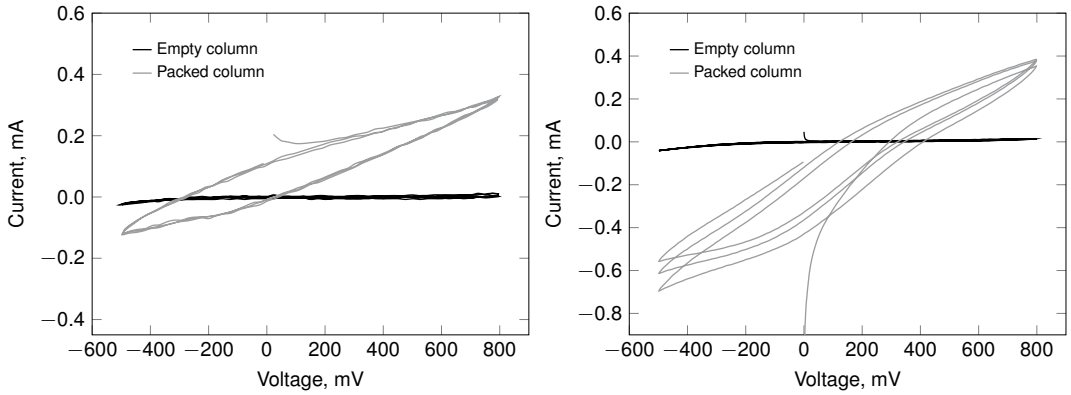

(a) CNT-K matrix.

(b) IoLiTec-CNT matrix.

Figure 5.3: Cyclic voltammetry experiments to analyze the input of the column components to capacitive processing. (a) CNT-K matrix, DI-water, 1.0 mL/min, 1.0 mV/s, 3 cycles, adapted from Trunzer *et al.* [19]. (b) IoLiTec-CNT matrix, DI-water, empty column: 1.5 mL/min, 2.0 mV/s, 3 cycles; packed bed column: 1.0 mL/min, 1.0 mV/s, 3 cycles.

Based on these results, a more significant number of electrically charged binding sites and a higher adsorption capacity is expected for the IoLiTec-CNT than for CNT-K. The determined differences in the current response make the specific material properties particularly important to identify the material's characteristics.

5.2.2 Particular Properties of the Multi-Walled Carbon Nanotubes

Several publications described the electrode structure and specific properties as decisive influencing factors on electrode performance [139]. For instance, a higher SSA as in microporous electrodes in a static system delivers a higher number of adsorption sites and a higher electrode capacity [140, 141]. In contrast, mesoporous or macroporous electrodes, like a homogeneous monolith, outplays in dynamic applications, promoting a faster charge/discharging due to smaller mass transfer limitations [48, 89, 142]. Besides, an oxygen functionalized electrode promotes the hydrophilic character of the material and improves the accessibility to the surface binding sites in aqueous systems [133, 143, 144].

It is known that differently synthesized MWCNT, and even different product batches, can vary in their properties [133, 145]. Moreover, bulk production, such as CVD, often causes not ideally shaped tubes with irregularities and defects. As differences in their current response are previously determined, the material properties of CNT-K and IoLiTec-CNT are characterized in detail to predict or explain the material's influence in further chromatographic and electrochemical studies. Comparing the synthesis protocols of the two manufacturers

first [17, 128], the MWCNT species are synthesized with CVD but differ in the catalyst used. Thus, CNT-K are synthesized with an iron-based catalyst and IoLiTec-CNT with an iron-nickel-aluminum-based catalyst. As catalyst residues from the synthesis are expected, the MWCNT particles are burned at 700 °C, where less than 1 % ash remains. Compared to the literature, the determined mass of the ash lies in the lower range [145]. The ash colors of the MWCNT materials differ as depicted in Figure A.7. While the ash of the IoLiTec-CNT has colored gray-blue, indicating total combustion of the carbon particles without catalyst residue, the color of the CNT-K's ash is brown-red, hinting at the presence of the oxidized catalyst, such as incomplete combustion of iron oxide. The catalyst residue remains after the recommended pre-purification of the CNT-K before usage, and thus can be an influencing parameter on the current response.

Specifications of the CNT-K

The impact of the synthesis on the CNT-K morphology is examined by investigating the morphology on different scales. Figure 5.4 illustrates exemplary pictures of the CNT-K taken with light, scanning electrode, and transmission electrode microscopy.

On the macroscale, as depicted in Figure 5.4a, the tubes form large, spongy agglomerates with an indefinable cotton ball structure. This agglomerate formation can be induced by the high aspect ratio and SSA [8], stimulating Van-der-Waals (VdW) interactions or $\pi - \pi$ stacking between the single tubes [146–148]. The sizes of the agglomerates in an aqueous solution are variable and lie in a broad range between 10 µm and 200 µm, as illustrated in Figure A.8. When the agglomerates are packed under flow in the column, they stick together and form monolithic structures. The mesoscopic view, in Figure 5.4b, illustrates CNT-K bundles and the formation of a fibril and very porous network. The measurable distance between the single

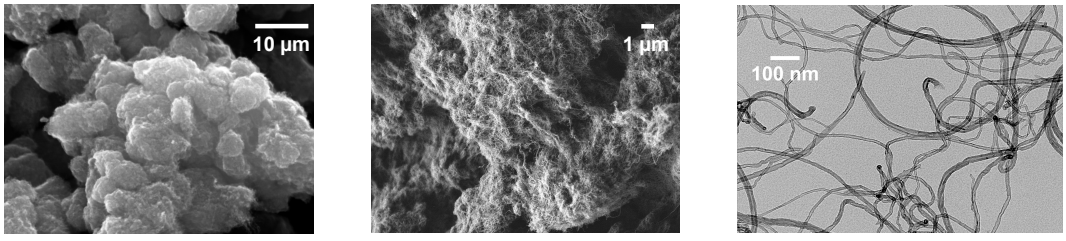

(a) Macroscale. **(b)** Mesoscale. **(c)** Microscale.

Figure 5.4: Morphology of CNT-K at different scales. (a) Macroscopic view of a MWCNT agglomerate (SEM taken by Marco Breidinger); (b) mesoscopic view of a MWCNT agglomerate (SEM taken by Katia Rodewald); (c) Microscopic view form single multi-walled carbon nanotubes (TEM taken by Dr. Sebastian Schwaminger). Adopted from Trunzer *et al.* [18]. Licensed under CC-BY-4.0 (https://www.mdpi.com/2076-3417/10/3/1133/htm).

tubes is several nanometers ($\gg 2\,\text{nm}$) and depicts a mesoporous system. As the agglomerates are dried to take the SEM pictures, they shrunk in volume, and the pore size becomes smaller. Thus, it is more likely that a macroporous MWCNT system exists in wet environment, as presented by Wang *et al.* [149]. Figure 5.4c depicts a TEM picture in which the single tubes are visible. These tubes own an outer diameter between 5 to 20 nm and an inner diameter between 2 to 10 nm, illustrated in Figure A.9. The resulting wall size is around 2 to 7 nm, with 6 to 20 layers when the space between the tubes is defined with 0.34 nm [150–153]. The number of walls correlates to the tube's electric conductivity. As MWCNT behave like graphene, the conductivity increases with increasing wall numbers as more electrons can be transported. Furthermore, the length of the MWCNT, which is measured up to 1000 nm in the TEM pictures, promotes a distinct conductivity and the potential distribution in the column. The longer the tubes are, the smoother the electron conductance can be.

The porous structure of the CNT-K agglomerates results in a specific surface area of around $200\,\text{m}^2/\text{g}$, which lies in an appropriate range for MWCNT with a mean outer diameter of around 15 nm as reported in the literature [145, 154]. Compared to single-walled carbon nanotubes with closed ends, the SSA of the MWCNT is only $1/6^{th}$; compared to SWCNT with open ends, it is $1/16^{th}$ [145]. However, SWCNTs are around 10 to 100 times more expensive, not fabricated on an industrial scale, and exist in three different conformations where only the armchairs are reliably metallic. As the MWCNT is naturally metallic due to its multi-layer structure [155], commercially available, and inexpensive, it is the preferred electrode material in comparison to SWCNT for preparative PCC.

Taking a closer look to the single tubes, as exemplarily depicted in the Figures A.10 and A.11, surface defects and the capped ends of the tubes are visible. Counting the ends of 245 CNT-K, over 87 % of the tubes are naturally end-capped by half-fullerenes. Thus, there is almost no access to the mesoporous interior of the MWCNT, and adsorption mainly occurs at the outer shells of the MWCNT. The specific structure of the MWCNT reflects that the surface of the bulk material is not smoothly grown and has numerous different surface defects, which arise during the catalytic synthesis. Bending, twists or coils due to C-ring defects are visible (C5 or C7 rings instead of C6 rings) [156, 157]. Besides, flaking of the multi-walls results in an irregular number of multi-walls for a single tube, similar to Yi *et al.* [158]. Furthermore, bamboo and cup-stacked formations can be observed [159, 160]. These defect sites are not balanced energetically and, therefore, highly reactive. They enable the formation of functional groups and define the surface charge. While smooth and as-grown MWCNT without defects or functionalization are mostly uncharged and behave hydrophobic [161, 162], defective MWCNT can change in their surface wettability [143, 144]. Surface functionalization during synthesis or enforced modification via chemical treatment can make the MWCNT either hydrophobic or hydrophilic, depending on the kind of functionalization [44, 163]. Hence,

the design of specific, environmentally adapted, functionalized MWCNT can improve the material's wettability and the accessibility to the binding sites. For instance, Lee *et al.* [146] showed that the zeta potential of pristine and unmodified CNT decreases from a rather neutral surface to a highly negatively charged surface when oxygen groups are present. The higher the number of oxygen-functionalized groups, the more negatively charged the surface becomes at a neutral pH-value which promote the interaction to counter-charged species.

The defective, random configured CNT-K particles therewith let expect a natural surface functionalization, which is described further in the following using XPS, potentiometric titration, and pH-shift experiments.

XPS measurements:

The results of the XPS measurements for CNT-K are illustrated in Figures A.12 and A.13, visualizing the presence of surface oxygen in different configurations. The carbon spectra in Figure A.12 indicate hydroxyl, carbonyl, or carboxylic groups [92, 164], whereas C=C bonds was indicated at 284.5 eV (sp^2 hybridized), C-O at 286.5 eV, and C=O at 287.7 eV. The broad peak tailing is related to $\pi - \pi$ characteristics, and C-N bonds can be expected at 285.8 eV. Furthermore, oxygen is determined as a single element, which minimum oxygen-to-carbon ratio is 5.7 %, calculated by dividing the oxygen peak area by the total carbon peak area. The result contradicts the manufacturer's description of non-functionalized MWCNT and corresponds to the description of oxygen-functionalized MWCNT [164–166]. Thus, according to Lee *et al.* [146] and Nicoletti *et al.* [67], the surface charge of the CNT-K is expected to be negative in aqueous systems when the surface oxygen groups are deprotonated.

Potentiometric titration:

The presence of a negatively charged CNT-K surface is confirmed in the results of the potentiometric titration experiments (see Figure A.18a). The results show no significant difference when differently concentrated particle slurries are analyzed, which might indicate a minor ion uptake of the CNT-K from the solution seems. The pH-dependent charge density profile in Figure A.18b depicts a mean charge density around -0.62 ± 0.14 mC/m^2 at neutral conditions. Depending on the MWCNT specifications, the results for CNT-K is lower than an example in literature, with ≈ -2.5 mC/m^2 [167], but still expected to be in a comparable range. The pH_{pzc}, respectively the IEP, is detected at pH 3.7 and describes the pH-value at which the surface charge density is zero. Thus, the CNT-K can be positively and negatively charged related to the pH-value of the system, which will affect the binding behavior of differently charged species. Compared to the literature, the calculated pH_{pzc} for CNT-K corresponds to the IEP determined by Ndunda *et al.* [166] (around 4 for oxidized MWCNT), and still comparable to the measurements of Sydorchuk *et al.* [168] (around 2).

pH-shift:

The pH_{pzc} determined in the acidic region for CNT-K is a key variable for adsorption processes and verified in additionally performed pH-shift experiments. Here, the IEP is characterized by an equality of initial pH-value pH_{set} and the one after equilibration pH_{is} [169, 170]. The simple method is used to quickly validate potentiometric titration experiments and investigate if the material has buffer properties (pH-plateau at equilibrium). The results for the CNT-K particles are depicted in Figure A.19a, and show that the pH-shift is not that significant. The IEP is determined around 3, which equals the data from the literature [166, 168] and the potentiometric experiments. As no pH-plateau is formed, the CNT-K have no buffer properties and indicate that the surface functionalization do not impact the surrounding aqueous phase distinctively. However, the intersection points at high acidic and high basic pH-value (below pH 4 and above pH 9) might be caused by the dominant amount of oxonium or hydroxyl ions diminishing the measurable effect on the pH-value.

Specifications of the IoLiTec-CNT

To identify possible differences between IoLiTec-CNT and CNT-K, the IoLiTec-CNT are analyzed similarly. The microscopy pictures are depicted in Figure A.14, showing a similar cotton ball structure than the CNT-K agglomerates. The single IoLiTec-CNT tubes further show a random bulk composition with open and closed tubes ($\approx 82\,\%$) and defects. The specific size distributions in Figure A.15 shows that the IoLiTec-CNT dimensions are almost identical to the CNT-K, with an outer diameter of 5 to 20 nm, and an inner diameter of 2 to 10 nm. There is also no distinct difference detected in the average wall size, which is around 2 to 6 nm, indicating that 6 to 18 tubes stacked into each other (compare CNT-K: 2 to 7 nm, 6 to 20 layers). The maximum length to measure was in the ten-micrometer region. The resulting SSA for IoLiTec-CNT is around $210\,m^2/g$, and a little higher than the one of CNT-K ($200\,m^2/g$), which could be caused by the slight differences in the MWCNT dimensions or the particle density. Due to the existence of surface defects, IoLiTec-CNT have a surface oxygen content of 5 % (cf. A.16 and A.17), which is close to the one of CNT-K.

While both MWCNT seem almost similar in the first screening, the surface influence in an aqueous medium is analyzed further to understand the differences in the material's current response. The results for the potentiometric titration experiments are illustrated in Figure A.18c and visualize a distinctive mass-dependent shift regarding the slurries' titration curve. The calculated surface charge density is depicted in Figure A.18d, lying within an average of around -2.62 ± 0.24 mC/m^2 which is comparable to Smith *et al.* [167]. It is four times higher than the one of CNT-K at similar conditions. Hence, a higher attraction of contrary charged molecules is expected, resulting in a potentially higher adsorption amount for the IoLiTec-CNT than for the CNT-K. The pH_{pzc} is identified at 4.4 (cf. 3.7 for CNT-K),

identifying that the deprotonation of the IoLiTec-CNT surface functional groups begins at lower acidic conditions. Besides, the steep decline of the surface charge density curve indicates that the IoLiTec-CNT react more sensitive to the pH-value of the surrounding environment. The pH-shift experiments in Figure A.19b confirm the IEP region (around 4) and visualize buffering properties and higher ion uptake of the IoLiTec-CNT at moderate pH conditions. The mass-dependent pH-effect of the IoLiTec-CNT show that the particle's influence on the environment is could not only be given by the SSA (cf. mass-independent effect of CNT-K). Moreover, the charge density and pH-sensitivity of the IoLiTec-CNT cannot be reduced to the amount of surface oxygen. For instance, it might be caused by the kind of surface functional group or the defective sites that trigger the uptake or release of oxonium or hydroxyl ions. Hypothetically, specific surface groups can favor small ions to penetrate through the sp2-hybridized carbon rings as well as benefit physisorption or chemical reactions changing the dissociation equilibrium. In conclusion, the surface of the MWCNT is too complex to be described sufficiently, but it is to keep in mind that it controls the interfacial processes and can massively influence the current response.

Interplay of MWCNT and Water

Knowing that the surface charge properties directly affect the material's hydrophobic or hydrophilic character, the interplay between MWCNT and water is analyzed further. A hydrophilic character of the MWCNT material is expected from the surface functionalization and desired as PCC function in aqueous environments. Thus, a high wettability advantage accessibility of the target analytes to the binding sites and benefits the column capacity.

In contact with water, the surface self-charging defines the MWCNT three-dimensional arrangement. While the delocalized sp2-hybridized system triggers bundling via VdW forces, the deprotonated oxygen functionalized groups support electrostatic repulsion [171, 172]. As the functionalization of the MWCNT preferably takes place at the surface defects, a random and local charge distribution is expected along a MWCNT tube and in the agglomerates. Contact angle measurements identified a contact angle of around 60 to 80 ° for CNT-K. The result corresponds to the value determined by Schwaminger *et al.* [129] and represents a slightly hydrophilic character.

Another method to identify the interplay of MWCNT and water was found in water storage and drying experiments. Once dissolved in water, the CNT-K own extraordinary properties to keep over 93 wt−% of water after centrifugation. This indicates that 1 g of wet CNT-K pellet contains only 7 wt−% of CNT-K tubes, resulting in a water adsorption factor of 13.3 per own weight and surface coverage of 2222 molecules of water on 1 nm^2 of CNT-K surface. This high affinity of the MWCNT to water can be caused by specific surface functionalization and

high capillary forces inside the agglomerates [45]. In comparison to CNT-K, IoLiTec-CNT keeps around 91 wt−% of water (water adsorption factor 10.1), caused by the different surface properties.

Both materials capture an incredible amount of water, which leads the dry agglomerates to swell to over 125 % of their original volume when they are suspended. The agglomerate swelling causes a fluffy network and reflects a macroporous system, causing small mass transfer limitations in dynamic applications. As centrifugation forces compress the agglomerates to a larger degree than when they are packed under flow in the chromatography column, the pore size distribution and the water content inside the packed bed matrix are expected even higher. For this reason, the average weight of dry CNT-K possible to be packed in a defined column volume is low with 0.5 g (SSA of the packed bed $\approx 100\,m^2/g$) and water is the dominant component in the system, responsible for the matrix structure and the interfacial effects.

To compare the water storage capability of MWCNT to other commercially available materials, graphene (used as electrode material in CDI) and silica (used as stationary phase in chromatography) were selected. The results for the calculated water adsorption factors are illustrated in Figure A.21, showing that the water adsorption factor of CNT-K is several times higher than the one of graphene (2.7), and the one for porous silica (1.7). Concerning the specific surface area of the materials, CNT-K can bind almost 20x more water per unit area ($0.0664\,g_{Water}/m^2_{solid}$) than graphene ($0.0036\,g_{Water}/m^2_{solid}$) and silica ($0.0034\,g_{Water}/m^2_{solid}$). As the CNT-K have the smallest SSA, the result is extraordinary and might be caused by free and bound water. *Free water* is stored due to capillary forces inside the spongy macroporous agglomerate and will make up the largest part. *Bound water* is expected when the functional groups form strong water-MWCNT interactions resulting in water shells or water clusters [166, 173]. Besides, encapsulation of water in the lattice fringes at the tube walls [152, 174], or in the mesopores o the open tubes (around 13 %) [175] could exist, which could be one explanation for the pH-shift. As bound water will form the EDL and affect the mass transfer at the solid-liquid interface, its theory is analyzed further in drying experiments (see Figure A.22 and the Equations A.1 to A.3). The data show that 1 g of wet CNT-K needs around 30 h to be completely dry, while the same amounts of silica and graphene are entirely dried after 2 h. Hence, the determined drying time of CNT-K is 15 times higher and seems to be necessary to vaporize the large amount of free and bound water. The assumption of bound water is analyzed further in thermogravimetric analysis (TGA), which results are depicted in Figure A.23a for wet CNT-K. The steep weight loss and the increasing ion current for water at low temperatures (peak between 100 °C and 200 °C) indicate the vaporization of free water in the wet pellet [159]. A second weight loss occurs at higher temperatures (between 500 °C and 800 °C), which correlates to total combustion of the surface-oxygen functionalized MWCNT [146, 163, 176]. The curves detected for the dried CNT-K (cf. Figure A.23a) show

no mass loss at low temperatures, confirming the absence of free water, and a one at the high temperature, confirming total combustion of MWCNT. As the measured amount of CO_2 is almost zero at high temperature but the H_2O signal increases, the data might indicate bound water as a specific component at the MWCNT surface.

A more detailed study of the material properties would go beyond the scope of this thesis. However, it is successfully shown how important it is to understand the surface properly. Thus, the MWCNT are identified as macroporous, cotton-ball like agglomerates. They have a hydrophilic character and an outstanding water binding capability. The oxygen-containing surface causes a pH_{pzc} in the acidic region and a naturally negative surface charge at neutral conditions, which can favor the interaction with water and positively charged molecules. Besides, an assumption about free and bound water is formulated, particularly interesting as water molecules will decisively impact the interfacial processes and the EDL formation. It is shown that even if the MWCNT material properties have similar morphology, crucial differences in the solid surface/liquid interactions can affect the adsorption behavior and the electrochemical performance of the PCC process.

5.2.3 Interaction of CNT-K with Organic Molecules in DI-water

To investigate the fundamental interaction mechanisms between MWCNT and various analyte molecules, static binding capacity (SBC) experiments were performed in an open system without external influences. As the adsorption depends on the de-/protonation of the functional surface groups and the molecules at specific environmental conditions, identifying the natural interaction mechanism is relevant for interpreting the adsorption behavior in dynamic separation processes. Based on the material characterization section, it is assumed that the negatively charged CNT-K will favorably electrosorb counter-charged molecules at neutral or basic conditions. Below the IEP (pH < 4), when the CNT-K surface is neutral or slightly positively charged, negatively charged molecules are expected to be bound.

The following small organic molecules are selected to study the static binding adsorption behavior, as they form the basis for peptides, proteins, and polymers (see Figure A.2):

- Maleic acid (MA) – the cis-isomer of butenedioic acid, the strong acid tends to spontaneously deprotonate in aqueous solution and exists as single or double negatively charged molecules in neutral conditions;
- Fumaric acid (FA) – the trans-isomer of butenedioic acid, the double protonated acid has a higher dissociation constant than MA and a worse dissolubility in water;

- Histidine (His) – an aromatic amino acid with a second basic functional group;
- Phenylalanine (Phe) – an amino acid with an aromatic side chain;
- Tryptophan (Trp) – an amino acid with an aromatic side chain; and
- Alanine (Ala) – an amino acid containing besides an amino-carboxylic group, only a methyl rest. Its small size defines a compact and spherical structure.

The carboxylic acids are completely deprotonated (for acid constants see Table A.1) at neutral conditions, owning a negative charge character like the CNT-K at a similar pH-value. The interaction between the MWCNT and MA or FA molecules is expected to be small due to repulsive electrostatic forces. All amino acids are ampholytes, able to react as acid or basis at the corresponding pH-value. At their IEP value (for further details, see Table A.1), the net charge of the amino acids is neutral; however, both the positively charged amino and the negatively charged carboxylic group are de-/protonated. Based on the study of Butyrskaya *et al.* [177], it is expected that alanine interacts with the CNT-K only over the amino group, forming electrostatic interactions or hydrogen bindings. The other amino acids can also interact over their aromatic side chain formin $\pi-\pi$ bindings. The aromatic molecules are not spherically compact, which is why their interaction with the surface can depend on steric effects and the energetically favored three-dimensional arrangement.

Adsorption Isotherms of Small Organic Molecules in DI-water

In the first experimental serie, the natural adsorption amount of various analytes on the MWCNT is studied at moderate conditions (neutral for the carboxylic acids and at the IEP for the amino acids). The adsorption amount (load q) of the MWCNT was calculated from the supernatant related to the inserted mass of the wet CNT-K pellets. The loads plotted in Figure 5.5 refer to the dry mass of the MWCNT, which was transferred over the wet-dry correlation ($m_{CNT-K,dry} = 0.07 \cdot m_{CNT-K,wet}$, see Section 5.2.2) and are published in Trunzer *et al.* [18].

Figure 5.5a illustrates a linear adsorption isotherm for the carboxylic acids, which is equal (excluding the outlier of FA) for both isomers and independently of the molecule solubility in DI-water. Thus, the dried CNT-K can adsorb around 100 mg/g of the carboxylic acids at similar conditions ($c_{eq} = 5\,\mathrm{g/L}$), visualizing an unexpected interaction between the double negatively charged molecules and the slightly negatively charged MWCNT surface. This phenomenon might be explained when the acid molecules precipitate or crystallize on the surface [178, 179]. Besides, MA and FA could interact with the CNT-K surface over the sp2-hybridized system, by weak polar bindings or over existing hydrogen clusters at the MWCNT shell.

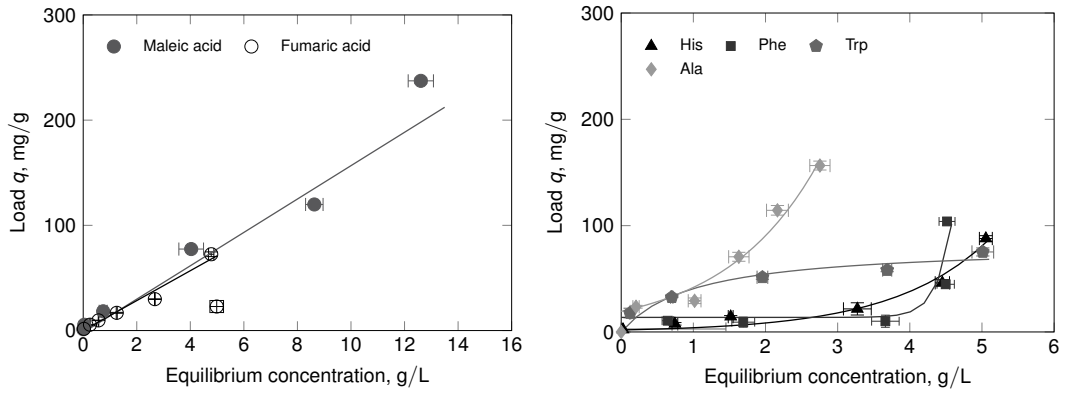

(a) Caboxylic acids.

(b) Amino acids.

Figure 5.5: Static binding capacity of (a) carboxylic acids and (b) amino acids to determine the interaction mechanism of the organic molecules with the CNT-K. The experiments were performed with wet, centrifuged CNT-K, the adsorbed amount is related to the dry mass. RT, 24 h, 500 rpm, pH 7 for carboxylic acid, pH at IEP for amino acids, two to three technical replicates. Adapted from Trunzer *et al.* [18].

Further reasons for different interaction mechanisms can also be found in the theory of Vardanega and Picaud [180], who described a delocalized SWCNT surface as a surface with mutual polarization. Thus, spontaneous, positive polarization can induce electrostatic interaction between the negatively charged molecules and the surface. Besides water clusters, surface defects and functional groups can induce different adsorption behaviors. The various distribution of these factor sites along a MWCNT makes it impossible to describe the MWCNT as net charge carriers, so the complex interaction mechanism cannot be reduced to a single criterion.

The adsorption behavior of the amino acids at their IEPs shows that each species has a different kind of adsorption affinity (cf. Figure 5.5b). As expected, the highest mass-related and molar-related adsorption amount is reached by compact alanine in the examined concentration range, showing a multi-layer adsorption behavior. A preferred encapsulation of this amino acids inside open tubes [180–182] instead of the outer shell is refused as the MWCNT are mostly end-capped. Thus, a more probable reason is the high charge density of the small molecule, which therewith can be strongly attracted via electrostatic interactions. The adsorption isotherm of tryptophan follows a Langmuir trend, with a maximum load of 75 mg/g. In contrast, the adsorbed amount of the other aromatic amino acids tends to increase exponentially with increasing analyte concentration. Electrostatic interactions between the amphoteric group of the aromatic amino acids and the MWCNT are expected to be the primarly bindings at lower concentration [172]. Dominating $\pi - \pi$ bindings are expected at higher concentrations, caused by the specific concentration gradient favoring the energetically balanced interactions between delocalized systems and the phenyl group [183].

In this experimental series, Phe seems to adsorb only at very high concentrations, which is why it has to be said in advance, that the results of the following pH-dependent SBC study show a different adsorption behavior. The reason is the sensitivity of Phe in the investigated environmental conditions and, more appropriately, the changed operating conditions between the experimental series (see Section 4.3).

While the SBC experiments showed that various interaction mechanisms between charged molecules and the MWCNT are possible, the effect of the surrounding environment on the adsorption behavior was not considered in this series. Thus, pH-dependent static binding experiments are performed in the next step. The aim is to identify expected differences in the adsorption behavior when the charges of the MWCNT surface and the target molecules vary depending on the pH-value.

pH-dependent Adsorption Behavior in Different Media

While the SBC experiments presented before were performed to screen the adsorption behavior of different molecules, the investigation of the pH-dependent SBC experiments concentrated on the role of the solid-liquid interface, including the impact of water. For that reason, the calculation of the adsorbed amount was extended in order to include the dilution factor of the wet MWCNT pellets ($m_{CNT-K,dry} = 0.07 \cdot m_{CNT-K,wet}$) resulting in a load q^* for the pH-dependent SBC experiments (see Equations A.4 to A.13).

The pH-dependent SBC experiments are a contribution to the publication in Wagner *et al.* [20], using maleic acid and phenylalanine as the analytes (protonation schemes in 2.1 and 2.2) and pH-pre-adjusted DI-water, as well as 0.5 mM, and 5.0 mM PBS as solvents. MA is selected as a dense, single charge carrier (negatively charged above pH = 2), which electrosorptive character is confirmed in the proof-of-concept. Phe is selected as an aromatic multiple charge carrier (IEP = 5.5), able to be positively ($pK_a = 2$) and negatively ($pK_b = 9$) charged. The experiments using DI-water are performed to analyze the net adsorption behavior without pH-regulating components and additional ions. Phosphate buffers were used to analyze if the expected pH-changes can be balanced and if additional ions impact the adsorption behavior cooperatively or competitively.

The results are presented in two parts: (1) the analysis of the occurring pH-changes when the wet CNT-K pellets are incubated with specific analyte solutions (cut-out for MA and Phe in DI-water in Figure 5.6), and (2) the pH-dependent adsorption capacities of the CNT-K at equilibrium (cf. Figure 5.7). More information about the single pH-changes of the mixtures are given in Figure A.24. The individual results are illustrated in Figure A.25 for maleic acid and in Figure A.26 for phenylalanine.

(1a) Analysis of the pH-Effect using Maleic Acid as an Analyte

The pH-shift experiments already showed that the pH-value of pH-pre-adjusted DI-water changes slightly when coming into contact with the CNT-K particles. Thus, it is expected that the pH-value of the incubated MA solution also changes when it is in contact with self-charged particles. However, this expectation is not confirmed as the pH-value of the control samples (without particles), and the one of the particle slurries did not show decisive changes at equilibrium ($pH_{is} = pH_{set} \pm 0.8$; see Figure 5.6a). Compared to the pH-shift of the MWCNT/DI-water experiments, MA molecules seem to stabilize the EDL and diminishes the pH-effect. Only one significant pH-decline was measured at basic conditions, where the pH-value drops from 9.5 to 8.0. A possible reason for this phenomenon is not found yet, as the carboxylic acid molecules and the CNT-K surface are completely deprotonated at basic pH-value, which is why electrostatic repulsion is expected between all components: the tubes, the MA molecules, and the hydroxide ions regulating the basic pH-value. Moreover, the influence of the adsorption of MA can be neglected, as the impact of the adsorption process of maleic acid is excluded at basic pH-values, where the load is minimal.

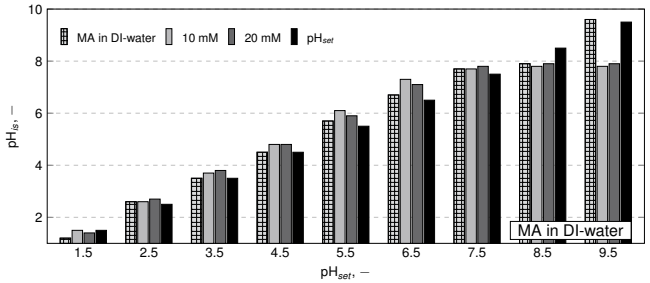

(a) pH-development of MA in DI-water.

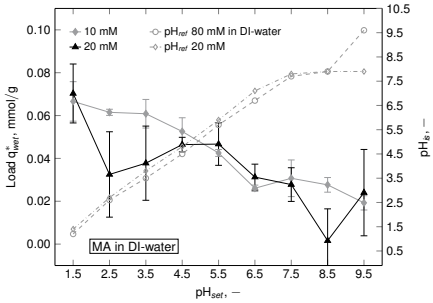

(b) Load of MA in DI-water.

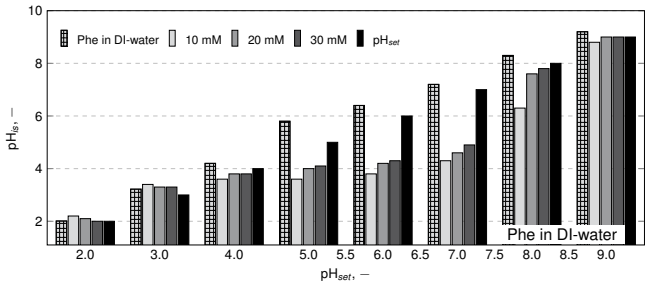

(c) pH-development of Phe in DI-water.

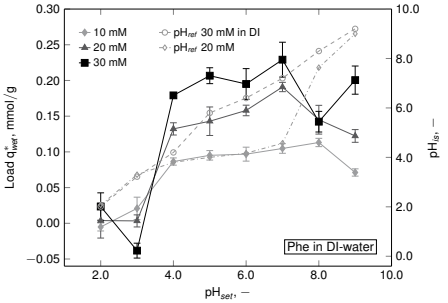

(d) Load of Phe in DI-water.

Figure 5.6: Overview of the pH-depended adsorption study of maleic acid and phenylalanine on CNT-K in DI-water. Subfigures (a,b) represent MA and (c,d) Phe in DI-water. Subfigures (a,c) show the load related to the initial pH-value, (b,d) visualize the pH-value after equilibration. Results are elaborated in Figure A.25 for MA and Figure A.26, adapted from Wagner *et al.* [20].

In contrast, the adsorbed amount of maleic acid is highest in the acidic region (see Figure 5.6b), in which the analyte and the MWCNT surface are neutral or counter-charged. Thus, the maximum adsorption amount $q^* = 0.08\,\mathrm{mM/g}$ is determined at pH = 1.5 which confirms the presence of electrostatic interaction and indicates that 43 % of the available particle surface (for the calculation, see Equations A.14 to A.18) is covered. As expected, the adsorbed amount decreases with increasing pH-value, reaching around $0.04\,\mathrm{mM/g}$ at neutral conditions and is minimum when repulsion of the completely deprotonated species is dominant. Nevertheless, a small load is detected even at basic conditions, which can be caused by mutual surface charges of the MWCNT expecting to occur over the whole pH-range.

When the two introduced calculation methods for pH-dependent and pH-independent SBC are compared by transferring the corrected load q^* of the 10 mM sample at neutral conditions into the load q, the adsorbed amount is equal. However, the trend of the adsorption amount of MA in the pH-dependent study is not linearly increasing with higher analyte concentration, as it was detected for the pH-independent study. The observation may result in the changed experimental conditions. It might be neglected as the surface of the CNT-K is yet not covered entirely but can indicate a linear adsorption regime at higher concentrations.When a buffer is used as a solvent, the expected linear adsorption amount related to the initial concentration is visible. The presence of buffer ions does not change the pH-value over time, indicating that no further ion transfer occurs at the surface. Besides the stabilized protonation states, the additional buffer ions do not affect the binding capacity significantly.

As the pH-dependent effect on the load of MA is focused in this study, the irregularities are not analyzed further but should be studied further for interpreting the interaction effects in detail. All results are summarized in A.25 for MA dissolved in different solvents.

(1b) Analysis of the pH-Effect using Phenylalanine as an Analyte

When phenylalanine is used as an analyte, the pH-shift is much more significant. Especially in the moderate pH-region of DI-water (Figure 5.6c) and for the low concentrated buffer. The δpH varies from -1.0 to more than $+2.5$, reaching a plateau at around $\mathrm{pH}_{is} = 4$. The results indicate that the interaction of Phe with the interface promotes the pH-effect. As such large pH-shifts are not measured for the control samples, the effect must result from the interplay between the particle's surface, the solvent, and the molecules. Thus, the molecule constitution seems to be a critical value, as the maleic acid experiments did not show this effect. When a higher concentrated buffer is used, its ion concentration can balance the pH-changes, and the pH-shift is diminished. Besides, the pH-gap decreases with increasing analyte concentrations and the increasing adsorption amount of Phe molecules, also highlighting that the pH-shift strongly depends on the interaction between Phe and CNT-K.

The highest binding capacity is determined when the CNT-K are neutral to negatively charged, while Phe exists as a neutral or positive molecule at $pH_{is} = 4$. This behavior is favored weak electrostatic or preferably aromatic interactions [183]. The concentration-dependent adsorption amount increases for all solvents with increasing analyte concentration. It is highest with around 0.20 mM for a 30 mM solution. Therewith, the surface coverage is more than 150 %, which hints at a multi-layer behavior as also determined in the previous SBC experiments. In strong acidic or basic pH-regions, the load is minimum, as both the analyte and the surface are similarly protonated or deprotonated, and electrostatic repulsion seems to dominate other interaction forms.

As already indicated, the results of the pH-dependent SBC experiments contradict the study of the pH-independent study, as the load of Phe increases even at low inlet concentrations for the pH-dependent experiments using DI-water, while the adsorption of Phe only took place at high inlet concentrations in the SBC study with neutral pH-value. If the loads are converted, the load determined in the pH-dependent SBC is 2 to 3 times higher at similar conditions than in the experiments with constant pH-value. Consequently, the different preparation methods and the material batches affect the experimental results significantly and challenge a quantitative interpretation.
However, a qualitative statement about the pH-depended adsorption behavior can certainly be made. The detailed look at the interfacial effects confirms the assumption that the adsorption of charged molecules strongly depends on the surrounding environment, especially the pH-value at equilibrium. Moreover, the expected complexity of the interaction mechanisms could be successfully highlighted. It is confirmed that the particles, the analyte, and the surrounding environment affect each other.

All results are summarized in A.26 for Phe dissolved in different solvents.

(2) The Impact of the Equilibrium pH-Value on the Adsorption

Finally, the gained knowledge about the pH-shift of the slurry and the MA or Phe adsorption amount is summarized in Figure 5.7, in which their adsorption amount is related to the equilibrium pH-value after incubation.

Figure 5.7a reflects the adsorption behavior of 10 mM and Figure 5.7c the one for 20 mM MA in different solvents, showing that adsorbed amount of MA decreases with increasing equilibrium pH-value. The calculated loads are identical when pH_{is} is equal. Consequently, it is emphasized that the adsorption amount must not depend on the initial but the equilibration conditions. However, the detected load of MA on CNT-K is comparably low to other carbon species like activated carbon (AC). Thus, AC can bind twice as much MA at similar

experimental conditions [20]. Reason can be the different morphology of the two materials, different pore size distributions, and surface areas, which is around 64 % larger for the AC (AC = 18 m^2, CNT-K = 11 m^2). Besides, the surface functional groups will influence the adsorption amount as well [184].

The results for a 10 mM and a 20 mM Phe analyte are presented in Figures 5.7b and 5.7d. As expected, the load of Phe depends significantly on the equilibrium pH-value and is highest at the energetically favored equilibrium ($pH_{is} = 4$). The Figures visualize that the binding affinity of carbon material to aromatic molecules is higher than for small carboxylic acids. However, compared to AC, the adsorption amount of Phe on CNT-K is still only $1/10^{th}$ [20]. Transferred to a SSA-dependent load, AC can only bind 1.2x as much MA but 6.1x as much Phe than CNT-K. The phenomenon must be a consequence of the different surface properties and material structures, which is why a detailed analysis of the pore sizes and the two material surfaces' properties must be performed in future research to understand this phenomenon.

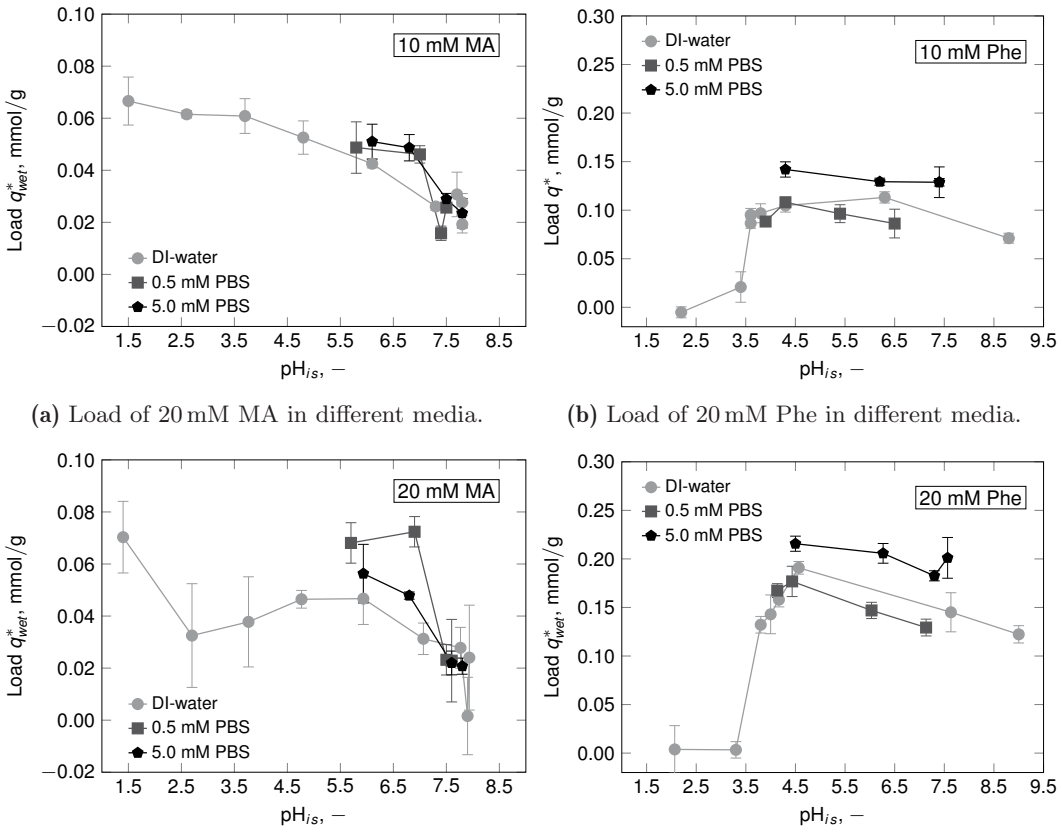

(a) Load of 20 mM MA in different media.

(b) Load of 20 mM Phe in different media.

(c) Load of 20 mM MA in different media.

(d) Load of 20 mM Phe in different media.

Figure 5.7: pH-dependent adsorption of 10 mM (a, b) or 20 mM (c, d) maleic acid (a, c) and phenylalanine (b, d) on CNT-K, when DI-water, 0.5 mM or 5.0 mM phosphate buffer are used as solvents. Supplemented data in Figures A.25 and A.26 for Phe. Contribution to Wagner *et al.* [20].

Investigating the effect of the different solvents on the adsorption of MA and Phe, a cooperative behavior of buffer ions can only be presumed. Thus, buffer ions might promote the adsorption of MA on the CNT-K at moderate conditions, as MA dissolved in PBS reaches slightly higher loads than DI-water at similar pH-values. Moreover, the presence of a large number of buffer ions can favor the adsorption amount of Phe. However, the data set is too small to get valid qualitative information.

The SBC experimental series showed that the surface's pH-dependency and the individual specifications of the target analyte and the solvent are decisive influencing factors of the adsorption kind and the binding capacity. Thus, it is determined that the pH-effect is more pronounced for the aromatic amino acid than for the single charge-carrying carboxylic acid but can be diminished when buffers are used. Moreover, it could be shown that Phe has a higher adsorption capacity as it can interact electrostatically and over the aromatic system.

All results presented in this Chapter answer RQ 2 and achieved information about the setup validity, the electrode morphology, and the natural binding affinity. These findings form the basis of working in a dynamic system.

Key findings of Section 5.2 (cf. RQ 2)

⇒ The membrane is the most critical component in the setup.

⇒ The MWCNT matrix is the only capacitive unit that triggers the process.

⇒ The cotton-ball like MWCNT agglomerates exist as a loose, macroporous net.

⇒ The centrifuged MWCNT keep 93 wt − % of water.

⇒ Interfacial water controls the EDL and the mass transfer at the surface.

⇒ The end-capped MWCNT allow electrosorption only on the tube's outer shell.

⇒ IoLiTec-CNT affect the aqueous dissociation equilibrium more than CNT-K.

⇒ The MWCNT have a natural affinity to adsorb small organic molecules.

⇒ Aromatic interaction favors the adsorption amount and dominate electrostatic ones at higher analyte concentrations.

⇒ Electrosorption is distinct when surface and species are counter-charged.

⇒ Despite repulsive forces MA binds on MWCNT over the delocalized group.

⇒ Phe/MWCNT interactions affect the dissociation equilibrium.

⇒ The use of buffers diminish the pH-shift, stabilizing the water-dominated EDL.

⇒ The target's capacity is not influenced by buffer ions in static conditions.

5.3 Combining Electrochemistry and Chromatography

After a detailed setup characterization, the behavior of the particulate matrix in the flow-through system must be analyzed as it is the critical component for capacitive processing. Functioning simultaneously as a chromatographic stationary phase and an electrically triggered working electrode, chromatographic and electrochemical studies are performed, which have individual characterization methods to describe and verify the different packed bed requirements. First, a chromatographic analysis of the MWCNT matrix structure is performed, as presented in Section 5.3.1, to investigate the packed bed homogeneity and the number of theoretical plates. A study with different electrochemical analysis methods follows, presented in Section 5.3.2, to determine the impact of faradaic and capacitive current, as well as the development of the electrochemical double layer. Finally, chromatographic and electrochemical methods are combined in an analysis protocol, used to evaluate the column's quality and performance over time (see Section 5.3.3).

This Section addresses RQ 3 and focuses on the verification of the different analysis methods. The chromatographic and electrochemical characterization is performed with CNT-K and IoLiTec-CNT electrodes, always using DI-water as a mobile phase. Some results are partially published in Trunzer *et al.* [18].

5.3.1 Chromatographic Characterization of MWCNT as Packed Bed Electrode

The heart of the PCC column is the particulate packed bed, which should function as a homogeneous fluid-flow distributor. Since the column's packing process can be affected by the wire or the non-uniform particles, a tracer analysis is performed before electrochemical characterization to determine the chromatographic quality. As the tracer ions used do not interact with the stationary phase, the resulting peak shape visualizes convection, dispersion, and diffusion effects. To determine the column porosity ϵ_{col} of the packed bed, blue dextran is used as a none-pore-penetrating tracer, NaCl is used as a pore-penetrating tracer to determine the total porosity ϵ_{tot} of the column (see Theory Section 2.2).

It is mentioned in advance that the MWCNT are highly affine to polymers (see Section 5.6.2), wherefore blue dextran turned out to be not a suitable tracer. The strong interactions between the molecule and the MWCNT result in no or a minor UV-Vis signal due to strong fraction dilution, which is why the breakthrough peaks are often not measurable. It was only possible to determine the column porosity for one single column experimentally to $\epsilon_{col} = 0.48$.

If NaCl is used as a standard pore-penetrating tracer, a pronounced detector signal was recorded, which is used to calculate the asymmetric factor A_s (packed bed homogeneity) and the $HETP$ (peak resolution and purity). A representative ideal salt tracer peak is depicted in Figure A.27, with a Gaussian shape and a small peak fraction. Table A.2 summarizes the characteristic numbers for one CNT-K packed bed column during its operating time. The results are reproducible and identify an ideal CNT-K column with an average asymmetric factor of around 1.18. The calculated $HETP$ is around 0.0465 cm, showing that the used MWCNT packing includes more than 105 theoretical plates (bed height = 5 cm). Both parameters highlight that the CNT-K packing provides a homogeneous fluid flow-through not affected by dispersion or mass transfer effects. Moreover, the calculated ϵ_{tot} for the ideal column is ≈ 0.86 indicating a highly porous, monolithic packed bed. The result correlates with the expectation of the high amount of stored water forming the packed bed morphology.

The validity of the CNT-K packing is confirmed when its characteristic parameters are compared to a standard IEX packing, as well as to the results of Brammen *et al.* [15] (see Table 5.1). Thus, the CNT-K packing achieves column parameters in the acceptable range of preparative chromatography, and even better ones than the Baytubes C 150 P packing did: $A_s = 1.36$ and $HETP = 0.3$ cm.

Table 5.1: Specific chromatographic parameters for various best-performing CNT-K columns. Column 1 used for experimental calculation and simulative estimation (NaCl and dextran tracer, transport dispersive model including ϵ_{col} and ϵ_{bead}, see Figure A.28a); column 2 used for simulative estimation (NaCl tracer, equilibrium dispersive model including ϵ_{tot}, see Figure A.28b). The data are compared to an ideal CNT-K column (Table A.2), to results of Brammen *et al.* [15] and to general IEX data [3, 22, 132].

Parameter	$\mathbf{A_s}$, –	$\mathbf{D_{ax}}$, mm^2/s	$\epsilon_{\mathbf{col}}$, –	$\epsilon_{\mathbf{bead}}$, –	$\epsilon_{\mathbf{tot}}$, –	**HETP,** cm
Ideal CNT-K	1.18	–	–	–	0.86	0.047
Exp$_{Col1}$	2.13	0.04	0.48	0.67	0.83	–
Sim$_{Col1}$	*Col 1*	0.03	0.46	*Col 1*	*Col 1*	–
Sim$_{Col2}$	–	0.08	*non*	*non*	0.78	–
Brammen	1.36	–	–	–	–	0.3
IEX	0.8 to 1.4	0.01 to 1.50	0.2 to 0.4	0.5 to 0.9	0.8 to 0.9	–

Simulation is performed to precise ϵ_{col} and ϵ_{tot}, and to get more information about the axial dispersion effects inside the macroporous system (axial dispersion coefficient, D_{ax}). The results for the calculated and estimated values are added to Table 5.1. The simulation is exemplarily listed for two different CNT-K columns.

Column 1 is analyzed as the only column providing a NaCl and a blue dextran signal (see Figure A.28a). The simulation focus was set on the target parameters ϵ_{col} and D_{ax}, which could be calculated experimentally (Exp_{Col1}) and precised in simulation (Sim_{Col1}) using a transport dispersive model (information about non-pore-penetrating and pore-penetrating peak necessary). Comparing the data sets gained, the calculated and the estimated D_{ax} are almost equal and describe a preparative column with homogeneously, well-distributed fluid flow. Moreover, the experimentally calculated ϵ_{col} was confirmed in the simulation, and showed that the macroporous MWCNT matrix has a slightly higher interstitial column volume than standard IEX columns.

Column 2 is used as a standard CNT-K column in which only a NaCl signal was measurable (see Figure A.28b). The simulation focus (Sim_{Col2}) was set on determining ϵ_{tot} and D_{ax} using a simplified equilibrium dispersive model (information about pore-penetrating tracer sufficient). With the reduced model, the total column porosity was estimated to $\epsilon_{tot} = 0.78$ and the axial dispersion to $D_{ax,Col2} = 0.08\,\text{mm}^2/\text{s}$ by implementing the NaCl tracer peak. The differences in the parameter sets between column 1 and column 2 visualize the difference of various MWCNT columns, even when the peak shape is ideal. This kind of simulation was also used for several other columns. Some of these were tailing ($A_s > 3$) and results in $D_{ax} \geq 0.4\,\text{mm}^2/\text{s}$, however its mass transfer effects are still in an acceptable range (cf. Figure 5.8). All other MWCNT matrix characteristics are comparable to IEX columns and strengthen the non-uniform CNT-K matrix's applicability as an alternative to hierarchically arranged spherical packed IEX columns.

Both simulation methods achieved in reflecting the real mass transfer effects occurring in the loose network of MWCNT. Moreover, it is shown that the simulated parameter sets of two differently implemented MWCNT columns are in a similar range. As ChromX is designed for spherical particle packing, it is shown that the software can also be used to describe more complex packings, which particle structure cannot be defined by numbers. However, the simulation models based on NaCl tracer analysis are not yet specific enough to describe MWCNT columns in general. For this reason, the fluid dynamic model must be adapted for each column, which is why a prediction about the potential-dependent adsorption behavior using an enlarged Langmuir model is not yet possible but would be an exciting prospect for the PCC process design.

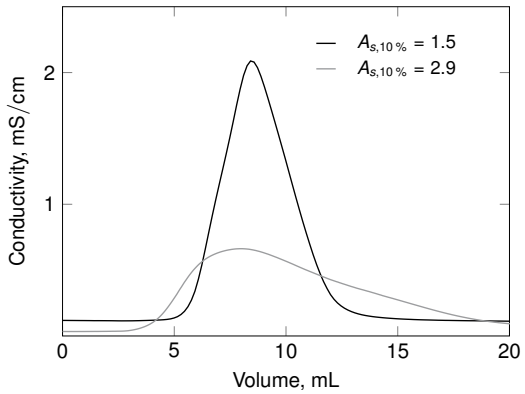

Figure 5.8: Tracer peaks of two different CNT-K columns. CNT-K matrix, DI-water, 1.5 mL/min (black line), 1.0 mL/min (grey line) 50 µL, 1 M NaCl. Partially adapted from Trunzer *et al.* [18].

Finally, reproducible packing of the random cotton-ball like CNT-K agglomerates is a big challenge in this thesis. A direct comparison of the column response is difficult when each matrix varies in its agglomerate morphology, and moreover when the installed wire contact disturbs the homogeneity. Thus, when the column is fronting after packing due to channels around the wire or at the membrane wall, the PCC column cannot be used for chromatographic processing. When the tracer run of a MWCNT packing identifies tailing due to dispersive effects, the columns might be still used as a suitable capacitive cell that guarantees sufficient contact area and good potential distribution. Two possible scenarios that can exist after packing are imprinted in Figure 5.8, showing an ideally Gaussian peak and a tailing column with high axial dispersion. The requirements on the electrochemical quality are discussed in the next section.

5.3.2 Electrochemical Characterization of the MWCNT Electrode

The electrochemical analysis is performed after the chromatographic characterization to identify the cell's electrochemical quality and performance. Since an electrochemical analysis protocol for 3D flow cells has not yet been explicitly defined, this Section analyses the significance of the various electrochemical analysis methods reflecting the current response of an ideally packed column. Hence, open circuit potential (OCP) measurements are performed to study the net surface charge of the MWCNT matrix electrode, and chronoamperometry, as well as cyclic voltammetry (CV) are used to analyze the impact of constant and gradient potential applications on the development of the solid-liquid interface.

In this Section CNT-K and IoLiTec-CNT are analyzed on their current response. DI-water is used as mobile phase media to concentrate on the influence of the material properties only.

OCP Analysis

Each electrochemical column characterization begins with OCP measurements to determine the working electrode's net charge. Knowing about the initial conditions helps to understand which electric force input is necessary to change the electrode's charge and consequently discuss the influence of the potential applied on the environment.

Contrary to the self-charging of the MWCNT in an open system where no external influencing factors are present, the self-charging of the MWCNT electrode in a closed system depends on the surrounding medium and components. Hence, the OCP of a CNT-K column flushed with DI-water lies between +300 mV and +500 mV and differs between different columns depending on the matrix structure. The OCP for IoLiTec-CNT packed beds is in a similar range but can even be measured higher for some columns (+300 to + 800 mV), which may result from the IoLiTec-CNT higher surface charge density.

The positive OCP identifies the MWCNT electrodes as naturally positively charged, which contradicts the results from the material characterization experiments identifying negatively charged particles in DI-water suspension (see Section 5.2.2). This phenomenon can be caused by spontaneous redox-reactions or a shift of the surface polarization, changing the working electrode's surface charge [180, 185, 186]. Additionally, the formation of water shells around the tubes can cause a positive polarization and promote hydrogen bindings [187, 188]. The positive net charge indicates that applying a positive potential to the MWCNT will have a minor impact on the EDL rearrangement than applying a negative potential affecting the surface properties more significantly.

As the OCP is a critical value impacting the adsorption behavior and strength of charged species to the MWCNT, it must be investigated for each material and each column matrix due to the various matrix properties.

Chronoamperometry Analysis

Chronoamperometry is a valuable method, which comes very close to PCC's operation mode, as constant potential is applied to modify the surface charge of the MWCNT packing. Each potential change induces a re-equilibration of the EDL and a specific capacitive and faradaic storage of ions. In this thesis, chronoamperometry is performed to highlight the potential-dependent effects of the solid-liquid interface, which knowledge is essential to design an energetically favorable electrode with maximum performance and understand the natural capacity of the electrode in dependency of the time. However, chronoamperometry, as performed in this

thesis, is not a widely used analytical method to characterize flow-through electrodes. Charge-discharge studies dominate in CDI [88, 91, 185], in which two potential values are applied repetitively measuring the conductivity deviations to determine the electrode's adsorption capacity.

Chronoamperometry experiments are performed over a broad range of electric potentials, expecting that the degree of disorder enforced by the electric charge density leads to different current responses. Based on Ohm's law, it is expected that the current response increases with increasing potential value. Simultaneously, the specific electrosorption amount, which equals the number of ions stored in the EDL, will increase. Exemplary results of a series of chronoamperometry experiments for an ideally packed CNT-K column are illustrated in Figure 5.9 (column A, cf. the chromatogram in Figure 5.11a).

The individual chronoamperograms for an experimental series between ±100 mV and ±800 mV in Figure 5.9a reflect the expected more significant current response with increasing potential. These curves are analyzed on:

- the *mean current*; is calculated as average current after the EDL rearrangement at equilibrium. It correlates to the faradaic current and indirectly to the resistance part of the column (see Figure 5.9b);
- the *electric charge* (el. charge); is calculated as area integral of the curve. It is proportional to the adsorbed amount of ions (electrode capacity) related to the sum of capacitive and faradaic current (see Figure 5.9c); and
- the *gradient* of the curve at the very beginning (calculated between 20 and 50 s). The steeper the gradient, the smaller the EDL rearrangement time (see Figure 5.9d), and the EDL extension are. However, the sensitive calculation is used only to visualize the EDL rearrangement time differences and cannot be used as a quantitative value.

Analyzing the column's current response on these parameters show that the mean current, the electric charge, and the EDL rearrangement time increase with increasing potential. As a higher potential induces a higher surface charge density, more ions can be electrosorbed. The Stern layer gets more compact and the diffusive layer extends in width towards the bulk due to higher attraction forces. When the current profiles of a positive and negative applied potential are compared, a higher mean current and a higher electric charge are detected for the negative potential. Reflecting the OCP value, the delta between −800 mV and the OCP (around +300 mV to +500 mV) is larger than the one for +800 mV, which confirms that a higher force input reaches a more distinct current profile and a higher electric charge.

The mean current profile is illustrated in the current/potential diagram in Figure 5.9b. When the mean current is unequal to zero after equilibration, faradaic current exists. The presence of faradaic current conflicts with the assumption of PCC working as an ideal capacitor, which mean current will be zero after charging. Thus, the PCC flow-through cell is identified as a non-ideal capacitor (pseudo-capacitor). When the mean current is plotted over the applied potential, the values increase linearly in the lower potential region below ±500 mV and become more distinct in the higher potential regions. A possible reason for the steep increase is the more distinct activation of faradaic current at higher potentials, inducing additional electron transfer as a cause of redox-reactions at the MWCNT surface functional groups.

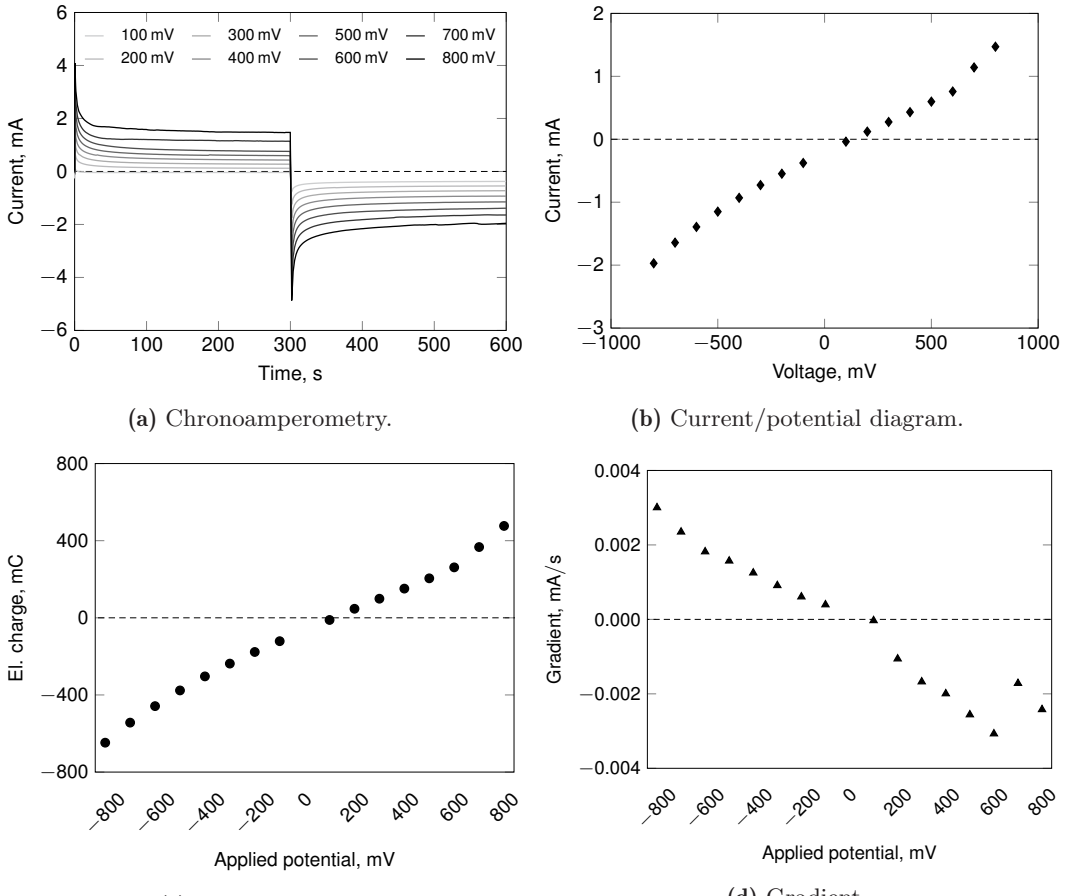

(a) Chronoamperometry.

(b) Current/potential diagram.

(c) Electric charge.

(d) Gradient.

Figure 5.9: Chronoamperometry measurements of a qualitatively valid CNT-K column (column A). (a) Exemplary chronoamperograms, (b) current/potential diagram of the mean current after EDL rearrangement plotted over the potential applied, (c) electric charge, (d) current gradient at the beginning. CNT-K matrix, DI-water, 1.0 mL/min, hold time 300 s. Chromatogram in Figure 5.11a. Partially adapted from Trunzer *et al.* [18].

There is only a single point in which the mean current is zero, at +138 mV, indicating the operating point where the CNT-K matrix is expected to behave as an energetically feasible, ideal capacitor. However, the electric charge at this point is too small for economic processing (see Figure A.30c). The higher the electric charge of the column is, the higher is its capacity, which should be maximum for adequate processing. In total, the chronoamperograms show that electric charge depends on the potential applied and therewith on the electrode rearrangement time (see Figure A.30d), its capacity, as well as the electrode and electrolyte resistance affecting the ionic movement [189].

Comparing the EDL rearrangement time of a PCC column with an ideal capacitor, it is much higher for the PCC flow-through column than that of an ideal static capacitor, where charging takes only a few seconds [189, 190]. The phenomenon is caused due to the presence of mass transfer limitations [94], such as flow-dependent convective and diffusion regimes inside the MWCNT electrode, increasing the column resistance. Moreover, the distance between the MWCNT in a macroporous system can cause a longer equilibration time than in a microporous system.

To verify chronoamperometry as a suitable characterization method, a repetition of four chronoamperometry experiments is performed for one column, using an ascending and descending order (from positive to negative and from high potential to low potential, and vice versa) of potential application. Evaluating the results, the deviations between the mean currents and the column's electric charges at different measurements are minor and in an acceptable range to confirm reproducibility (see Figure A.29). However, comparing the current/potential diagram of this CNT-K column to the previously introduced column, in Figure 5.9b, significant differences in the mean current are detected, caused by the morphological and structural differences of the packed beds even when the resin material is similar.

Besides, the current response of IoLiTec-CNT electrodes is examined, which results are illustrated in Figure A.30. The current profile of the chronoamperograms in Figure A.30a equal the ones of the CNT-K packing. The mean current (Figure A.30b), the electric charge (Figure A.30c), and the EDL rearrangement time (Figure A.30d) increase with increasing potential value. Eye-catching is the high current value immediately at the beginning of the experiment and after equilibration, which is two times higher than that of a CNT-K matrix. It is expected that the higher conductivity of the IoLiTec-CNT favors the column's electrical charge and confirms the assumption of material-dependent electrode responses.

The chronoamperometrical analysis showed that potential-dependent effects at the solid-liquid interface can be visualized, identifying well-packed PCC columns as a non-ideal capacitor with a capacitive and a faradaic part. While the experimental results are reproducible

for one material, the differences between the current responses of different packings and different materials are distinct, highlighting the setup sensitivity of capacitive processing. As pre-charging of the column is comparable to chronoamperometry measurements, it is crucial to be aware that a specific amount of the mobile phase's ions is always stored in the EDL.

Cyclic Voltammetry Analysis

Cyclic voltammetry experiments are performed to study the impact of a continuously changing electric potential on the current response, identifying smooth rearrangement or an irreversible modification of the EDL. Figure 5.10 represents CV of two ideally packed MWCNT matrix and visualizes that the packed bed structure and properties affect the current response. The determination corresponds to the observation of Chen *et al.* [191] who reported that the CV shape depends strongly on the tubes' electric properties and the three-dimensional arrangement of the MWCNT in a volume.

The black-colored CV of CNT-K column A, as already depicted in Figure 5.3, indicates an elliptic shape and a congruent increase and decrease of the current. The EDL rearrangement is stable for several cycles, and neither fluctuation nor redox-peaks are visible. The CV indicate electrostatic interactions at the solid-liquid interface [138]. The voltammogram's angular shift is caused by the fluid dynamical impact, which consequences shear forces and increases the liquid resistance. Nevertheless, leakage current can exist as the column is built as a series connection of resistance [134]. Nevertheless, the detected current profile is similar to a shifted rectangular CV shape of an almost ideal capacitor.

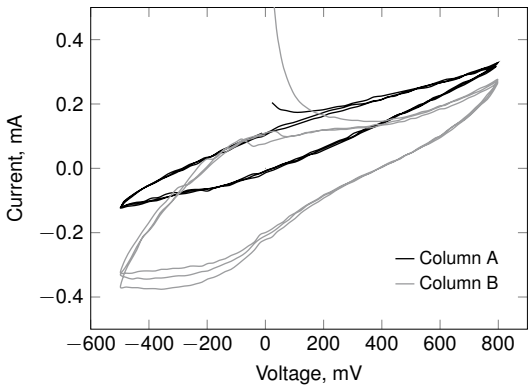

Figure 5.10: Cyclic voltammetry measurements of a well-packed CNT-K column. Column A: CNT-K matrix, DI-water, 1.0 mL/min 1.0 mV/s, 3 cycles (data correspond to Figure 5.3); Column B: CNT-K matrix, 1.5 mL/min 1.0 mV/s, 3 cycles.

The CV of CNT-K column B deviates from column A and highlights the influence of the matrix structure. It reaches higher currents and represents a more conductive matrix with a higher charge density distribution. The smooth elliptic curve identifies a reversible electrostatic formation of the EDL and a slight redox-peak between -200 to $+200\,\mathrm{mV}$ (compare to Chen *et al.* [191]). The sharp peak at high positive potential [140, 191], can be caused due to water decomposition (see also Section 2.4, reaction equations 2.12 to 2.14). When the CV curves are not overlapping at negative potentials [190] the surface is irreversible functionalization over time (see also Section 2.4, reaction equations 2.15 and 2.17).

The specific electric capacity is calculated as a gradient of the electric charge over the potential applied. It depicts the binding amount in the positive or negative charging periods, which are quite similar for both CNT-K columns (0.4 to $0.5\,\mathrm{mF/g}$, see Table 5.2). Therefore, the different current profiles seem to have little influence on the electric capacity caused when the capacitive part of the MWCNT electrode is limited and does not change, however faradaic current increases the electron flow. Compared to the literature, in which the electric capacity of carbon aerogel gels is given higher than $10\,\mathrm{F/g}$ [140, 142, 191], the one of the MWCNT columns is worse. A possible reason is the use of DI-water as mobile phase, while in literature highly concentrated electrolytes are used. Another reason is the low packing density and the small SSA of the macroporous MWCNT electrode. Besides, static conditions favor a distinct equilibrium, while the fluid flow limits the dynamic equilibrium.

As Yang *et al.* [142] reported that the electrode morphology significantly influences column performance, a redesign of the PCC column allowing a higher packing density or electrode mass can benefit the column response. However, the optimization of the PCC process is not part of this thesis, which is why although the knowledge about the little electric capacity of the CNT-K matrix is essential for comparison to other capacitive systems in the future, it is not relevant for the research focusing on the process fundamentals.

Table 5.2: Electric capacity (el. capacity) of two CNT-K columns, calculated as gradient of the electric charge over the potential applied in the negative/positive (neg/pos) charging regions of one exemplary cycle. CNT-K matrix, DI-water, $1.0\,\mathrm{mL/min}$, $1\,\mathrm{mV/s}$. The stability index in brackets.

Value	**Column A**	**Column B**
El. capacity$_{neg}$**,** mF/g (Stability index, –)	0.424 (0.9851)	0.448 (0.6430)
El. capacity$_{pos}$**,** mF/g (Stability index, –)	0.524 (0.9994)	0.408 (0.9099)

CV for two IoLiTec-CNT columns are illustrated in Figure A.31, and equals the CNT-K columns. Hence, column A of IoLiTec-CNT shows an elliptic shape with a reversible, capacitive current profile in the positive region. At high negative potential, the maximum current changes for each cycle, caused by irreversible faradaic reactions (cf. Section 5.3.3, column aging). The CV of column B is more distinct and indicating capacitive and faradaic current, especially in the negative region (peak current at -200 to 0 mV). Although the CV shapes of the CNT-K and the IoLiTec-CNT are comparable, the current responses of the IoLiTec-CNT electrode matrix is higher than the CNT-K. The results highlight the differences between the two materials' column response, which is attributed to the surface properties and the surface charge distribution.

Finally, the electrochemical analysis protocol can be used to describe the interfacial effects of the MWCNT electrode. It is highlighted that differently from dispersed pristine material, the MWCNT matrix has a positive net charge. A pseudo-capacitive behavior is identified, in which the column's electric charge increases with increasing potential value, increasing EDL rearrangement time, and decreasing column resistance. Moreover, it is confirmed that the matrix structure or the material properties influence the current response significantly.

5.3.3 Aging of the MWCNT matrix

After successfully validating the applicability of chromatographic and electrochemical analytical methods for MWCNT electrodes, the knowledge is combined to visualize the influence of matrix homogeneity and potential distribution on column performance over time. It is known that the electrode's performance depends on the matrix structure. Moreover, it is expected that altering the surface charges or external factors such as liquid flow could affect the fragile, macroporous MWCNT structure, which is why the current deviations have to be recorded over time. These possible structural or electrochemical changes are named *aging*. This Section aims to achieve knowledge about the column performance and answer RQ 3 by recording the electrode's quality from the beginning of a column's life until its break-up. Moreover, material aging is studied.

The characterization experiments are performed for CNT-K and IoLiTec-CNT in a DI-water system. The chromatographic tracer analysis is enhanced with simulation in ChromX. The results presented are partly published in Trunzer *et al.* [18].

Material Aging

When conductive particles are electrochemically charged inside an aqueous system, reversible or irreversible redox-reactions can occur at the surface above a critical potential. Irreversible modification might be undesired as it can lead to a surface functionalization or a deposition of the material. To investigate if material aging occurs, the surface properties of the MWCNT materials are examined before and after electrochemical treatment using XPS measurements. A detailed summary about the surface elements is listed in Table 5.3, or depicted in the balances in Figure A.13 for CNT-K and Figure A.17 for IoLiTec-CNT.

Changes in the surface oxygen amount of CNT-K and IoLiTec-CNT are determined already after acidic treatment in the purification step, which can be caused due to the extraordinary affinity of water increasing the amount of surface oxygen or due to acidic functionalization of the surface. However, when the MWCNT function as an electrode, the surface oxygen amount is more than double as high for CNT-K and almost two times higher for IoLiTec-CNT electrodes. Here, redox-activation at high positive or negative potential causes the covalent surface functionalization (see Equations 2.12 to 2.17) [133, 140, 190, 191]. Nitrogen is also detected on the surface of electrochemically treated CNT-K in which tryptophan was used as an analyte. Moreover, surface nitrogen and surface phosphate exist on the IoLiTec-CNT matrix treated with tryptophan as analyte and phosphate buffer as mobile phase. Thus, the amount and kinds of surface functional groups increase during operation, depending on the surrounding environment and affecting the specific surface properties of both MWCNT.

Table 5.3: Aging of the MWCNT surface properties comparing differently treated CNT-K (cf. Figures A.12 and A.13) and IoLiTec-CNT (cf. Figures A.16 and A.17): Untreated powder, purified MWCNT (acidic treatment), and particles used as electrode matrix for several (> 40) working hours. The element to carbon ratios are calculated from the corresponding XPS spectra.

CNT-K	**O/C**	**N/C**
Untreated powder	0.057	–
Purified powder	0.069	–
Column 1	0.165	–
Column 2	0.138	0.0089
Column 3	0.142	0.0052

IoLiTec-CNT	**O/C**	**N/C**	**P/C**
Untreated powder	0.050	–	–
Purified powder	0.071	–	–
Column	0.139	0.0089	0.0023

pH-shift experiments also highlight the surface aging of differently treated IoLiTec-CNT electrodes. As presented in Figure A.20, the results indicate that the IEP varies for the different electrodes depending on their operation time and experimental treatment. Thus, the impact is more distinct for columns 1, 2, and 3, which had a longer lifetime than the other columns. The larger pH-shift for these three columns reflects a larger number of surface functional groups. Specific reasons for the determined IEP shift towards neutral conditions must be found in the complexity of the surface properties and their impact on hydroxyl release or oxonium adsorption.

It is yet unknown if surface oxygen improves or reduces the electrode performance [192]. Thus, oxygen functionalization can be advantageous, as the increasing amount of hydrophilic groups increases the wettability of the MWCNT [92, 193, 194]. The increased accessibility for the molecules on the surface can increase the electrode's capacity [195]. Besides, they can be triggered selectively via electric potential and advantage separation or purification processes [137, 196]. On the other hand, it will be disadvantageous, when the redox-functionalization only happens locally, primarily at the defective functional sites of the MWCNT [159]. The irregular electron flow can decrease the column capacity. The observation of Yi *et al.* [158], who claimed that electrochemically triggered redox-reactions irreversibly damage the tube morphologies, was not detected in the experiments (see size distribution in Figure A.9).

Chromatographic Aging

Chromatographic aging is expected when changes in the surface properties modify the surface charge of the MWCNT. Protonated or deprotonated surface functional groups can lead to repulsion or attraction of the tubes [189] and finally to bundling or unbundling of the agglomerates [147]. Moreover, the monolithic net of MWCNT can be affected by fluid dynamics, in which convective forces can compress or rearrange the agile structure. The direct intervention in the matrix structure positively affects the column performance when the packing's homogeneity increases, but more often, it impacts the electrode performance negatively, as an inhomogeneous matrix increases the column resistance and decreases the electrode capacity.

Several tracer experiments are performed during a CNT-K column's operation time (lifetime) to investigate the expected chromatographic aging and visualize the changes in the matrix structure. Exemplary chromatograms are presented for two CNT-K columns A and B in Figure 5.11. At the beginning of the column's life, both columns showed a comparably homogeneously packed bed and are electrochemically valid (for column A see Figure 5.9, and for column B see Figure A.36). After around 80 operating hours, the tailing of the tracer peak of column A increases, as V_R does ($A_{s,initial} = 2.9$ to $A_{s,end} = 3.4$, see Figure 5.11a). Thus, the

packing losses its homogeneous structure and the axial dispersion increases, in addition, a loss of particle-particle contacts is expected. This behavior will reduce the electron transfer of the matrix and lead to a higher column resistance (cf. Figure 5.12). Another example for column aging is imprinted in Figure 5.11b. The peak at the early life of column B is almost Gaussian ($A_{s,initial} = 1.5$) and consequences a longer column lifetime due to a more homogeneous matrix arrangement. After more than 300 operating hours, the retention volume decreases, and a shoulder is observed in the tracer peak. Fluid dynamical compression of the MWCNT matrix can cause the shift of the peak maximum, the peak shoulder can result when channels become present inside the matrix or if dead zones are pronounced. Even if the asymmetric value of column B is 2.0 after aging, which is better than the start value of column A, the peak shape describes a broken packing that cannot be used for chromatographical processing anymore.

Figure A.32 in the supplementary information illustrates the chromatograms for two exemplary IoLiTec-CNT packed bed columns. Similarly to the CNT-K, the packings are homogeneous at the beginning of their life, showing an ideal peak shape (column A: $A_{s,initial} = 0.9$, column B: $A_{s,initial} = 0.8$). After several operating hours ($> 120\,\mathrm{h}$), the matrix homogeneties decreases (column A: $A_{s,end} = 1.3$, column B: $A_{s,end} = 7.8$) and both columns break-up.

Independently of the MWCNT species, tracer analysis visualize that the chromatographic packed bed's quality suffers over time. To precise the changes of the column porosity and the axial dispersion, an exemplary IoLiTec-CNT column A is investigated via simulation.

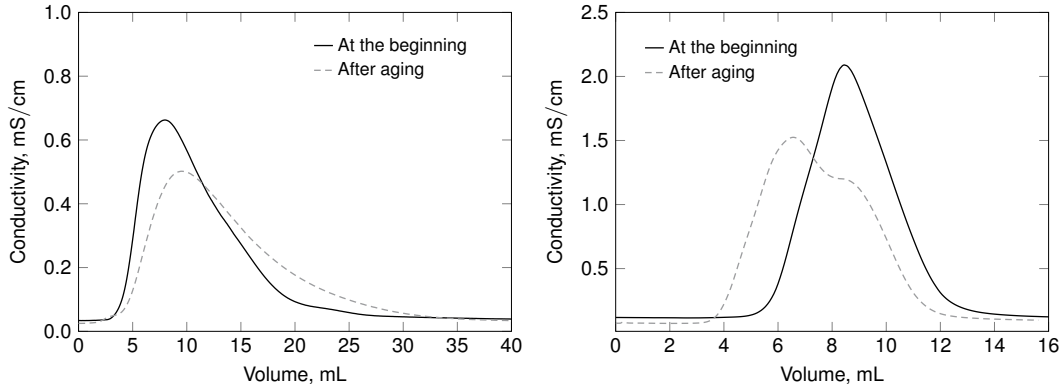

(a) Column A. **(b)** Column B.

Figure 5.11: Structural aging of a CNT-K electrode. The tracer experiments are performed at the beginning of the column life and after several hundred working hours. Column A: CNT-K matrix, 80 working hours DI-water, 1 mL/min, 50 µL, 1 M NaCl. Adapted from [18] (cf. Figure 5.12 and Figure A.35). Column B: CNT-K matrix, > 300 working hours, DI-water, 1.5 mL/min, 50 µL, 1 M NaCl. Cf. Figure A.36 and Table A.4.

Simulative Visualization of Chromatographic Aging for an IoLiTec-CNT column

Simulation with ChromX is used to precise the information about ϵ_{tot} and D_{ax}, which are important parameters to describe the packing's structure over time (see also Section 5.3.1). There are two methods used to determine an adequate parameter set for simulation: (1) both parameters, D_{ax} and $\epsilon_{tot,sim}$ were estimated from the implemented chromatograms; and (2) $\epsilon_{tot,calc}$ was calculated from the tracer experiments (see Equation 2.6), and only D_{ax} was estimated. The simulation is performed for 25 tracer runs, which were distributed over the 120 operating hours.

The simulation results reflect the measured tracer peak profiles at the beginning of the column's life, depicted in Figure A.33a. Over time, the homogeneity of the packed bed suffers, and tracer peak shape deviates from a Gaussian peak to such an extent that it could not be simulated adequately any longer than run 20 (see Figure A.33b).
Figure A.34 visualizes the changes of D_{ax} and ϵ_{tot} over time and indicates the column's structural break-up after run 15. Comparing the results of the different simulation methods in Table 5.4 no distinct differences are determined, verifying the simulation results.

Table 5.4: Estimated parameters to describe the CNT-K column's aging.

Parameter	**Method 1,** $\epsilon_{tot} \neq const.$	**Method 2,** $\epsilon_{tot} = const.$
$\mathbf{D_{ax}}$**,** mm^2/s	0.50	0.51
$\epsilon_{\mathbf{tot}}$**,** –	0.67	
$\epsilon_{\mathbf{tot,calc}}$**,** –		0.63

Hence, additionally performed simulation turns out very useful to describe the aging progress and indicate credible information on the structural aging. In future research, it might be a suitable tool to predict the MWCNT packing's efficiency and the structural aging based on the initial homogeneity and the fluid dynamical impact.

Finally, the chromatographic analysis showed that each MWCNT column ages over time when the packing loses its homogeneity or when it is compressed. However, investigating the different operation times of the columns, the structural aging process seems to depend strongly on the initial structure of the MWCNT electrode. Experience showed that the more ideal the packing quality is at the beginning the longer the column life is.

Electrochemical Aging

The material analysis and the chromatographic study visualized that the electrode's life cycle changes the surface properties and the matrix structure. Hence, it is assumed that the column's current response changes similarly. The degree of electrochemical aging is studied over time, targeting to gain information on how the changes influence the interfacial effects.

Based on the gained knowledge, there are two types of electrochemical aging possible:

1. *Structural aging due to a restructuring of the matrix*:
   A decrease in column performance can be caused when a loss of particle-particle contacts decreases the radial potential distribution. The decreasing amount of binding sites disadvantage the column capacity. Structural aging can be determined chromatographically. It is induced by fluid flow or by altering the surface charge.

2. *Aging of the surface properties*:
   Faradaic current can cause covalent reactions and change the surface properties irreversibly depending on the surrounding environment. Repulsion or attraction of the charged surface functional groups can cause a restructuring of the MWCNT matrix [147, 189] and induce structural aging. The increasing number of surface functional groups can promote or minor the electron transport along the tubes, and therewith the column capacity.

Analysis of Electrochemical Aging using Chronoamperometry

A first example for chronoamperometric aging is depicted for the representative CNT-K column A in Figure 5.12 (cf. chromatograms in Figure 5.11a). The chronoamperograms detected are ideal at the beginning of the column's life. With increasing dispersion effects, the current response decreases over time (80 operating hours). This structural aging causes an increase of the column resistance with decreasing mean current. Simultaneously, the EDL rearrangement time decreases, and the area integral results in a smaller electric charge (cf. Figure A.35). Thus, the detected chronoamperograms indicate a decrease in the column's capacitive and faradaic current response. An overview of the chronoamperometric aging by numbers is given in Table A.3, showing that the mean current of column A is only 55 % at +800 mV and 44 % at −800 mV after aging. The electric charge is only 66 %, respectively 54 %, and the gradient is three times higher at a positive potential.

The decrease of the point of zero current and the OCP of column A ($OCP_{initial} = +402\,mV$; $OCP_{end} = +256\,mV$) further indicates a larger number of negatively charged surface functional groups and highlights the change of the material properties. The functional groups seem to increase the column resistance due to passivation [140, 158].

In contrast, an increasing column capacity, as Otero *et al.* [189] reported when the surface properties are modified, is determined for the CNT-K column B (300 working hours, cf. chromatograms in Figure 5.11b). The results of the chronoamperometry experiments are presented in Figure A.36, an overview of the characteristic numbers is given in Table A.4. The current response shows an increase of I_{mean} and the EDL rearrangement time over the life of column B. The electric charge increases additionally and is more than doubled after aging when more binding sites are available due to surface functionalization [133, 155, 165, 195].

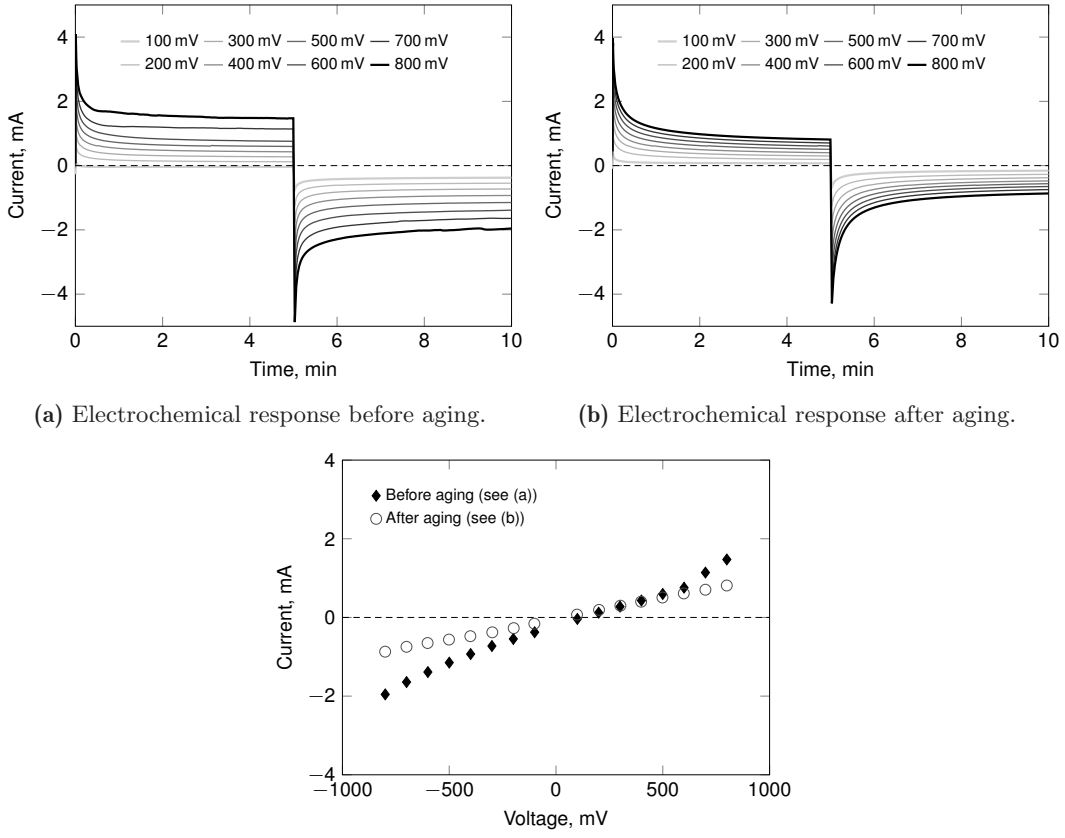

(a) Electrochemical response before aging.

(b) Electrochemical response after aging.

(c) Current/potential diagram.

Figure 5.12: Chronoamperometry to visualize the aging behavior of the CNT-K column A. (a) Electrode response at the beginning of the column life, (b) electrode response after aging, (c) current/potential diagram. CNT-K matrix, 1.0 mL/min, DI-water. Information about the electric charge is illustrated in Figure A.35, the corresponding tracer profiles in Figure 5.11a. Adapted from Trunzer *et al.* [18].

The aging of this column favors the electrode capacity with increasing capacitive and faradaic current. Nevertheless, the column's life ends with structural damage of column B being unable to be used for further operation.

Notwithstanding the opposite aging effects of column A and B, a combination of both is determined for a third CNT-K column C (120 working hours), making the description of the reproducible aging a challenge. The results of column C are depicted for the sake of completeness in Figure A.38 and summarized in Table A.5.

Comparing the aging behavior of all three CNT-K columns schematically in Table 5.5, significant differences in the long-time performance are determined for each specific column depending on the matrix structure and the agglomerate's properties. An initial prediction of the column performance over time is therewith impossible.

Table 5.5: Chronoamperometrical aging behavior of three CNT-K columns. DI-water, 1.0 mL/min. Resistance R, capacitive current I_{cap}, faradaic current I_{farad}.

Parameter	**Figure**	$\mathbf{I}_{mean}$	**R**	**Gradient**	**El. charge**	$\mathbf{I}_{cap}$	$\mathbf{I}_{farad}$
Column A	Figure 5.12	$\downarrow$	$\uparrow$	$\downarrow$	$\downarrow$	$\downarrow$	$\downarrow$
Column B	Figure A.36	$\uparrow$	$\downarrow$	$\uparrow$	$\uparrow$	$\uparrow$	$\uparrow$
Column C	Figure A.39	$\uparrow_+, \downarrow_-$	$\downarrow_+, \uparrow_-$	$\uparrow_+, \downarrow_-$	$\uparrow_+, \downarrow_-$	$\uparrow_+, \downarrow_-$	$\uparrow_+, \downarrow_-$

The material's dependency of the aging behavior is also investigated for two IoLiTec-CNT electrodes: column A (cf. Figure A.39 and Table A.6) and column B (cf. Figure A.40 and Table A.7). The electrochemical aging correlates to CNT-K column B and reaching higher capacitive and faradaic currents at the end. Consequently, an increase in the column capacity is observed. The fact that both IoLiTec-CNT columns show similar aging may be caused by the more pronounced current response. However, the observation that only one type of aging occurs for the IoLiTec-CNT cannot yet be established as no more IoLiTec-CNT columns has been studied.

Finally, the chronoamperometrical study shows an impact of the increasing surface functionalization on the capacitive and faradaic parts. An increase or decrease of the column capacity is possible, which depends strongly on the MWCNT matrix structure and the kind and degree of the aging effects. As aging is time-dependent, it is a challenge to identify and control the column quality and its specific condition at a specific operation time. A good understanding of the interplay of structural and electrochemical aging is therewith necessary to describe the long-term column performance.

Investigating the Electrochemical Aging using Cyclic Voltammetry

The CV profile of an exemplary CNT-K column at a specific operation time is illustrated in Figure 5.13. A distinct change of the current profile occurs in the current profile at high negative potentials, decreasing between the first and the last cycle. This observation was also made by Ye *et al.* [140], who described it as passivation of the electrode surface due to redox-reactions. However, it is assumed that the CV will equalize once over time when the reactive surface sites are completely functionalized. As this irreversible modification primarily occurs below −500 mV for the CNT-K electrodes, most experiments were performed until this potential limit to prevent electrolysis. Contrary to the negative potential region, reversible capacitive forces are detected at positive potentials where no aging is visible as the difference between OCP and applied potential is too small to activate redox-reactions.

Analyzing the aging behavior CNT-K column B via CV capacitive and faradaic aging is determined, as imprinted in Figure A.37. The column's total electric charge increases over time as the current particularly increases in the positive potential region, where a slight redox-peak is visible after aging. This reversible peak current can be caused by irreversible surface modification creating more binding sites and promoting the column capacity. The observation of a current decrease in the negative potential region of the CV after aging contradicts the results of chronoamperometry which depicted a smaller column resistance.
On the contrary, the results of the chronoamperometry and the cyclic voltammetry experiments of CNT-K column C (see Figure A.38b and Figure A.38c) behave almost equal and correlates for both methods. The column resistance increases at a negative potential, where irreversible redox-reaction are present, while the induced surface functionalization leads to reversible redox-reactions at a positive potential.

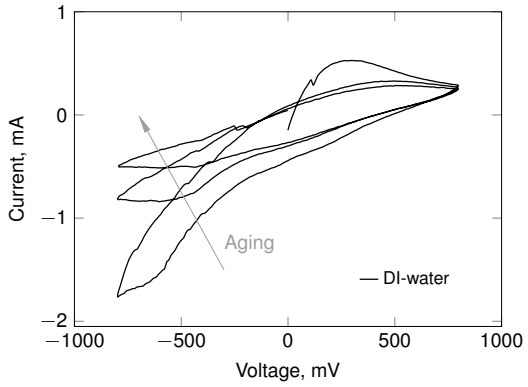

Figure 5.13: Cyclic voltammetry to visualize irreversible aging of a CNT-K column. CNT-K matrix, DI-water, 1.0 mL/min, 1 mV/s. Adapted from Trunzer *et al.* [18]).

The CV curves to study the aging of two IoLiTec-CNT electrodes (A and B) are illustrated in Figure A.41. The current profile increases at positive and negative potential and advantages of the column capacity. Moreover, a reversible redox-peak, visible at low positive potential, promotes the column capacity after aging. Both results correspond to the determination in the chronoamperometry experiments (see Figure A.39 and Figure A.40).

Comparing the two electrochemical analysis methods, the time-independent information of chronoamperometry and the time-dependent information of cyclic voltammetry can differ. While the CV measurements succeeded in describing redox-activity at a specific potential, chronoamperometry is necessary to describe the total current response at equilibrium. Thus, sometimes not only one method is sufficient to describe the effects at the solid-liquid interface adequately, and both methods are recommended to gain an overall view of the aging behavior.

RQ 3 is fulfilled as the presented chromatographic and electrochemical analysis protocol is suitable for describing the MWCNT column performance over time. It is determined that material characterization is necessary to explain the changes of the MWCNT surface properties at the beginning and end of a column's life. Tracer analysis succeeds in visualizing changes in the matrix structure and dispersive effects. Electrochemical aging is induced when the MWCNT surface is chemically modified. The aging process can advantage the electrode performance when the redox-active groups are able to promote the column capacity. However, it disadvantage when structural aging reduces the electrode performance and leads to the break-up of the matrix. As electrochemical and structural aging are creeping processes, quantitative processing is impossible.

An Outlook on Regeneration

The knowledge about the electrode's aging is in its infancy and must extended when a PCC long-term usage is desired. To prevent electrochemical aging, for instance, Su *et al.* [137, 196] recommend an explicitly surface modification due to oxidation or polymerization to diminish undesired side reactions and simultaneously trigger selective, redox-activation of the binding sites at a specific potential. Structural aging of the fragile MWCNT matrix can probably be prevented by installing an electrode with a higher mass or hierarchical structure.

While preconditioning the MWCNT to overcome electrochemical aging was not the aim of this thesis, the stabilization of the matrix structure was focused. Therefore, a regeneration protocol was developed, taking advantage of the electrochemically induced surface charge modification. Repeatedly enforcing attraction or repulsion between the charged tubes by applying maximum potential in charge-discharge experiments (see also Section 5.4) induces

a structural modification of the MWCNT net. The matrix structure homogeneity can be improved by rearranging the macroporous network and delay the column break-up. The chromatogram of a destroyed and regenerated column can be found in Figure A.42. The initial tracer peak reflects high dispersion, which is minored after the charge discharging cycle and the column fulfills the electrochemical requirements again.

Key findings of Section 5.3 (cf. RQ 3)

⇒ Ideal MWCNT matrix have comparable properties to IEX columns.

⇒ Simulation can be used to describe the matrix characteristics.

⇒ The packing of reproducible MWCNT columns is challenging.

⇒ The packing structure and the material properties affect the current response.

⇒ MWCNT electrodes are naturally positively charged.

⇒ MWCNT electrodes function as pseudo-capacitors.

⇒ The column's electric charge depends on the potential applied, the EDL rearrangement time, and the specific capacitive and faradaic current.

⇒ The potential-dependent interfacial effects are reversible and irreversible.

⇒ Aging affects the column performance, which differs at each operating time.

⇒ A structural loss of the matrix diminishes the column capacity.

⇒ Surface functionalization promotes capacitive and faradaic current.

⇒ The knowledge about aging is essential for process design and operation.

5.4 Potential Impact on the Column Response

After successfully characterizing the MWCNT electrode, this Section focuses RQ 4 and aims to determine how an applied potential, the fluid flow, and the surrounding environment affects the chromatographic column response.

The ability to adsorb a target molecule via potential is the working principle of CDI and PCC. However, they differ, as CDI cells continuously attract or repell ions from the mobile phase medium, e.g., a saline solution, while in chromatography, the target species are loaded on the column and eluted smoothly at different conditions. To characterize PCC and CDI relationship, charge-discharge experiments with DI water and a salt solution as mobile phases

are performed first. The focus is on determining changes in conductivity, UV-Vis, and pH-value that occur when the potential applied changes the interfacial properties.

Moreover, the potential-dependent adsorption behavior of maleic acid as representative biomolecule is investigated in potential-step and potential-gradient experiments. Based on the observation of Chu *et al.* [120] as well as Strohl and Dunlap [95] who worked with an EMLC column, it is expected that the flow rate affects the column capacity inversely. Moreover, the potential value and the scan rate will impact the electrosorptive process [118, 191].

The experiments are performed exclusively with CNT-K packed bed electrodes and have been presented and discussed in Trunzer *et al.* [19] first.

Charge-discharge Experiments

By steadily altering the potential, the ability of purification and concentration of a salt solution is investigated for the PCC flow-through column. These charge-discharge experiments are performed with 10 mM NaCl as representative for a saline mobile phase. The influence of the potential on the electrodes' capacity is studied by recording the electrolyte ion concentration, which is varied due to electrosorption [89, 91]. To determine the natural potential effect on conductivity, DI-water is used as a mobile phase. Related to Luo *et al.* [37] and Tang *et al.* [197], it is expected that the pH-value is also affected by electric potential. For instance, the pH-value can increase or decrease due to attraction or repulsion of oxonium or hydroxyl ions in the mobile phase or when electrolysis shifts the balance. The impact of the pH-value does not affect the salt ion's charge, so its impact is rarely studied for CDI cells. However, it is a critical parameter in chromatographic application controlling the surface and the molecule's charge and, in addition to that, the interaction behavior, respectively, the column capacity (cf. pH-dependent SBC in Section 5.2.3).

Figure 5.14 represents the potential-dependent conductivity and pH-value profile of a CNT-K electrode. Unlike the CDI, where WE and CE adsorb ions, the PCC column functions mainly with the particulate WE, which triggers the adsorption/desorption process. The CE is shielded by the CEX membrane and does not affect the adsorption process of the other species ($SSA_{Membrane} << SSA_{MWCNT}$). The conductivity signal decreases during the charging phase at positive potential when anions are adsorbed. When the potential is inverted to a negative value, the conductivity signal increases. The anions are repelled, but cations can now adsorb to the MWCNT surface. The ions' impact on the measurable conductivity depends, e.g., on their specific charge density, molar conductivity, and hydrodynamic radius. A schematic illustration about the PCC's charging/discharging principle can be found in an excursus in the supplementary information (see Figure A.53).

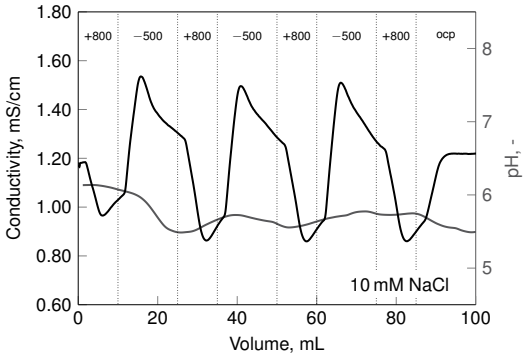

(a) 10 mM NaCl, +800 mV/−500 mV.

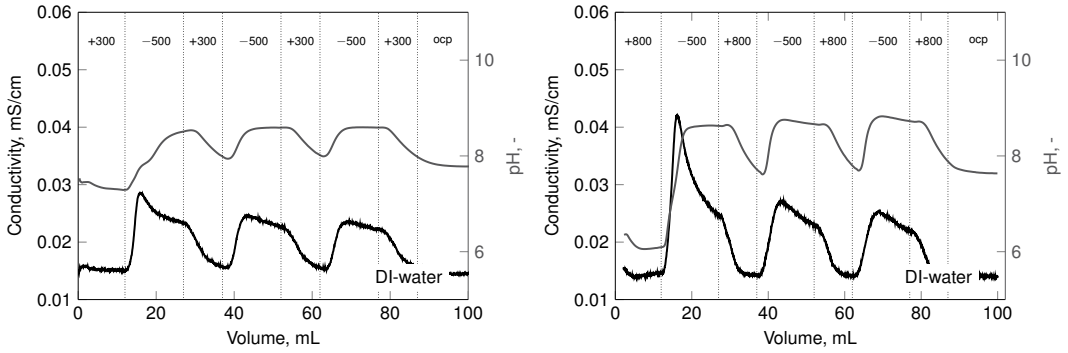

(b) DI-water, +300 mV/−500 mV.

(c) DI-water, +800 mV/−500 mV.

Figure 5.14: Charge-discharge experiments related to CDI to study the impact of potential (+800 mV or +300 mV /−500 mV) on the surrounding mobile phase medium and the interfacial effects. CNT-K matrix, (a) 10 mM NaCl or (b, c) DI-water, 1 mL/min. Adapted from Trunzer *et al.* [19].

Discussing the Potential Impact on the Conductivity Signal

When DI-water is used as a mobile phase, only oxonium and hydroxyl ions are present that can be adsorbed, inducing weak conductivity fluctuation. In contrast, the electrolyte fluctuation is much more significant, indicating that a larger number of ions are adsorbed. Consequently, the higher the electrolyte concentration is, the more ions can be attracted at a specific potential [197]. When the electrode surface is saturated, the electrode capacity is maximum, and a breakthrough peak is observed. For instance, Li *et al.* [94] determined an increasing electrode capacity with increasing potential value, but no differences when the maximum of ions was adsorbed from solution, even when the electrolyte concentration is doubled. Based on the EDL, the extension of the diffusive layer increases with a higher ion concentration. Moreover, the Stern layer gets more compact the more ions are adsorbed [87, 142, 198].

Analyzing the conductivity signal related to the capacity, the amplitudes equal over the three cycles when salt is the electrolyte. No aging effect is detected and the entirely adsorption/desorption amount is calculated to 2.6 ± 0.24 mS mL/cm for the adsorption phase

(chloride anions) and $2.4 \pm 0.20\,\mathrm{mS\,mL/cm}$ for the desorption phase (sodium cations). The DI-water results at $+800\,\mathrm{mV}$ show that the first peak area is almost twice as large as that of the subsequent peaks. This observation can be explained by disturbing the ion concentration in bulk at OCP by suddenly applying a fluid flow. Before the interface is rearranged, the excess ions are eluted. Applying an electric potential can increase this effect even more. Since the conductivity signal of DI water is small, this phenomenon is detected more clearly than other mobile phase media.

The experiment highlights that the determined conductivity profile equals typical CDI results and identifies that the flow-through MWCNT electrode operates capacitor-like, continuously separating ions from the mobile phase and concentrating it during the discharging phase. The immediate adsorption of ions from the mobile phase consequences a net load of the electrode any time before chromatographic experiments are performed. Therewith, binding sites are pre-occupied, which could affect the adsorption capacity of a target molecule species.

Discussing the Potential Impact on the pH-value

Analyzing the impact of potential on the pH-value, only small fluctuations can be determined for the electrolyte. The present salt ions replace surface water and stabilize the EDL diminishing the potential-dependent pH-shift. In contrast, the pH-shift is enormous when DI-water is used. The adsorption and release of hydroxyl or oxonium ions at the surface cause measurable fluctuations over several pH-steps (for a detailed description, see Figure A.53). Thus, oxonium ions are adsorbed at the cathode, or hydroxyl ions are generated due to redox-reactions at the negatively charged surface. The pH-value increases distinctively to basic conditions ($\Delta\mathrm{pH} = +1.5$). However, the pH-value always stabilizes back to its origin at a positive potential, reasoned by the natural positive charge of the electrode ($\mathrm{OCP} > 0$), which is already saturated with water or hydroxyl ions. As the difference between the positive applied potential and the OCP is small, the additional adsorption of hydroxyl ions is neglectable, while the interaction of the oxonium ions and the contrary charged surface is more pronounced and can be detected. Since water electrolysis occurs at the anode, building oxonium and hydroxyl ions equally, this reaction kind does not affect the pH-value. These results equal the observation of Luo *et al.* [37]. They further reported that the pH-effect becomes smaller when the potential in the charging phase decreases [37]. This effect, however, was not conspicuous for the MWCNT electrode as the profiles for $+800\,\mathrm{mV}$ respectively $+300\,\mathrm{mV}$ in the charging phase show only a slight difference. Nevertheless, the recorded fluctuation of the pH-value and conductivity indicates a higher column capacity when higher attraction forces are present [91].

A similar experiment, discussed in the following for another column (see Figure 5.19b), showed an even more significant influence on the pH-value, increasing up to $\Delta pH = +4.0$. The different results for two different CNT-K columns reflect the influence of the matrix structure once more. With an outlook on chromatographic processing, the pH-shift to basic conditions will affect the binding behavior of pH-sensitive molecules and even lead to denaturation of proteins or enzymes. Nevertheless, it is yet unknown if the pH-shift might also be advantageous for selective processing and elution.

Possibility of Regeneration

The notable side-effect of the charge-discharge series is the possibility of matrix regeneration. The surface charge is much more distinct when salt ions build the EDL enforcing attraction and repulsion between the single tubes, than when water is around. Thus, the matrix structure varies dynamically via repulsion and attraction between the tubes, and the structural degradation can be suspended, making the column packed bed homogeneously structured again (cf. Section 5.3.3 and Figure A.42). Nevertheless, the steadily rearrangement of the matrix can also be a disadvantage causing the packing break-up.

In summary, the determined knowledge about the potential impact on the environment is essential for PCC operation. With the capability to store ions from the mobile phase, the PCC capacitive character and its relationship to CDI are confirmed. The interaction between the charged surface and the surrounding environment causes an occupancy of binding sites, which might affect the column's capacity for the target molecules. Moreover, the impact of potential on the pH-value, which controls the surface and the molecule's charge, could advantage or disadvantage the column performance depending on the application's objective.

The Degree of Column's Pre-charging on Potential-step Experiments

To understand the extend of the interaction between charged ions of the mobile phase and the charged surface takes place, the potential-dependent effect is investigated chromatographically. The selected analytes were NaCl (a representative electrolyte in CDI) and Na_2HPO_4 (a standard mobile phase medium at IEX). Moreover, the experiments are performed with DI-water as a target analyte as it is the primary component in the aqueous system.

The results are depicted in Figure 5.15 illustrating the chromatograms of the potential-step and -gradient experiments. Different potentials are applied in the adsorption phase to visualize the potential-depended column capacity. The adsorption at OCP is also analyzed to investigate the natural column capacity for different species.

Studying the DI-water profiles at a positive potential, no changes in the conductivity signal are detected. When the potential is inverted, the negative potential induces elution and a conductivity peak is recorded caused by the rearrangement of the EDL and the elution of the repelled ions. This behavior was also determined in the previous charge-discharge experiments (cf. Figure 5.15a). The peak area equals the amount of adsorbed species in the adsorption phase, which increases with increasing positive potential. The higher the attraction forces are, the larger the desorption peak is as more adsorbed ions can be repelled. As DI-water was not only the analyte but simultaneously the mobile phase, the application of a negative potential did not induce any changes in the output signal. The experiment identifies a pre-load of the column with ions from the environment, occurring at any time when the column is pre-charged by applying a positive or negative potential.

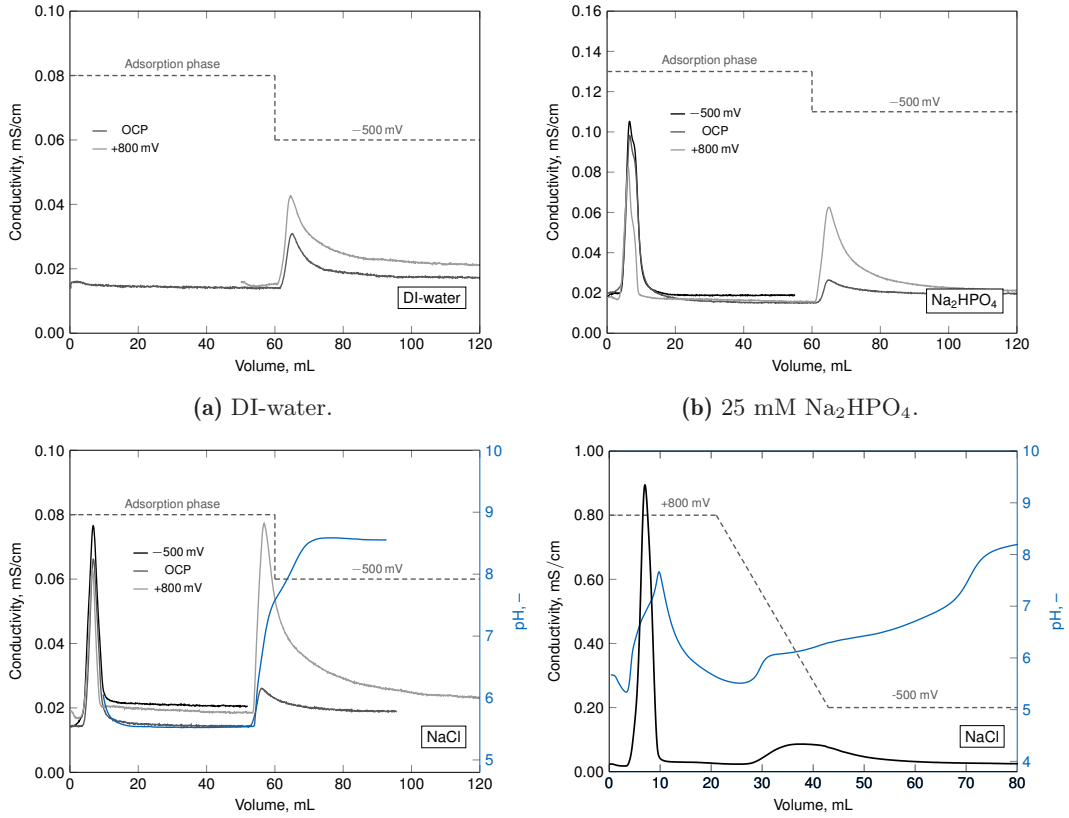

(a) DI-water.

(b) 25 mM Na_2HPO_4.

(c) Pot-step for 25 mM NaCl.

(d) Pot-grad for 500 mM NaCl.

Figure 5.15: Impulse injection experiment to study the natural (OCP) and electrically enforced adsorption of NaCl and Na_2HPO_4 as analytes. Potential-step and potential-gradient experiments with various potentials in the adsorption phase and −500 mV in the desorption phase. CNT-K matrix, DI-water, 1.5 mL/min, 50 µL, 25 mM, or 500 mM NaCl, 25 mM Na_2HPO_4, gradient −1 mV/s. Adapted from Trunzer *et al.* [19].

Examining the chromatogram of sodium phosphate (phosphate buffer, PBS), an overload of the column is detected in the adsorption phase (see Figure 5.15b). The breakthrough amount corresponds to the injected amount of phosphate ions that do not interact with the surface. The column is loaded at its maximum. When desorption is induced, the previously adsorbed phosphate ions are eluted (see curves of +800 mV and OCP). At −500 mV, non of the negatively charged species is bound, and the maximum peak area correlates to the injection amount. Thus, the total peak area in a chromatogram equal the injection amount. Therewith, the difference between the injection amount and the breakthrough amount at a positive potential should correspond to the maximum amount of ions adsorbed. However, analyzing the chromatograms, it is conspicuous that the adsorption amount does not equal the elution amount. This phenomenon is caused by the amount of already stored water molecules at the MWCNT surface at rest, repelled at a negative potential simultaneously with the analyte. The elution peak therewith depicts the sum of pre-adsorbed ions from the mobile phase and the analyte adsorbed during loading. As the pH-effect occurring in the desorption phase also falsifies the conductivity signal, quantitative balancing is impossible. By numbers, the calculated desorption peak areas of the DI-water experiment (0.22 mSmL/cm) and the PBS experiment (0.37 mSmL/cm) correspond to the elution amount of previously adsorbed ions. Therewith, the PBS peak area is 0.15 mSmL/cm excluding the pH-effect.

The Figures 5.15c and 5.15d illustrate a potential-step experiment with a lower (25 mM) and a potential-gradient experiment with a higher (500 mM) concentrated NaCl analyte. The potential-step chromatograms with the lower concentrated NaCl analyte equal the one of PBS, and confirm the overlaying amount of various repulsed species in the elution peak.

The influence of the potential on the pH-value is again highlighted for the NaCl experiments. When the potential is changed immediately, a fast pH-shift to basic conditions occurs. When the potential drops slowly, it delays the pH-shift and increases the pH-value steadily to basic conditions. Besides, it occurs independently from the analyte injection concentration.

The different pH-shifts, as well as the detected differences in the elution peak shapes are caused by the potential-dependent interfacial effects and mass transfer limitations occurring by immediate or smooth rearrangement of the interface. While the potential-step experiments induce a sharp increasing elution peak due to the immediate repulsion of many adsorbed species with a strong tailing, the gradient experiment causes a Gaussian-like elution peak with a minor degree of disorder until the EDL is rearranged. Thus, a highly concentrated product might be gained in the small peak fraction of the step-wise elution, while a gradient elution diminishes undesired mass transfer effects and might achieve higher fraction volume. Hence, optimal process control depends on the desired process objective: a higher yield or

a purer fraction. While a gradient potential control could be the better choice for selective separation when differently charged molecule species are dissolved at different potentials.

In summary, the potential-dependent adsorption study shows that no quantitative balance is possible as the additional adsorption of mobile phase ions to the target ions or the pH-shift influences the output signal. Therefore, relative balancing is further used to visualize the differences in the adsorption/desorption behavior. Moreover, a column pre-load is detected expected to affect the capacity of the electrode depending on the mobile phase composition. Therefore, it is crucial to study the specific interaction behavior at the solid-liquid interface later presented in Section 5.6.

Enhancement of the Process Operation

As it is determined that the process operation over potential-step or potential-gradient affects the process performance, the potential-dependent interaction of maleic acid, as a representative organic molecule, is investigated. Therefore, the elution behavior of maleic acid is analyzed when the gradient rates differ. In addition, the impact of the fluid flow on the column capacity is analyzed. It is expected that both the flow rate and the potential rate impact the time-dependent EDL formation. A longer contact time will advantage the adsorption amount while a faster repulsion can favor desorption [95, 97, 120, 191].

Figure 5.16a illustrates a potential-gradient experiment in which the gradient rate is kept constant, but the flow rates differ in the adsorption phase. The data show that the column capacity decreases with increasing flow rate (see magnification in Figure 5.16c). The result correlates to the studies of Strohl and Dunlap [95], and Chu *et al.* [120], who stated that a decrease in contact time and an increase of shear forces at the surface caused by a higher flow rate decrease the EDL extension and the adsorption capacity. While the higher flow rate is identified as disadvantageous in the adsorption phase, it promotes the desorption by diminishing dispersion and diffusion effects. Moreover, increasing shear forces preventing the ions from further interactions with the electrode material.

The gradual elution is analyzed for an exemplary slower and faster scan rate applying 0.5 mL/min in the adsorption phase and 1.5 mL/min in the desorption phase. As illustrated in Figure 5.16b (and Figure 5.16d), the chromatogram does not show and elution peak for the lower scan rate of −1 mV/s. The slower elution might cause diluted fraction, which cannot be recorded. When the experiment is performed with −5 mV/s, an elution peak is visible. As expected, the higher potential rate promotes the repulsive forces over a shorter time and concentrates the eluted species in smaller fractions.

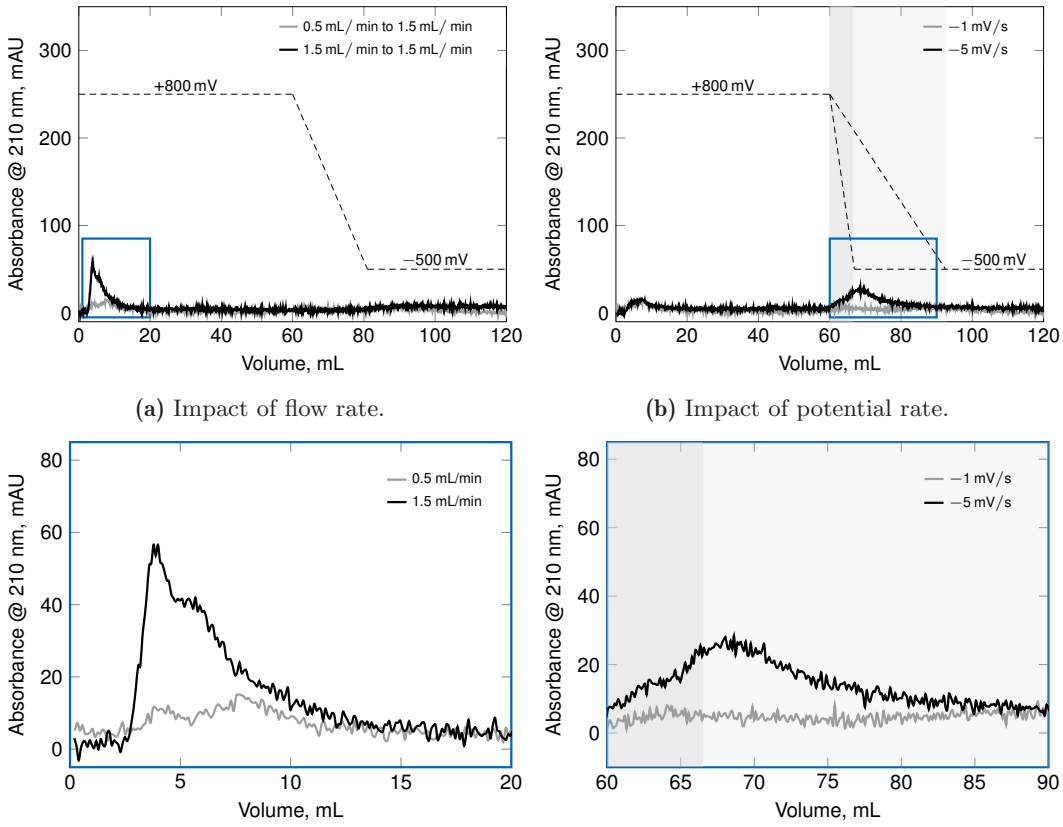

(a) Impact of flow rate.

(b) Impact of potential rate.

(c) Magnification of a).

(d) Magnification of b).

Figure 5.16: Potential-gradient experiment to study the impact of flow rate and scan-rate on the column capacity. CNT-K matrix, DI-water, 25 mM maleic acid, pH 7, a) adsorption phase: 0.5 or 1.5 mL/min, desorption phase: 1.5 mL/min, gradient −1 mV/s; b) adsorption phase: 0.5 mL/min, desorption phase 1.5 mL/min, gradient −1 or −5 mV/s. Adapted from Trunzer *et al.* [19].

In summary, higher flow rates or steeper potential-gradients favor the desorption as the contact time between molecules and surface is minimized. Purer fractions are reached when an immediate elution is induced. A longer contact time and smaller shear forces favor the molecule adsorption and increase the column capacity.

This Section answers RQ 4 by manifesting that the potential value in the adsorption phase, the fluid flow, and the desorption kind affect the column response. Thus, the optimal PCC design depends on its specific objective and is finally a trade-off multiple factors that diminish or amplify each other.

Key findings of Section 5.4 (cf. RQ 4)

⇒ The MWCNT flow-through electrode can continuously electrosorb and desorb species from the mobile phase and equals a CDI system.

⇒ Higher potential and electrolyte concentration increases the electrode capacity.

⇒ Electrode's pre-charging induces a primary EDL formed with ions from the mobile phase.

⇒ Step-elution causes a simultaneous repulsion of any adsorbed species.

⇒ Applying $-500\,\mathrm{mV}$ in the desorption phase causes a pH-shift towards basic conditions, which can advantage or disadvantage the elution of biomolecules.

⇒ A flow rate of $0.5\,\mathrm{mL/min}$ promotes the target's adsorption and increases the electrode's capacity.

⇒ Faster flow rates during desorption prevent molecule/surface interactions and shorten the operation time.

⇒ Immediate repulsion cause a small, highly pure target fraction.

⇒ A steep gradient of $-5\,\mathrm{mV/s}$ favors the target yield and reduces mass transfer limitations.

⇒ Potential-gradient elution can benefit selective desorption.

⇒ Optimal processing depends on its target and is a trade-off multiple parameters.

5.5 Versatility and Impact of the Mobile Phase

As the surrounding environment is identified as a critical influencing factor impacting the process performance, detailed knowledge about the mobile phase is necessary. While the previous Section screened the potential impact on the separation processes itself, this Section addresses RQ 5 and investigates the impact of the surrounding environment on the interface.

Determining that a lower flow rate promotes the adsorption, the flow rate's impact is examined chromatographically and electrochemically in Section 5.5.1. It is assumed that the flow rate will directly affect the EDL extension and therewith the effects at the solid-liquid interface. Knowing that ions from the mobile phase are adsorbed any time when potential is applied, it is expected that various ion species and concentrations will form the EDL differently, which is investigated in Section 5.5.2. By studying the impact of the surrounding environment on

maleic acid's adsorption in Section 5.5.3 it is analyzed if the column's pre-charging induces a competitive or cooperative behavior for the binding sites.

Here, CNT-K are considered as primary electrode material. Parts of the Sections 5.5.1 and 5.5.2 are already published in Trunzer *et al.* [19], results presented in Section 5.5.3 can be found in Trunzer *et al.* [18]. In some Subsections, IoLiTec-CNT electrodes are presented additionally for validation and comparison.

5.5.1 Dependency of the Column Response on the Fluid Flow

A chromatographic and an electrochemical perspective is performed to gain overall information about the flow rate's impact on the response. An excursus on tracer analysis is given to investigate convective and dispersive mass transfer effects. An electrochemical analysis is used to study the fluid flow impact on the solid-liquid interface and the current response.

The Impact of the Flow Rate on the Chromatographic Effect

The impact of the flow rate on the retention time and the mass transfer inside the macroporous system is investigated in tracer experiments. The typical chromatograms are illustrated in Figure A.43 for a CNT-K and in Figure A.44 for a IoLiTec-CNT packed bed.

As expected, the retention time decreases with increasing flow rate. This will cause a decrease in the target/surface contact time when interactions are possible. It is further assumed that a higher throughput diminishes diffusion and the film layer extension due to increasing shear forces at the interface. Moreover, the dominant convective forces will reduce the accessibility of binding sites, causing a decrease in the column capacity (cf. Section 5.4).

Differently to microporous systems, where a higher fluid flow decisively impacts the mass transfer (cf. HETP theory), the flow-dependent effects of the macroporous MWCNT system seem almost neglectable. As the tracer peak shapes do not differ distinctively at various flow rates, the shift between the diffusion/dispersion regime and the convective regime can only be assumed around 1.5 mL/min by evaluating several PCC columns. A convection-dominating macroporous system exists, in which the adsorption amount will strongly depend on the interfacial (film-diffusion) effects.

Electrochemical Response of the Column at Different Flow Rates

The impact of the fluid flow on the potential-dependent solid-liquid interface is investigated focusing the extension of the EDL and the part of capacitive and faradaic current.

OCP Measurements

The results for the OCP measurements are summarized in Table A.8 for both MWCNT materials. A decrease of the OCP is detected for increasing flow rates in a CNT-K electrode, caused when the convective forces are strong enough to suppress the film layer extension and reveal the natural negative surface charge of the particles [95, 120]. Hence, the positive character of the MWCNT electrode surface decreases with increasing flow rate.

Differently to the CNT-K electrodes, the effect is not detected for the IoLiTec-CNT column. This can be caused when more water molecules are stored at the IoLiTec-CNT surface due to its higher charge density. Hence, flow-dependent changes of the more pronounced EDL are possible but might not be detectable.

Chronoamperometry Analysis

Chronoamperometry experiments are performed at five different flow rates, which results are illustrated in Figure 5.17 for a CNT-K electrode (supplements in Figure A.45). The exemplary curves for a lower and a higher flow rate (0.1 mL/min and 2.5 mL/min), as well as a lower and a higher potential (±100 mV and ±800 mV) show a more distinct current profile at higher potentials combined with lower flow rates. While the higher potential value increases the attraction forces, the lower fluid flow increases the contact time. Both promote capacitive and faradaic current and increase the column capacity.

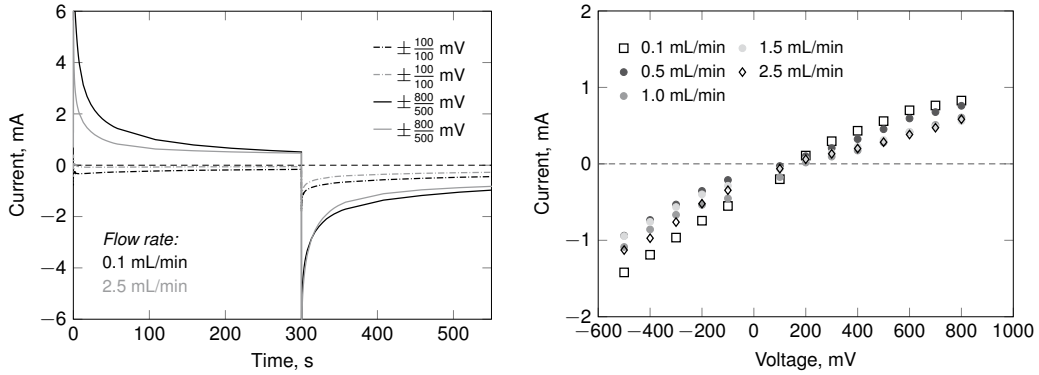

(a) Exemplary chronoamperograms. **(b)** Current/potential diagram.

Figure 5.17: Chronoamperometric study about the impact of the flow rate on the potential-dependent interface. CNT-K matrix, DI-water, various flow rates. Supplements in Figure A.45. Adapted from Trunzer *et al.* [19].

The column resistance increases with the flow rate, caused by higher throughput, higher shear forces, and the reduction of the EDL extension. Simultaneously, the EDL rearrangement time is shortened, and the electric charge decreases. The flow rate's effect emerges most clearly in the positive potential region where the mean current increases in decreasing order of the flow rate. The break-point expected in the tracer analysis can be precised to 1 mL/min when the dispersion or diffusion regime is replaced by the convective forces [91, 199–201]. Above this point, the electric charge stagnates as the column pressure of the macroporous electrode does not change significantly. In comparison, microporous CDI cells can be run to a critical value of several liters per minute as the throughput, and the system pressure increases the adsorption capacity.

Investigating the flow rate's influence on the current response of an IoLiTec-CNT column (see Figure A.46), similar results are obtained. Thus, independent of the material characteristics, increasing flow rates decrease the mean current, electric charge, and current gradient of the macroporous electrode.

The gained results correlate to the adsorption study and show that a slow flow rate promotes capacitive and faradaic current and increases the column capacity. Thus, a minimal flow rate of, e.g., 0.5 mL/min, is recommended for adsorption processes, guaranteeing a high column capacity, while a faster one can be established in the desorption phase, diminishing mass transfer effects and allowing an adequate processing time.

Cyclic Voltammetry Measurements

Cyclic voltammetry is performed to investigate the impact of the fluid flow on the continuous change of the EDL and the capacitive and faradaic current. The achieved results for a CNT-K electrode are imprinted in Figure A.47a, the one for the IoLiTec-CNT do not significantly differ and is added in Figure A.47b. Both show that higher fluid flow causes a less pronounced CV shape. Thus, the CV for 0.1 mL/min is distinctive, indicating a high capacitive current and redox-activity at a moderate positive potential. In contrast, the faradaic part diminishes at 2.5 mL/min, as the increased fluid flow hinders the ions from interacting with the surface. Moreover, the boundary current becomes smaller at a negative potential, indicating a higher column resistance at the positive and negative regions.

Since the time-dependent and -independent effects differ in intensity, the chronoamperometry and cyclic voltammetry methods together complete the findings and confirm that the flow rate affects the current response. It is shown that slow flow rates promote the adsorption capacity, while higher ones suppress the ion/surface interactions, a trade-off between a slower flow rate in the adsorption and a higher one in the desorption phase is recommended for optimized processing.

5.5.2 The Selection of the Mobile Phase Medium

The charge-discharge experiments using salt compared to DI-water pointed out that the surrounding environment affects the column capacity. Vice versa, it was determined that the applied potential impacts the pH-value of the mobile phase, which will trigger the surface and the molecule's charge. As these effects will appear on the solid-liquid interface, the EDL development is studied based on the statement of Li *et al.* [202], who ask the fundamental question of what is the connection between electrode and electrolyte.

Before starting the discussion, it is essential to know that PCC was once designed to separate biomolecules. As a close relationship to CDI was determined, the research focus is extended to study the adsorption behavior of different metal salt ions in detail. Understanding the effects on the MWCNT solid-liquid interface for small ions first can later be transferred to discuss more complex biotechnological separation systems later in process development. Based on the literature, it is expected that the electrode resistance will decrease with increasing electrolyte concentration, simultaneously increasing the electrode capacitance [190]. A higher concentrated solution promotes a faster electrosorption rate and a smaller concentration gradient. A more compact Stern layer and a distinct diffusive layer is the consequence [93, 198]. It is also revealed that ion species with a higher charge density, e.g., divalent cations, adsorb more preferably at a counter-charged surface than monovalent cations. On the contrary, monovalent anions own a higher electronegativity and replace divalent anions at the binding sites [54, 187, 203]. Besides, valance state, molar conductivity, hydration ratio, as well as the steric hindrance of the ions impact the adsorption behavior, wherefore smaller ions are preferably adsorbed compared to larger molecules [92, 198].

The electrochemical characterization is performed for CNT-K electrodes analyzing the current response of different media: DI-water, phosphate buffer (as a standard buffer in chromatography), and NaCl, KCl, as well as $CaCl_2$ (typical electrolytes in CDI). Moreover, different electrolyte concentrations are examined. The presented analysis builds on investigating the impact of the PBS first, published in Trunzer *et al.* [18]. The excursus about the impact of and on the pH-value is published in Trunzer *et al.* [18, 19]. The examination of the different electrolytes' impact on the current response is presented in Trunzer *et al.* [19].

The Impact of Phosphate Buffer on the Current Response

To investigate how different media impact the current response of a CNT-K column, chronoamperometry experiments are performed first. DI-water is used as the primary mobile phase, 10 mM PBS is selected as a standard chromatographic mobile phase media.

The current/potential diagram in Figure 5.18 summarizes the key results of the chronoamperometric measurements imprinted in Figure A.49. The data show more distinctive current profiles and higher faradaic currents for the ion-rich buffer than for DI-water. The longer EDL rearrangement time promotes capacitive current and indicates a significant extension of the diffusion layer. Moreover, a faster electrosorption rate is assumed when more ion/surface contacts are possible [93, 198]. A simultaneously performed aging study visualizes that the resistance increases independently from the mobile phase medium when structural aging dominates.

CV experiments visualize the systems' capacitive character (see Figure 5.19), which is more significant when a buffer is used. As expected, the higher amount of ions in the solution favors the column's electric charge and capacity. When conductivity and pH-value are recorded simultaneously, the pH-fluctuations are much more significant for DI-water (ΔpH = $\pm$4) than for PBS (ΔpH = $\pm$0.2). Therewith, the previously observed stabilization effect at the potential-controlled interface when buffer respectively electrolyte ions are present is confirmed.

How ions with different properties affect the EDL structure is analyzed in the following. Since both the conductivity and the pH-value are influenced by the potential, and vice versa, the current response is examined for different pH-adjusted water first, followed by an analysis of different salt solutions used as mobile phase.

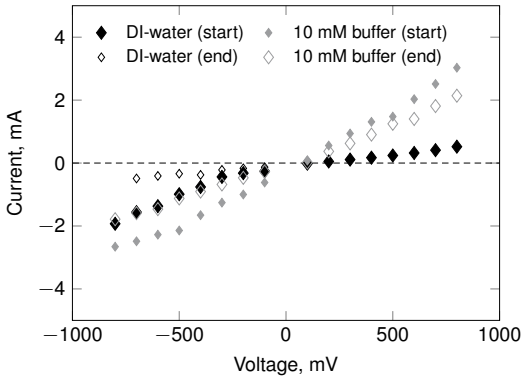

Figure 5.18: Current/potential diagram to illustrate the differences in the current response of a CNT-K column using DI-water (a, b) and 10 mM phosphate buffer (c, d). Current response at the beginning (a, c) and the end (b, d) of the column life. See chromatograms in Figure A.48b and chronoamperograms in Figure A.49. CNT-K matrix, 1 mL/min, pH 7. Adapted from Trunzer *et al.* [18].

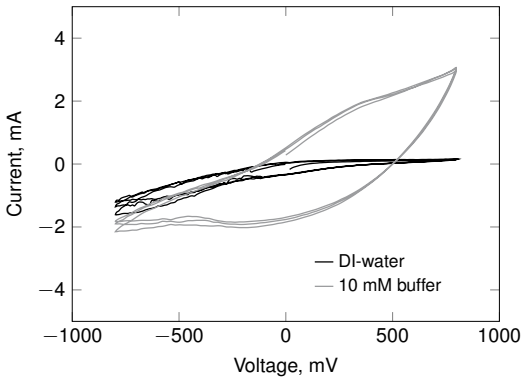

(a) Cyclic voltammogram.

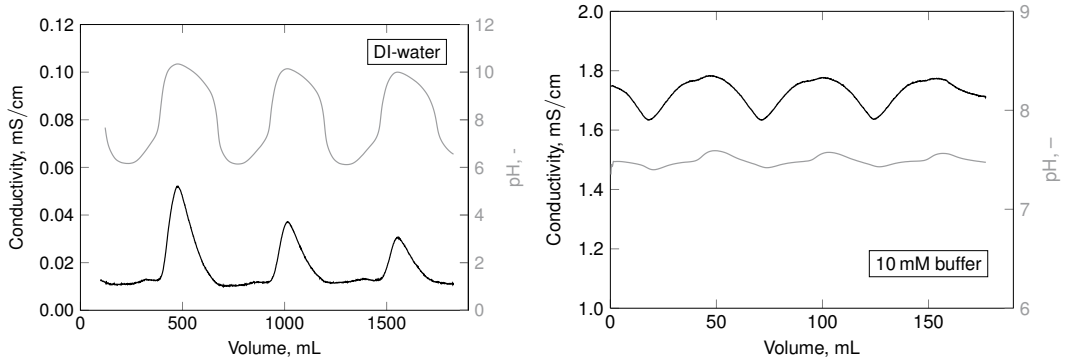

(b) DI-water.

(c) 10 mM phosphate buffer.

Figure 5.19: Cyclic voltammetry to compare the potential effect on conductivity and pH-value when DI-water and 10 mM phosphate buffer is used as mobile phase media. CNT-K matrix, DI-water, 1 mL/min, 0.1 mV/s, 10 mM phosphate buffer, 1 mL/min, 1.0 mV/s, 3 cycles. Adapted from Trunzer *et al.* [18].

The Impact of the pH-value on the Current Response

To identify if the mobile phase's pH-value dominates the current response or if the mobile phase properties are affected stronger by the applied potential, pH-pre-adjusted DI-water (pH $\approx$ 6; 7; 8; 9) is used. This pH-region is of particular interest as a negative potential applied to the MWCNT matrix continually shifts the pH-value towards basic conditions.

The OCP measurements results are listed in Table A.9, but do not show a clear pH-dependent correlation. There could be a slight decrease to a lower positive net potential with increasing pH-value that might be caused due to attracting hydroxyl ions from the solution or releasing oxonium ions from the surface to balance the interface. However, the experimental data available is small and does not allow proper conclusions yet.

Exemplary chronoamperograms are illustrated in Figure 5.20 (cf. Figure A.50), and CV are illustrated in Figure A.51. Both measurements record only a slight increase of the capacitive and faradaic part with increasing pH-value. This is not necessarily related to the excess of interfacial hydroxyl triggering the EDL formation but to sodium cations introduced into the system by pH-titration.

In contrast to the small impact of the pH-value on the current response, it is known that the potential influence on the pH-value is enormous (see Figure A.52). This phenomenon was also observed by Ban *et al.* [204] and Mirmohseni *et al.* [205], who stated that the pH-shift intensity depends on the electrode cell and material. For the MWCNT electrodes, it is of particular interest that the mobile phase's final pH-value always results in an average between 8.5 and 9.0, independently from the starting conditions (here, OCP and chronoamperometry measurements were performed without a break before taking the CV). This can be caused when the small but defective and functionalized electrode's SSA favors faradaic current at a negative potential, inducing water splitting and the increase of the pH-value.

Finally, this electrochemical study shows that an increasing concentration of pH-regulating ions does not cause measurable changes in the EDL development. On the contrary, the potential significantly affects the mobile phase's pH-value. To diminish the undesired pH-shift which can affect the molecule's protonation state, enzyme activity and protein structure in bio-broth, electrolytes are screened as an alternative to organic buffers.

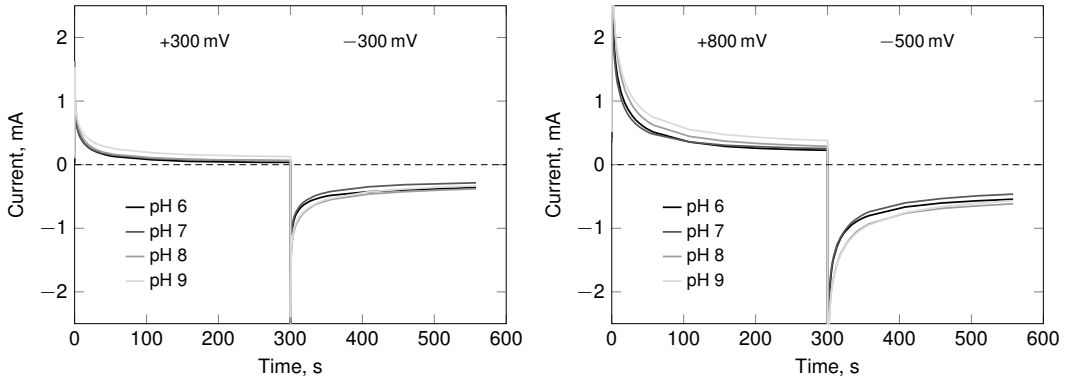

(a) Chronoamperogram at ±100 mV. **(b)** Chronoamperogram at +800/ − 500mV.

Figure 5.20: Chronoamperometry experiments to study the impact of the pH-value on the potential-dependent interface. CNT-K matrix, 1 mL/min. Supplementary information in Figure A.50. Adapted from Trunzer *et al.* [19].

The Impact of the Electrolyte Concentration and Composition on the Current Response

The influences of the ionic concentration and the salt composition of the mobile phase are investigated, comparing the current response of NaCl, KCl, and $CaCl_2$. Based on the determinations of Chung *et al.* [92] and Tanigaki *et al.* [198], differences in the current response are expected, as the salt cations own a different valency, hydration radius, and charge density distribution. Besides the ion's character, the electrolyte concentration is a key trigger in capacitive processing based on the physical requirement that the more ions are available of one species, the more ions can be bound until saturation (cf. adsorption isotherms).

Both the impact of the electrolyte composition and concentration form the basis for different EDL theories [29, 31, 202, 206], summarizing that the electrode capacity will be higher when the Stern layer is compact and the diffusive layer more significant. This can be achieved for cations with small radii or hydration shells and anions with high electronegativity. Simultaneously, a higher bulk concentration favors film diffusion and a distinct potential distribution inside the column. Finally, higher attraction forces extend the EDL and the adsorption rate.

Performing OCP measurements for a CNT-K electrode using differently concentrated salt solutions, no clear tendency is found for the lower concentrated salts, in which OCP fluctuates between +107 and +227 mV (see Table A.10). The OPC is a little lower than the one measured in DI-water and indicates that the salt ions affect the EDL. Nevertheless, the OCP of higher concentrated salts decreases significantly in the order NaCl < KCl < $CaCl_2$, achieving negative values by replacing the water shell. This indicates that any surrounding environment forms a specific EDL and defines the primary target/MWCNT interactions.

Results from a $+800/-500$mV chronoamperometry experiments comparing the current response of a 1 mM and a 10 mM salt electrolyte are illustrated in Figure 5.21 (supplements in Figure A.54). The current profile of DI-water is included to visualize the differences between the primary medium and the aqueous electrolytes. A direct comparison to the previously performed PBS experiments cannot be made as two different columns are used.

Independent of the salt concentrations, both current profiles increase in the order NaCl < KCl < $CaCl_2$. However, the mean current of the 10 mM salts do not increase by a multiple factor that was expected from the electrolyte concentrations (cf. Figures 5.21b and 5.21d). This indicates that the electrolyte concentration only slightly affects the faradaic character when the column is operated time-independently. The main difference is determined in the capacitive part, increasing distinctively with the electrolyte concentration and highlight the expected higher column capacity with decreasing concentration gradient of the film layer.

CV experiments are used to identify the dynamic solid-liquid interface formation (see Figure A.55), confirming the chronoamperometry results as the column's total electric charge increases with increasing electrolyte concentration. The reversible increase and decrease of the current indicate that capacitive current dominates, however, a slight increase of faradaic current is observed at moderate potential when the higher number of surface ions favor electron transfer.

The increasing order NaCl < KCl < $CaCl_2$ of the EDL rearrangement time corresponds to the character and number of cations and anions. Comparing NaCl and KCl, the anions are equal. However, the sodium cation is adsorbed faster than the potassium due to its smaller ionic radius and higher charge density. In contrast, the potassium ions' adsorption is slower, and the larger radius minors the concentration directly at the interface but increases the diffusive layer extension.

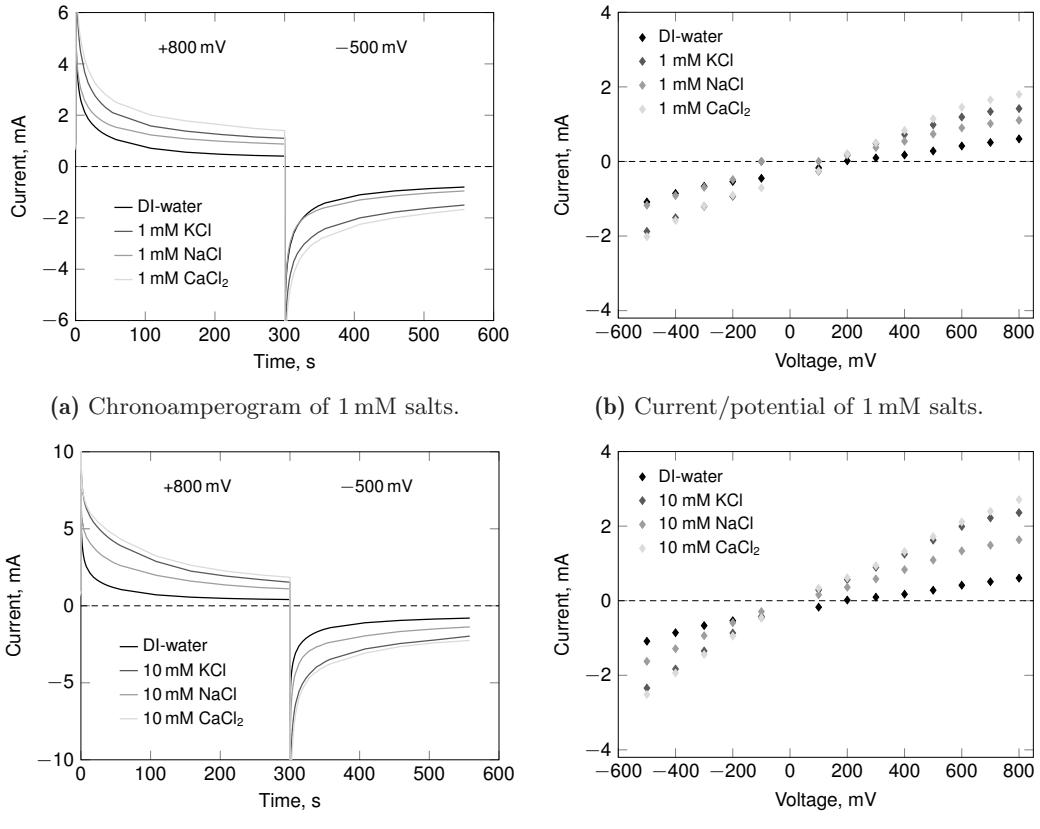

(a) Chronoamperogram of 1 mM salts.

(b) Current/potential of 1 mM salts.

(c) Chronoamperogram of 10 mM salts.

(d) Current/potential of 10 mM salts.

Figure 5.21: Chronoamperometry experiments visualizing the impact of the salt composition and concentration on the current response of the column. CNT-K matrix, DI-water, 1 mM, 10 mM NaCl, KCl, $CaCl_2$, 1 mL/min. See also Figure A.54. Adapted from Trunzer *et al.* [19].

Comparing the divalent salt with the monovalent salts, $CaCl_2$ has the most distinct current profile. However, the calcium ion has the smallest radius and the highest charge density distribution (highest ionic mobility and binding affinity), the two chloride ions (lowest charge density and largest ionic radius) decrease the EDL rearrangement time. The effect of the ion's specific properties on the current response is even more significant, comparing $CaCl_2$ and KCl. Thus, the smaller calcium ion compensates almost for the poor diffusion properties of the potassium and chloride. Nevertheless, it is expected that chloride ions' attraction to the counter-charged surface can increase the column's electric charge, being able to compact the Stern layer by striping their hydration shell due to the high electronegativity.

The experiments presented only investigated single salt solutions, but literature makes the electrosorption behavior of complex salt mixtures an important topic to understand the interfacial effects. Thus, cooperative or competitive behaviors of different species at a charged surface were already studied experimentally [54, 187, 203] or theoretically [206, 207] in numerous publications. It was determined that ions with a higher binding affinity block binding sites and desorb worse, while ions with a lower binding affinity can be repulsed electrostatically [207, 208]. A time-dependent replacement can also occur, shifting the adsorption amount of the target species. This specific knowledge about the different adsorption rates and affinities of mixtures is essential to design an optimal multi-variant separation process. Therefore, it is important to further analyze the adsorption behavior of small ions and large molecules, and their contribution to the dynamical EDL development.

5.5.3 Competition for Binding Sites

Finally, the chromatographic binding behavior of maleic acid is investigated based on the expectation of cooperative or competitive behavior with ions adsorbed from the surrounding mobile phase. As determined by Yang *et al.* [172] and other researchers, it is expected that the presence of metal ions reduces the adsorption capacity of MWCNT for organic molecules when binding sites are pre-occupied. Nevertheless, the blockage of bindings sites at the surface can induce different binding sites, therefore promoting specific molecules' interaction with the EDL. Besides, no impact on the column's capacity would be achieved when the pre-adsorbed ions are replaced by the target ones [209–211]. Finally, the selectivity and capacity of an electrode is a compromise of the electrode surface properties, the EDL formation, and the operation time [209, 212].

As the previous analysis showed that metal salts and buffer ions could interact with the charged electrode surface, two scenarios are investigated in the following:

1. the impact on adsorption capacity of a target molecule carried by a buffer
   – PBS anions are pre-adsorbed, blocking the positively charged binding sites before the negatively charged MA molecules are injected; and
2. the impact on adsorption of a target molecule when it is dissolved in a salt solution
   – salt anions compete with similarly charged MA molecules for binding sites.

Impact of the Mobile Phase on Adsorption Capacity

The impact of the mobile phase composition on the column capacity is investigated in a series of potential-step experiments, already published in Trunzer *et al.* [18].

The achieved chromatograms for a DI-water and a PBS system in Figure 5.22 (detailed balance in Figure A.63) using maleic acid as a negatively charged target species indicate maximum adsorption at +800 mV and a total repulsion at −800 mV. Comparing the results of the DI-water and the PBS systems at a positive potential, the relative adsorption amount of maleic acid is smaller in a PBS system. Thus, more maleic acid molecules are adsorbed in DI-water (around 92 %) than in PBS (around 43 %). As quantitative balancing is not possible, the relative adsorption amount is calculated as the ratio between the breakthrough peak area and the elution peak, .

The expected existence of occupied binding sites from the buffer anions is confirmed, as a competitive behavior of phosphate and maleic acid molecules is determined. Reflecting the results from the electrochemical characterization, PBS promotes the current response and suppresses the pH-effect, and achieves higher electric charges. Nevertheless, in chromatographic experiments, PBS failed.
Combining the results, it could be possible that the overall column capacity is smaller when DI-water is the mobile phase, but the adsorption capacity of the target molecules is more selective and therewith higher. Thus, the chromatographic and electrochemical aim of reaching a high column capacity could be controversial when mixtures exist. Analyzing two different viewpoints: the higher electrolyte concentration can be advantageous for wastewater purification as the higher conductivity favors electrosorption from a continuous system. In contrast, separation processes for a specific target molecule could be optimally designed when the ion content of the surrounding environment is small. The operating condition therewith must be adapted to the aim of the process design.

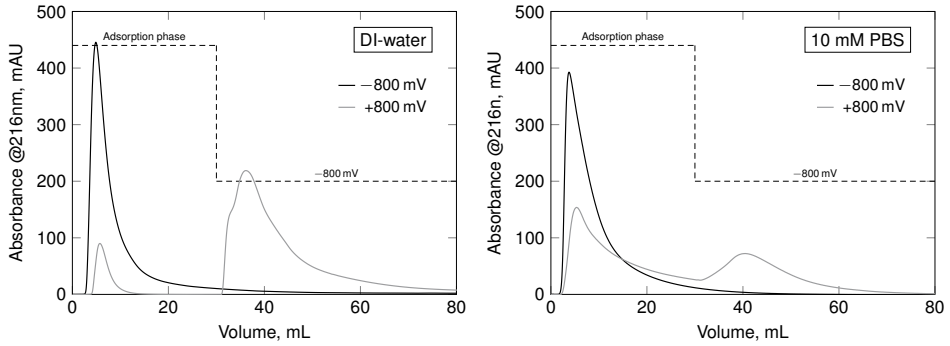

(a) Mobile phase DI-water. **(b)** Mobile phase 10 mM phosphate buffer.

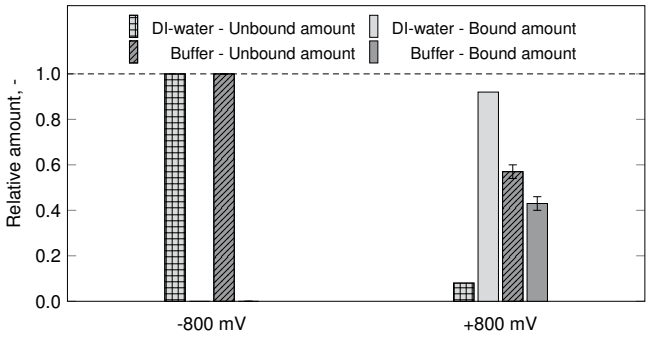

(c) Ratio of the target in the adsorption/desorption phase.

Figure 5.22: Excerpt of the potential-step experiment to determine the impact of the mobile phase composition on the column capacity. CNT-K matrix, 1 mL/min DI-water or 10 mM phosphate buffer, pH 7. Adsorption phase: +800 or −800 mV, desorption phase: −800 mV. 50 µL, 5 g/L maleic acid, 216 nm, pH 7. Cut-out of Figure A.63a, adapted from Trunzer *et al.* [18].

Sample Mixtures and the Impact of the Target's Column Capacity

In the second study, the adsorption behavior of the target molecule dissolved in a salt solution is examined. DI-water is the mobile phase, keeping the ion uptake during the pre-charging minimal, while pure MA, MA/NaCl or MA/$CaCl_2$ (1:1) mixtures are injected. The experiment is also performed on the expertise of Chen *et al.* [213], who showed that similarly charged ions/molecules compete for binding sites and reduce the target's column capacity.

Figure 5.23a visualizes the potential-step chromatograms of MA/DI-water or MA/NaCl solutions that are enlarged with a salt elution step to study the binding strength. The results indicate that MA is entirely adsorbed at the positive applied potential for both solutions. However, only a part of MA is repelled via potential. Much more molecules seem to be eluted during the salt step. This observation identifies the presence of a second, stronger binding behavior between MA and the charged surface as only the expected electrostatic one. Hence,

two interaction forms are possible: weak electrosorptive forces –broken via electric potential, and stronger ionic or hydrogen bindings –dissolved over ion-exchange.

The relative balance of both experiments is illustrated in Figure 5.23b. It is challenging to identify an explicit cooperative or competitive binding behavior yet, as the data available are small and the relative balancing causes inconsistencies between the adsorption amounts. However, a similar pattern emerges for all experiments: MA is bound in the adsorption phase, desorbed via potential, and eluted when salt is the eluent. For another depiction see Figure A.57 and Figure A.56 for the potential-gradient chromatograms.

Comparing the results achieved for MA/NaCl mixtures with potential-gradient experiments using MA/$CaCl_2$ mixtures as an analyte (see Figure A.59). The chromatograms for both mixtures are almost equal, no distinctive differences are determined in the adsorption, desorption, and salt elution steps. Thus, no influences of different salt compositions on the binding behavior at the solid-liquid interface are detected yet in this setup.

The calculated relative amounts visualizes that a small amount of the MA molecules bind already at the negative potential. This might be caused by a natural affinity of MA interacting over the delocalized group, as well as over ionic, or hydrogen bindings with the MWCNT surface, which could not be identified in the previous experiments without salt elution. Nevertheless, a falsification of the low UV-Vis signal cannot be excluded using high salt concentrations in the elution step as the data set is small.

When the desorption amount of the different experiments performed with positive potential in the adsorption phase is compared, it is noticeable that the highest amount of MA is desorbed electrochemically when a moderate potential (+300 mV) is applied previously. The lower charge density at the MWCNT surface can induce weaker bindings, dissolvable over electric potential, than higher potential values where the attraction forces promote strong adsorption.

In summary, the investigation about the impact of the surrounding environment on the target's capacity showed that

1. the presence of ions in the mobile phase shows a clear impact on the column capacity. Pre-adsorbed ions block the binding sites and decrease the column capacity for the target molecules; however, they promote the column's electric charge.
2. the presence of salt in the sample mixture does not affect the column's target capacity. The expected competitive behavior for the binding sites is not confirmed for this MWCNT flow-through electrode but must be further regarded in future research.

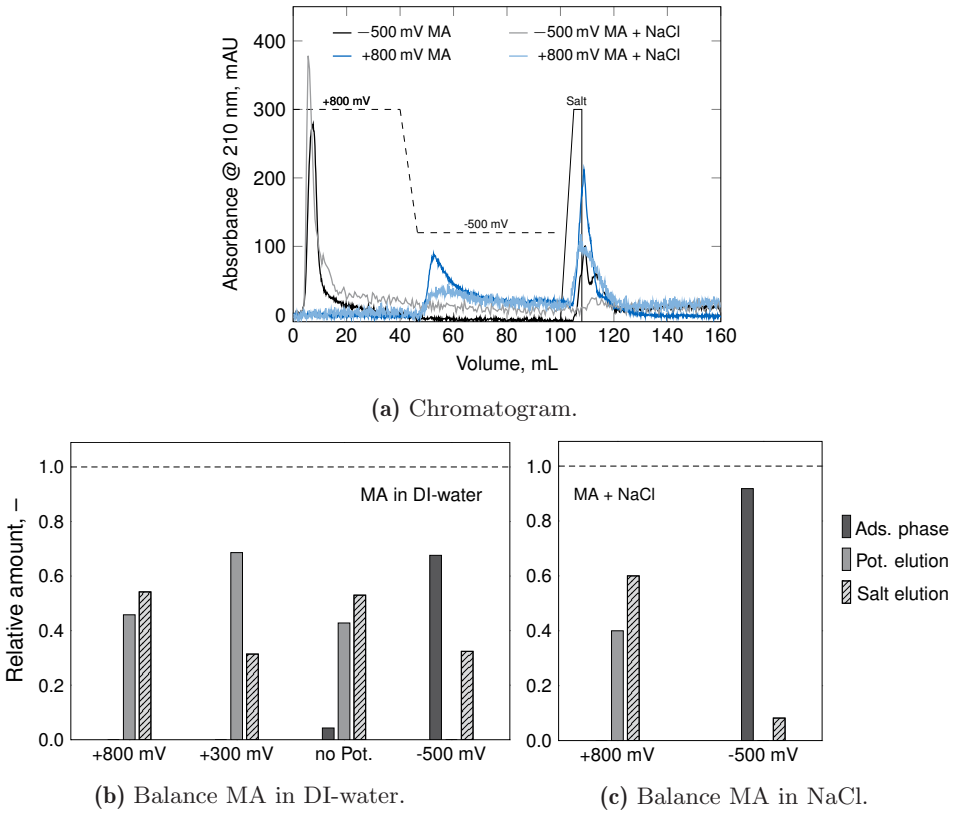

(a) Chromatogram.

(b) Balance MA in DI-water.

(c) Balance MA in NaCl.

Figure 5.23: Potential-gradient experiments and resultant balance, performed to study the adsorption capacity of maleic acid as target molecule in DI-water and in NaCl at different potentials applied. CNT-K matrix, DI-water, adsorption phase 0.5 mL/min, desorption phase 1.5 mL/min, analyte: 50 µL, 25 m/M (stoichiometric ratio 1:1), pH 7, 210 nm, potential gradient −5 mV/second, salt elution: 1 M NaCl, 8 mL. The single chromatograms can be found in Figure A.58 including the pH-value. Further information are imprinted in Figure A.56 for the maleic acid adsorption at different potential and Figure A.57 for the total balance. Adapted from Trunzer *et al.* [19].

Identifying the surrounding environment as a critical parameter affecting the column's current response, RQ 5 is successfully answered. Thus, it is shown that the column performance depends significantly on the flow rate as well as the composition and concentration of the mobile phase. As numerous species will exist in real biotechnological sample mixtures, a compromise between selecting the mobile phase and the targeted column capacity must be found. Moreover, the cooperative or competitive impact between the ions of the surrounding environment and the target species must be considered. For that reason, it is inevitably to study the adsorption behavior of mixtures for the target process further.

Key findings of Section 5.5 (cf. RQ 5)

⇒ The flow rate affects the film layer extension and controls the electrode charge.

⇒ Higher attraction forces and a longer contact time favors capacitive and faradaic current and benefits redox-activity.

⇒ Above a flow rate of 1.0 mL/min convection dominates the mass transfer in the macroporous MWCNT electrodes.

⇒ The electric potential affects the pH-value but not conversely.

⇒ 10 mM electrolytes promote the electrode performance, increasing mainly the capacitive part than provoking faradaic reactions.

⇒ The EDL formation depends on the ions' valency, increasing the electrode's electric charge in the order NaCl < KCl < $CaCl_2$.

⇒ Na^+ compacts the Stern layer, while K^+ delays the EDL rearrangement and promotes the diffusive layer formation.

⇒ The highly electronegative Cl^- can promote the Stern layer capacity striping off the hydration shell.

⇒ Pre-adsorbed ions from the mobile phase reduce the column capacity for a specific target species.

⇒ Additives, such as chloride salts, in the target sample, show no competitive or cooperative behavior.

⇒ Higher potentials cause stronger bindings than moderate potential favoring electrostatic interaction.

5.6 Adsorption Behavior of Inorganic and Organic Ions

Today, several researchers report the feasibility of carbonaceous nanomaterials for preparative and analytical PCC (see Figure 3.1). Besides some differences in process control, their research studies have one important aspect in common: a potential-dependent retention time shift of the target species along the column is recorded. This was not detected yet neither for CNT-K nor for IoLiTec-CNT columns. As the species' specific retention is the key for selective separation, the adsorption mechanism between inorganic and organic species and the MWCNT are investigated in this Section, aiming to answer RQ 6 and analyze whether the potential-triggered particulate packed bed is a suitable electrode for designing a potential-controlled separation process.

The interaction kind of salts is analyzed first and presented in Section 5.6.1. The investigation of the natural and potential-dependent adsorption affinities between various organic species to the MWCNT follows in Section 5.6.2. The studies are performed for CNT-K electrodes using DI-water as a mobile phase medium.

The presented results are partially published in Trunzer *et al.* [18, 19]. Besides, a part of the results was already discussed in the previous Sections 5.4 and 5.5.

5.6.1 Salt as Adsorptive

The adsorption mechanism of different salts are studied further as it was determined that the PCC setup does not only function as the designed chromatographic stationary phase for batch separation but is suitable to continuously purify and concentrate electrolytes.

Therefore, potential-step and -gradient experiments are performed with salts from the Hofmeister series. Manilo *et al.* [214] stated a correlation to the adsorption capacity for acidic functionalized polymers on basis of the EDL formation. Thus, the interaction behavior of NaCl, KCl, $MgCl_2$, $CaCl_2$, Na_2HPO_4, as well as Guanidium-SCN is investigated. $FeCl_3$ and $AlCl_3$ were selected additionally as representatives for trivalent cations. The salt's chromatograms of the potential-step experiments are summarized in Figure A.60. The corresponding balances are imprinted in Figure 5.24.

The salt interaction mechanisms are first investigated at a negatively charged electrode, where the cations can be electrosorbed, while the anions will be entirely repelled (see Figure 5.24a). The relative balance between the breakthrough peak at $-500\,\mathrm{mV}$ and the injection amount illustrates the minimum possible amount of cations interacting with the surface. In contrast to the results from the electrochemical characterization experiments using salt as an electrolyte, this data shows almost no adsorption when monovalent and divalent salts are injected pulse-wise. The low injection concentration and the small contact time might be a reason. The calculated relative unbound amount of the salts deviate due to signal fluctuations between 0.98 to 1.15 and indicate a total repulsion of the injected species. However, significant adsorption is measured for the trivalent salts at a negative potential (over 50 %). This high adsorption amount can be caused as Al^{3+} and Fe^{3+} have the highest charge density and highest mobility in the system, which promote particularly strong bindings to the counter-charged surface [214]. Moreover, the trivalent cations can form irreversible clusters with the CEX membrane, reducing the breakthrough amount. As there is no clear trend of the cation's potential-dependent adsorption in order of the Hofmeister salts determined, the assumption based on the work of Manilo *et al.* [214] could not be confirmed for the CNT-K matrix.

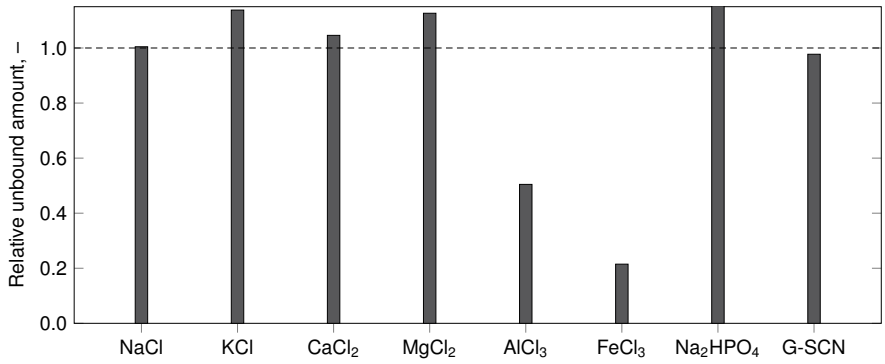

(a) Breakthrough amount at −500 mV relative to the bypass amount.

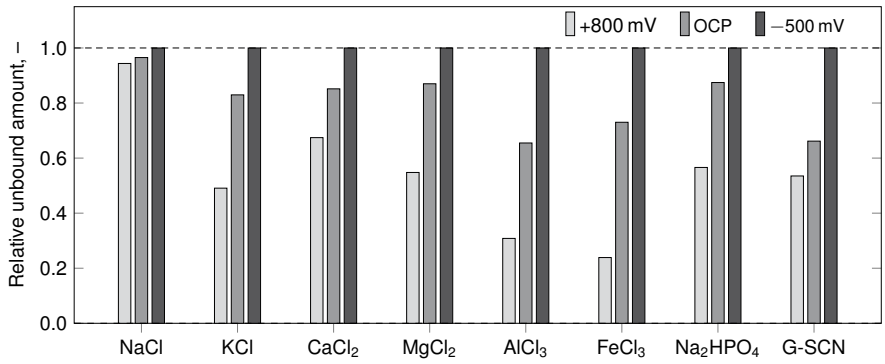

(b) Breakthrough amount in the adsorption phase relative to −500 mV.

Figure 5.24: Potential-step experiments to study the interaction between different salts as an analyte and the MWCNT. CNT-K matrix, DI-water, 1.5 mL/min, 50 µL, 25 mM. The corresponding chromatograms are illustrated in Figure A.60. Adapted and enlarged from Trunzer *et al.* [19].

Figure 5.24b depicts the impact of positive potential on the electrosorption of the salt anions plotting the unbound amount in the adsorption phase related to the breakthrough amount at −500 mV. The balance indicates an increasing adsorption amount with increasing surface charge density and increasing anion concentration. Although the anions have a low charge density, their small hydration radius and their high electronegativity promote the adsorption to the charged surface building a compact stern layer. The average adsorption amount of the monovalent and divalent chloride salts, as well as phosphate and thiocyanate at a high positive potential, is around 50 %, the trivalent salts up to 80 %. The difference between NaCl and KCl is comparably high to the other salts. As the interaction of the potassium cation was excluded in the previous study, a proper explanation for the high adsorption amount of the single chloride ion is not found yet and might be caused by the column aging.

An excursus is performed to analyze the suitability of NaCl as a tracer. The criterion that the tracer and stationary phase do not interact with each other can be confirmed after this experimental series. Unlike the conductivity fluctuation measured for NaCl as an electrolyte,

the results of the potential-dependent impulse experiments showed a minor effect on the adsorption of NaCl at OCP and no effect at a negative potential. Thus, the usage of the low concentrated NaCl as a suitable tracer is possible. Moreover, the highly concentrated standard tracer can be used without affecting the results as the high ion amount overlaps the potential effect (see Figure A.61).

In summary, the adsorption behavior of monovalent or divalent salts as a tracer and the charged MWCNT is less significant at positive and negative potential than the one of trivalent salts. However, as an effect is present, the surrounding ions' influence on the potential-controlled separation of multicomponent mixtures is amplified.

5.6.2 Interaction Study of Organic Molecules and the Electrode Cell

To summarize the achieved information focusing on a biotechnological application's design, the basic interaction of organic molecules with the CNT-K is analyzed to accentuate the potential-dependent and -independent adsorption behavior of different charge carriers. Thus, the interaction kind and binding strength are analyzed for:

- Maleic acid (MA) – which is used as the standard analyte. It is expected that the small negative charged carrier only interacts electrostatically with a positively charged surface;
- Ascorbic and salicylic acid – as negatively charged molecules carrying an aromatic group, expected to interact electrostatically or over the aromatic system;
- Histidine (His), phenylalanine (Phe) and tryptophan (Trp) – as a representative for an amphiphilic molecule and carrier of an aromatic ring, which can form electrostatic or aromatic interactions;
- Lysine (Lys) – as a basic peptide amino acid, which could bind over VdW and electrostatic interactions;
- Blue dextran – as a large organic molecule where polymer wrapping and $\pi - \pi$ binding can dominate the binding;
- Green fluorescent protein (GFP) – as a common, representative protein for bio-molecule screening applications with various interaction possibilities;
- Lysozyme (Lyz) – as a representative enzyme with various interaction possibilities;
- Ribovlavin – as a vitamin with various interaction possibilities; and
- Uracil – as a nucleobase, expected to interact over hydrogen bonds.

The chemical structures of the molecules are imprinted in Figures A.2 and A.3, while the corresponding information about the acidity is summarized in Table A.1. The used injection concentrations are listed in Table A.11.

This interaction study builds on the statements of Di Giosa *et al.* [63] and Yang *et al.* [172], who reported that larger molecules, which carry numerous and various polarized or charged surface groups, would interact differently with the MWCNT compared to single-charge carrying species. Electrostatic interactions, e.g., $\pi - \pi$ stacking, can occur between an aromatic residue and the delocalized MWCNT surface. Moreover, hydrophilic interactions are expected between aliphatic groups and the hydrated MWCNT surface. VdW interactions can cause protein wrapping or coating [44, 179]. Besides, hydrogen bonds, covalent bonds, and VdW can exist, challenging to isolate a dominant interaction between a molecule and the MWCNT [63, 67, 172]. With the increasing complexity and multi-valent structure of the molecules, it is expected that selective potential-controlled separation will be a challenge.

Natural Interaction Affinity of Organic Molecules with MWCNT

To identify the natural binding behavior, impulse injection experiments are performed at OCP. A salt elution step is added to regenerate the column and to evaluate ionic binding behaviors. The chromatograms are illustrated in Figure A.62. The balance of the relative breakthrough and elution amounts of different organic molecules are imprinted in Figure 5.25, visualizing that all molecules are adsorbed partially or entirely at OCP and eluted through salt displacement. Although the molecules' natural adsorption to the membrane cannot be excluded, the membrane area is negligible compared to the MWCNT matrix area. The interaction between molecules and MWCNT is much more likely and highlights a binding behavior between the slightly positively charged MWCNT electrode and all kinds of molecules at dynamic conditions. As only a few injected sample molecules show breakthrough peaks in the adsorption phase, the column capacity is sufficient for the experimental conditions.

As the molar concentrations of His, Phe, and ascorbic acid (32 mM, 30 mM, and 28 mM) are in a similar range, the breakthrough amount as well as the adsorption amount seem to depend strongly on the interaction kind. Comparing the adsorption amount of ascorbic acid, which is only bound to 40 %, and salicylic acid, which is completely bound, the significant binding difference must be found in the chemical structure. Ascorbic acid contains a C5 group and more hydroxyl-groups, while salicylic acid has an aromatic ring and a carboxyl group. The interaction of ascorbic acid with the MWCNT is weaker, expected mainly due to hydrogen binding, while aromatic interactions favor the strong adsorption of salicylic acid. A similar phenomenon occurs if histidine is compared with phenylalanine, which confirms aromatic binding as a dominating interaction form.

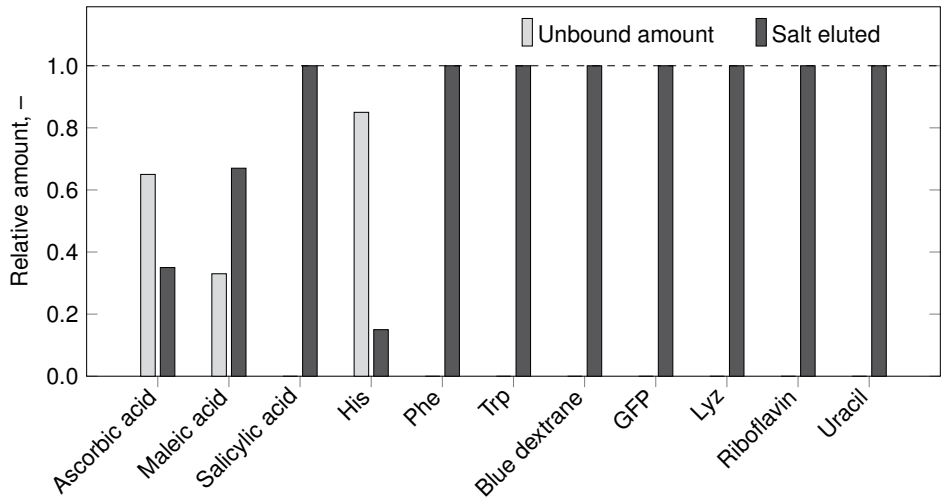

Figure 5.25: Balance of the interaction study to identify the binding affinity of different organic molecules to MWCNT in a 3D flow-through cell. No potential applied, CNT-K matrix, DI-water, Adsorption phase: 0.5 mL/min, Desorption phase 1.5 mL/min, Salt elution: 1.5 mL/min, 1 mM NaCl, 7.5 mL, Analyte injection: 50 µL, various concentrations, various wavelengths. The chromatograms are illustrated in Figure A.62.

Breakthrough due to overloading is detected for maleic acid (5 g/L, equals 43 mM), also determined in several previous studies at OCP. The partial amount of adsorbed molecules can be eluted with NaCl (see later Table A.11). The salt displacement of maleic acid confirms an electrosorptive, and an ionic binding character that distinguishes MA as a suitable molecule to study the potential-dependent effects at the solid-liquid interface.

All experimental results are balanced in Table A.11, showing that the sum of the breakthrough and elution amount is smaller, respectively, much smaller, than the injection amount (exception maleic acid). The high adsorption strength can be caused due to multiple interaction mechanisms, which are in particular expected for the large molecules, leading to irreversible binding and non-covalent surface functionalization [77, 150, 215], which can neither be displaced with salt nor, as assumed, via electric potential.

In summary, a natural binding affinity of various organic molecules to the MWCNT is determined, caused by the different charge densities of the molecules, and the different localized charged groups on the MWCNT. Consequently, the MWCNT seem to be more a super-adsorbents with a high binding affinity to all kinds of molecules than a selective chromatographic separation medium. In order to investigate whether these strong interactions can be broken via potential control, potential-dependent adsorption experiments are performed for exemplary molecules.

Potential-dependent Adsorption with Maleic Acid

The reversible electrosorption ability of maleic acid on the positively charged MWCNT makes the small, negatively charged molecule interesting for a detailed study about the potential-dependent adsorption behavior. Besides, MA is selected to compare the column performance of the CNT-K particles with the results of Knizia *et al.* [12] (glassy carbon electrode) and Brammen *et al.* [15] (MWCNT type Baytubes C 150 P).

The results presented are performed for three independent CNT-K columns, using potential-step experiments to investigate the reproducibility of the 3D flow-through MWCNT system (see Figure 5.26). As expected, the adsorbed amount of MA increases, corresponding to the applied potential's attraction forces. As the adsorption process already begins at $-300\,\mathrm{mV}$, the applied negative potential seems too weak to restrain mutual interactions and the formation of local positive surface charges. The differences between the replicates show that the column capacity depends strongly on the matrix structure and the current response.

Investigating the retention time of MA, e.g., in Figures A.63 or A.64, no potential-dependent time-shift is visualized, contradicting the results of Knizia *et al.* [12] and Brammen *et al.* [15]. Therewith, the CNT-K electrode's operation equals more a typical CDI cell [94], than a chromatographic column making a specific separation of organic mixtures yet a challenge.

Balancing the maximum adsorption amount at $+800\,\mathrm{mV}$, $3.7\,\mu\mathrm{mol/g}$ of maleic acid are adsorbed for a specific CNT-K column. Compared to data from the literature, this adsorption capacity is worse. Thus, it is five times smaller than the one determined for the Baytubes C 150 P [15], which is around $20\,\mu\mathrm{mol/g}$ for one-fourth of the inlet concentration (conditions: 1 mM PBS, pH 7). As an almost identical PCC setup is used in the work of Brammen *et al.* [15] and in this thesis, it is proven that the material properties and the packed bed structure cause these immense differences. Thus, comparing the material specifications (manufacturers information [216, 217], see Table A.12), it is determined that the Baytubes C 150 P material is less dense and thus able to be packed more compact than the CNT-K. Moreover, the Baytubes C 150 P have a higher SSA which advantages the electrode capacity. However, the specific material configuration is based on more parameters, such as the surface functionalization, the number of defects, and the presence of catalyst residue, which could not be identified. Since the synthesis protocol of Baytubes C 150 P and the CNT-K is based on the same patent that Bayer MaterialScience AG has handed over to Future Carbon GmbH, it is emphasized how sensitive the column's performance is on the material properties.

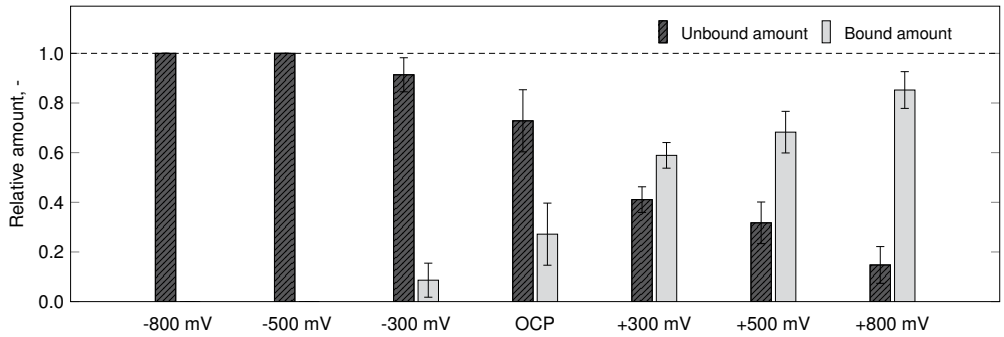

Figure 5.26: Potential-dependent adsorption experiments for maleic acid as target analyte to determine the reproducability of three CNT-K columns. Potential-step experiments, CNT-K matrix, DI-water, 1 mL/min, 50 µL, 5 g/L, 216 nm, pH 7. The adsorption was performed at various potentials (x-axis), the desorption potential was −800 mV. Adapted from Trunzer *et al.* [18].

Since no further data on the binding capacity of MA to MWCNT can be found in the literature for chromatographic applications, some comparable values for MWCNT electrodes are determined for capacitive processes using NaCl. For instance, Wang *et al.* [149] designed a macroporous MWCNT sponge with a low SSA able to bind 4 mg/g (68 µmol/g) NaCl (c_0 = 60 mg/L, SSA: 80 m^2/g, 1.2 V). Besides, they developed a CNT-CNF electrode with a similar SSA than CNT-K, able to adsorb 3 mg/g (SSA: 200 m^2/g) [149]. Comparable values are reached for a CNT-CNF monolith designed by Wang *et al.* [89, 90] (56.8 µmol/g NaCl, c_0 = 2 mM, SSA: 210 m^2/g, 1.2 V). The lowest capacity was determined in the literature for a CNT-CNF monolith, which adsorbs only half as much (1.6 mg/g, ≈ 27 µmol/g NaCl, c_0 = 50 µS/cm, SSA: 211 m^2/g, 1.2 V) [218].

However, the monolith described by Nie *et al.* [218] still adsorb six times more ions than the CNT-K matrix does, expected to be caused by the material properties but also the macroporous structure of the CNT-K packed bed [89, 90], reducing the number of binding sites. Besides, the small packing density [83] and the enormous amount of water stored inside [173], affect the matrix structure and interface. As it was not able to pack more CNT-K into the PCC column, the tightest packed column contains only about 0.5 g MWCNT (100 m^2/g). In future designs, the CNT-K electrodes could be improved with a redesign of the electrode setup, increasing the electrode mass, or an effective surface functionalization to generate more specific binding sites [143]. Nevertheless, all researchers used different setups, different materials, and experimental conditions, which makes a direct comparison impossible. To finally design an applicable laboratory, or industrial technology, the CNT-K column's capacity must be extremely increased to stand at least the state-of-the-art. Moreover, the total column performance must be improved to advantage PCC instead of common separation technologies.

Table 5.6: Comparison of the adsorption affinity of different carbon electrodes used in chromatographic application targeting MA, or used in CDI targeting NaCl. The listed electrode capacities are rounded values.

Author	**Material**	**SSA,** m^2/g	**Capacity,** mg/g / µmol/g
This research	CNT-K	200	$4 \cdot 10^{-3}$ / $3.4 \cdot 10^{-8}$
This research	IoLiTec-CNT	210	$3 \cdot 10^{-3}$ / $2.6 \cdot 10^{-8}$
Brammen *et al.* [15]	Baytubes C 150 P	220	$2 \cdot 10^{-2}$ / $1.7 \cdot 10^{-7}$
Wang *et al.* [149]	MWCNT sponge	80	4 / 68
	CNT-CNF monolith	200	3 / 51
Wang *et al.* [89, 90]	CNT-CNF monolith	210	3 / 57
Nie *et al.* [218]	CNT-CNF monolith	211	2 / 34

A brief overview of various CNT-K column capacities determined in different potential-step experiments using MA as a target is summarized in Table 5.7. There, a column is investigated, loading with MA ($c_0 = const.$) when DI-water or PBS is used as mobile phase media (cf. Figure A.63). It is determined that the load is 4.0 µmolg of MA when DI-water functions as a mobile phase. However, when 10 mM PBS is used, half of the binding sites are pre-occupied, decreasing the capacity of MA to 1.8 µmol/g.

Investigating the column capacity for another CNT-K matrix in dependency of the target's injection concentration (see Figure A.64), it is shown that the higher MA concentration ($c_0 = 5\,g/L$, maximal column load $q_{max} = 3.4\,\mu mol/g$) causes overloading. In contrast, when $c_0 = 2\,g/L$ is injected, the molecules are completely adsorbed ($q = 1.7\,\mu mol/g$). The load difference shows that the binding sites are not entirely occupied, indicating the optimal column performance is in between.

The strong material influence on the adsorption capacity is highlighted in Figure A.65, when the potential-dependent adsorption experiments are performed for IoLiTec-CNT at similar conditions. First, it is conspicuous that IoLiTec-CNT electrodes run up to ±1.2 V without water decomposition, which is comparable to setups from the literature. In contrast to the CNT-K (±0.8 V), this can be caused when IoLiTec-CNT produce a smooth electron transfer due to the absence of catalyst residues and different reactive sites preventing water decomposition at low potentials or by generating further binding sites.

Table 5.7: Maximum column capacity for a CNT-K electrode, related on the dry CNT-K mass, if maleic acid is used as target analyte. Data correspond to different experiments regarding the influence of different inlet concentrations (c_0) and the mobile phase medium.

Experiment	**Results**	**Capacity,** µmol/g	$\mathbf{c_0}$**,** g/L	**Mobile phase**
Reproducability	Figure 5.26	3.7	5	DI-water
DI-water vs. PBS	Figure A.63	4.0	5	DI-water
DI-water vs. PBS	Figure A.63	1.9	5	10 mM PBS
Concentration	Figure A.64	1.7	2	DI-water
Concentration	Figure A.64	3.4	5	DI-water

While the column capacities of IoLiTec-CNT and CNT-K electrodes equals at similar initial conditions ($q = 3.0$ to $4.0\,\mu mol/g$ for $c_0 = 5\,g/L$), it differs in the total column capacity. Thus, IoLiTec-CNT and adsorb around $q = 6.0\,\mu mol/g$ MA ($c_0 = 10\,g/L$) at maximal potential applied. With the absence of a breakthrough peak in the adsorption phase, this behavior indicates a linear adsorption amount. As in the material and electrochemical characterization assumed, a much higher total column capacity is detected for the IoLiTec-CNT than for the CNT-K. At all, the IoLiTec-CNT electrode is able to adsorb more ions than CNT-K, however, it cannot reach the high adsorption amount of the Baytubes C 150 P (cf. Table 5.6).

The experiments using maleic acid as a target analyte showed that the potential-dependent adsorption and desorption for small, uniform charged molecules is possible. The column capacity increases with increasing potential and increasing inlet concentration until a breakpoint is reached. It is successfully determined that the column capacity depends primarily on the setup, the material properties, and the mobile phase composition. The selection of the column design therewith becomes essential for PCC development.

Potential-dependent Adsorption with Complex Analytes

In the last study, the potential-dependent adsorption behaviors of more complex analytes are examined: the amino acids phenylalanine and lysine, and the protein GFP. Based on the study at OCP, an aromatic binding is expected for Phe; VdW for Lys; as well as multiple unspecific bindings for GFP. The aim is to investigate if the adsorption behavior of these representatives of organic molecules can be triggered electrochemically and if all bindings can be broken via potential change.

The chromatograms of the three analytes are illustrated in Figure 5.27, showing that Phe and Lys are not entirely bound at negative potential, while GFP was completely adsorbed at similar conditions. When a positive potential is applied, only Lys is not entirely bound.

The determined low binding affinity of the amino acids at negative potential can be caused when the charged molecules are repelled, while the multiple polarization of GFP adsorbs to the MWCNT independently of the applied potential. Therewith, the interaction between GFP and the MWCNT is too strong to be broken electrochemically. When a positive potential is applied, Phe interacts with the electron-lacking surface via its aromatic group. Lys might not be decisively attracted by increasing positive potential, as its side-chain favors VdW interaction. Thus, there is still a breakthrough peak of Lys, even at a high positive potential. Potential inversion leads to elution of Phe when +300 mV was applied in the adsorption phase but not for +800 mV. This phenomenon can be caused when higher attraction forces are provoked by a higher potential leading to strong bindings that cannot be dissolved

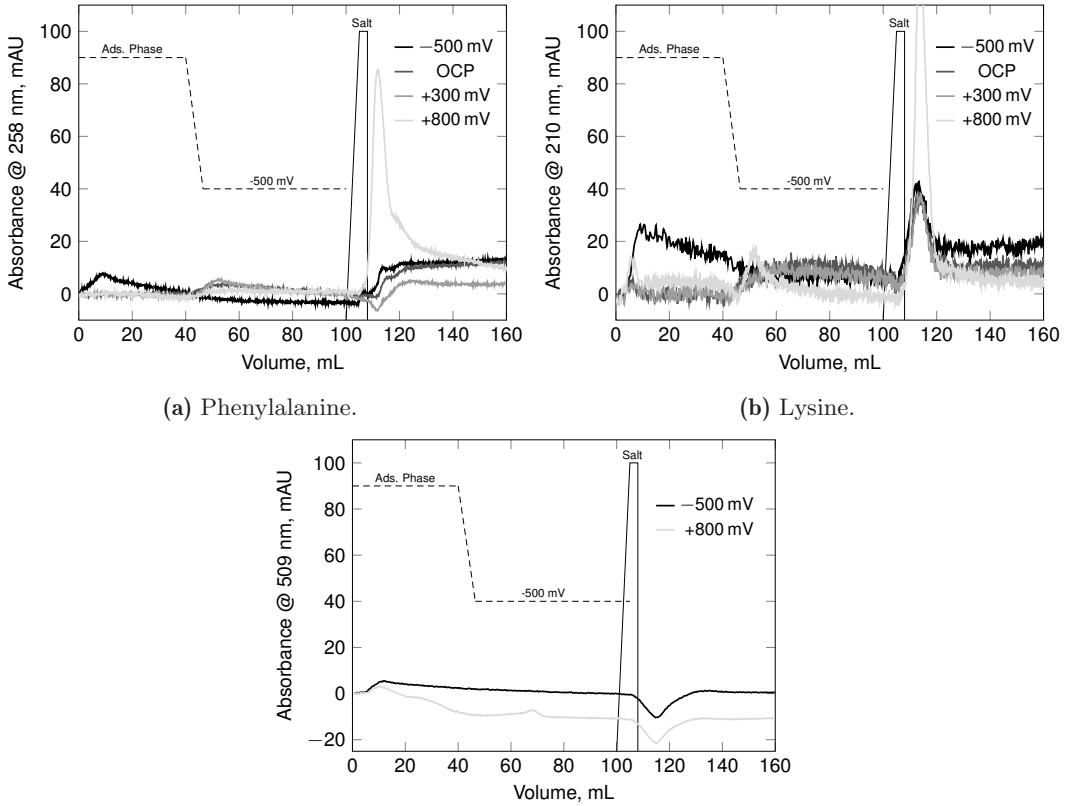

(a) Phenylalanine.

(b) Lysine.

(c) GFP.

Figure 5.27: Interaction study between different organic molecules and CNT-K at various potentials. CNT-K matrix, DI-water, Adsorption phase: 0.5 mL/min, Desorption phase 1.5 mL/min, −5 mV/min, Salt elution: 1.5 mL/min, 1 mM NaCl, 8 mL, Analyte injection: 50 µL 25 mM, pH 7.

electrochemically. Moreover, it is possible that higher attraction triggers the energetically preferred spatial position of Phe and strengthens the binding [63, 183]. On the contrary, Lys can elute via electric potential electrochemically independently of the potentials applied in the adsorption phase. The balance is illustrated in Figure A.66 (MA is plotted for comparison).

This Chapter answers RQ 6 by confirming that the CNT-K behave as strong adsorbents, able to bind differently sized, charged, and polarized molecules over distinct binding types. While this ability initially appears to be a decisive advantage, it reduces the suitability of the MWCNT for selective potential-controlled separation. Often, potential triggers total adsorption, but the potential inversion cannot break the bindings again. When eluents are used to regenerate the matrix, the only outstanding advantage of PCC in comparison to IEX is its versatility in operation mode.

Summarizing this thesis, no chromatographic separation of a binary mixture could be presented. Nevertheless, the essential process parameters that allow capacitive processing could be identified successfully. Besides, numerous concepts for a re-design of PCC using MWCNT could be derived. Moreover, the fact that organic molecules interact distinctively with the MWCNT electrode can provide the basis for developing PCC into a chromatographic system. However, further research is necessary for advancing the research idea into practical preparative processing on laboratory- and industry-scale.

Key findings of Section 5.6 (cf. RQ 6)

⇒ Impulse-wise injected, low concentrated mono- or divalent salt cations are not attracted to the counter-charged surface.

⇒ The adsorption of injected anions increases with increasing concentration.

⇒ Trivalent salts show the highest adsorption amount on various charged surfaces.

⇒ Based on their specific characteristics, all kinds of organic molecules bind differently to the MWCNT surface.

⇒ Molecules carrying an aromatic ring (salicylic acid or Phe) are stronger adsorbed than similar molecules carrying C5 groups (ascorbic acid or His).

⇒ $\pi - \pi$ bindings dominate VdW interactions.

⇒ Electrostatic repulsion is not sufficient to elute multi-binding molecules.

⇒ The MWCNT behave more like a super-adsorbent than a selective resin.

⇒ Potential-controlled separation is reproducible for uniform charge-carrying species identifying maleic acid as a crucial species for comparing different materials and setups.

⇒ The total adsorption capacity of CNT-K matrix is 4 µmol/g, which is only $1/4^{th}$ of Baytubes C 150 P and several times smaller CNT-monolith.

⇒ The total column capacity of IoLiTec-CNT indicates a linear adsorption regime in between the potential boundaries.

6 Findings Referred to the Research Questions

The key findings that contributed to closing the research gap and successfully implementing an overall PCC process description using MWCNT as resin are summarized in Table 6.1. The results are presented based on the previously formulated research questions (RQ, see Section 3.4) and accentuate the fundamental aspects necessary to understand capacitive process design.

Overall, it is successfully proved that both MWCNT materials, CNT-K and IoLiTec-CNT, function simultaneously as a working electrode and a chromatographic fixed bed (**RQ 1**). The material structure and its specific properties are characterized on various aspects (**RQ 2**), which knowledge formed the basis to describe the EDL formation chromatographically and electrochemically (**RQ 3**). Moreover, it is visualized how the operating conditions, such as potential, flow rate and elution kind, affect the column response (**RQ 4**) as well as how the surrounding environment triggers the capacitive character of the electrode cell (**RQ 5**). Finally, it is confirmed that the MWCNT behave capacitive for small, single charged species, while they behave more like a super-adsorbent for species carrying multiple charged groups. Thus, different binding kinds are identified between a specific analyte and the resin (**RQ 6**).

However, a potential-dependent retention time shift enabling chromatographic separation of biomolecular mixtures could not be identified. Although convinced that PCC with MWCNT is a promising and economically feasible alternative to IEX, process development is still in its infancy, it requires further research in all research questions presented.

Table 6.1: Summary and conclusions from the research questions. The successfully answered RQ are marked with ✓, *o* indicates partially answered RQ.

Research question			**Key findings**	**Section**
RQ 1	Is the setup of the PCC column feasible for a potential-dependent separation process?	✓	A successful proof-of-concept was obtained for both materials CNT-K and IoLiTec-CNT.	5.1
RQ 2	Does the MWCNT materials' specific properties influence the process performance?	*o*	The determined differences in the material properties could be used to predict and explain the column response. However, the analysis performed were not detailed to thoroughly depict the material's specific interfacial effects.	5.2
RQ 3	Can a combination of conventional chromatographic and electrochemical analysis methods be employed to describe the potential-dependent effects at the solid-liquid interface?	✓	Combining conventional chromatographic and electrochemical characterization methods succeeds in describing the EDL and the resulting electrode quality for both MWCNT materials.	5.3
RQ 4	Does the operation conditions influence the column performance?	*o*	The column's capacitive and chromatographic character enable continuous purification but must be adjusted for each setup. The column performance depends on the process target and is a trade-off between the surrounding environment, fluid flow rate, as well as potential and elution kind. The detailed interplay between all process operating factors is not analyzed yet.	5.4

Research question			Key findings	Section
RQ 5	Does the surrounding environment impact the chromatographic and electrochemical response of the column?	✓	Fluid flow rate, as well as composition and concentration of the mobile phase, decisively influence the EDL properties. The column capacity depends on the time-dependent Stern and diffusive layer formation, as well as the competition and cooperation for binding sites between the target species and the additives in mixtures or carrier media.	5.5
RQ 6	Do differently charged inorganic and organic species interact differently with an electrically charged MWCNT surface?	*o*	Charged or polarized species interact with the MWCNT depending on their valency, charge density, and structure. Reversible, electrosorptive interactions are determined for uniform charge-carrying species. Stronger interactions exist for various multiple charge-carrying species making the MWCNT a super-adsorbent. As these interactions cannot be broken by electric potential alone, the potential-controlled separation of biomolecules is not yet applicable using CNT-K or IoLiTec-CNT electrodes.	5.6

7 Summary and Outlook

Potential-controlled chromatography was designed as a versatile separation and purification technology for various kinds of charged and polarized ions and molecules. Initially, analytical approaches were developed since Knizia *et al.* [12] and Kocak *et al.* [13] introduced a preparative application at the turn of the millennium. Brammen *et al.* [15] followed and established MWCNT as an innovative resin characterized by high SSA and exceptional mechanical as well as chemical properties.

Since the application of Brammen *et al.* [15] was presented as a cost-effective and promising alternative to IEX, this thesis focused on the advancement and detailed research on MWCNT as a resin for an applicable biotechnological PCC. The overall objective was to develop a general guideline for a bio-compatible PCC design based on the process's fundamental influencing factors. Christwanto *et al.* [219] claimed that the solid-liquid interface is built on a complex parameter space that cannot be described sufficiently. However, it is the driving force for capacitive processing and has to be understood in detail. Therefore, this thesis aspires to a multi-variant analysis to identify the EDL formation and its contribution to the process target. Based on this motivation, six research questions were formulated (see Table 6.1) to investigate the 3D flow-through PCC using MWCNT types CNT-K and IoLiTec-CNT as new resins on its natural operating conditions.

The previous Section summarized that all these six research questions were investigated and could be answered successfully or partially successfully. Although, some remained open, and new ones arose. The knowledge achieved in this thesis is now referred back to the fundamentals for selective capacitive processing (see Table 1.1), and Table 7.1 summarizes whether the advanced PCC process development applies to the hypotheses made.

HT 1: The application of an electric potential to carbonaceous nanoparticles influences its surface properties.

The PCC process analysis showed that the conductive MWCNT can be triggered via electric potential inducing electrosorption and desorption of small ions and molecules. The electric potential thereby modifies the surface properties of the working electrode and activates capacitive and faradaic currents. RQ 1, 2, and 4 build on this hypothesis and reflect the fundamental statement.

HT 2: Porous flow-through electrodes are suitable for selective chromatographic separation of organic molecules.

The proof-of-concept showed that both nano-particulate MWCNT materials can work simultaneously as a working electrode and stationary phase material. The setup characterization identifies a macroporous, well-distributed packed bed, which function as a pseudo-capacitor. The PCC process is veriefied as a continuous purification and concentration of salt ions from the mobile phase. However, it functions as a super-adsorbent for various multiple-charged molecules. The expected potential-dependent retention time shift was not detectable neither for the CNT-K nor the IoLiTec-CNT electrodes. The hypothesis was the fundament for RQ 1 and 6, targeting a selective chromatographic separation of molecule mixtures but could not be verified yet.

HT 3: The interplay between setup, material, surrounding environment and target species affect the potential-dependent process performance.

An interplay between multiple factors like setup, material, surrounding environment, and the target analytes' structure is determined, affecting the process performance. Thus, it is verified that the current response and the column capacity depends on

1. the material morphologies and properties promoting the target species' adoption;
2. the fluid flow, which decreases the contact time with increasing flow rate;
3. the mobile phase concentration and composition triggering the EDL properties; and
4. the target valency and structure, which defines the interaction kind.

Finally, RQ 3, 4, and 5 followed this hypothesis and verified that the column performance is a trade-off between different operating parameters, which has to be considered for future process development.

Table 7.1: Review as to whether the hypotheses put forward are suitable (✓) for the argumentation of PCC process development or could not be verified (*o*).

Hypothesis		Conclusion
HT 1	The application of an electric potential to carbonaceous nanoparticles influences its surface properties.	✓
HT 2	Porous flow-through electrodes are suitable for selective chromatographic separation of organic molecules.	*o*
HT 3	The interplay between setup, material, surrounding environment and target species affect the potential-dependent process performance.	✓

This thesis's significant findings are highlighted at the end of each discussion of the research questions (key findings in framed box). The achieved knowledge provides instructions for future preparative PCC process development for biotechnological applications with MWCNT as resin. Extracting the fundamental key parameters that influence the process performance, a detailed analysis protocol exists to understand the electrode performance and the interplay between chromatographic setup and capacitive operation.

Some critical aspects were only touched upon and must be further investigated for an optimized implementation, affecting the system's performance:

- The PCC setup used is complex, including a wire contact and an IEX membrane to control the process. It is challenging to handle and makes reproducible process control difficult. Moreover, these components are interfering factors and contribute to the column's response and aging in a yet unknown way. These components must either be examined in detail or eliminated in a redesign.
- The fragile MWCNT electrode shows a distinct chromatographic and electrochemical aging. Faradaic current induces redox-reactions and surface functionalization, modifying the electrode operating conditions over time. The resulting repulsion and attraction forces between the charged tubes as well as the fluid flow modify the matrix structure. It is not possible to identify the specific electrode properties at any time steps during

processing. Specific surface functionalization through passivation or polymer functionalization could prevent this aging.

- The high water storage capability of the MWCNT defines the macroporous matrix and forms the primary EDL. It causes a positively charged electrode surface promoting the electrosorption of counter-charged. Besides, it influences the mass transfer inside the column. This specific configuration reduces column performance and cannot yet compete with conventional separation applications such as industrially established CDI cells with microporous plate electrodes. An increase in electrode mass and SSA, possibly realized by monolith, is recommended for future processing.
- The MWCNT have an extraordinary binding affinity to all kinds of charged or polarized ions and molecules. While weak electrosorptive, VdW, or ionic interaction of small species can be broken via applied potential, the adsorption behavior of multi-polarized or -charged large molecules is irreversible. Thus, selective separation is a challenge and cannot be realized with the setup used. In this case, also selective functionalization triggering specific, reversible interactions might be an advance.

Some solution proposals to overcome PCC's weaknesses are given in the following.

The specific functionalization of the MWCNT or the implementation of inert composite materials could prevent aging and promote selective and reversible processing. This contribution and publications in the literature [134] showed that pristine bulk CNT electrodes achieve lower capacities than other carbon-based electrodes (e.g., activated carbon or graphene), which own high electrode capacity due to a microporous system which a large accessible area. For instance, Han *et al.* [143] determined that novel carbon with a hierarchical structure and various covalent or non-covalent surface functionalizations are promising electrode materials. They claim that these electrodes benefit from excellent surface wetting and accessibility to numerous binding sites. Song *et al.* [220] highlighted a specific functionalization of the electrode material using quinones, which can be triggered via redox-activation at a specific potential. They further recommended easy-to-synthesize oxygen-doped carbon structures as an excellent material for pseudo-capacitors that suspend aging and guarantee reversible processing and high purity. Ahirrao and Jha [93] spin-coated graphitic carbon with a MWCNT/graphene oxide composite and therewith prevent the fragile electrode from re-stacking, providing simultaneously a maximum accessible surface area improving the capacity for NaCl ions. The contribution of Xie *et al.* [221] convinces with the composition of activated carbon and CNT, which causes a highly conductive and stable framework that can be implemented for long-term processes. It was also possible to synthesized bio-compatible fibers [222] triggering biotechnological implementation of PCC. Finally, many approaches exist in the literature, promoting the design of specific MWCNT electrode material for selective separation.

The use of functionalized or composite materials is often accompanied by monolithic structures, which installation in the PCC setup can improve the MWCNT current response and prevent structural aging. The hierarchical structure promotes more particle-particle contracts and therewith a high potential distribution inside the system. The electrode mass can be increased when particle swelling and the amount of stored water are reduced in the MWCNT matrix. The increasing current flow will advantage the number of binding sites, the surface charge density, and the electrode capacity [223, 224]. A stable network can also prevent structural rearrangement and increase the column's operation time. Moreover, monoliths with a pre-assembled and reproducible configuration can simplify the handling of the PCC column. For instance, Deng *et al.* [48] summarized that monolith with a homogeneous framework, a porous structure, and mechanical stability provide an efficient pathway for fast electrons transfer and ion transport as well as guarantee accessible surface sites additionally. Kohli *et al.* [88] implemented mesoporous carbon aerogels in CDI and advantage the scale-up of stacked electrodes achieving a high setup performance. Recently, Song *et al.* [220] installed redox-active carbon in energy storage devices, engineering an extraordinary ion and electron transport in the meso- and microporous structure. Therefore, using monolith instead of particulate packed beds might be successful.

Since the EDL is identified as the heart for PCC, defining the specific column capacity, its response, and dependency on external parameters should be analyzed further. By identifying water as the dominant component and driving force within the MWCNT matrix electrode, the main influencing parameter of electrode resistance and mass transfer effects at the solid-liquid interface was revealed. A suitable method, which can be added to the electrochemical protocol presented, is electrochemical impedance spectroscopy (EIS). For instance, one could address the studies of Rommerskirchen *et al.* [201], who used EIS to study the impact of the electrode mass, electrolyte composition, and flow rate on the current response. With this methodology, it would be possible to identify the different resistances in the system and estimate where optimization is needed. Moreover, Lenz *et al.* [225] recently implemented a new analysis strategy for EIS evaluation to visualize how the macroscopic or microscopic structures of different carbon materials affect the kinetic properties inside the electrode cell. Thus, EIS might be a valuable supplement for electrochemical characterization screening new designs and investigating, e.g., aging effects or the contribution of setup components.

Finally, there is still a long way to go before developing an optimal PCC setup for selective capacitive separation and its scale-up to laboratory and industrial applications. Nevertheless, looking forward to a 'greener' future, potential-controlled chromatography will be an economically feasible alternative to ion-exchange chromatography.

Bibliography

1. Schrader, U., Silberzahn, T., Szlezak, N. & Raven, M. *Top oder Flop? Die medizinische Biotechnologie in Deutschland am Scheideweg* (ed McKinsey&Company) 2018.
2. BIOCOM AG. *Die deutsche Biotechnologie-Branche 2019* (ed BIOCOM AG) 16.04.2021. `biotech-nologie.de`.
3. Harrison, A., Todd, P. W., Rudge, S. R. & Petrides, D. P. *Bioseparations science and engineering* 2. Edition (Oxford University Press, 2015).
4. Straathof, A. in *Comprehensive Biotechnology* (ed Elsevier) 811–814 (Elsevier, 2011).
5. Elsevier B.V. *Scopus* (ed Elsevier B.V.) 18.10.2020. `scopus.com/home.uri`.
6. Tang, W., Liang, J., Di, H., Gong, J., Tang, L., Liu, Z., Wang, D. & Zeng, G. Various cell architectures of capacitive deionization: Recent advances and future trends. *Water research* **150,** 225–251 (2019).
7. Notarianni, M., Liu, J., Vernon, K. & Motta, N. Synthesis and applications of carbon nanomaterials for energy generation and storage. *Beilstein J. Nanotechnol.* **7,** 149–196 (2016).
8. Pomerantseva, E., Bonaccorso, F., Feng, X., Cui, Y. & Gogotsi, Y. Energy storage: The future enabled by nanomaterials. *Science* **366** (2019).
9. Saeed, K. & Ibrahim. Carbon nanotubes-properties and applications: A review. *Carbon letters* **14,** 131–144 (2013).
10. Blair, J. W. & Murphy G. W. Electrochemical demineralization of water with porous electrodes of Large Surface area. *SWCC* **27,** 206–223 (1960).
11. Voorhies, J. D. & Davis, S. M. Coulometry with the carbon black electrode. *Anal. Chem.,* 1855–1857 (1960).
12. Knizia, M. W., Vuorilehto, K., Schrader, J. & Sell, D. Potential-controlled chromatography of short-chain carboxylic acids. *Electroanal.* **15,** 49–54 (2003).
13. Kocak, F., Vuorilehto, K., Schrader, J. & Sell, D. Potential-controlled chromatography for the separation of amino acids and peptides. *J. Appl. Electrochem.* **35,** 1231–1237 (2005).

14. HTW Hochtemperatur-Wekstoffe GmBH. *Sigradur G: E-Mail* (ed Bioseparation Engineering Group, attn. Tatjana Trunzer) 29.01.2018.

15. Brammen, M., Fraga-García, P. & Berensmeier, S. Carbon nanotubes-A resin for electrochemically modulated liquid chromatography. *J. Sep. Sci* **40,** 1176–1183 (2017).

16. Future Carbon GmbH. *Price list: E-Mail* (ed Bioseparation Engineering Group, attn. Tatjana Trunzer) 9.03.2020.

17. IoLiTec Ionic Liquids Technologies G,bH. *Price list: E-Mail* (ed Bioseparation Engineering Group, attn. Tatjana Trunzer) 17.05.2019.

18. Trunzer, T., Stummvoll, T., Porzenheim, M., Fraga-García, P. & Berensmeier, S. A carbon nanotube packed bed electrode for small molecule electrosorption: An electrochemical and chromatographic approach for process description. *Appl. Sci.* **10,** 1133 (2020).

19. Trunzer, T., Fraga-García, P., Tschuschner, M. P. A., Voltmer D. & Berensmeier, S. The electrosorptive response of a carbon nanotube flow-through electrode in aqueous systems. *Chem. Eng. J.* **428,** 131009 (2021 // 2022).

20. Wagner, R., Bag, S., Trunzer, T., Fraga-García, P., Wenzel, W., Berensmeier, S. & Franzreb, M. Adsorption of organic molecules on carbon surfaces: Experimental data and molecular dynamics simulation considering multiple protonation states. *J. Colloid Interf. Sci.,* 424–437 (2021).

21. Schmidt-Traub, H., Schulte, M. & Seidel-Morgenstern, A. *Preparative Chromatography* 2. Edition (Wiley-VCH, 2012).

22. Carta, G. & Jungbauer, A. *Protein chromatography: Process development and scale-up* (Wiley-VCH, 2010).

23. Helmholtz, H. Ueber einige Gesetze der Vertheilung elektrischer Ströme in körperlichen Leitern mit Anwendung auf die thierisch-elektrischen Versuche. *Ann. Phys. Chem.* **165,** 211–233 (1853).

24. Helmholtz, H. Studien über electrische Grenzschichten. *Ann. Phys. Chem.* **243,** 337–382 (1879).

25. Gouy, M. Sur la constitution de la charge électrique à la surface d'un électrolyte. *J. Phys. Theor. Appl.* **9,** 457–468 (1910).

26. Chapman, D. L. LI. A contribution to the theory of electrocapillarity. *Philos. Mag.* **25,** 475–481 (1913).

27. Schmidt-Böcking, H., Reich, K., Templeton, A., Trageser, W. & Vill, V. Otto Stern, Zur Theorie der elektrolytischen Doppelschicht. *Z. Elektrochem.,* 197–206 (1924).

28. Bard, A. J. & Faulkner, L. R. *Electrochemical methods : fundamentals and applications* 2. Edition (John Wiley & Sons, Inc., 2001).

29. Kilic, M. S., Bazant, M. Z. & Ajdari, A. Steric effects in the dynamics of electrolytes at large applied voltages. I. Double-layer charging. *Physical review. E, Statistical, nonlinear, and soft matter physics* **75,** 021502 (2007).

30. Biesheuvel, P. M., Fu, Y. & Bazant, M. Z. Diffuse charge and Faradaic reactions in porous electrodes. *Phys. Rev. E* **83,** 061507 (2011).

31. Biesheuvel, P. M., Porada, S., Levi, M. & Bazant, M. Z. Attractive forces in microporous carbon electrodes for capacitive deionization. *J. Solid State Electrochem.* **18,** 1365–1376 (2014).

32. Li, J., Pham, P. H. Q., Zhou, W., Pham, T. D. & Burke, P. J. Carbon nanotube-electrolyte interface: Quantum and electric double layer capacitance. *ACS nano* **12,** 9763–9774 (2018).

33. De Souza, J. P., Goodwin, Z. A. H., McEldrew, M., Kornyshev, A. A. & Bazant, M. Z. Interfacial layering in the electric double layer of ionic liquids. *Phys. Rev. Lett.* **125** (2020).

34. Kang, B., Tang, H., Zhao, Z. & Song, S. Hofmeister series: Insights of ion specificity from amphiphilic assembly and interface property. *ACS omega* **5,** 6229–6239 (2020).

35. Porada, S., Zhao, R., van der Wal, A., Presser, V. & Biesheuvel, P. M. Review on the science and technology of water desalination by capacitive deionization. *Prog. Mater. Sci.* **58,** 1388–1442 (2013).

36. Li, Q., Zheng, Y., Xiao, D., Or, T., Gao, R., Li, Z., Feng, M., Shui, L., Zhou, G., Wang, X. & Chen, Z. Faradaic electrodes open a new era for capacitive deionization. *Adv. Sci.* **7,** 2002213 (2020).

37. Luo, K., Niu, Q., Zhu, Y., Song, B., Zeng, G., Tang, W., Ye, S., Zhang, J., Duan, M. & Xing, W. Desalination behavior and performance of flow-electrode capacitive deionization under various operational modes. *Chem. Eng. J.* **389,** 124051 (2020).

38. Tian, S., Wu, J., Zhang, X., Ostrikov, K. & Zhang, Z. Capacitive deionization with nitrogen-doped highly ordered mesoporous carbon electrodes. *Chem. Eng. J.* **380,** 122514 (2020).

39. Schmidt, V. M. *Elektrochemische Verfahrenstechnik: Grundlagen, Reaktionstechnik, Prozeßoptimierung* (Wiley-VCH, 2003).

40. De Volder, M. F. L., Tawfick, S. H., Baughman, R. H. & Hart, A. J. Carbon nanotubes: present and future commercial applications. *Science* **339,** 535–539 (2013).

41. Eatemadi, A., Daraee, H., Karimkhanloo, H., Kouhi, M., Zarghami, N., Akbarzadeh, A., Abasi, M., Hanifehpour, Y. & Joo, S. W. Carbon nanotubes: properties, synthesis, purification, and medical applications. *Nanoscale Res. Lett.* **9,** 393 (2014).

42. Venkataraman, A., Amadi, E. V., Chen, Y. & Papadopoulos, C. Carbon nanotube assembly and integration for applications. *Nanoscale Res. Lett.* **14,** 220 (2019).

43. Hilding, J., Grulke, E. A., George Z., Z. & Lockwood, F. Dispersion of carbon nanotubes in liquids. *J. Disper. Sci. Technol.* **24,** 1–41 (2003).

44. Nakashima, N. Soluble carbon nanotubes: Fundamentals and applications. *Int. J. Nanosci.,* 119–137 (2005).

45. Whitten, P. G., Spinks, G. M. & Wallace, G. G. Mechanical properties of carbon nanotube paper in ionic liquid and aqueous electrolytes. *Carbon* **43,** 1891–1896 (2005).

46. Ehsani, A., Heidari, A. A. & Shiri, H. M. Electrochemical pseudocapacitors based on ternary nanocomposite of conductive polymer/graphene/metal oxide: an introduction and review to it in recent studies. *Chem. Rec.* **19,** 908–926 (2019).

47. He, Y., Zhuang, X., Lei, C., Lei, L., Hou, Y., Mai, Y. & Feng, X. Porous carbon nanosheets: Synthetic strategies and electrochemical energy related applications. *Nano Today* **24,** 103–119 (2019).

48. Deng, X., Li, J., Ma, L., Sha, J. & Zhao, N. Three-dimensional porous carbon materials and their composites as electrodes for electrochemical energy storage systems. *Mater. Chem. Front.* **3,** 2221–2245 (2019).

49. Bacakova, L., Pajorova, J., Tomkova, M., Matejka, R., Broz, A., Stepanovska, J., Prazak, S., Skogberg, A., Siljander, S. & Kallio, P. Applications of nanocellulose/ nanocarbon composites: Focus on biotechnology and medicine. *Nanomaterials* **10** (2020).

50. Zhang, S., Jia, Z., Liu, T., Wei, G. & Su, Z. Electrospinning nanoparticles-based materials interfaces for sensor applications. *Sensors* **19** (2019).

51. Agüí, L., Yáñez-Sedeño, P. & Pingarrón, J. M. Role of carbon nanotubes in electroanalytical chemistry: A review. *Anal. Chim. Acta* **622,** 11–47 (2008).

52. Power, A. C., Gorey, B., Chandra, S. & Chapman, J. Carbon nanomaterials and their application to electrochemical sensors: A review. *Nanotechnol. Rev.* **7,** 19–41 (2018).

53. Gaikwad, M. S. & Balomajumder, C. Capacitive deionization for desalination using nanostructured electrodes. *Anal. Lett.* **49,** 1641–1655 (2016).

54. Luciano, M. A., Ribeiro, H. & Bruch, G. E. Silva, G. G. Efficiency of capacitive deionization using carbon materials based electrodes for water desalination. *J. Electroanal. Chem.* **859,** 113840 (2020).

55. Beeram, S. R., Rodriguez, E., Doddavenkatanna, S., Li, Z., Pekarek, A., Peev, D., Goerl, K., Trovato, G., Hofmann, T. & Hage, D. S. Nanomaterials as stationary phases and supports in liquid chromatography. *Electrophoresis* **38,** 2498–2512 (2017).

56. Socas-Rodríguez, B., Herrera-Herrera, A. V., Asensio-Ramos, M. & Hernández-Borges, J. Recent applications of carbon nanotube sorbents in analytical chemistry. *J. Chrom. A* **1357,** 110–146 (2014).

57. Raunika, A., Raj, S. A., Jayakrishna, K. & Sultan, M. T. H. Carbon nanotube: A review on its mechanical properties and application in aerospace industry. *IOP Conf. Ser.: Mater. Sci. Eng.* **270,** 012027 (2017).

58. Kim, T., Cho, M. & Yu, K. J. Flexible and stretchable bio-integrated electronics based on carbon nanotube and graphene. *Materials* **11** (2018).

59. Su, S. & M Kang, P. Recent advances in nanocarrier-assisted therapeutics delivery systems. *Pharmaceutics* **12** (2020).

60. Deshmukh, M. A., Jeon, J.-Y. & Ha, T.-J. Carbon nanotubes: An effective platform for biomedical electronics. *Biosens. Bioelectron.* **150,** 111919 (2020).

61. Kumari, M., Liu, C.-H., Wu, W.-C. & Wang, C.-C. Gene delivery using layer-by-layer functionalized multi-walled carbon nanotubes: design, characterization, cell line evaluation. *J. Mater. Sci.* **56,** 7022–7033 (2021).

62. Fahmy, S. A., Alawak, M., Brüßler, J., Bakowsky, U. & El Sayed, M. M. H. Nanoenabled bioseparations: Current developments and future prospects. *BioMed Res. Int.* **2019,** 4983291 (2019).

63. Di Giosia, M., Valle, F., Cantelli, A., Bottoni, A., Zerbetto, F., Fasoli, E. & Calvaresi, M. Identification and preparation of stable water dispersions of protein - Carbon nanotube hybrids and efficient design of new functional materials. *Carbon* **147,** 70–82 (2019).

64. Herrera-Herrera, A. V., González-Curbelo, M. Á., Hernández-Borges, J. & Rodríguez-Delgado, M. Á. Carbon nanotubes applications in separation science: A review. *Anal. Chim. Acta* **734,** 1–30 (2012).

65. Liang, X., Liu, S., Wang, S., Guo, Y. & Jiang, S. Carbon-based sorbents: Carbon nanotubes. *J. Chrom. A* **1357,** 53–67 (2014).

66. Cserháti, T. Carbon-based sorbents in chromatography. New achievements. *BMC* **23,** 111–118 (2009).

67. Nicoletti, M., Capodanno, C., Gambarotti, C. & Fasoli, E. Proteomic investigation on bio-corona of functionalized multi-walled carbon nanotubes. *BBA-Gen Subjects* **1862,** 2293–2303 (2018).

68. Hussain, C. M., Saridara, C. & Mitra, S. Altering the polarity of self-assembled carbon nanotubes stationary phase via covalent functionalization. *RSC Adv.* **1,** 685 (2011).

69. Al-Othman, Z. A. & Wabaidur, S. M. Application of carbon nanotubes in extraction and chromatographic analysis: A review. *Arab. J. Chem.* **12,** 633–651 (2019).

70. Yu, J.-G., Zhao, X.-H., Yang, H., Chen, X.-H., Yang, Q., Yu, L.-Y., Jiang, J.-H. & Chen, X.-Q. Aqueous adsorption and removal of organic contaminants by carbon nanotubes. *Sci. Total Environ.* **482-483,** 241–251 (2014).

71. Ravelo-Pérez, L. M., Herrera-Herrera, A. V., Hernández-Borges, J. & Rodríguez-Delgado, M. A. Carbon nanotubes: Solid-phase extraction. *J. Chrom. A* **1217,** 2618–2641 (2010).

72. Zhang, W., Wan, F., Zhu, W., Xu, H., Ye, X., Cheng, R. & Jin, L.-T. Determination of glutathione and glutathione disulfide in hepatocytes by liquid chromatography with an electrode modified with functionalized carbon nanotubes. *J. Chrom. B* **818,** 227–232 (2005).

73. Hu, W., Hong, T., Gao, X. & Ji, Y. Applications of nanoparticle-modified stationary phases in capillary electrochromatography. *TrAC* **61,** 29–39 (2014).

74. Chen, J.-L. Multi-wall carbon nanotubes bonding on silica-hydride surfaces for open-tubular capillary electrochromatography. *J. Chrom. A* **1217,** 715–721 (2010).

75. Zhang, Y.-N., Niu, Q., Gu, X., Yang, N. & Zhao, G. Recent progress on carbon nanomaterials for the electrochemical detection and removal of environmental pollutants. *Nanoscale* **11,** 11992–12014 (2019).

76. Ye, J.-S. & Sheu, F. S. Functionalization of CNTs: New routes towards the development of novel electrochemical sensors. *Curr. Nanosci.,* 319–327 (2006).

77. Yang, N., Chen, X., Ren, T., Zhang, P. & Yang, D. Carbon nanotube based biosensors. *Sens. Actuator B Chem.* **207,** 690–715 (2015).

78. Rivas, G. A., Rodríguez, M. C., Rubianes, M. D., Gutierrez, F. A., Eguílaz, M., Dalmasso, P. R., Primo, E. N., Tettamanti, C., Ramírez, M. L., Montemerlo, A., Gallay, P. & Parrado, C. Carbon nanotubes-based electrochemical (bio)sensors for biomarkers. *Appl. Mater. Today* **9,** 566–588 (2017).

79. Lombardi, I., Bestetti, M., Mazzocchia, C., Cavallotti, P. L. & Ducati, U. Electrochemical Characterization of Carbon Nanotubes for Hydrogen Storage. *Electrochem. Solid-State Lett.* **7,** A115 (2004).

80. Giménez, P., Mukai, K., Asaka, K., Hata, K., Oike, H. & Otero, T. F. Capacitive and faradic charge components in high-speed carbon nanotube actuator. *Electrochim. Acta* **60,** 177–183 (2012).

81. Kado, Y., Soneda, Y., Hatori, H. & Kodama, M. Advanced carbon electrode for electrochemical capacitors. *J. Solid State Electrochem.* **23,** 1061–1081 (2019).

82. Dubey, R. & Guruviah, V. Review of carbon-based electrode materials for supercapacitor energy storage. *Ionics* **25,** 1419–1445 (2019).

83. Yang, Z., Tian, J., Yin, Z., Cui, C., Qian, W. & Wei, F. Carbon nanotube- and graphene-based nanomaterials and applications in high-voltage supercapacitor: A review. *Carbon* **141,** 467–480 (2019).

84. Kyaw, H. H., Myint, M. T. Z., Al-Harthi, S. & Al-Abri, M. Removal of heavy metal ions by capacitive deionization: Effect of surface modification on ions adsorption. *J. Hazard.* **385,** 121565 (2020).

85. Xing, W., Liang, J., Tang, W., Di H., Yan, M., Wang, X., Luo, Y., Tang, N. & Huang, M. Versatile applications of capacitive deionization (CDI)-based technologies. *Desalination* **482,** 114390 (2020).

86. Blaedel, W. J. & Strohl, J. H. Continuous quantitative electrolysis. *Anal. Chem.,* 1245–1251 (1964).

87. Farmer, J. C., Bahowick, S. M., Harrar, J. E., Fix, D. V., Martinelli, R. E., Vu, A. K. & Carroll, K. L. Electrosorption of chronium ions on carbon aerogel electrodes as a means of remediating ground water. *Energy & Fuels,* 337–347 (1997).

88. Kohli, D. K., Bhartiya, S., Singh, A., Singh, R., Singh, M. K. & Gupta, P. K. Capacitive deionization of ground water using carbon aerogel based electrodes. *Desalination Water Treat.* **57,** 26871–26879 (2016).

89. Wang, X. Z., Li, M. G., Chen, Y. W., Cheng, R. M., Huang, S. M., Pan, L. K. & Sun, Z. Electrosorption of ions from aqueous solutions with carbon nanotubes and nanofibers composite film electrodes. *Appl. Phys. Lett.* **89,** 053127 (2006).

90. Wang, X. Z., Li, M. G., Chen, Y. W., Cheng, R. M., Huang, S. M., Pan, L. K. & Sun, Z. Electrosorption of NaCl Solutions with Carbon Nanotubes and Nanofibers Composite Film Electrodes. *Electrochem. Solid-State Lett.* **9,** E23 (2006).

91. Aldalbahi, A., Rahaman, M., Almoiqli, M., Hamedelniel, A. & Alrehaili, A. Single-walled carbon nanotube (SWCNT) loaded porous reticulated vitreous carbon (RVC) electrodes used in a capacitive deionization (CDI) cell for effective desalination. *J. Nanomater.* **8** (2018).

92. Chung, S., Kang, H., Ocon, J. D., Lee, J. K. & Lee, J. Enhanced electrical and mass transfer characteristics of acid-treated carbon nanotubes for capacitive deionization. *Curr. Appl. Phys.* **15,** 1539–1544 (2015).

93. Ahirrao, D. J. & Jha, N. Comparative study on the electrosorption properties of carbon fabric, functionalized multiwall carbon nanotubes and solar-reduced graphene oxide for flow through electrode based desalination studies. *Carbon* **152,** 837–850 (2019).

94. Li, H., Liang, S., G., M., L., G., L., J. & He, L. The study of capacitive deionization behavior of a carbon nanotube electrode from the perspective of charge efficiency. *Water Sci. Technol.* **71,** 83–88 (2015).

95. Strohl, J. S. & Dunlap, K. L. Electrosorption and separation of quinones on a column of graphite particles. *Anal. Chem.,* 2166–2170 (1972).

96. Ghatak-Roy, A. R. & Martin, C. R. Electromodulated ion exchange chromatography. *Anal. Chem.,* 1574–1575 (1986).

97. Ting, E.-T. & Porter, M. D. Column design for electrochemically modulated liquid chromatography. *Anal. Chem.,* 94–99 (1998).

98. Fujinaga, T., Nagai, T., Okazaki, S. & Takagi, C. Study of the electrolytic chromatography. A new separation method of several metal ions. *Nippon Kagaku Zasshi,* 194–942 (1963).

99. Okazaki, S. Fundamental studies on the electrolysis with the glassy carbon column electrode. *Revie of Polarography,* 154–166 (1968).

100. Deinhammer, R. S., Ting, E.-T. & Porter, M. D. Electrochemically modulated liquid chromatography (EMLC): A new approach to gradient elution separation. *J. Electroanal. Chem.,* 295–299 (1993).

101. Fujinaga, T. Electrolytic chromatography and coloumetric detection with the column electrode. *Pure Appl. Chem.,* 709–726 (1971).

102. Wang, J. Reticulated virteous carbon - A new versatile electrode material. *Electrochim. Acta,* 1721–1726 (1981).

103. Antrim, R. F., Scherrer, R. A. & Yacynych, A. M. Electrochromatography - A preliminary study of the effect of applied potential on a carbonaceous chromatographic column. *Anal. Chim. Acta,* 283–286 (1984).

104. Ge, H. & Wallace, G. G. Characterization of conducting polymeric stationary phases and electrochemically controlled high-performance liquid chromatography. *Anal. Chem.,* 2391–2394 (1989).

105. Abdel-Latif, M. S. & Porter, M. D. Potentiostatic and galvanostatic modulation of liquid chromatography. *J. Liq. Chromatogr. Relat. Technol.* **21,** 2281–2296 (1998).

106. Ting, E.-T. & Porter, M. D. Separation of benzodiazepines using electrochemically modulated liquid chromatography: Efficient separations from changes in the voltage applied to a porous graphitic carbon stationary phase. *J. Chrom. A,* 204–208 (1998).

107. Keller, D. W. *Electrochemically modulated liquid chromatography: Theoretical investigations and apllications from the perspectives of chromatography and interfacial electrochemistry* Dissertation (Iowa State University, Iowa, 2005).

108. Yakes, B. J., Keller, D. W. & Porter, M. D. Electrochemically modulated liquid chromatographic separation of triazines and the effect of pH on retention. *J. Chromatogr. A* **1217,** 4395–4401 (2010).

109. Nagaoka, T., Kakao, N., Tabusa, K., Yano, J. & Ogura, K. Dynamic elution control in electrochemical ion chromatography using pulse pertubation of stationary phase potential. *J. Electroanal. Chem.,* 283–286 (1994).

110. Meyer, R. E. & Posey, F. A. Separation and analysis of iodide, bromide, and chloride ions with the packed-bed silver electrode. *J. Electroanal. Chem. Interf. Electrochem.,* 377–386 (1974).

111. Eggli, R. Electrochemical flow-through detector for the determination of cystine and related compounds. *Anal. Chim. Acta,* 253–259 (1978).

112. Muna, G. W., Swope, V. M., Swain, G. M. & Porter, M. D. Electrochemically modulated liquid chromatography using a boron-doped diamond particle stationary phase. *Journal of chromatography. A* **1210,** 154–159 (2008).

113. Saitoh, K., Koichi, K., Yabiku, F., Noda, Y., Porter, M. D. & Shibukawa, M. On-column electrochemical redox derivatization for enhancement of separation selectivity of liquid chromatography: Use of redox reaction as secondary chemical equilibrium. *J. Chromatogr. A,* 66–72 (2008).

114. Ge, H. & Wallace, G. G. Electrochemically controlled liquid chromatography on conducting polymer stationary phases. *J. Liq. Chromatogr.* **13,** 3245–3260 (1990).

115. Deinhammer, R. S., Porter, M. D. & Shimazu, K. Retention characteristics of polypyrrole as a stationary phase for the electrochemically modulated liquid chromatographic (EMLC) separations of dansyl amino acids. *J. Electroanal. Chem.,* 35–46 (1995).

116. Abdel-Latif, M. S. & Porter, M. D. Effect of electrolytes on the retention behavior of some benzenesulfonates in electrochemically modulated liquid chromatography. *Talanta,* 681–687 (1998).

117. Weisshaar, D. E. & Porter, M. D. Site-specific voltage control of adsorption on glassy carbon electrodes. *Electrochem. Commun.,* 758–761 (2001).

118. Ting, E.-T. *Electrochemically-modulated liquid chromatography (EMLC): Column design, retention processes, and application* Dissertation (Iowa State University, Iowa, 1997).

119. Deng, H., van Berkel, G. J., Takano, H., Gazda, D. & Porter, M. D. Electrochemically modulated liquid chromatography coupled on-line with electrospray mass spectrometry. *Anal. Chem.* **72,** 2641–2647 (2000).

120. Chu, A. K., Fleischmann, M. & Hills, G. J. Packed bed electrodes: The electrochemical extraction of copper ions from dilute aqueous solutions. *J. Appl. Electrochem.,* 323–330 (1974).

121. Tsuda, T. Chromatographic behavior in electrochromatography. *Anal. Chem.,* 1677–1680 (1988).

122. Antrim, R. F. & Yacynych, A. M. The effect of supporting electrolytes in electrochromatography. *Anal. Lett.* **21,** 1085–1096 (1988).

123. Abdel-Latif, M. S. & Porter, M. D. Effects of electrolytes on manipulation of the stationary phase in electrochemically modulated liquid chromatography. *Anal. Lett.* **31,** 1743–1756 (1998).

124. Ponton, L. M. & Porter, M. D. Electrochemically modulated liquid chromatographic separations of inorganic anions. *J. Chromatogr. A* **1059,** 103–109 (2004).

125. Ponton, L. M. & Porter, M. D. High-speed electrochemically modulated liquid chromatography. *Anal. Chem.,* 5823–5828 (2004).

126. Ponton, L. M., Keller, D. W., Siperko, L. M., Hayes, M. A. & Porter, M. D. Investigation of adsorption thermodynamics at electrified liquid–solid interfaces by electrochemically modulated liquid chromatography. *J. Phys. Chem. C* **123,** 28148–28157 (2019).

127. Soto, R. J., Hayes, M. A. & Porter, M. D. Electrochemically modulated liquid chromatography in fused silica capillary columns. *Anal. Chem.* **91,** 13994–14001 (2019).

128. Future Carbon GmbH. *Material properties CNT-K: E-Mail* (ed Bioseparation Engineering Group, attn. Tatjana Trunzer) 15.01.2018.

129. Schwaminger, S. P., Begovic, B., Schick, L., Jumani, N. A., Brammen, M. W., Fraga-García, P. & Berensmeier, S. Potential-controlled tensiometry: A tool for understanding wetting and surface properties of conductive powders by electroimbibition. *Anal. Chem.* **90,** 14131–14136 (2018).

130. Lützenkirchen, J., Preočanin, T., Kovačević, D., Tomišić, V., Lövgren, L. & Kallay, N. Potentiometric titrations as a tool for surface charge determination. *Croat. Chem. Acta* **85,** 391–417 (2012).

131. GoSilico GmbH. *ChromX* 2021. `https://gosilico.com/chromx/`.

132. GoSilico GmbH. *ChromX: User's Guide* (ed GoSilico GmbH) 16.04.2021. `https://gosilico.com/chromx`.

133. Obradović, M. D., Vuković, G. D., Stevanović, S. I., Panić, V. V., Uskoković, P. S., Kowal, A. & Gojković, S. A comparative study of the electrochemical properties of carbon nanotubes and carbon black. *J. Electroanal. Chem.* **634,** 22–30 (2009).

134. Gu, W. & Yushin, G. Review of nanostructured carbon materials for electrochemical capacitor applications: Advantages and limitations of activated carbon, carbide-derived carbon, zeolite-templated carbon, carbon aerogels, carbon nanotubes, onion-like carbon, and graphene. *WIREs Energy Environ* **3,** 424–473 (2014).

135. Jia, B. & Zhang, W. Preparation and application of electrodes in capacitive Deionization (CDI): A state-of-art review. *Nanoscale Res. Lett.* **11,** 64 (2016).

136. Membranes International Inc. *CMI-7000 Cation Exchange Membranes: Technical specifications* (ed Membranes International Inc.) 14.04.2021. `ionexchangemembranes.com`.

137. Su, X. & Hatton, T. A. Electrosorption at functional interfaces: From molecular-level interactions to electrochemical cell design. *PCCP* **19,** 23570–23584 (2017).

138. Pan, L., Wang, X., Gao, Y., Zhang, Y., Chen, Y. & Sun, Z. Electrosorption of anions with carbon nanotube and nanofibre composite film electrodes. *Desalination* **244,** 139–143 (2009).

139. LI, L.-X. & LI, F. The effect of carbonyl, carboxyl and hydroxyl groups on the capacitance of carbon nanotubes. *New Carbon Mater.* **26,** 224–228 (2011).

140. Ye, J.-S., Liu, X., Cui, H. F., Zhang, W.-D., Sheu, F.-S. & Lim, T. M. Electrochemical oxidation of multi-walled carbon nanotubes and its application to electrochemical double layer capacitors. *Electrochem. Commun.* **7,** 249–255 (2005).

141. Dai, K., Shi, L., Fang, J., Zhang, D. & Yu, B. NaCl adsorption in multi-walled carbon nanotubes. *Materials Letters* **59,** 1989–1992 (2005).

142. Yang, K.-L., Yiacoumi, S. & Tsouris, C. Electrosorption capacitance of nanostructured carbon aerogel obtained by cyclic voltammetry. *J. Electroanal. Chem.,* 159–167 (2003).

143. Han, B., Cheng, G., Wang, Y. & Wang, X. Structure and functionality design of novel carbon and faradaic electrode materials for high-performance capacitive deionization. *Chem. Eng. J.* **360,** 364–384 (2019).

144. Zhan, Y., Nie, C., Li, H., Pan, L. & Sun, Z. Kinetics and isotherm studies on electrosorption of NaCl by activated carbon fiber, carbon nanotube and carbon nanotube-carbon nanofiber composite film. *Phys. Status Solidi C* **9,** 55–58 (2012).

145. Birch, M. E., Ruda-Eberenz, T. A., Chai, M., Andrews, R. & Hatfield, R. L. Properties that influence the specific surface areas of carbon nanotubes and nanofibers. *Ann. Occup. Hyg.* **57,** 1148–1166 (2013).

146. Lee, J., Kim, M., Hong, C. K. & Shim, S. E. Measurement of the dispersion stability of pristine and surface-modified multiwalled carbon nanotubes in various nonpolar and polar solvents. *Meas. Sci. Technol.* **18,** 3707–3712 (2007).

147. Hodge, S. A., Fogden, S., Howard, C. A., Skipper, N. T. & Shaffer, M. S. P. Electrochemical processing of discrete single-walled carbon nanotube anions. *ACS nano* **7,** 1769–1778 (2013).

148. Lee, H. D., Yoo, B. M., Lee, T. H. & Park, H. B. Defect-free surface modification methods for solubility-tunable carbon nanotubes. *J. Colloid Interf. Sci.* **509,** 307–317 (2018).

149. Wang, L., Wang, M., Huang, Z.-H., Cui, T., Gui, X., Kang, F., Wang, K. & Wu, D. Capacitive deionization of NaCl solutions using carbon nanotube sponge electrodes. *J. Mater. Chem.* **21,** 18295 (2011).

150. Kharissova, O. V. & Kharisov, B. I. Variations of interlayer spacing in carbon nanotubes. *RSC Adv.* **4,** 30807–30815 (2014).

151. Belin, T. & Epron, F. Characterization methods of carbon nanotubes: A review. *Mater. Sci. Eng., B* **119,** 105–118 (2005).

152. Gogotsi, Y., Naguib, N. & Libera, J. In situ chemical experiments in carbon nanotubes. *Chem. Phys. Lett.* **365,** 354–360 (2002).

153. Li, H., Kang, W., Yu, Y., Liu, J. & Qian, Y. Synthesis of bamboo-structured carbon nanotubes and honeycomb carbons with long-cycle Li-storage performance by in situ generated zinc oxide. *Carbon* **50,** 4787–4793 (2012).

154. Peigney, A., Laurent, C., Flahaut, E., Bacsa, R. R. & Rousset, A. Specific surface area of carbon nanotubes and bundles of carbon nanotubes. *Carbon* **39,** 507–514 (2001).

155. Minnikanti, S., Skeath, P. & Peixoto, N. Electrochemical characterization of multiwalled carbon nanotube coated electrodes for biological applications. *Carbon* **47,** 884–893 (2009).

156. Ebbesen, T. W. & Takada, T. Topological and SP3 defect structures in nanotubes. *Carbon* **33,** 973–978 (1995).

157. Iijima, S., Brabec, C., Maiti, A. & Bernholc, J. Structural flexibility of carbon nanotubes. *J. Chem. Phys.* **104,** 2089–2092 (1996).

158. Yi, Y., Tornow, J., Willinger, E., Willinger, M. G., Ranjan, C. & Schlögl, R. Electrochemical degradation of multiwall carbon nanotubes at high anodic potential for oxygen evolution in acidic media. *ChemElectroChem* **2,** 1929–1937 (2015).

159. Shanmugam, S. & Gedanken, A. Generation of hydrophilic, bamboo-shaped multiwalled carbon nanotubes by solid-state pyrolysis and its electrochemical studies. *J. Phys. Chem. B* **110,** 2037–2044 (2006).

160. Ma, W., Zhou, Z., Li, G. & Li, P. Effect of catalyst film thickness on growth morphology, surface wettability and drag reduction property of carbon nanotubes. *High Temp. Mater. Proc.* **35,** 857–863 (2016).

161. Tzeng, Y., Chen, Y., Sathitsuksanoh, N. & Liu, C. Electrochemical behaviors and hydration properties of multi-wall carbon nanotube coated electrodes in water. *Diam. Relat. Mater.* **13,** 1281–1286 (2004).

162. Walther, J. H., Jaffe, R., Halicioglu, T. & Koumoutsakos, P. Carbon nanotubes in water: Structural characteristics and energetics. *J. Phys. Chem. B* **105,** 9980–9987 (2001).

163. Muratov, D. S., Stolyarov, R. A. & Gromov, S. V. Surface structure and adsorption characteristics of COOH-functionalized multi-wall carbon nanotubes. *BioNanoSci.* **8,** 668–674 (2018).

164. Zajíčková, L., Kučerová, Z., Buršíková, V., Eliáš, M., Houdková, J., Synek, P., Maršíková, H. & Jašek, O. Carbon nanotubes functionalized in oxygen and water low pressure discharges used as reinforcement of polyurethane composites. *Plasma Processes Polym.* **6,** S864–S869 (2009).

165. Frackowiak, E., Metenier, K., Bertagna, V. & Beguin, F. Supercapacitor electrodes from multiwalled carbon nanotubes. *Appl. Phys. Lett.* **77,** 2421–2423 (2000).

166. Ndunda, E. N. & Mizaikoff, B. Multi-walled carbon nanotubes: innovative sorbents for pre-concentration of polychlorinated biphenyls in aqueous environments. *Anal. Methods* **7,** 8034–8040 (2015).

167. Smith, B., Wepasnick, K., Schrote, K. E., Bertele, A. R., Ball, W. P., O'Melia, C. & Fairbrother, D. H. Colloidal properties of aqueous suspensions of acid-treated, multi-walled carbon nanotubes. *Environ. Sci. Technol.* **43,** 819–825 (2009).

168. Sydorchuk, V., Poddubnaya, O. I., Tsyba, M. M., Zakutevskyy, O., Khyzhun, O., Khalameida, S. & Puziy, A. M. Activated carbons with adsorbed cations as photocatalysts for pollutants degradation in aqueous medium. *Adsorption* **25,** 267–278 (2019).

169. Hameed, B. H., Tan, I. & Ahmad, A. L. Adsorption isotherm, kinetic modeling and mechanism of 2,4,6-trichlorophenol on coconut husk-based activated carbon. *Chem. Eng. J.* **144,** 235–244 (2008).

170. Rezvani, M., Najafpour, G. D., Mohammadi, M. & Zare, H. Amperometric biosensor for detection of triglyceride tributyrinbased on zero point charge of activated carbon. *Turk. J. Biol.* **41,** 268–277 (2017).

171. Kharissova, O. V., Kharisov, B. I. & Casas Ortiz, E. G. de. Dispersion of carbon nanotubes in water and non-aqueous solvents. *RSC Adv.* **3,** 24812 (2013).

172. Yang, K. & Xing, B. Adsorption of organic compounds by carbon nanomaterials in aqueous phase: Polanyi theory and its application. *Chem. Re* **110,** 5989–6008 (2010).

173. Woodard, F. E., McMackins, D. E. & Jansson, R. Electrosorption of organics on three dimensional carbon fiber electrodes. *J. Electroanal. Chem. Interf. Electr.* **214,** 303–330 (1986).

174. Tomo, Y., Askounis, A., Ikuta, T., Takata, Y., Sefiane, K. & Takahashi, K. Superstable ultrathin water film confined in a hydrophilized carbon nanotube. *Nano Lett.* **18,** 1869–1874 (2018).

175. Kyakuno, H., Fukasawa, M., Ichimura, R., Matsuda, K., Nakai, Y., Miyata, Y., Saito, T. & Maniwa, Y. Diameter-dependent hydrophobicity in carbon nanotubes. *J. Chem. Phys.* **145,** 064514 (2016).

176. Pang, L. S. K., Saxby, J. D. & Chatfield, S. P. Thermogravimetric analysis of carbon nanotubes and nanoparticles. *J. Phys. Chem.* **97,** 6941–6942 (1993).

177. Butyrskaya, E. V., Zapryagaev, S. A. & Izmailova, E. A. Cooperative model of the histidine and alanine adsorption on single-walled carbon nanotubes. *Carbon* **143,** 276–287 (2019).

178. Balavoine, F., Schultz, P., Richard, C., Mallouh, V., Ebbesen, T. W. & Mioskowski, C. Helical crystallization of proteins on carbon nanotubes: A first step towards the development of new biosensors. *Angew. Chem. Int. Ed.* **38,** 1912–1915 (1999).

179. Balamurugan, K. & Subramanian, V. Length–dependent stability of alpha–helical peptide upon adsorption to single–walled carbon nanotube. *Biopolymers* **99,** 357–369 (2013).

180. Vardanega, D. & Picaud, F. Detection of amino acids encapsulation and adsorption with dielectric carbon nanotube. *J. Biotechnol.* **144,** 96–101 (2009).

181. Al Garalleh, H., Thamwattana, N., Cox, B. J. & Hill, J. M. Encapsulation of L-Histidine amino acid inside single-walled carbon nanotubes. *J. Biomater. Tissue Eng.* **6,** 362–369 (2016).

182. Al Garalleh, H., Garaleh, M. & Alabadleh, G. Mathematical model for the encapsulation of Alanine amino acid inside a single-walled carbon nanotube. *Adsorption* (2019).

183. Chang, C. M. & Jalbout, A. F. Metal induced amino acid adsorption on nanotubes. *Thin Solid Films* **518,** 2070–2076 (2010).

184. Li, S., Li, H., Wang, X., Song, Y., Liu, Y., Jiang, L. & Zhu, D. Super-hydrophobicity of large-area honeycomb-like aligned carbon nanotubes. *J. Phys. Chem. B* **106,** 9274–9276 (2002).

185. Cohen, I., Avraham, E., Bouhadana, Y., Soffer, A. & Aurbach, D. The effect of the flow-regime, reversal of polarization, and oxygen on the long term stability in capacitive de-ionization processes. *Electrochim. Acta* **153,** 106–114 (2015).

186. Schrader, C. *OCP and pzc: E-Mail* (ed Bioseparation Engineering Group, attn. Tatjana Trunzer) 7.11.2019.

187. Sun, Z., Chai, L., Shu, Y., Li, Q., Liu, M. & Qiu, D. Chemical bond between chloride ions and surface carboxyl groups on activated carbon. *Colloids Surf. A* **530,** 53–59 (2017).

188. Sun, Z., Li, Q., Chai, L., Shu, Y., Wang, Y. & Qiu, D. Effect of the chemical bond on the electrosorption and desorption of anions during capacitive deionization. *Chemosphere* **229,** 341–348 (2019).

189. Otero, T. F., Martinez, J. G. & Asaka, K. Faradaic and capacitive components of the CNT electrochemical responses. *Front. Mater.* **3,** 358 (2016).

190. Barisci, J. N., Spinks, G. M., Wallace, G. G., Madden, J. D. & Baughman, R. H. Increased actuation rate of electromechanical carbon nanotube actuators using potential pulses with resistance compensation. *Smart Mat. Struct.* **12,** 549–555 (2003).

191. Chen, J. H., Li, W. Z., Wang, D. Z., Yang, S. X., Wen, J. G. & Ren, Z. F. Electrochemical characterization of carbon nanotubes as electrode in electrochemical double-layer capacitors. *Carbon,* 1193–1197 (2002).

192. Mustafa, I., Al Shehhi, A., Al Hammadi, A., Susantyoko, R., Palmisano, G. & Almheiri, S. Effects of carbonaceous impurities on the electrochemical activity of multiwalled carbon nanotube electrodes for vanadium redox flow batteries. *Carbon* **131,** 47–59 (2018).

193. Barisci, J. N., Wallace, G. G. & Baughman, R. H. Electrochemical studies of single-wall carbon nanotubes in aqueous solutions. *J. Electroanal. Chem.,* 92–98 (2000).

194. Boehm, H. P. Surface oxides on carbon and their analysis: A critical assessment. *Carbon* (2002).

195. Li, H., Pan, L., Lu, T., Zhan, Y., Nie, C. & Sun, Z. A comparative study on electrosorptive behavior of carbon nanotubes and graphene for capacitive deionization. *J. Electroanal. Chem.* **653,** 40–44 (2011).

196. Su, X. & Hatton, T. A. Redox-electrodes for selective electrochemical separations. *Adv. Colloid Interface Sci.* **244,** 6–20 (2017).

197. Tang, K., Yiacoumi, S., Li, Y. Gabitto, J. & Tsouris, C. Optimal conditions for efficient flow-electrode capacitive deionization. *Sep. Purif.* **240,** 116626 (2020).

198. Tanigaki, N., Murata, K., Kukobat, R., Futamura, R., Hayashi, T. & Kaneko, K. Electric field assisted ion adsorption with nanoporous SWCNT electrodes. *Adsorption* **25,** 1035–1041 (2019).

199. Kihara, S. Analytical chemical studies on electrode processes by column coulometry: Basic studies on the column electrode. *J. Electroanal. Chem.,* 31–44 (1973).

200. Huang, G.-H., Chen, T.-C., Hsu, S.-F., Huang, Y.-H. & Chuang, S.-H. Capacitive deionization (CDI) for removal of phosphate from aqueous solution. *Desalination Water Treat.* **52,** 759–765 (2014).

201. Rommerskirchen, A., Kalde, A., Linnartz, C. J., Bongers, L., Linz, G. & Wessling, M. Unraveling charge transport in carbon flow-electrodes: Performance prediction for desalination applications. *Carbon* **145,** 507–520 (2019).

202. Li, J., Pham, P. H. Q., Zhou, W., Pham, T. D. & Burke, P. J. Carbon-nanotube-electrolyte interface: Quantum and electric double layer capacitance. *ACS nano* **12,** 9763–9774 (2018).

203. Sun, Z., Chai, L., Liu, M., Shu, Y., Li, Q., Wang, Y. & Qiu, D. Effect of the electronegativity on the electrosorption selectivity of anions during capacitive deionization. *Chemosphere* **195,** 282–290 (2018).

204. Bán, A., Schäfer, A. & Wendt, H. Fundamentals of electrosorption on activated carbon for wastewater treatment of industrial effluents. *J. Appl. Electrochem.,* 227–236 (1998).

205. Mirmohseni, A., Price, W. E. & Wallace, G. G. Electrochemically controlled transport of small charged organic molecules across conducting polymer membranes. *J. Membrane Sci.,* 239–248 (1995).

206. Grahame, D. C. Diffuse double layer theory for electrolytes of unsymmetrical valence types. *J. Chem. Phys.* **21,** 1054–1060 (1953).

207. Chang, L., Zhou, Y. & Duan, X. Kinetics and equilibrium studies on the electrosorption of anions with activated carbon electrodes. *Desalination Water Treat.* **52,** 6549–6555 (2014).

208. Gao, Y., Pan, L., Li, H., Zhang, Y., Zhang, Z., Chen, Y. & Sun, Z. Electrosorption behavior of cations with carbon nanotubes and carbon nanofibres composite film electrodes. *Thin Solid Films* **517,** 1616–1619 (2009).

209. Zhang, X., Zuo, K., Zhang, X., Zhang, C. & Liang, P. Selective ion separation by capacitive deionization (CDI) based technologies: a state-of-the-art review. *Environ. Sci.: Water Res. Technol.* **6,** 243–257 (2020).

210. Nikitas, P. A thermodynamic method for the determination of the adsorbed layer thickness and the size ratio parameter. *J. Electroanal. Chem.,* 147–154 (1988).

211. Hassanvand, A., Chen, G. Q., Webley, P. A. & Kentish, S. E. A comparison of multicomponent electrosorption in capacitive deionization and membrane capacitive deionization. *Water research* **131,** 100–109 (2018).

212. Mubita, T. M., Dykstra, J. E., Biesheuvel, P. M., van der Wal, A. & Porada, S. Selective adsorption of nitrate over chloride in microporous carbons. *Water research* **164,** 114885 (2019).

213. Chen, Z., Zhang, H., Wu, C., Wang, Y. & Li, W. A study of electrosorption selectivity of anions by activated carbon electrodes in capacitive deionization. *Desalination* **369,** 46–50 (2015).

214. Manilo, M. V., Lebovka, N. I. & Barany, S. Effects of sort and concentration of salts on the electrosurface properties of aqueous suspensions containing hydrophobic and hydrophilic particles: Validity of the Hofmeister series. *J. Mol. Liq* **276,** 875–884 (2019).

215. Chen, R. J., Zhang, Y., Wang, D. & Dai, H. Noncovalent sidewall functionalization of single-walled carbon nanotubes for protein immobilization. *J. Am. Chem. Soc.* **123,** 3838–3839 (2001).

216. Bayer MaterialScience. *Sicherheitsdatenblatt: Baytubes C 150 P*

217. Future Carbon GmbH. *EG-Sicherheitsdatenblatt: CNT-K* (ed Future Carbon GmbH)

218. Nie, C., Pan, L., Li, H., Chen, T., Lu, T. & Sun, Z. Electrophoretic deposition of carbon nanotubes film electrodes for capacitive deionization. *J. Electroanal. Chem.* **666,** 85–88 (2012).

219. Chriswanto, H., Teasdale, P. R. & Wallace, G. G. Characterisation of processes occurring at electrodynamic interfaces. *MSF* **189-190,** 179–184 (1995).

220. Song, Z., Miao, L., Li, L., Zhu, D., Lv, Y., Xiong, W., Duan, H., Wang, Z., Gan, L. & Liu, M. A universal strategy to obtain highly redox-active porous carbons for efficient energy storage. *J. Mater. Chem. A* **8,** 3717–3725 (2020).

221. Xie, J., Ma, J., Wu, L., Xu, M., Ni, W. & Yan, Y.-M. Carbon nanotubes in-situ cross-linking the activated carbon electrode for high-performance capacitive deionization. *Sep. Purif.* **239,** 116593 (2020).

222. Lynam, C., Grosse, W. & Wallace, G. G. Carbon-nanotube biofiber microelectrodes. *J. Electrochem. Soc.* **156,** P117 (2009).

223. Sun, L., Wang, X., Wang, Y. & Zhang, Q. Roles of carbon nanotubes in novel energy storage devices. *Carbon* **122,** 462–474 (2017).

224. Du, R., Zhao, Q., Zhang, N. & Zhang, J. Macroscopic carbon nanotube-based 3D monoliths. *Small* **11,** 3263–3289 (2015).

225. Lenz, M., Wagner, R., Hack, E. & Franzreb, M. Object-oriented modeling of a capacitive deionization process. *Front. Chem. Eng.* **2** (2020).

List of Figures

List of Tables

A Supplementary Information

The supplementary information presents results that support the complex research work and enlarge the discussion in Chapter 5.

A.1 State-of-the-Art

The percentage weighting of different research approaches on potential-controlled chromatography (PCC) or electrochemical modulated liquid chromatography (EMLC) is illustrated in Figure A.1 and enhances the summary presented in Table 3.1.

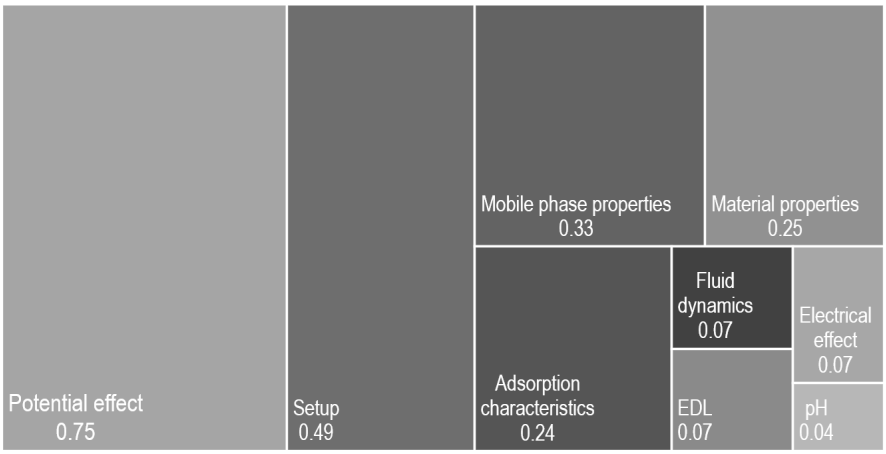

Figure A.1: Illustration about the percental weighting of the publications that build on potential-controlled chromatography or electrochemical modulated liquid chromatography. The illustration enhances Table 3.1.

A.2 Theoretical Basics

The chemical structures of different analytes are imprinted in the Figures A.2 and A.3. Table A.1 summarizes the acidic and basic constants and the pI-value of the different analytes used. The number of protonation states can be transferred from the equilibrium constants.

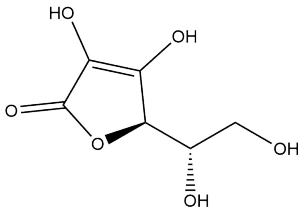

(a) Ascorbic acid.

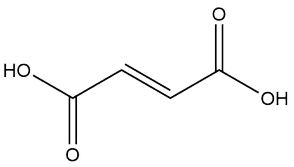

(b) Fumaric acid.

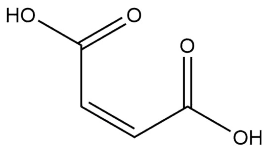

(c) Maleic acid.

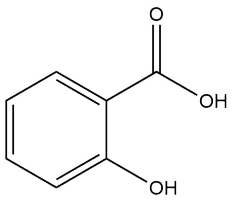

(d) Salicylic acid.

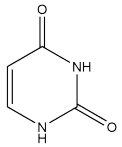

Uracil

(e) Uracil.

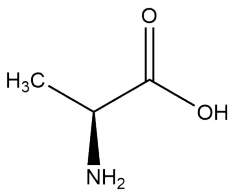

(f) Alanine.

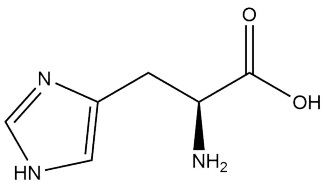

(g) Histidine.

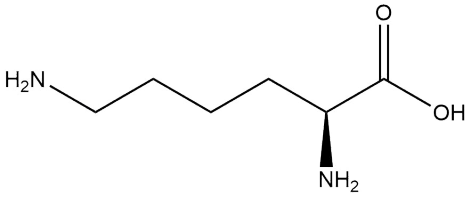

(h) Lysine.

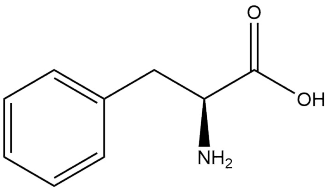

(i) Phenylalanine.

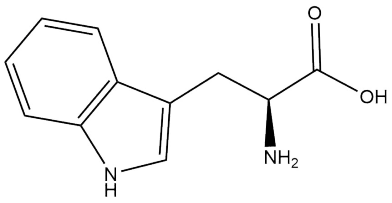

(j) Tryptophan.

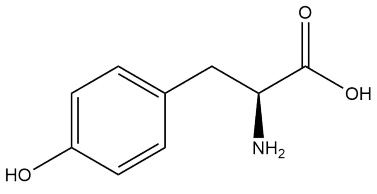

(k) Tyrosine.

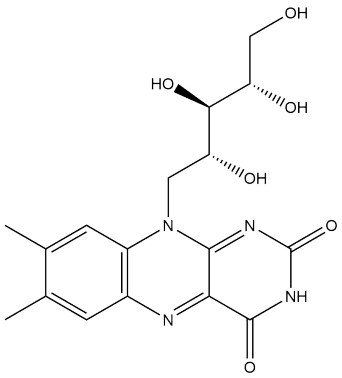

(l) Riboflavine.

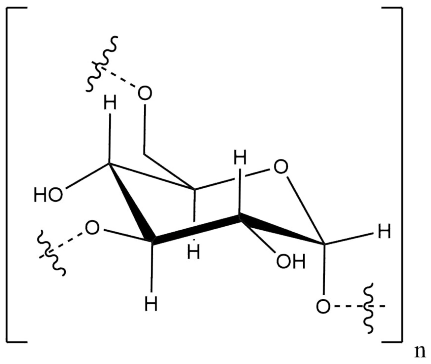

(m) Blue dextrane.

Figure A.2: Chemical structure of different organic analytes.

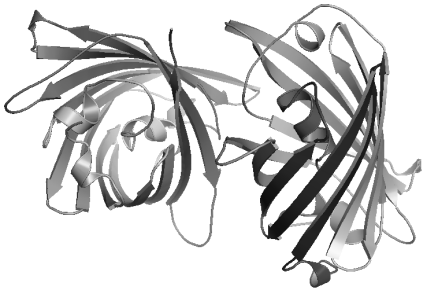

(a) GFP.

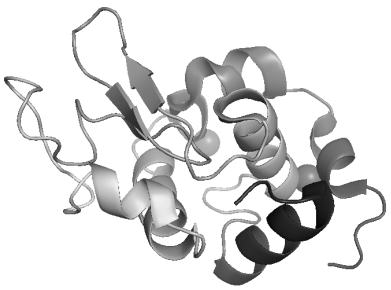

(b) Lysozyme.

Figure A.3: Chemical structure of two proteins.

Table A.1: Overview of the pK_a, pK_b and pI-value of different organic molecules. Exemplary protonation schemes can be found in Schemes 2.1 and 2.2.

Substance	$\mathbf{pK}_{a,1}$	$\mathbf{pK}_{a,2}$	$\mathbf{pK}_{a,2}$	$\mathbf{pK}_{COOH}$	**pI**	$\mathbf{pK}_{NH^{3+}}$	$\mathbf{pK}_{Sidechain}$
Ascorbic acid	4.3						
Maleic acid	1.9	6.5					
Fumaric acid	3.0	4.5					
Salicylic acid	2.8	12.4					
Phosphoric acid	2.1	7.2	12.4				
Alanine				2.3	6.1	9.9	
Histidine				1.8	7.6	9.1	6.0
Lysine				2.0	6.0	8.9	10.3
Phenylalanine				2.0	5.5	9.1	
Tryptophan				2.4	5.9	9.4	

A.3 Material and Methods

Figure A.4 depicts the single pieces of the PCC column used in and described in the Material and Methods Subsection (cf. Section 4.2).

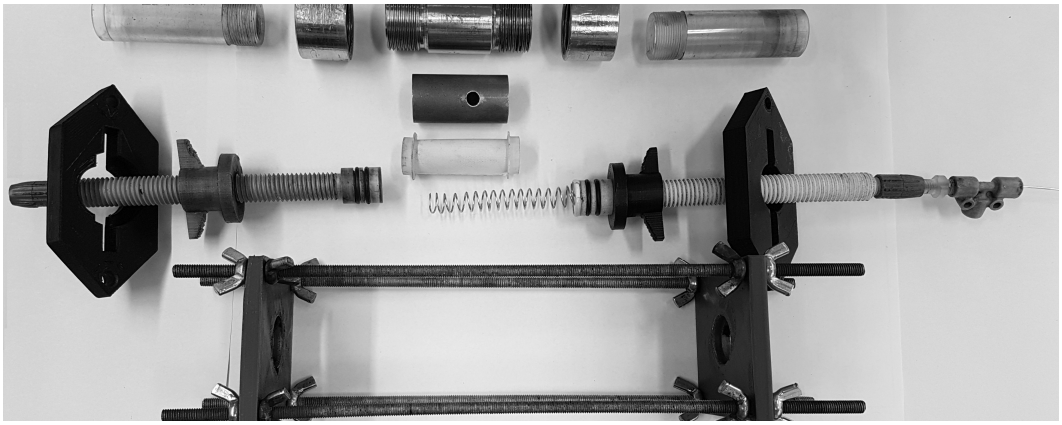

Figure A.4: Single pieces of the PCC column.

A.4 Proof-of-Concept

This Section complete Section 5.1 illustrating a potential-step and a potential-gradient experiment for an IoliTec-CNT packed bed column in Figure A.5.

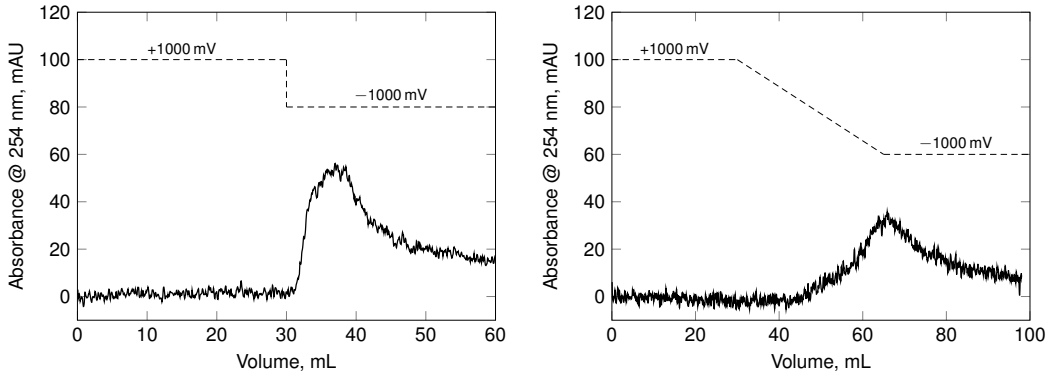

(a) Potential-Step. **(b)** Potential-gradient.

Figure A.5: Proof-of-concept for an IoLiTec-CNT packed bed electrode using maleic acid as a target analyte. (a) Potential-step experiment, (b) potential-gradient experiment. IoLiTec-CNT matrix, DI-water, 1.0 mL/min, 50 µL, 5 g/L maleic acid, pH 7, gradient −1 mV/s.

A.5 Material Characterization

This Section supports Section 5.2 with additional illustrations and data for the column and material characterization. Hence, Figure A.6 depicts various spectra of the EDX measurements of the CEX membrane and the stainless steel wire.

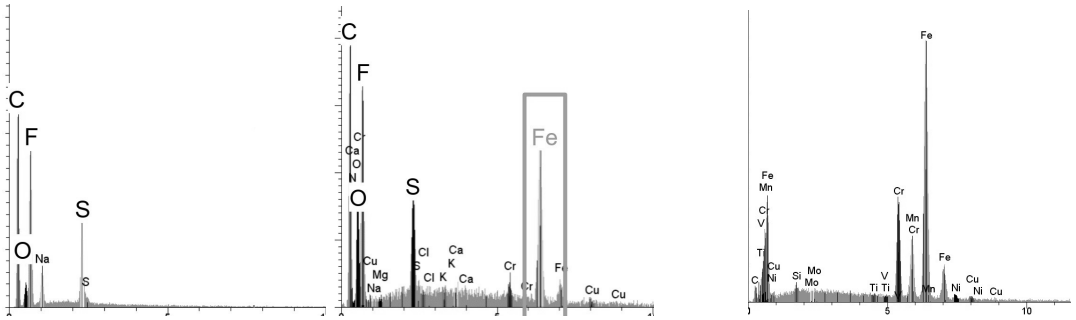

(a) Unused CEX membrane. **(b)** Used CEX membrane. **(c)** Stainless steel wire.

Figure A.6: Element screening of the CEX membrane and the stainless steel wire using EDX, before and after a column usage of over 500 working hours. Images taken by Marco Breidinger.

Figure A.7 represents the colored ash residue of the combusted CNT-K and IoLiTec-CNT material.

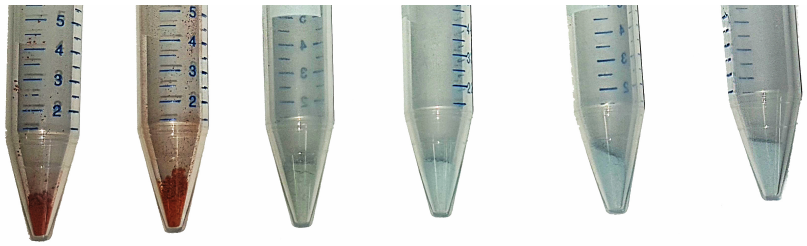

Figure A.7: Calcination of CNT-K and IoLiTec-CNT to analyze the ash residue. Muffle furnace, 700 °C, 1.5 h, from left: purified CNT-K, CNT-K powder, IoLiTec-CNT powder, purified IoLiTec-CNT, purified IoLiTec-CNT.

The next Figures summarize information about the material morphology and specific properties of the CNT-K (first subsection) and the IoLiTec-CNT (second subsection).

Morphology and Surface Properties of CNT-K

Figure A.8 illustrates the agglomerate size distribution of CNT-K. The particle size distribution for unused and used CNT-K is presented in Figure A.9. An illustration about end-capped and open-end CNT-K is depicted in Figure A.10, and different surface defects are highlighted in Figure A.11.

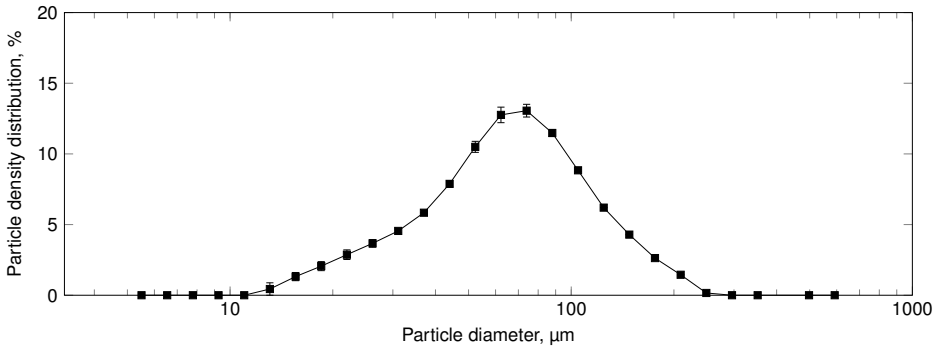

Figure A.8: CNT-K agglomerate size distribution in DI-water. Adapted from Trunzer *et al.* [18].

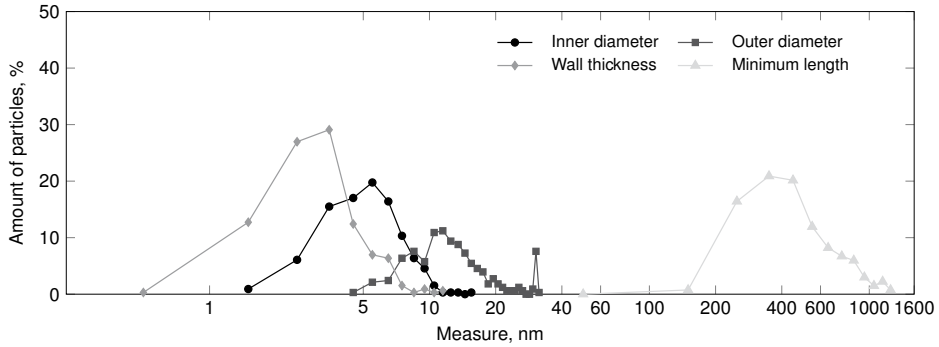

(a) CNT-K before use.

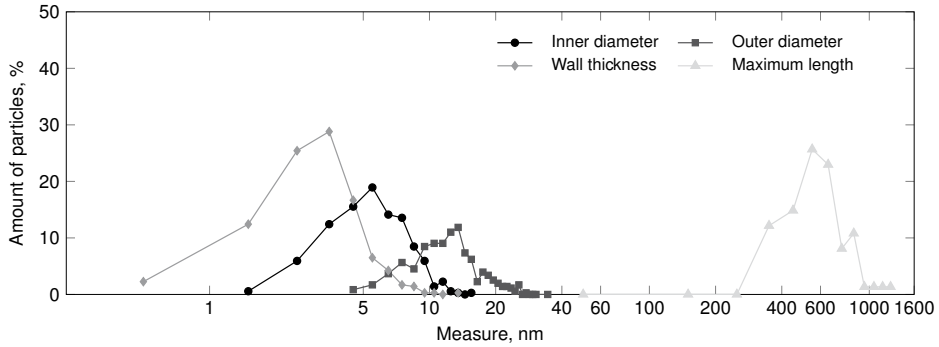

(b) CNT-K before use.

Figure A.9: CNT-K particle size distribution regarding the outer and inner diameter, the wall thickness and the maximum length to measure in TEM pictures. 330 particles counted for unused CNT-K, 355 particles counted for used CNT-K. Adapted and enlarged from Trunzer *et al.* [18].

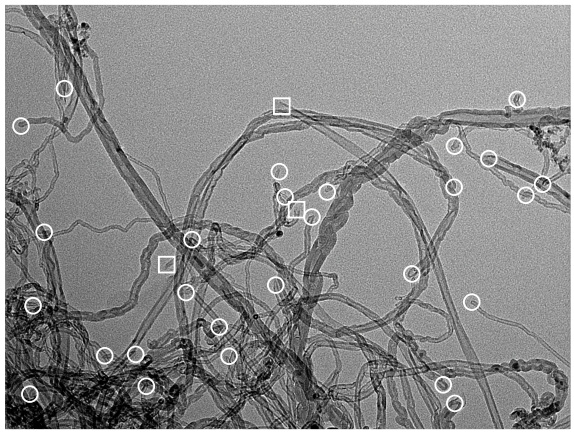

Figure A.10: End-capped CNT-K tubes (Image taken by Dr. Sebastian Schwaminger). Tubes without caps are marked with □, closed tubes are marked with ◯. Adapted from Trunzer *et al.* [18].

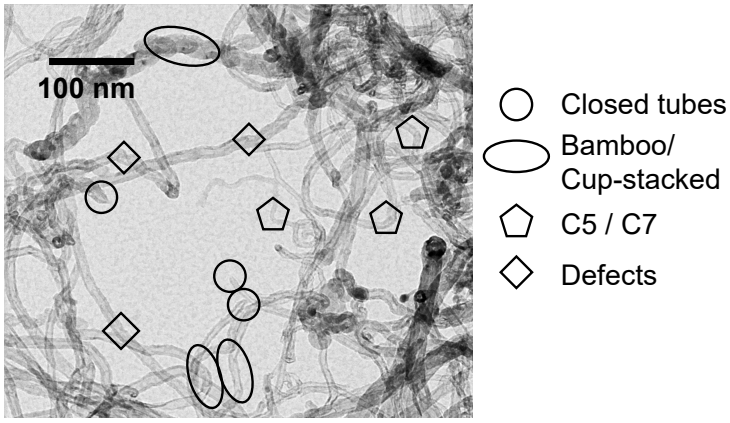

Figure A.11: Structural and surface defects of CNT-K. Image taken by Dr. Sebastian Schwaminger.

XPS spectra are illustrated in the Figures A.12 and A.13, highlighting the surface functionalization of CNT-K at different preparation conditions, an the corresponding balances.

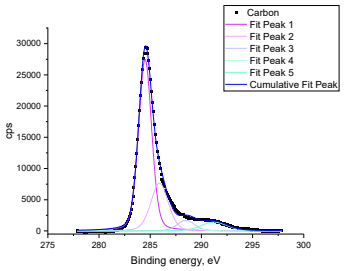

(a) Sample 1 - Carbon.

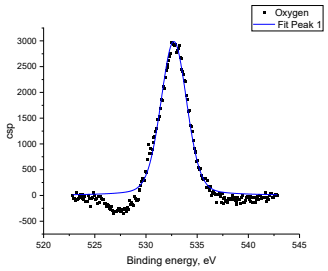

(b) Sample 1 - Oxygen.

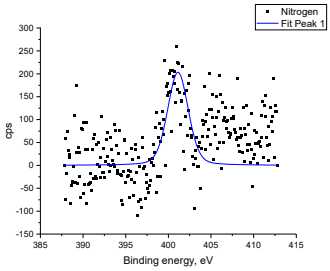

(c) Sample 1 - Nitrogen.

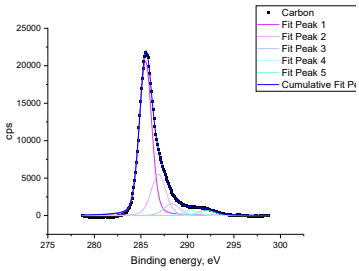

(d) Sample 2 - Carbon.

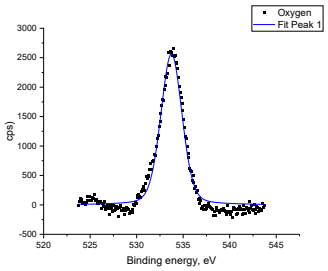

(e) Sample 2 - Oxygen.

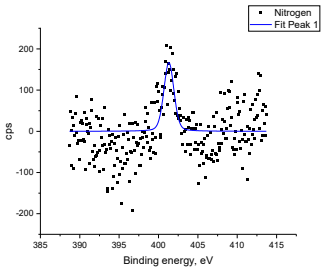

(f) Sample 2 - Nitrogen.

Figure A.12: XPS spectra to determine the surface constitution for differently treated CNT-K. C-C at 285 eV, C-O at 286 eV and C=O at 288 eV. O-C=O exist around 292 eV, and π-π at higher binding energies. Data taken with the support of Dr. Sebastian Schwaminger, Jasmin Heilingbrunner and Janine Raßloff. Adapted and enlarged from Trunzer *et al.* [18].

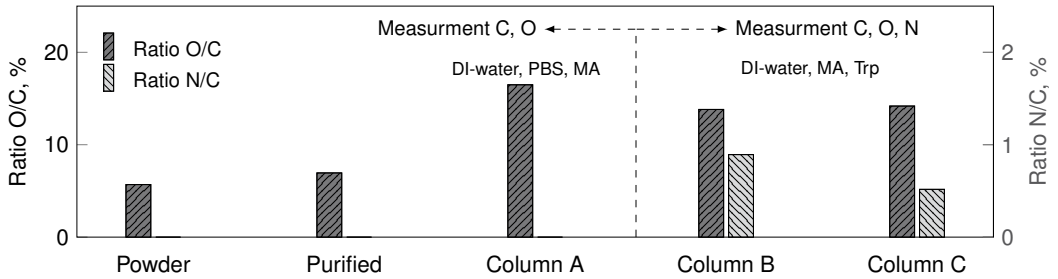

Figure A.13: Balance of the CNT-K surface elements calculated from XPS measurements in Figure A.12. Adapted and enlarged from Trunzer *et al.* [18].

Morphology and Surface Properties of IoLiTec-CNT

The morphology of the IoLiTec-CNT is visualized in the Figures A.14 and A.15.

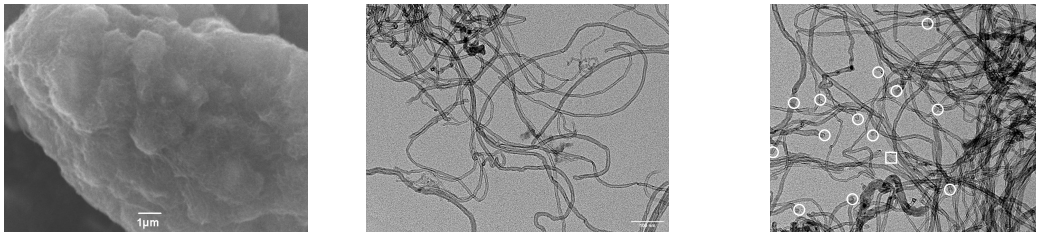

(a) Macroscale. **(b)** Microscale. **(c)** End capped tubes.

Figure A.14: Morphology of IoLiTec-CNT at different scales. (a) Macroscopic view (SEM taken by Ilse Schunn); (b) Microscopic view (TEM taken by Dr. Sebastian Schwaminger); (c) End-capped IoLiTeC-CNT (Image taken by Chiara Turrina). Open tubes □, closed tubes ◯.

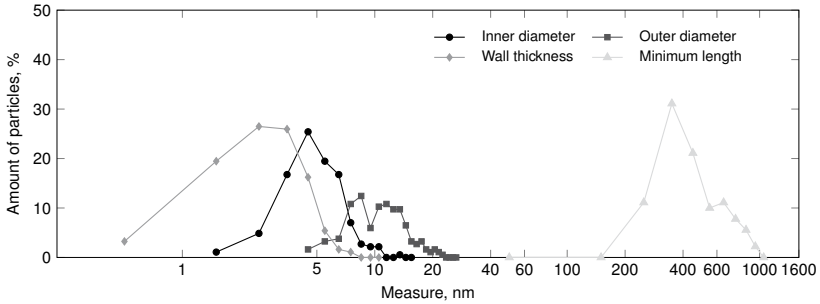

Figure A.15: IoLiTec-CNT particle size distribution of the outer and inner diameter, the wall thickness and the minimum length to measure in TEM pictures. 185 particles counted from TEM pictures.

Information about the XPS analysis are imprinted in Figure A.16 and Figure A.17.

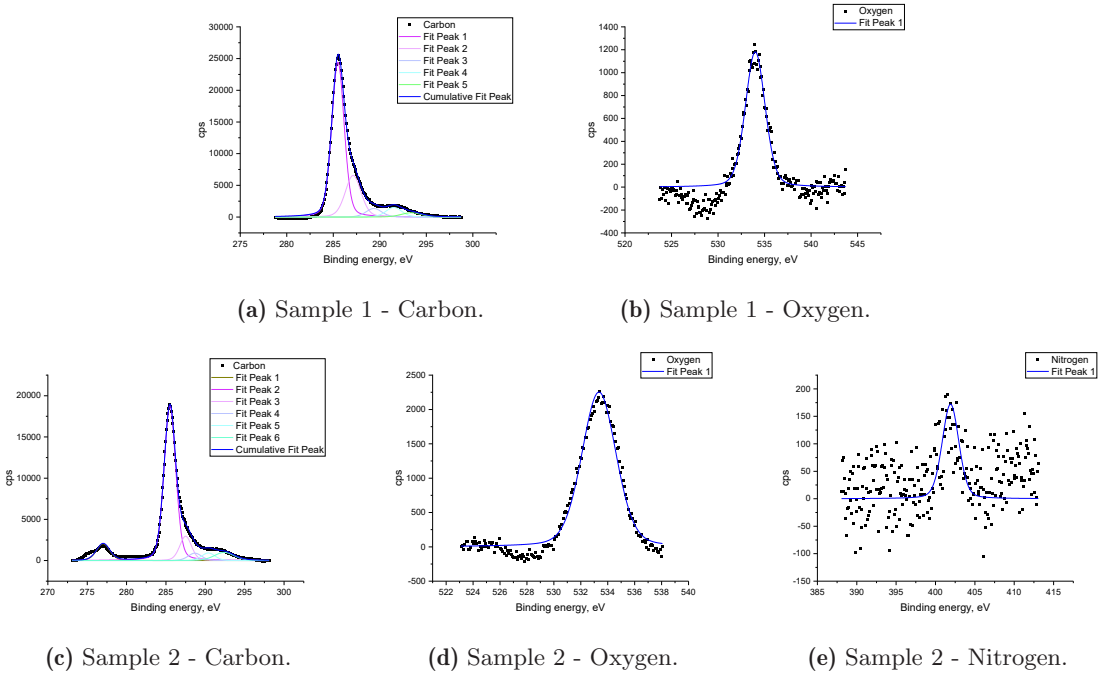

(a) Sample 1 - Carbon. **(b)** Sample 1 - Oxygen.

(c) Sample 2 - Carbon. **(d)** Sample 2 - Oxygen. **(e)** Sample 2 - Nitrogen.

Figure A.16: XPS spectra of IoLiTec-CNT to determine the surface constitution after different preparation conditions. XPS graphs for pristine and packed IoLiTec-CNT (see Figure A.17). C-C at 285 eV, C-O at 286 eV and C=O at 288 eV. Besides, O-C=O exist around 292 eV, and π-π at higher binding energies. Evaluated image taken with the support of Dr. Sebastian Schwaminger, Jasmin Heilingbrunner and Janine Raßloff.

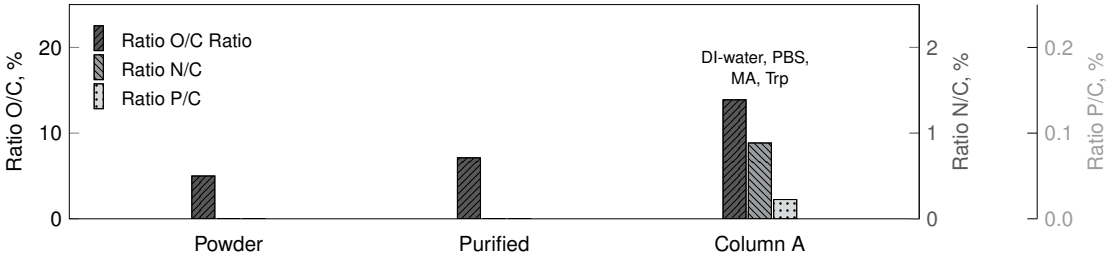

Figure A.17: XPS balance of IoLiTec-CNT. Evaluated image taken with the support of Dr. Sebastian Schwaminger, Jasmin Heilingbrunner and Janine Raßloff.

Determination of the IEP

Figure A.18 shows the titration curves and the charge distribution of both MWCNT species.

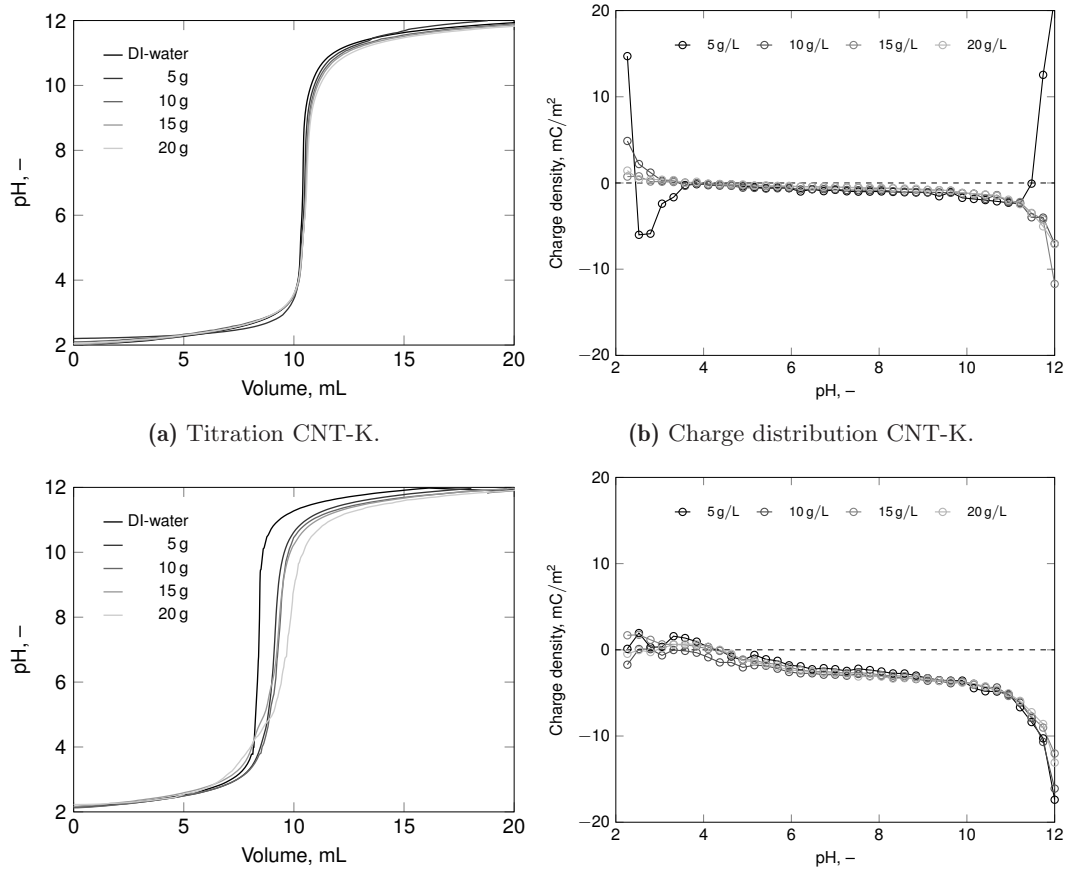

(a) Titration CNT-K.

(b) Charge distribution CNT-K.

(c) Titration IoLiTec-CNT.

(d) Charge distribution IoLiTec-CNT.

Figure A.18: Titration curves (a, c) and charge density distribution (b, d). CNT-K, IoLiTec-CNT, 0.1 M NaOH, 5 mL/min, pH = 2 to 12, experiment related to Lützenkirchen *et al.* [130].

pH-shift experiments for MWCNT surface characterization are depicted in Figure A.19. Figure A.20 highlights the material aging of the IoLiTec-CNT.

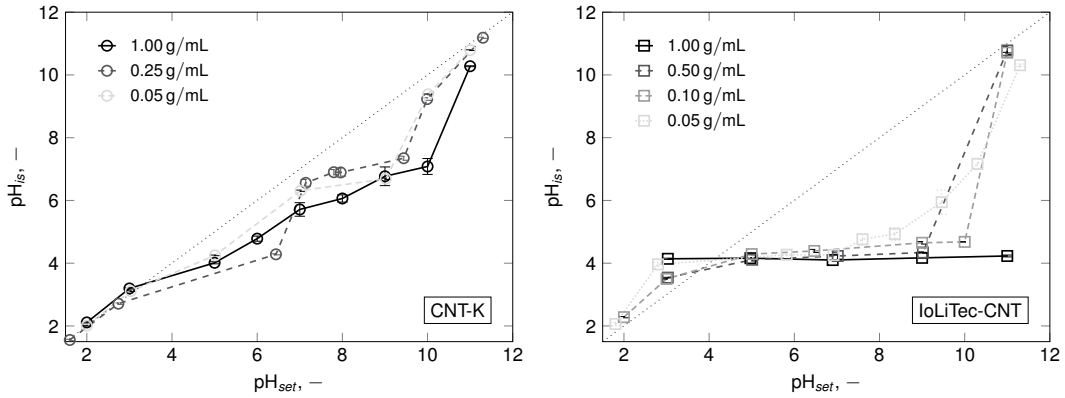

(a) CNT-K. **(b)** CNT-K.

Figure A.19: pH-shift experiments to determine the IEP. (a) CNT-K, 30 rpm; (b) IoLiTec-CNT, 200 rpm. RT, <40 h.

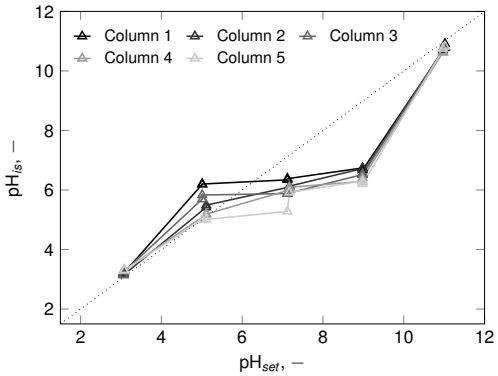

Figure A.20: pH-shift experiments to determine the IEP after aging. IoLiTec-CNT, 0.5 g, 40 h, RT.

CNT-K and Water

The water adsorption factor for CNT-K and other adsorbents is imprinted in Figure A.21.

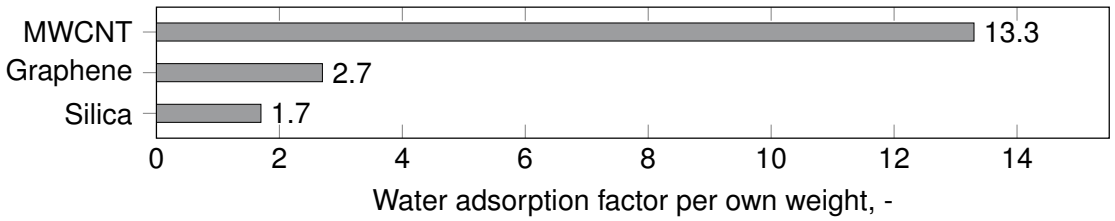

Figure A.21: Water adsorption factor of CNT-K, silica (SSA 700 m^2) and graphene (SSA 500 m^2). Adapted from Trunzer *et al.* [19].

The drying behavior of CNT-K, silica, and graphene is depicted in the equations A.1 to A.3, as well as in Figure A.22. Figure A.23 visualizes the results from the TGA experiments.

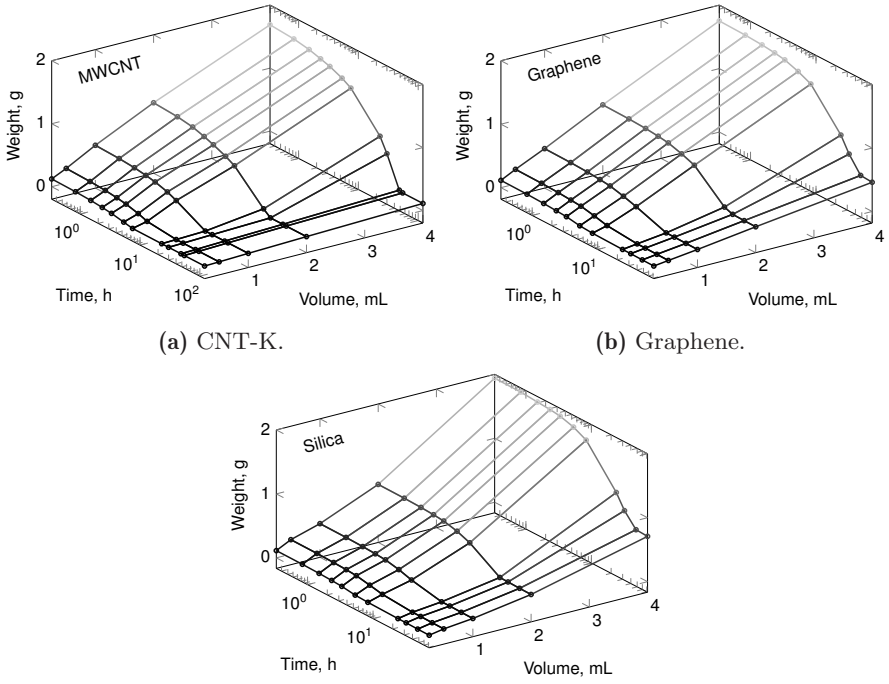

(a) CNT-K. **(b)** Graphene.

(c) Silica.

Figure A.22: Drying rate of CNT-K and different commercial chromatographic and CDI resins regarding the time dependency for different masses. Adapted from Trunzer *et al.* [19].

Study of the heat drying rate of wet CNT-K, in comparison with a typical chromatographic resin (silica, silica gel60, 40 to 63 µm, SSA 700 m^2, AppliChem GmbH) and a standard capacitive deionization electrode material (graphene platelets, >99.5 %, 2 nm, SSA 500 m^2, IoLiTec Ionic Liquids Technologies GmbH). The samples are dissolved in DI-water, a defined volume is centrifuged (5 min, 3200 xg), and dried over several hours in a 60 °C heating chamber. The heat drying rates are listed in A.1 to A.3 and in Trunzer *et al.* [19].

$$t_{CNT-K}\ [\mathrm{h}] = \frac{(1-0.07)\cdot mass_{wet}\ [\mathrm{g}]}{(0.007\cdot ln(mass_{wet}\ [\mathrm{g}])+0.03)} \tag{A.1}$$

$$t_{Graphene}\ [\mathrm{h}] = \frac{(1-0.27)\cdot mass_{wet}\ [\mathrm{g}]}{2.76e^{-2}\cdot (mass_{wet}\ [\mathrm{g}])^{0.306}} \tag{A.2}$$

$$t_{Silica}\ [\mathrm{h}] = \frac{(1-0.37)\cdot mass_{wet}\ [\mathrm{g}]}{2.45e^{-2}\cdot (mass_{wet}\ [\mathrm{g}])^{0.374}} \tag{A.3}$$

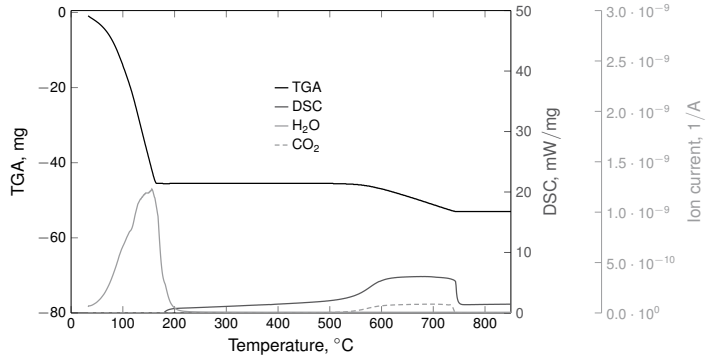

(a) Wet CNT-K.

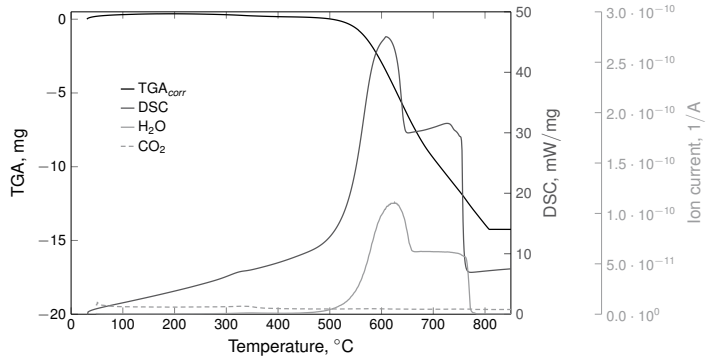

(b) Dry CNT-K.

Figure A.23: TGA experiments with wet and 4 h dried (60°C) CNT-K and dry CNT-K powder. Adapted from Trunzer *et al.* [19].

Static Binding Capacity

The calculation pathway for the static binding capacity ex- and including the water dissolution factor are represented in Equations A.4 to A.13.

$$c_{in,analyte} = c_{sup,analyte} + c_{ads,analyte} \tag{A.4}$$

$$m_{sup,analyte} = c_{sup,analyte} \cdot V_{sup,analyte} \cdot \bar{M}_{analyte} \tag{A.5}$$

$$m_{in,analyte} = c_{in,analyte} \cdot V_{ins,analyte} \cdot \bar{M}_{analyte} \tag{A.6}$$

$$m_{ads,analyte} = m_{in,analyte} - m_{sup,analyte} \tag{A.7}$$

$$q = \frac{m_{ads,analyte}}{m_{dry,CNT}} \tag{A.8}$$

$$m_{pellet,CNT} = m_{dry,CNT} + m_{pellet,water} \tag{A.9}$$

$$m_{dry,CNT} = 0.07 \cdot m_{pellet,CNT} \tag{A.10}$$

$$m_{pellet,water} = 1 - 0.07 \cdot m_{pellet,CNT} \tag{A.11}$$

$$c_{in,analyte}* = c_{in,analyte} \cdot \frac{V_{in,analyte}}{V_{pellet,water}} \tag{A.12}$$

$$q* = c_{ads,analyte} * /m_{dry,CNT} \tag{A.13}$$

The calculation pathway for the theoretical coverage of the CNT-K in static binding capacity experiments is described in the Equations A.14 to A.18. The area of a molecule was assumed to be less 1 nm^2, related to the length of the binding between different atoms.

$$m_{dry,CNT} = 0.07 \cdot m_{pellet,CNT} \tag{A.14}$$

$$A_{dry,CNT} = SSA_{CNT-K} \cdot m_{dry,CNT} \tag{A.15}$$

$$N_{ions} = c_{load,analyte} \cdot N_A \tag{A.16}$$

$$A_{covererage} = N_A \cdot A_{molceule} \tag{A.17}$$

$$Coverage = A_{cover}/A_{dry,CNT} \tag{A.18}$$

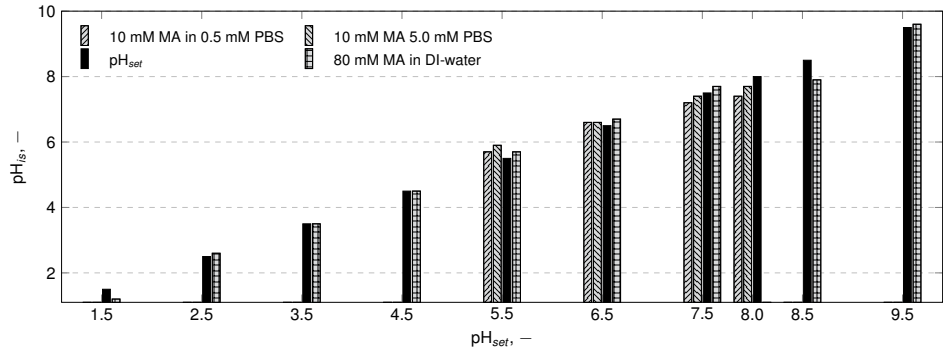

(a) pH-development in different media using maleic acid as analyte.

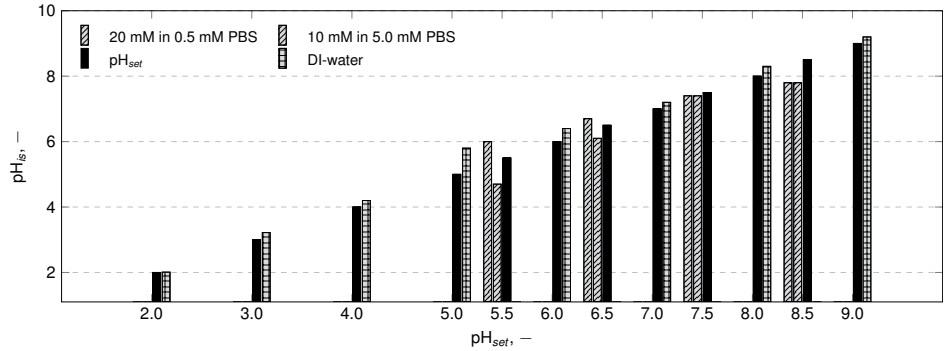

(b) pH-development in different media using phenylalanine as analyte.

Figure A.24: pH-shift of (a) maleic acid and (b) phenylalanine after incubation (DI-water, 0.5 and 5.0 mM phosphate buffer). pH_{set} symbolizes the pH-value at the beginning of the experiment (black bar as reading assistance), pH_{is} represents the pH-value after incubation time. The bars imprint analytes in different carrier media without particles (control samples). Results correspond to Wagner *et al.* [20].

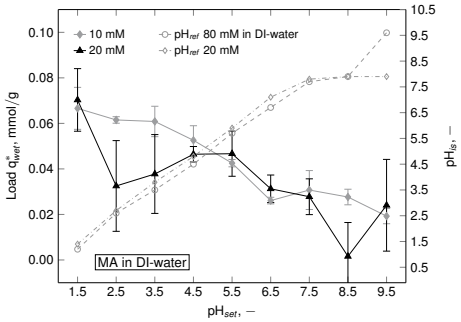

(a) Adsorption amount in DI-water.

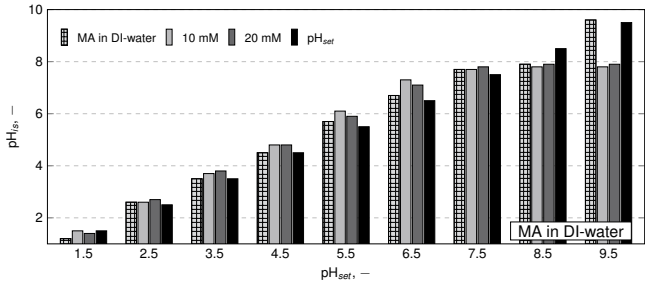

(b) pH-development in DI-water.

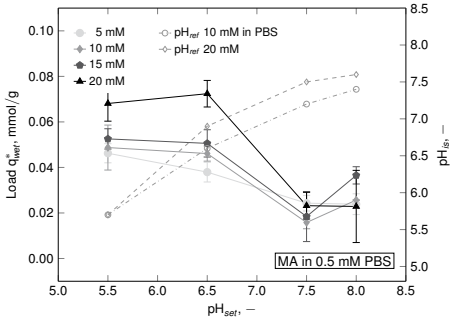

(c) Adsorption amount in 0.5 mM PBS.

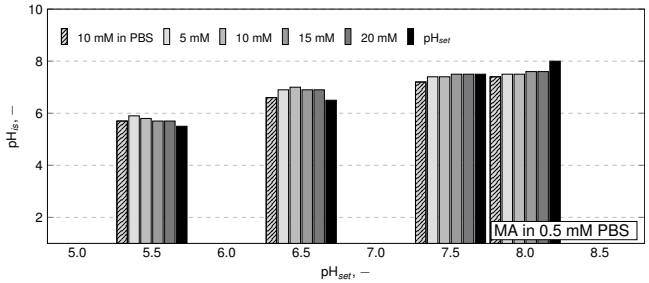

(d) pH-development in 0.5 mM PBS.

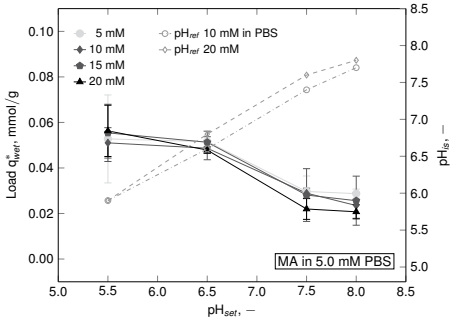

(e) Adsorption amount in 5.0 mM PBS.

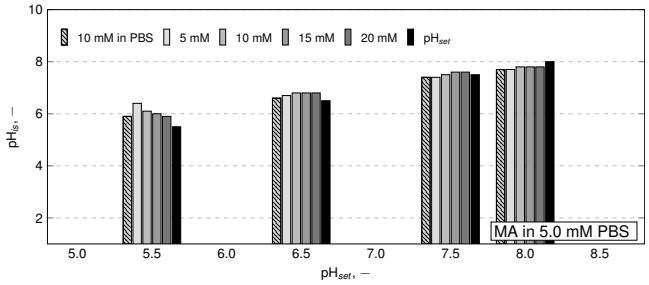

(f) pH-development in 5.0 mM PBS.

Figure A.25: pH-depended adsorption study of maleic acid on CNT-K in different solvents. Subfigures (a) DI-water, (c) 0.5 mM and (e) 5.0 mM phosphate buffer illustrate the corrected load (cf. Equations A.4 to A.13) of maleic acid at different pre-adjusted pH-values (pH_{set}). The pH_{is}-value of the 20 mM sample of maleic acid after equilibration and the pH-value of the control sample is included. The Subfigures (b,d,f) visualize the changes of the pH-value after incubation. Results correspond to published data in cooperation with Wagner *et al.* [20].

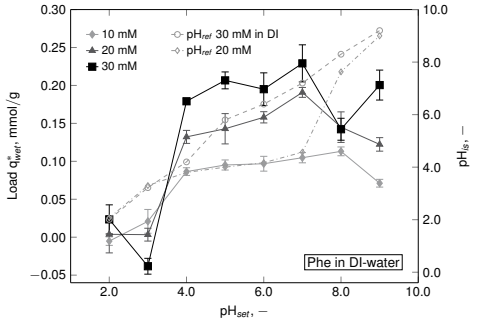

(a) Adsorption amount in DI-water.

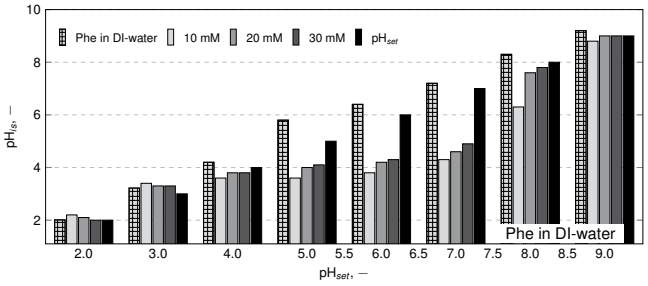

(b) pH-development in DI-water.

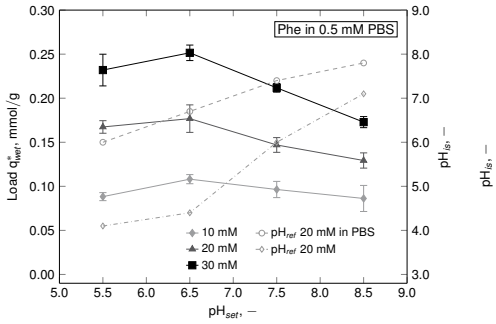

(c) Adsorption amount in 0.5 mM PBS.

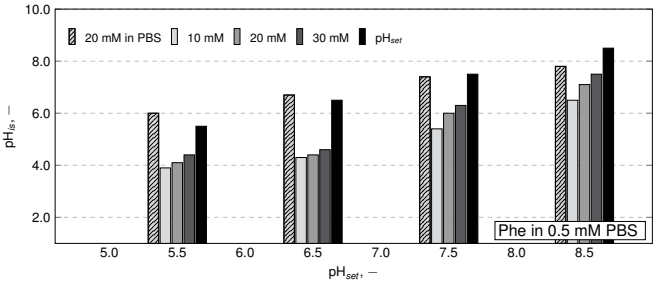

(d) pH-development in 0.5 mM PBS.

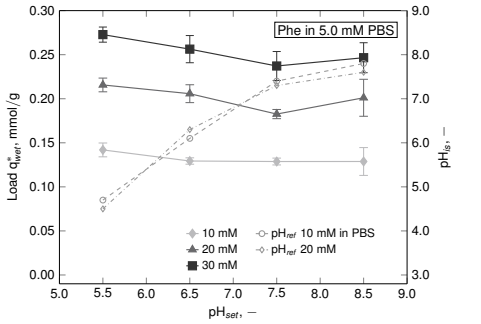

(e) Adsorption amount in 5.0 mM PBS.

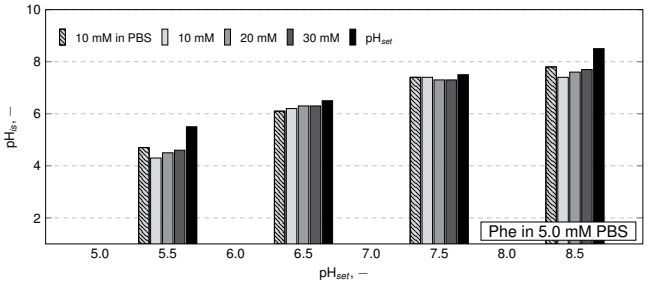

(f) pH-development in 5.0 mM PBS.

Figure A.26: pH-depended adsorption study of phenylalanine on CNT-K in different solvents. Subfigures (a) DI-water, (c) 0.5 mM and (e) 5.0 mM phosphate buffer illustrate the corrected load (cf. Equations A.4 to A.13) of phenylalanine at different pre-adjusted pH-values (pH$_{set}$). The pH$_{is}$-value of the 20 mM sample of phenylalanine after equilibration and the pH-value of the control sample is included. The Subfigures (b,d,f) visualize the changes of the pH-value pH$_{is}$ after 24 h incubation time. Results correspond to published data in cooperation with Wagner *et al.* [20].

A.6 Electrochemical and Chromatographic Characterization

This Section supports Section 5.3 including additional information about the chromatographic and electrochemical characterization of the MWCNT column, as well as its aging behavior.

Chromatographic Analysis

Enhancements to the tracer experiments are depicted in Figure A.27 and Table A.2. Figure A.28 presents the simulation results.

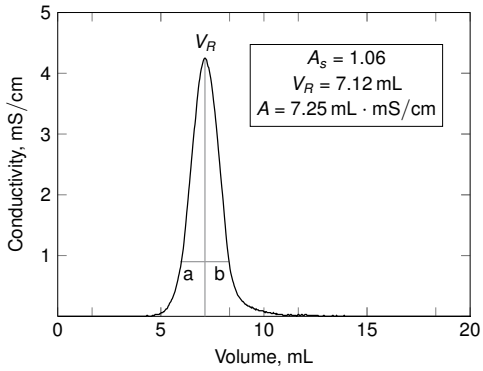

Figure A.27: Ideal tracer chromatogram including the typical parameters for characterization: retention volume V_R, asymmetric factor A_s and peak area A. CNT-K matrix, 1 mL/min, DI-water, 50 µL, 1 M NaCl. Adapted from Trunzer *et al.*[18].

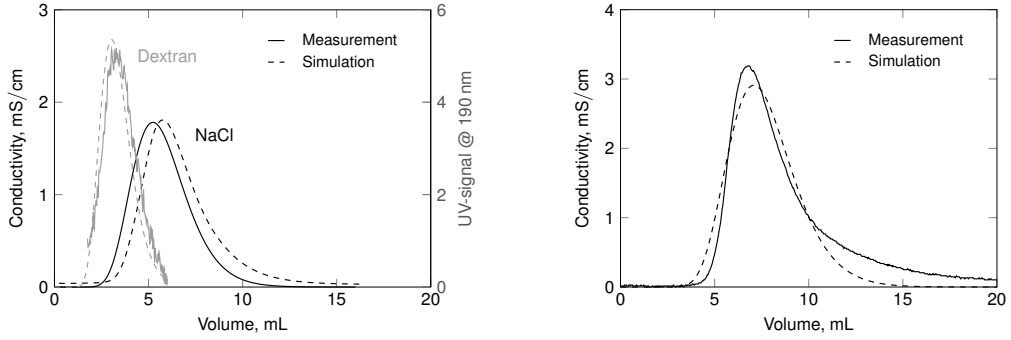

(a) Column 1. **(b)** Column 2.

Figure A.28: Simulation of the CNT-K column 1 (transport dispersive model, 1 M NaCl, 0.01 g/L blue dextran, 1 mL/min) and column 2 (equilibrium dispersive model, 1 M NaCl, 0.75 mL/min).

Table A.2: Ideal tracer characteristics including the retention volume V_R, the asymmetric factor A_s, the HETP value and the number of theoretical plates N for one CNT-K packed column using different mobile phases. CNT-K matrix, DI-water, 1 mM or 10 mM phosphate buffer, 1 mL/min, 50 µL, 1 M NaCl, Trunzer *et al.* [18].

Run	**Mobile phase**	V_R, mL	A_s	**HETP,** cm	N
1	DI-water	7.12	1.06	0.0482	103.64
2	DI-water	6.99	0.93	0.0451	110.96
3	DI-water	6.96	1.02	0.0474	105.56
4	1 mM buffer	6.96	1.10	0.0478	104.61
5	1 mM buffer	6.92	1.13	0.0455	109.80
6	10 mM buffer	6.82	1.31	0.0481	103.86
7	DI-water	6.86	1.13	0.0464	107.70
8	10 mM buffer	6.79	1.38	0.0499	100.19
9	DI-water	7.79	1.20	0.0417	120.04
10	DI-water	6.99	1.10	0.0452	110.59

Electrochemical Characterization

The results of chronoamperometry studies to determine the reproducability of the method are visualized in Figure A.30 and Figure A.29.

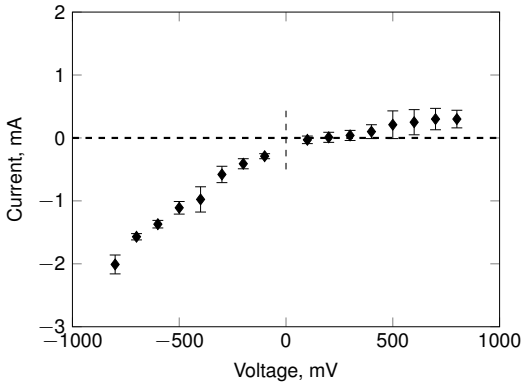

(a) Current/potential diagram.

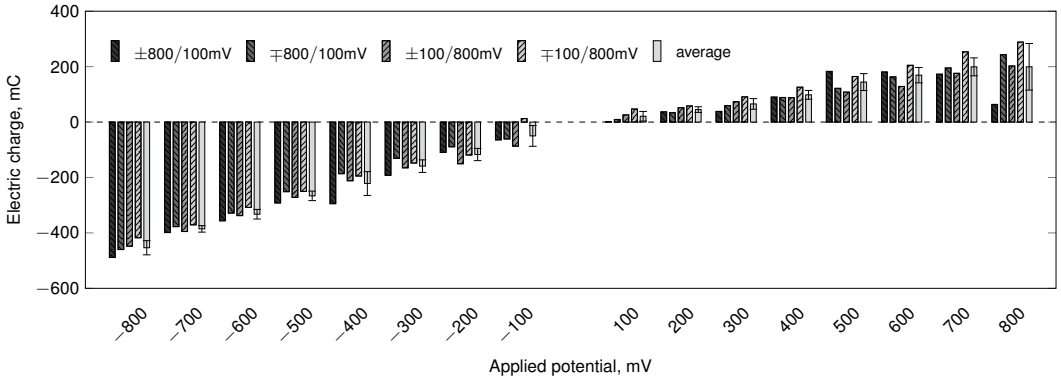

(b) Electric charge.

Figure A.29: Evaluation of the reproducability of chronoamperometry measurements for a CNT-K column. (a) Current/potential diagram, (b) electric charge. CNT-K matrix, DI-water, 1 mL/min. Adapted and enlarged from Trunzer *et al.* [18].

Chronoamperometry and cyclic voltammetry of an ideal IoLiTec-CNT matrix are visualized in Figures A.30 and A.31.

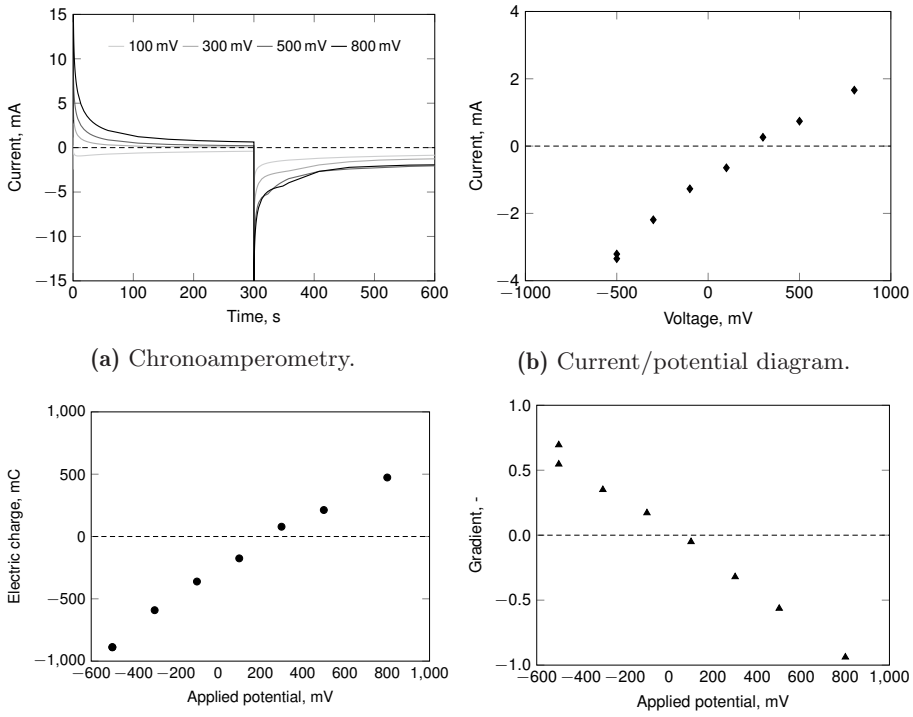

(a) Chronoamperometry.

(b) Current/potential diagram.

(c) Electric charge.

(d) Gradient.

Figure A.30: Chronoamperometry measurements of a qualitatively valid IoLiTec-CNT column. (a) Exemplary chronoamperogram, (b) current/potential diagram, (c) electric charge, (d) gradient of the decline at beginning. IoLiTec-CNT matrix, DI-water, 1.0 mL, hold time 300 s.

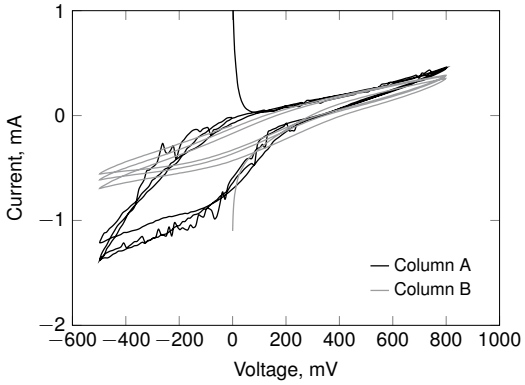

Figure A.31: Cyclic voltammetry measurements of two chromatographically valid IoLiTec-CNT packed column. IoLiTec-CNT matrix, DI-water, 1.0 mL/min 1.0 mV/s, 3 cycles. The measurement errors in CV of column B do not impact the interpretation of the results.

A.7 Electrode Aging

The results for the chromatographic aging of two IoLiTec-CNT matrix are illustrated in Figure A.32, enhanced by a simulative study imprinted in the Figures A.33 and A.34. Information about the electrochemical aging of three CNT-K matrix can be found in the Tables A.3, A.4 and A.5, as well as in the Figures A.35 to A.38.

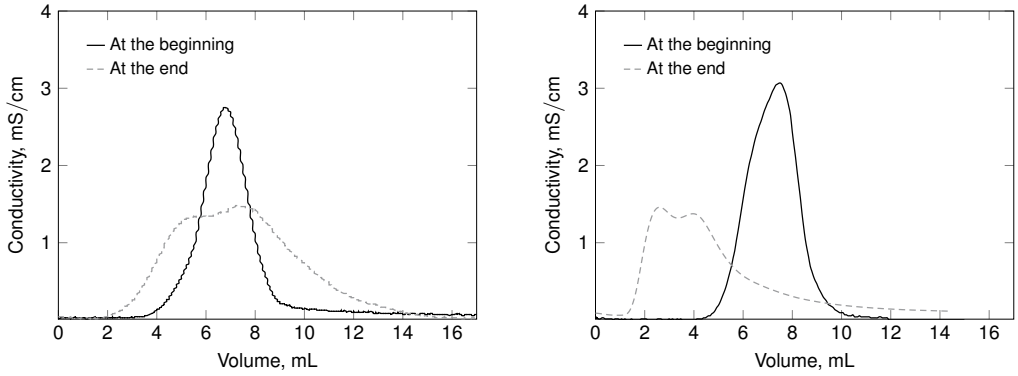

(a) Column A. **(b)** Column B.

Figure A.32: Tracer experiment as detection method for the structural aging of the IoLiTec-CNT electrodes A and B. The tracer peaks illustrate the matrix quality at the beginning and the end of the column life (> 120 working hours). IoLitec-CNT matrix, DI-water, 1 mL/min, 50 µL, 1 M NaCl.

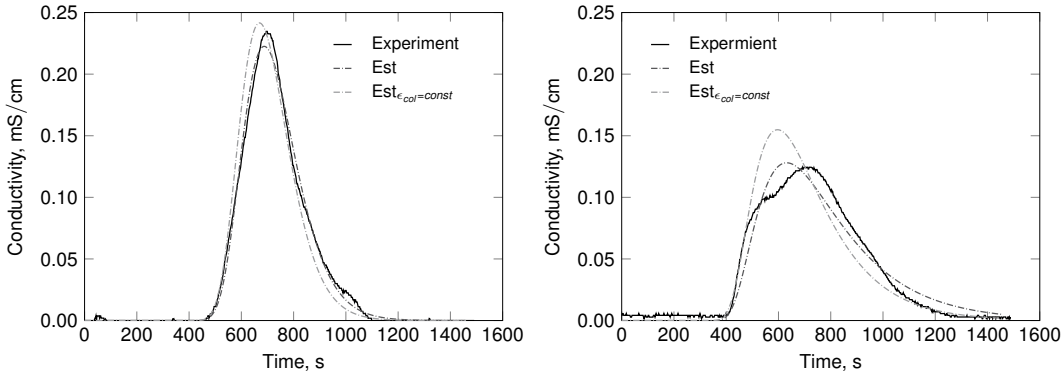

(a) At the beginning. **(b)** After aging.

Figure A.33: Measured and estimated tracer profile of a IoLiTec-CNT column at early life and at its end. Simulation: ChromX, equilibrium dispersive model, no isotherm model; Experiments: IoLiTec-CNT matrix, DI-water, 1 mL/min, 50 µL, 1 M NaCl.

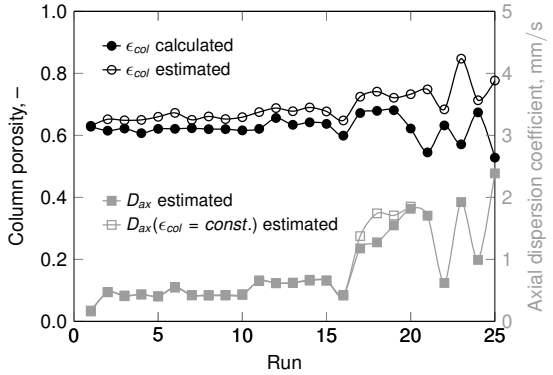

Figure A.34: Aging of the column porosity and the axial dispersion coefficient for the IoLiTec-CNT column A. Experiments: IoLiTec-CNT matrix, DI-water, 1 mL/min, 50 µL, 1 M NaCl. Simulation: ChromX, equilibrium dispersive model, no isotherm model.

Table A.3: Electrochemical aging CNT-K column A (> 400 working hours) by numbers . The listed results are taken from OCP and a chronoamperometry experiments (+800 mV to −800 mV). CNT-K matrix, DI-water, 1.0 mL/min, 300 s. This data correspond to the Figures 5.11a, 5.12, and A.35.

State	**I**$_{mean}$**,** mA	**El. charge,** mC	**Gradient,** –
At the beginning	+1.47 to –1.97	+476 to –648	–0.002 to +0.003
After aging	+0.81 to –0.87	+314 to –348	–0.006 to +0.004
Percentual aging	55% to 44%	66% to 54%	–

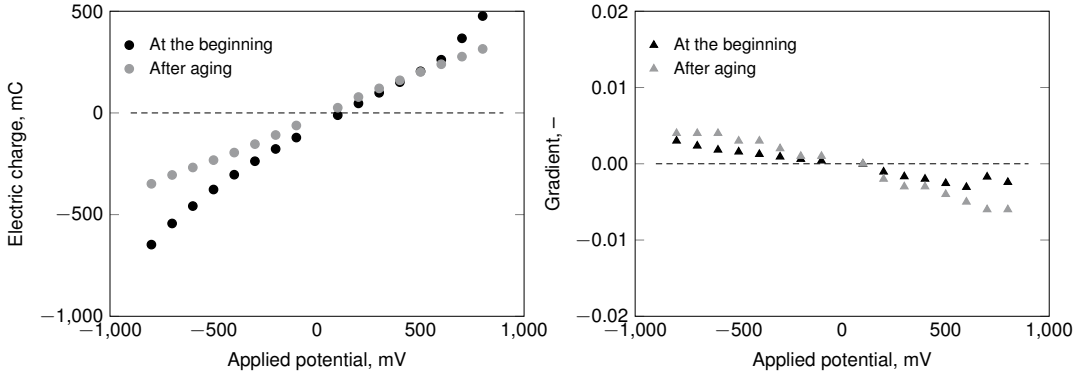

(a) Electric charge. **(b)** Gradient.

Figure A.35: Electrochemical aging of a CNT-K packed column A. (a) Electric charge and (b) gradient. Related to Figure 5.12, 5.11a and Table A.3. CNT-K matrix, 1 mL/min, DI-water. Adapted from Trunzer *et al.* [18].

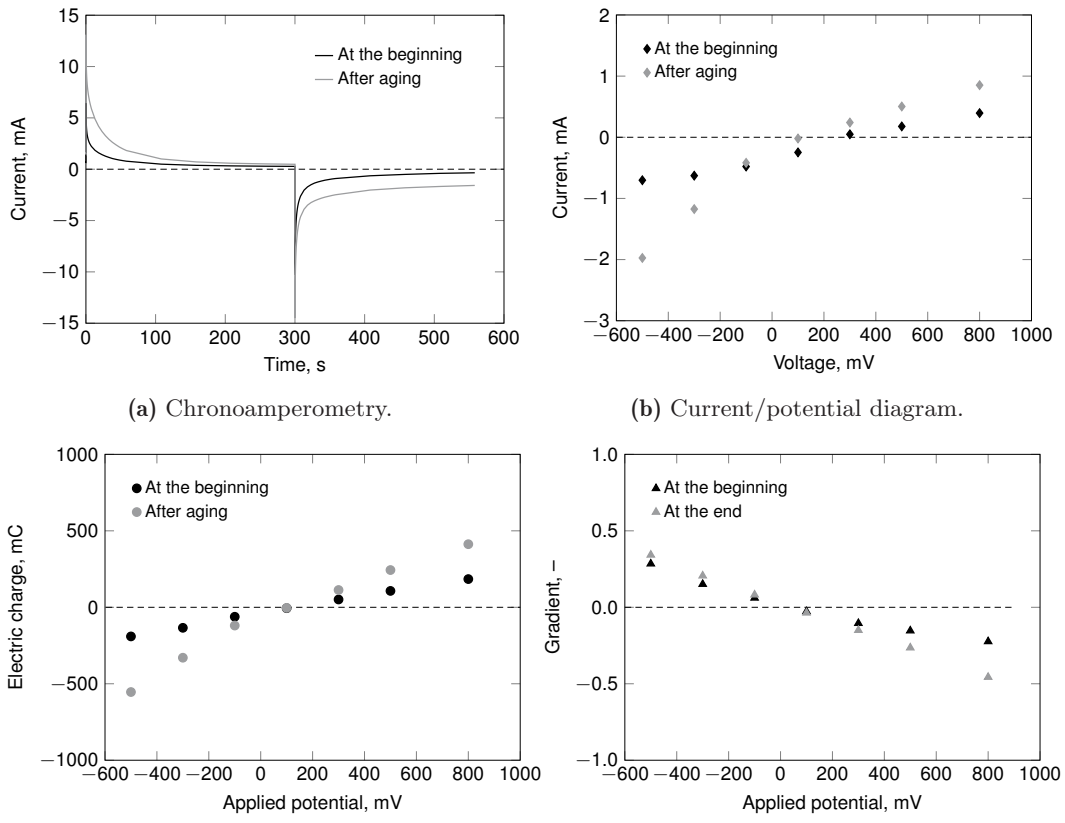

(a) Chronoamperometry. **(b)** Current/potential diagram.

(c) Electric charge. **(d)** Gradient.

Figure A.36: Chronoamperometry as detection method for the aging behavior of CNT-K column B (> 300 working hours). (a) exemplary chronoamperogram for a potential-step between +800 mV to −500 mV, (b) current/potential diagram, (c) electric charge, (d) gradient. CNT-K matrix, DI-water, 1.5 mL, 300 s. The results correspond to Figures A.4 and 5.11b.

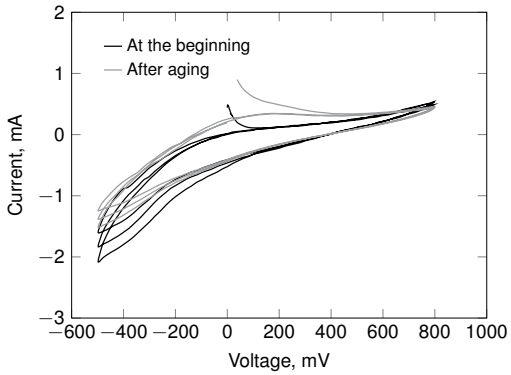

Figure A.37: Cyclic voltammetry to visualize the aging of a CNT-K column B. CNT-K matrix, DI-water, 1.5 mL/min, 1 mV/s. Data correspond to Figure 5.11b and Figure A.36.

Table A.4: Electrochemical aging of CNT-K column B by numbers (< 300 working hours). The listed results are taken from OCP and a chronoamperometry experiments (potential-step between +800 mV to −500 mV). CNT-K matrix, DI-water, 1.5 mL/min, 300 s. This data correspond to Figure 5.11b and Figure A.36.

State	**OCP,** mV	$\mathbf{I}_{mean}$**,** mA	**El. charge,** mC	**Gradient,** –
At beginning	+330	+0.40 to –0.70	+158 to –217	–0.24 to +0.30
At the end	+117	+0.85 to –1.97	+413 to –554	–0.47 to +0.34
Percentual aging	71%	213% to 281%	261% to 255%	–

Table A.5: Electrochemical aging of the CNT-K column C (> 120 working hours) by numbers. The listed results are taken from OCP and a chronoamperometry experiment (potential-step between +800 mV to −500 mV). CNT-K matrix, DI-water, 1.5 mL/min, 300 s. This data correspond to Figure A.38.

State	**OCP,** mV	$\mathbf{I}_{mean}$**,** mA	**El. charge,** mC	**Gradient,** –
At beginning	+422	+0.91 to –1.92	+259 to –427	–0.50 to +0.33
At the end	+140	+1.30 to –1.43	+323 to –343	–0.11 to +0.23
Percent aging	33%	143% to 74%	124% to 80%	–

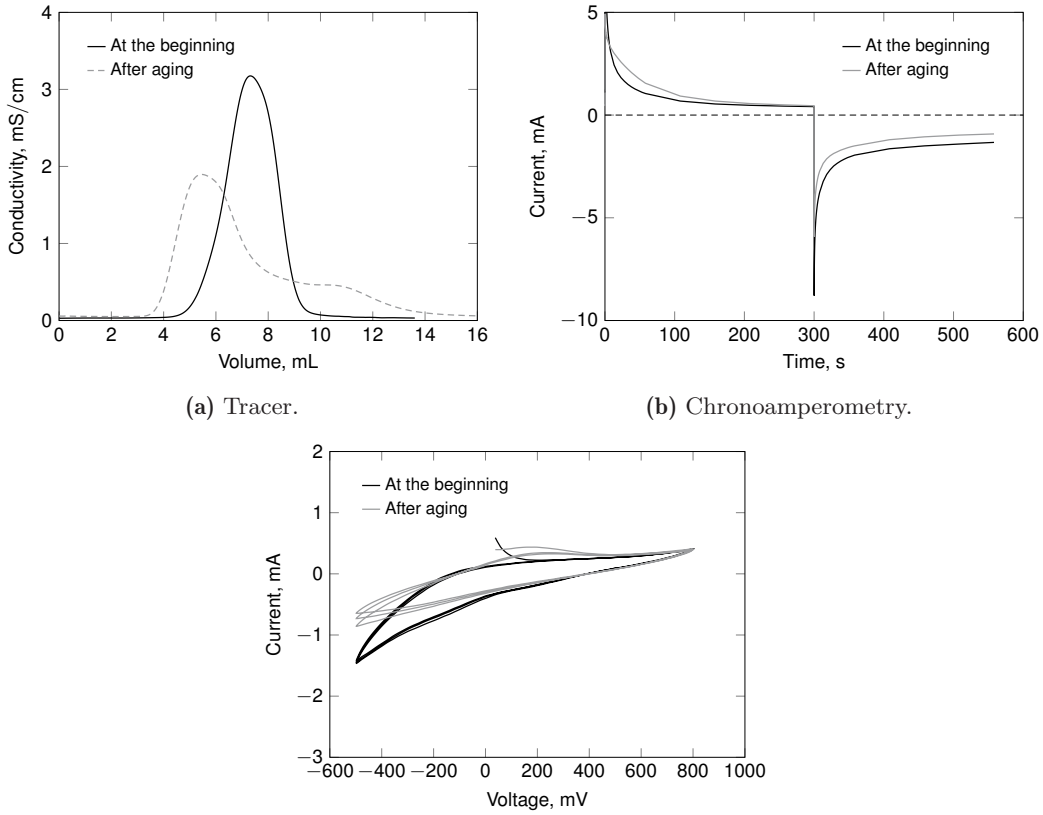

(a) Tracer.

(b) Chronoamperometry.

(c) Cyclic voltammetry.

Figure A.38: Chromatographic and electrochemical aging of CNT-K column C (> 120 working hours). (a) Tracer experiments, (b) exemplary chronoamperogram for a potential-step between +800 mV to −500 mV, (c) Cyclic voltammetry. CNT-K matrix, DI-water, 1.5 mL, 50 µL, 1 M NaCl, hold time 300 s, 1 mV/s, 3 cycles. These measurement correspond to Table A.5.

Data about the electrochemical aging of two IoLiTec-CNT matrix are illustrated in Table A.6 and Figure A.39, as well as in the chronoamperograms Table A.7 and Figure A.40. Cyclic voltammograms of two IoLiTec-CNT matrix are presented in Figure A.41.

Table A.6: Electrochemical aging of the IoLiTec-CNT column A (> 120 working hours) by numbers. The listed results are taken from OCP and a chronoamperometry experiments (potential-step between +500 mV to −500 mV). IoLiTec-CNT matrix, DI-water, 1.5 mL/min, 300 s. This data correspond to Figure A.39.

State	**OCP,** mV	$\mathbf{I}_{mean}$**,** mA	**El. charge,** mC	**Gradient,** –
At beginning	+352	+0.74 to –3.20	+213 to –888	–0.45 to +0.54
At the end	+103	+2.69 to –4.72	+700 to –1327	–0.49 to +0.40
Percentual aging	29%	363% to 174%	575% to 132%	–

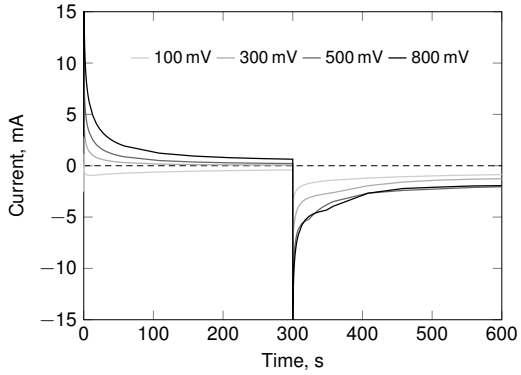

(a) Chronoamperometry at the beginning.

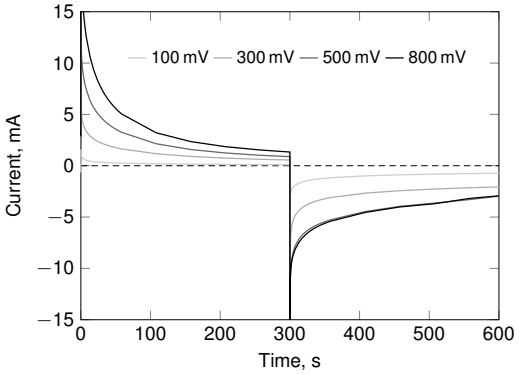

(b) Chronoamperometry after aging.

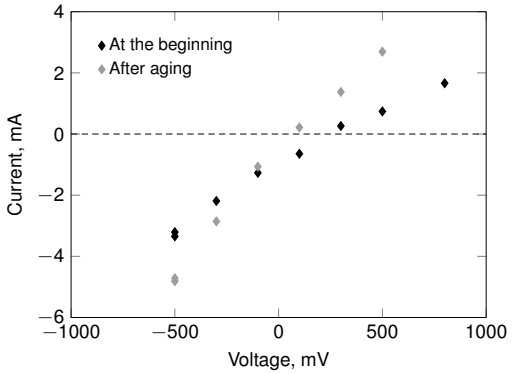

(c) Current/potential diagram.

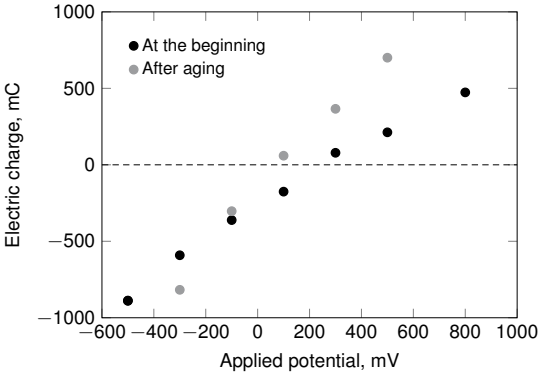

(d) Electric charge.

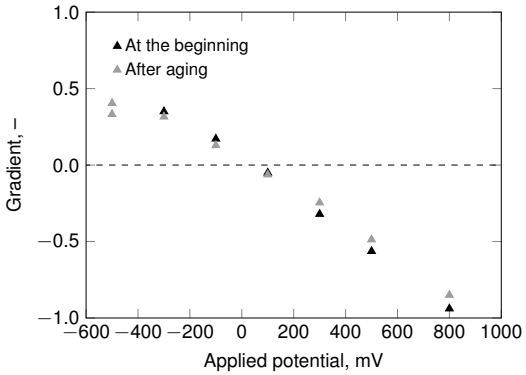

(e) Gradient.

Figure A.39: Chronoamperometry as detection method for the aging of a IoLiTec-CNT electrode column A (> 120 working hours). (a) exemplary chronoamperogram for a potential-step between +500 mV to −500 mV, (b) current/potential diagram, (c) electric charge, (d) gradient. IoLiTec-CNT matrix, DI-water, 1.0 mL, hold time 300 s. The chromatograms are illustrated in Figure A.32a, characteristic numbers are listed in Table A.6.

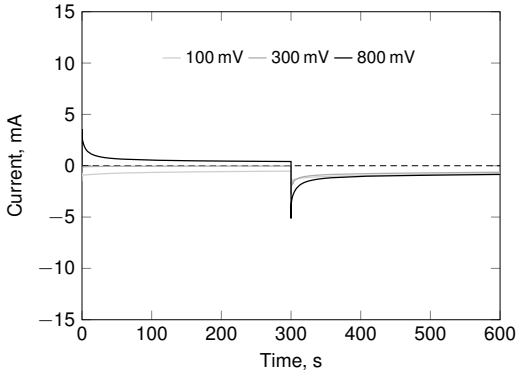

(a) Chronoamperometry at the beginning.

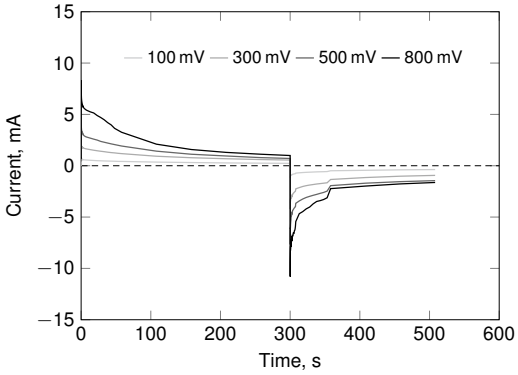

(b) Chronoamperometry after aging.

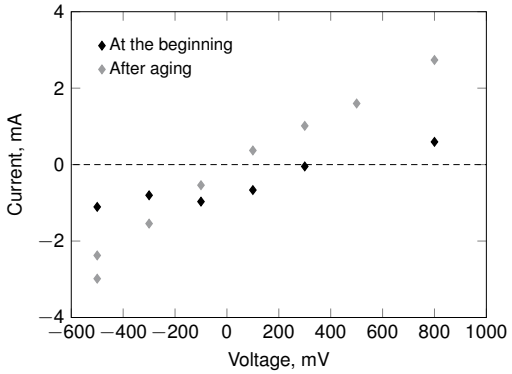

(c) Current/potential diagram.

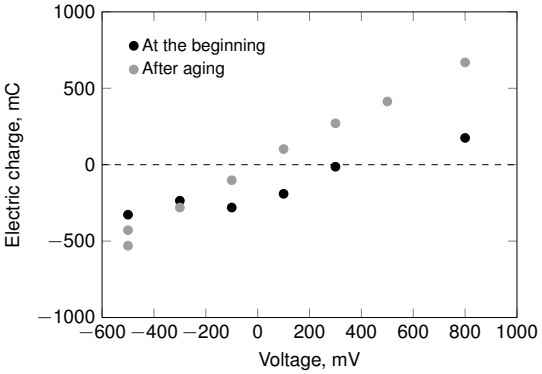

(d) Electric charge.

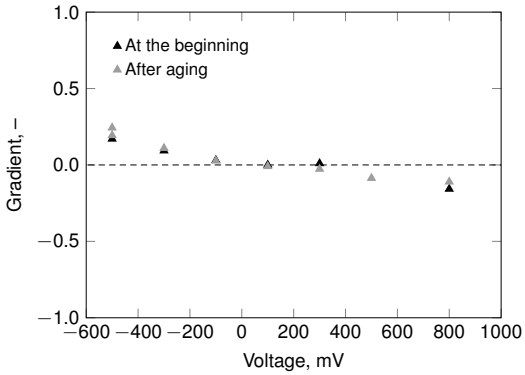

(e) Gradient.

Figure A.40: Chronoamperometry as detection method for the aging of a IoLiTec-CNT column B (> 120 working hours). (a) exemplary chronoamperogram for a potential-step between +500 mV to −500 mV, (b) current/potential diagram, (c) electric charge, (d) gradient. IoLiTec-CNT matrix, DI-water, 1.0 mL, hold time 300 s. These measurement correspond to Table A.7 and to Figure A.32b.

Table A.7: Electrochemical aging over 120 working hours of the IoLiTec-CNT column B by numbers. The results bases on OCP and chronoamperometry experiments as well as from a potential-step (±500 mV). IoLiTec-CNT matrix, DI-water, 1.5 mL/min, 300 s. See also Figures A.32b and A.40.

State	**OCP,** mV	$\mathbf{I}_{mean}$**,** mA	**El. charge,** mC	**Gradient,** –
At beginning	+402	+0.26 to -2.19	+ 79 to -519	-0.32 to +0.35
At the end	+256	+1.38 to -2.85	+366 to -817	-0.25 to +0.32
Percental aging	63%	328% to 150%	463% to 157%	–

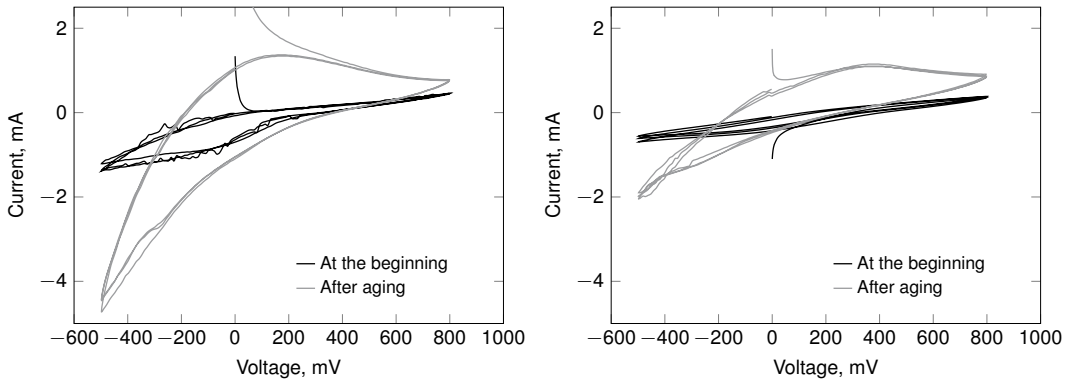

(a) Column A. **(b)** Column B.

Figure A.41: Cyclic voltammetry to visualize the aging of the two IoLiTec-CNT columns A and B. IoLitec-CNT matrix, DI-water, 1.0 mL/min, 1 mV/s.

Regeneration of the Column Matrix

Chromatograms before and after regeneration of CNT-K matrix are illustrated in Figure A.42.

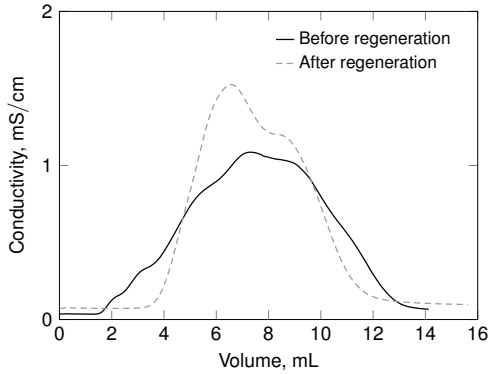

Figure A.42: Chromatograms before and after the regeneration of a CNT-K matrix (procedure cf. Figure 5.14). CNT-K matrix, DI-water, 1.5 mL/min, 50 µL, 1 M NaCl.

A.8 Impact of the Fluid Flow

This Section corresponds to Section 5.5.1, in which the effects of the fluid flow are investigated on the column's response. The results of the chromatographic study are represented in the first Subsection, the one of the electrochemical study in the second.

Chromatographic analysis

Figure A.43 illustrates the impact of the flow rate on the retention time and dispersion inside a CNT-K column, Figure A.44 the one for a IoLiTec-CNT column.

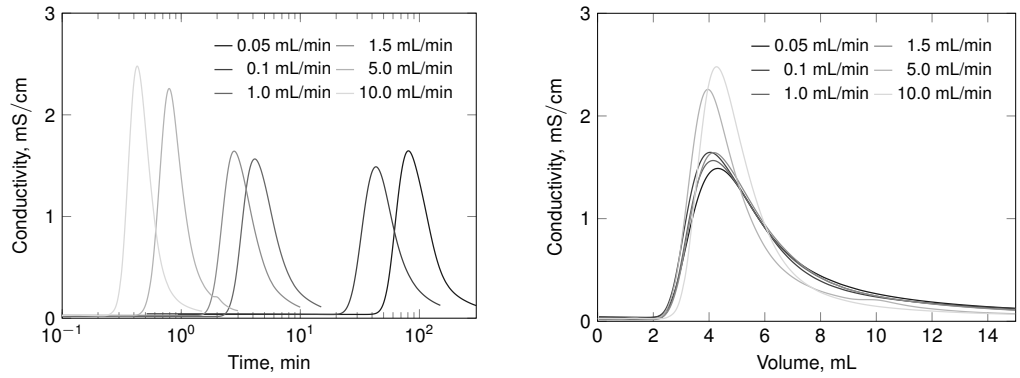

(a) Chromatogram over time. **(b)** Chromatogram over volume.

Figure A.43: Tracer experiment to illustrate the impact of the fluid flow for a CNT-K matrix chromatographically. CNT-K matrix, DI-water, various flow rates, 50 µL, 1 M NaCl. Adapted from Trunzer *et al.* [19].

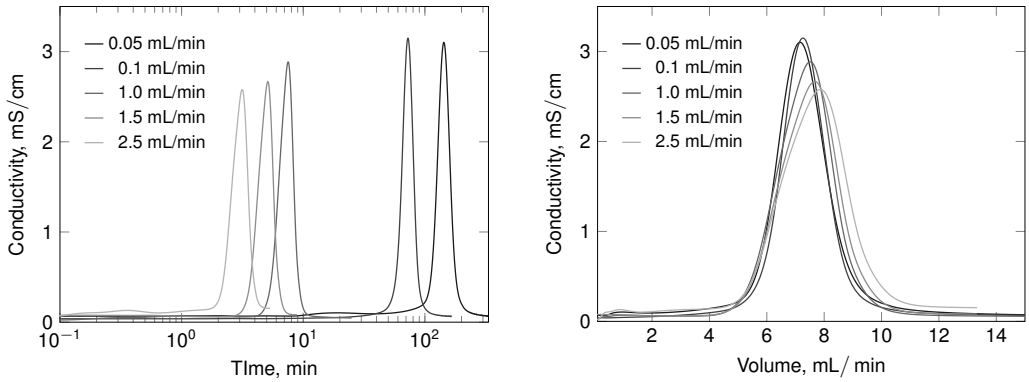

(a) Chromatogram over time. **(b)** Chromatogram over volume.

Figure A.44: Tracer experiment to illustrate the impact of the fluid flow for a IoLiTec-CNT matrix chromatographically. IoLiTec-CNT matrix, DI-water, various flow rates, 50 µL, 1 M NaCl. Adapted from Trunzer *et al.* [19].

Electrochemical analysis

Table A.8 summarizes the results of the OCP measurements for a representative CNT-K and IoLiTec-CNT column. The results for the chronoamperometric analysis are imprinted in Figure A.45 for the CNT-K and in Figure A.46 for the IoLiTec-CNT. Additional illustrations of the cyclic voltammograms are presented in Figure A.47.

Table A.8: Fluid flow impact on OCP. CNT-K and IoLiTec-CNT matrix, DI-water, various flow rates.

Flow rate, mL/min	**OCP(CNT-K),** mV	**OCP(IoLiTec-CNT),** mV
0.1	342	295
0.5	156	208
1.0	323	269
1.5	204	315
2.5	171	267

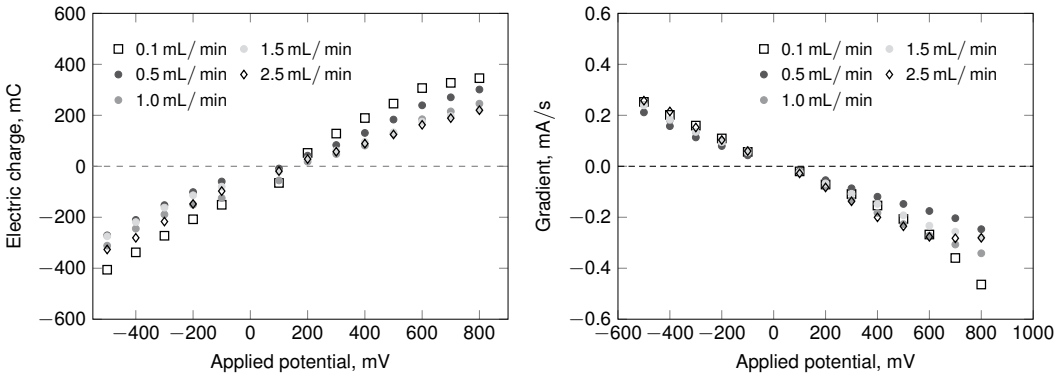

(a) Electric charge.

(b) Gradient.

Figure A.45: Supplements to the chronoamperometric study about the impact of the flow rate on a CNT-K matrix. CNT-K matrix, DI-water, various flow rates. See also Figure 5.17. Adapted from Trunzer *et al.* [19].

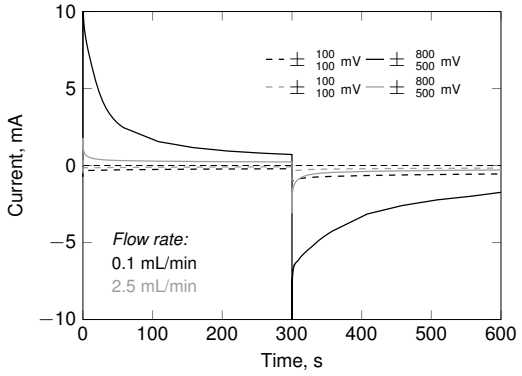

(a) Exemplary chronoamperometry.

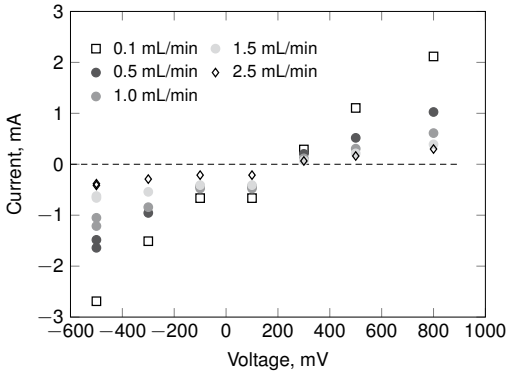

(b) Current/potential diagram.

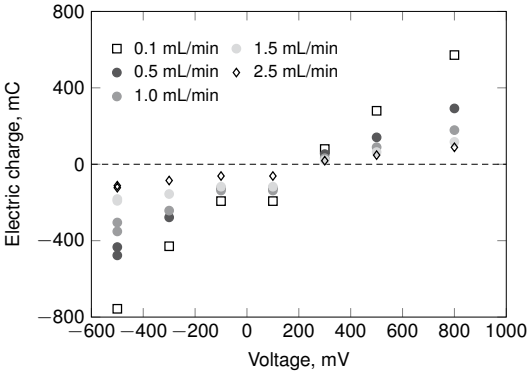

(c) Electric charge.

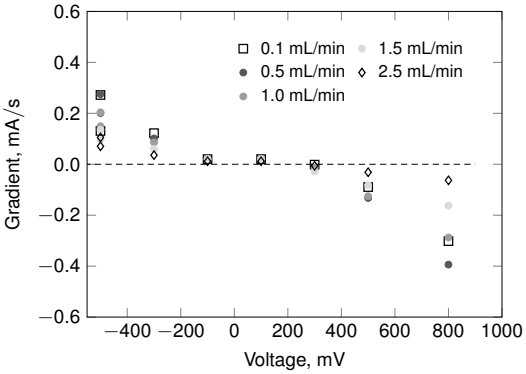

(d) Gradient.

Figure A.46: Chronoamperometry to study the flow rate's impact on the current response of a IoLiTec-CNT matrix. IoLiTec-CNT matrix, DI-water, various flow rates. See also Figure A.47b.

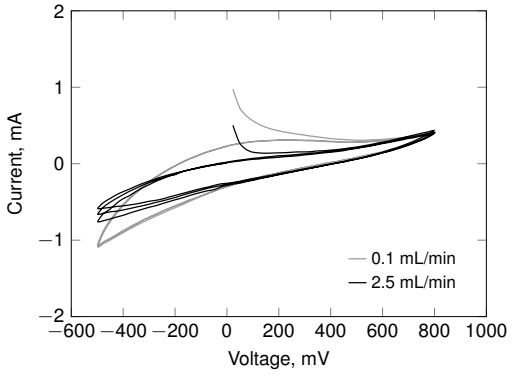

(a) CNT-K matrix.

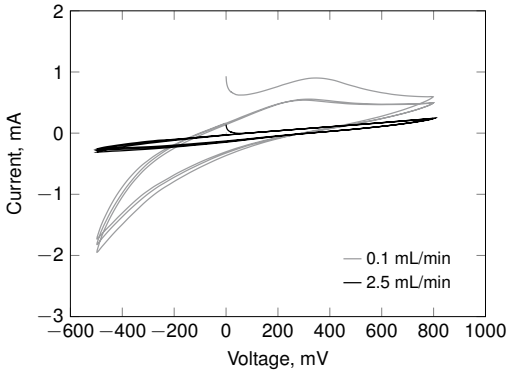

(b) IoLiTec-CNT matrix.

Figure A.47: Cyclic voltammogram of a CNT-K and a IoLiTec-CNT matrix at different flow rates. CNT-K and IoLiTec-CNT matrix, DI-water, 1.0 mV/s, 3 cycles. Adapted from Trunzer *et al.* [19].

A.9 Differences in the Mobile Phase Media

This Section supplements to Section 5.5 and enhances the study of the aging behavior of a column chromatographically and electrochemically. The pH-effect on and of the column response are depicted, as well as the impact of the concentration and composition of different electrolytes on the current response.

Chromatographic Aging

Figure A.48 illustrates the structural aging of two representative CNT-K columns.

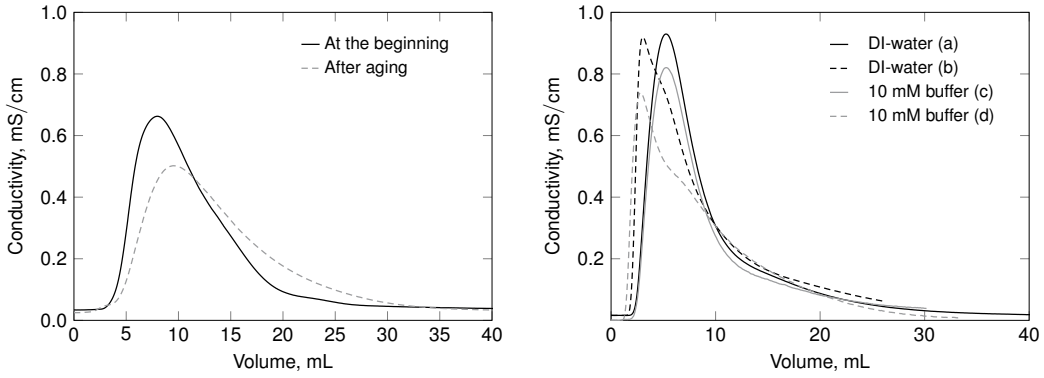

(a) Column 1. **(b)** Column 2.

Figure A.48: Chromatographic aging of two CNT-K columns using DI-water and 10 mM phosphate buffer as mobile phase. CNT-K matrix, 1 mL/min, 50 µL, 1 M NaCl. Adapted from Trunzer *et al.* [18].

Electrochemical Aging

Electrochemical aging using DI-water or PBS in a CNT-K is presented in Figure A.49.

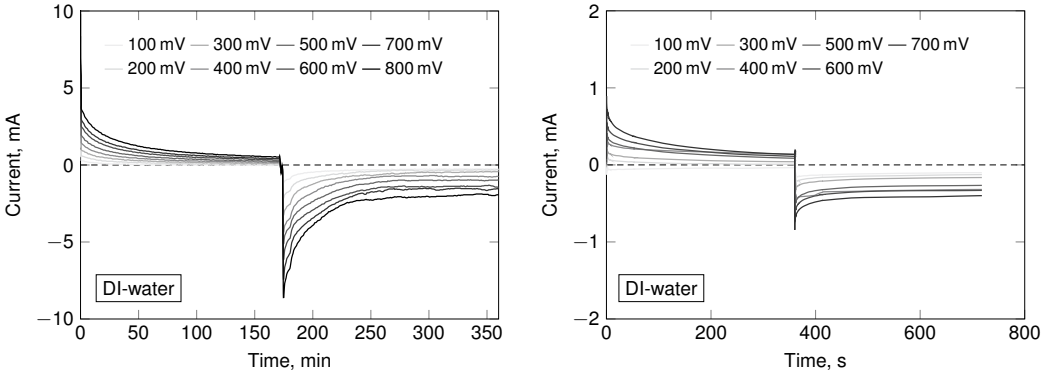

(a) DI-water before aging. **(b)** DI-water after aging.

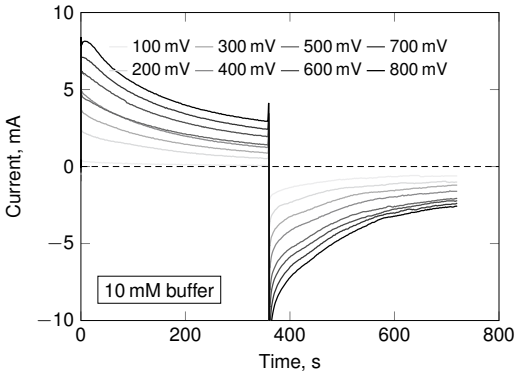

(c) 10 mM phosphate buffer before aging.

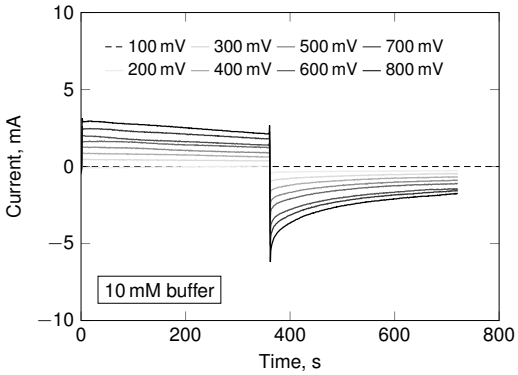

(d) 10 mM phosphate buffer after aging.

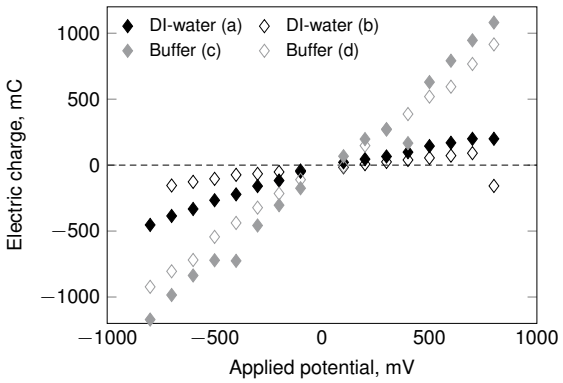

(e) Overview of the electric charge.

Figure A.49: Chronoamperometry measurements to compare the column response and the aging behavior if DI-water (a, b) or 10 mM phosphate buffer (c, d, pH 7.2) are used as mobile phase media. Data correspond to Figure 5.18. CNT-K matrix, 1 mL/min. Adapted from Trunzer *et al.* [18].

Impact of the pH-value

The pH-analysis is supplemented with results in Table A.9 (OCP), in Figure A.50 (chronoamperometry) and Figure A.51 (cyclic voltammetry). The effect on the potential is depicted in Figure A.52. A schematic representation is depicted in Figure A.53.

Table A.9: OCP measurements to study the pH-impact on the potential-dependent CNT-K interface. CNT-K matrix, pH-pre-adjusted DI-water, 1 mL/min.

$\mathbf{OCP}_{pH6}$, mV	$\mathbf{OCP}_{pH7}$, mV	$\mathbf{OCP}_{pH8}$, mV	$\mathbf{OCP}_{pH9}$, mV
324	191	275	138

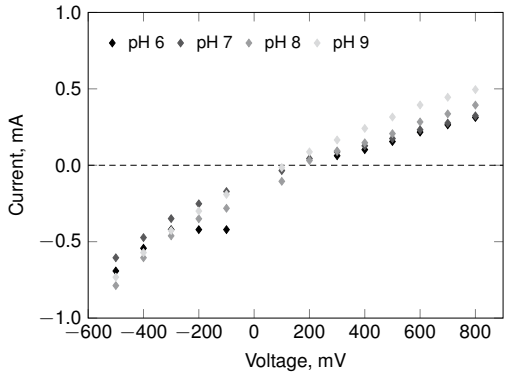

(a) Current/potential diagram.

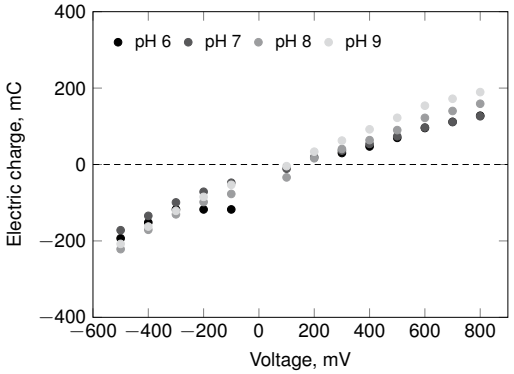

(b) El. charge.

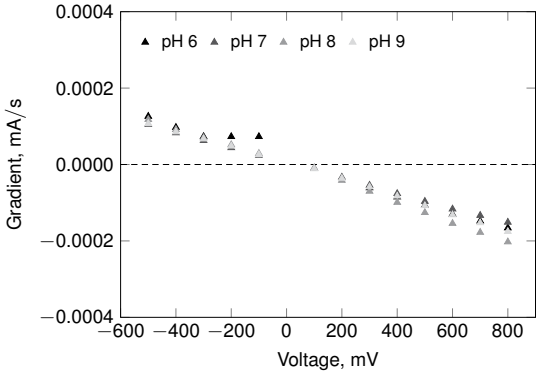

(c) Gradient.

Figure A.50: Further results of the chronoamperometry experiments to study the impact of the pH-value on the potential-dependent CNT-K interface. CNT-K matrix, 1 mL/min. Adapted from Trunzer *et al.* [19].

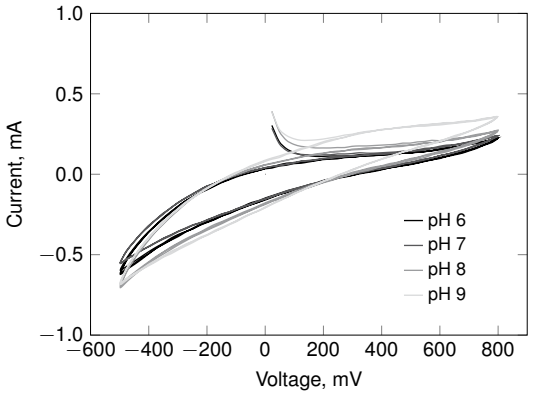

Figure A.51: Cyclic voltammogram to illustrate the impact of differently pH-pre-adjusted mobile phases on the current response of the CNT-K column. CNT-K matrix, DI-water, 1 mL/min, 1.0 mV/s, 3 cycles. Adapted from Trunzer *et al.* [19].

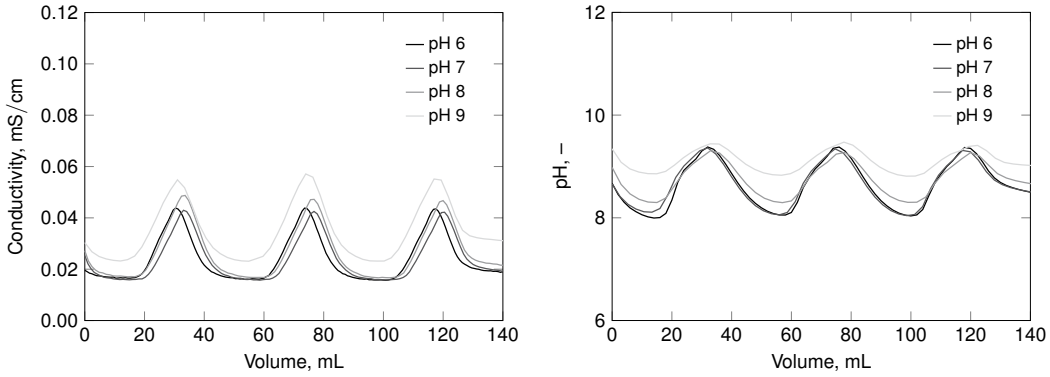

(a) Conductivity.

(b) pH-value.

Figure A.52: Illustration about conductivity and pH-deviation during cyclic voltammetry measurements when differently pH-preadjusted solvents are used. CNT-K matrix, DI-water, 1 mL/min, 1.0 mV/s, 3 cycles. Adapted from Trunzer *et al.* [19].

Impact of Potential on Conductivity and pH-value

When an electric potential is applied to the MWCNT matrix, the surface charge is modified. Figure A.53 depicts a simplified scheme about the charging process of the used MWCNT column and the expected impact on the conductivity and the pH-value to an electrolyte solution.

When a positive potential is applied to the MWCNT, the matrix works as an anode. Negatively charged ions are attracted to the charged matrix, while positively charged ions are repulsed. As a CEX membrane is installed, cations in the solution can permanently be adsorbed on the membrane surface. This effect is negligible as the contact area of the MWCNT is much larger. Moreover, the membrane has a constant number of binding sites while the one of the matrix varies depending on the potential. A higher positive potential induces a larger amount of binding sites for anions, which can cause a distinct decrease of the conductivity signal. However, when the difference between potential applied and the OCP is small, no conductivity changes are detectible. When the electrode functions as a cathode, the salt anions are repelled while cations are adsorbed. An increase in conductivity is detected.

Moreover, the surface charge affects the pH-value as the faradaic current can increase the concentration of oxonium or hydroxyl ions in solution (see Equations 2.12 to 2.17). The water ions in the solution can be adsorbed to the electrode changing the pH-value vise versa. Oxonium ions can bind to a negatively charged surface, increasing the pH-value, while a reduction of hydroxyl ions decrease it. Depending on the potential applied, the impact is higher when the MWCNT matrix function as a cathode (larger difference to OCP), activating water decomposition favors the generation of hydroxyl ions while oxonium ions can be adsorbed.

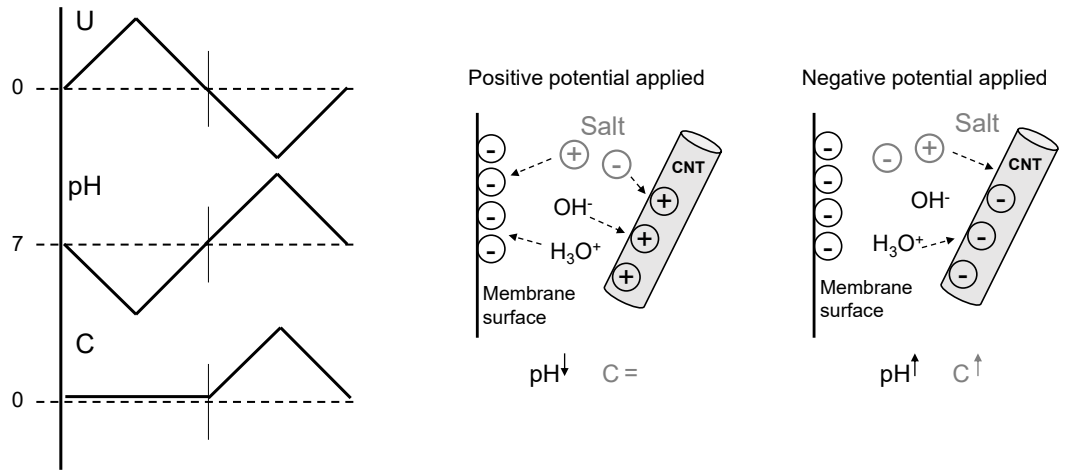

Figure A.53: Simplified illustration of the impact of applied electrical potential on the conductivity and the pH-value of the surrounding environment. Adapted from Trunzer *et al.* [18].

Impact of Salt Composition and Concentration

The impact of the salt electrolytes on the OCP are depicted in Table A.10, results of chronoamperometry and cyclic voltammetry are illustrated in Figure A.54 and Figure A.55.

Table A.10: OCP measurements to study the impact of surrounding environment on the potential-dependent CNT-K interface. CNT-K matrix, DI-water with adjusted pH-values, 1 mL/min.

Salt	**OCP**$_{1\,\mathrm{mM}}$, mV	**OCP**$_{10\,\mathrm{mM}}$, mV
NaCl	107	-2
KCl	227	-17
$CaCl_2$	215	-27

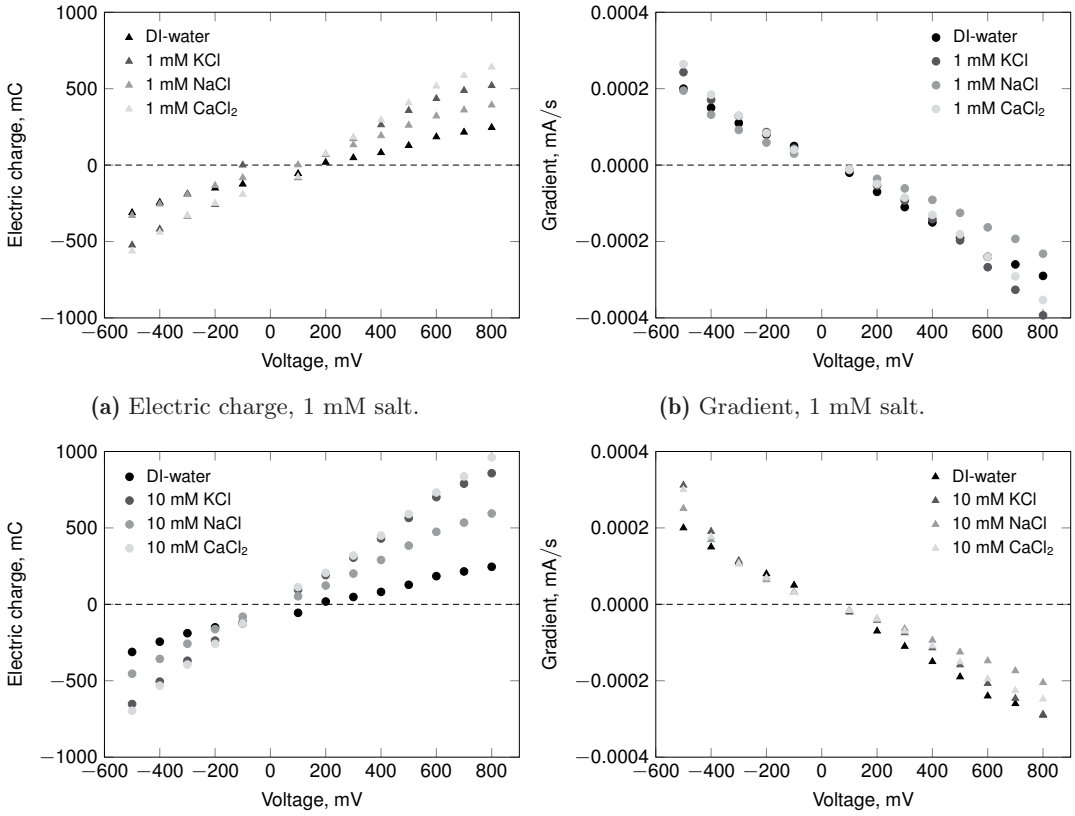

(a) Electric charge, 1 mM salt.

(b) Gradient, 1 mM salt.

(c) Electric charge, 10 mM salt.

(d) Gradient, 10 mM salt.

Figure A.54: Further information about chronoamperometry experiments to study the impact of the salt composition on the potential-dependent CNT-K interface. CNT-K matrix, DI-water, 1 mM, 10 mM NaCl, KCl, $CaCl_2$, 1 mL/min. See also Figure 5.21. Adapted from Trunzer *et al.* [19].

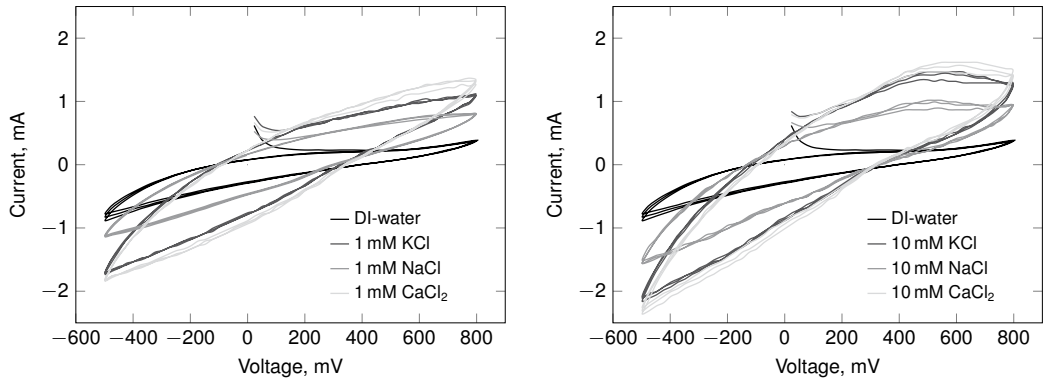

(a) 1 mM salt electrolytes.

(b) 10 mM salt electrolytes.

Figure A.55: Cyclic voltammetry experiments to study the impact of the salt composition on the potential-dependent CNT-K interface. CNT-K matrix, DI-water, 1 mM, 10 mM NaCl, KCl, $CaCl_2$, 1 mL/min, 1 mV/s, 3 cycles. Adapted from Trunzer *et al.* [19].

A.10 Competition for Binding Sites

This Section corresponds to Section 5.5.3, illustrating maleic acid chromatograms for potential-gradient experiments in Figure A.56. Figure A.57 depicts the relative balance of the adsorption amount of pure maleic acid or maleic acid dissolved in a salt mixture. Supplement information about the conductivity and pH-development recorded during the experiments are illustrated in Figure A.58. The impact of different salts in the injection mixture on the adsorption of maleic acid is visualized in the chromatograms in Figure A.59.

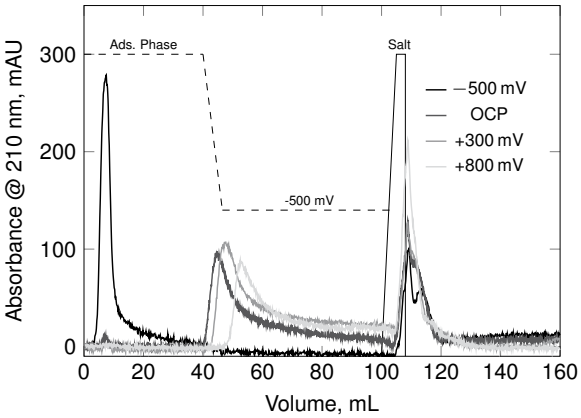

Figure A.56: Potential-gradient experiment with maleic acid as target analyte at different applied potentials. CNT-K matrix, DI-water, adsorption phase 0.5 mL/min, desorption phase 1.5 mL/min, analyte: 50 µL, 25 m/M, 210 nm, gradient −5 mV/s, salt elution: 1 M NaCl, 8 mL. See also Figure 5.23. Adapted from Trunzer *et al.* [19].

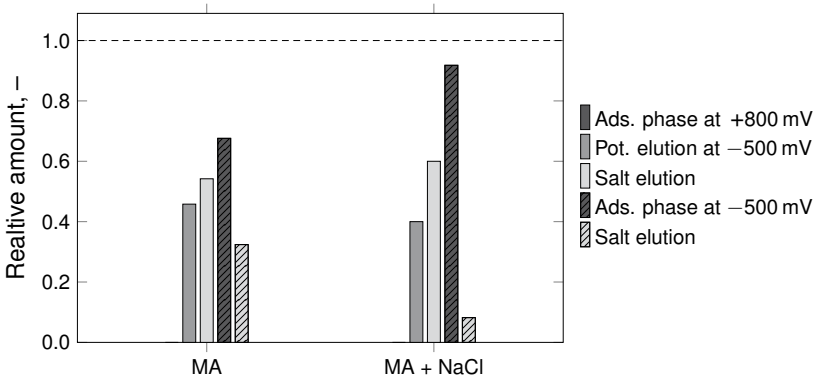

Figure A.57: Balance of potential-gradient experiments performed to study the adsorption capacity of maleic acid as target molecule competing with NaCl. CNT-K matrix, DI-water, adsorption phase 0.5 mL/min, desorption phase 1.5 mL/min, analyte: 50 µL, 25 m/M (stoichiometric ratio 1:1), 210 nm, gradient −5 mV/second, salt elution: 1 M NaCl, 8 mL. Adapted from Trunzer *et al.* [19].

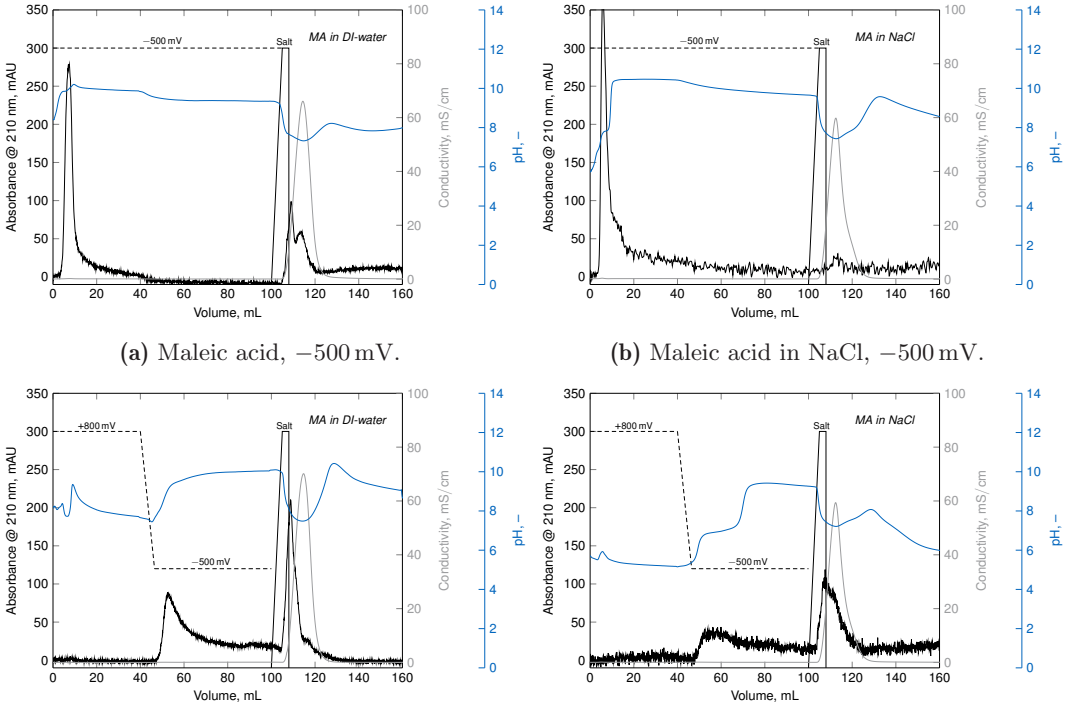

(a) Maleic acid, −500 mV.

(b) Maleic acid in NaCl, −500 mV.

(c) Maleic acid, +800 mV.

(d) Maleic acid in NaCl, +800 mV.

Figure A.58: Potential-gradient experiment to study the potential-dependent adsorption of maleic acid as analyte and the resulting pH-effect. CNT-K matrix, DI-water, adsorption phase: 0.5 mL/min, desorption phase 1.5 mL/min, 50 µL, 25 mM maleic acid, 25 mM maleic acid in 25 mM NaCl (stoichiometric ratio 1:1), gradient −5 mV/s, salt elution: 1 mM NaCl, 8 mL. Cf.Figure 5.2b.

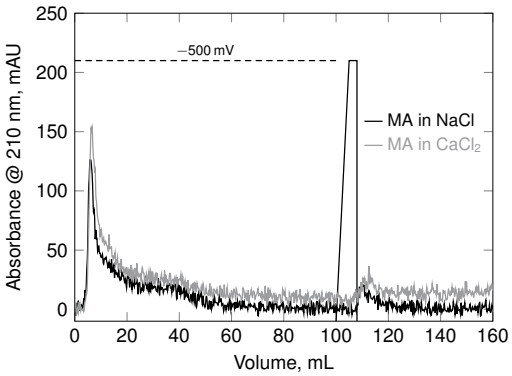

(a) Chromatogram, −500 mV.

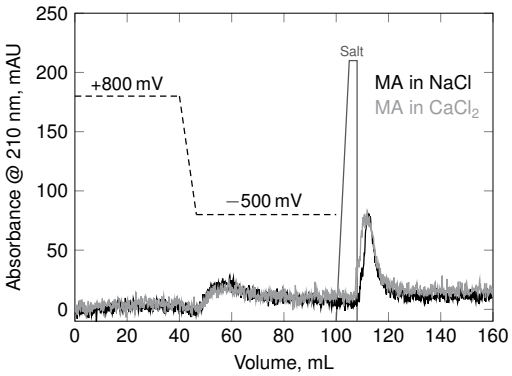

(b) Chromatogram, +800 mV.

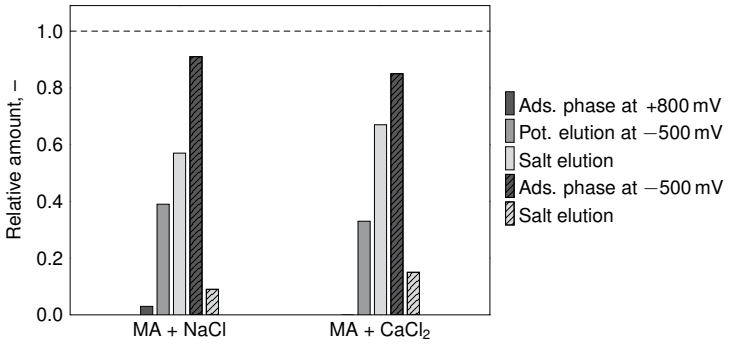

(c) Balance.

Figure A.59: Potential-gradient experiment and related balance using maleic acid as target analyte dissolved in NaCl or in $CaCl_2$ (stoichiometric ratio 1:1). CNT-K matrix, DI-water, adsorption phase 0.5 mL/min, desorption phase 1.5 mL/min, 50 µL, 12.5 mM maleic acid, pH 7, gradient −5 mV/s, salt elution: 1 mM NaCl, 8 mL.

A.11 Adsorption of Inorganic Molecules

The following chromatograms in Figure A.60 correspond to the potential-dependent salt adsorption experiments as discussed in Section 5.6.1. Figure A.61 represents the results of the potential-dependent tracer experiments with 1 M NaCl.

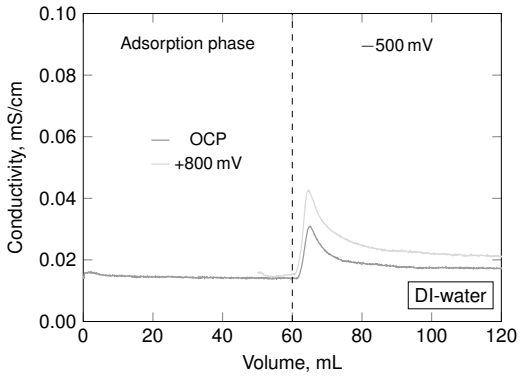

(a) DI-water only.

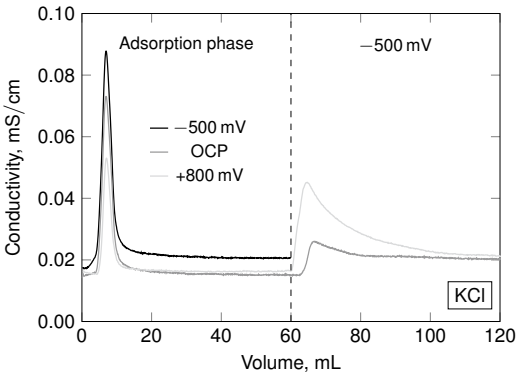

(b) KCl.

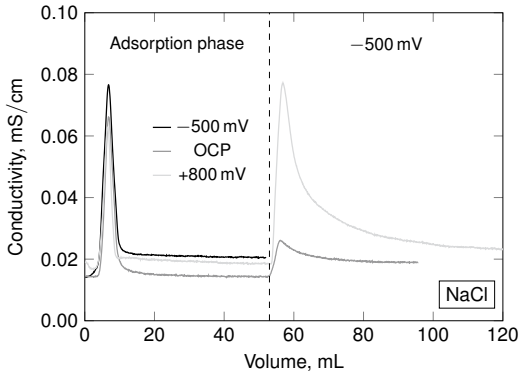

(c) NaCl.

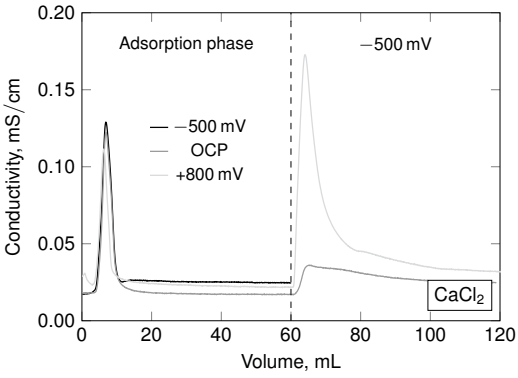

(d) $CaCl_2$.

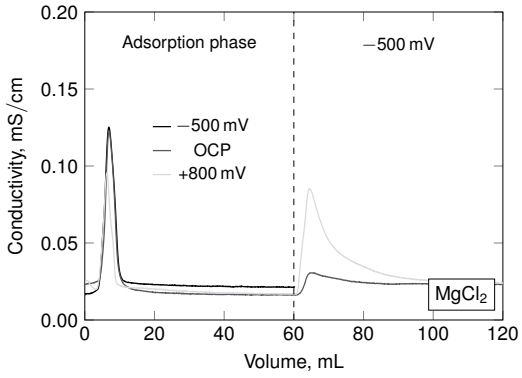

(e) $MgCl_2$.

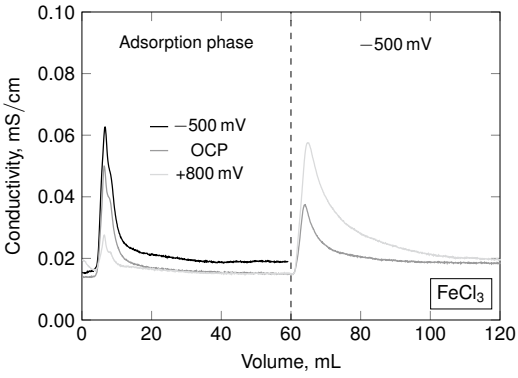

(f) $FeCl_3$.

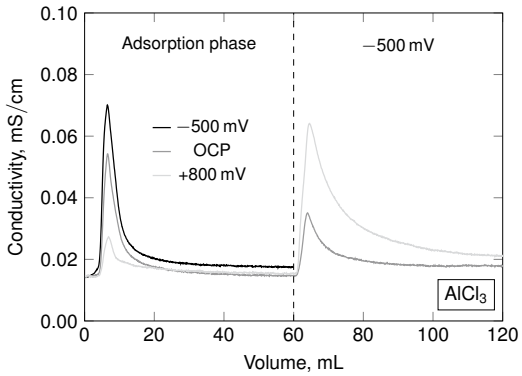

(g) $AlCl_3$.

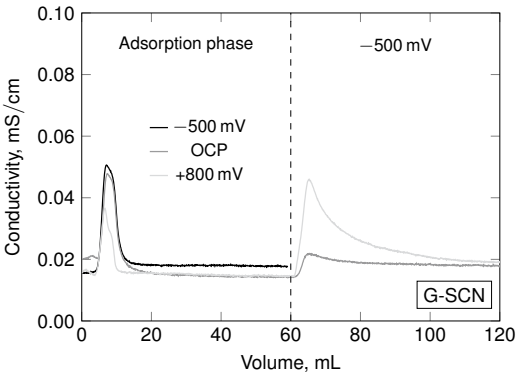

(h) G-SCN.

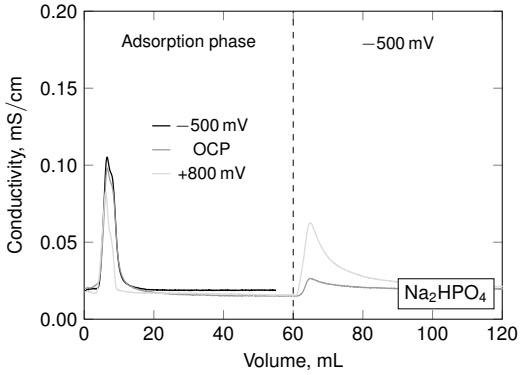

(i) Na_2HPO_4.

Figure A.60: Potential-step experiments to compare the potential-dependent interaction of different salts and MWCNT. CNT-K matrix, DI-water, 1.5 mL/min, 50 µm, 25 mM, Adapted from Trunzer *et al.* [19].

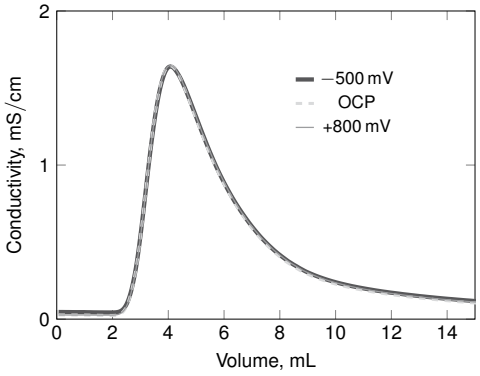

Figure A.61: Potential-dependent experiment to study the suitability of NaCl as a tracer. CNT-K matrix, DI-water, 1.5 mL/min, 50 µL, 1.0 mM NaCl. Adapted from Trunzer *et al.* [19].

A.12 Adsorption of Organic Molecules

The following Section belongs to Section 5.6.2. The Subfigures in Figure A.62 represents the different chromatograms about the adsorption study at OCP screening different organic molecules.

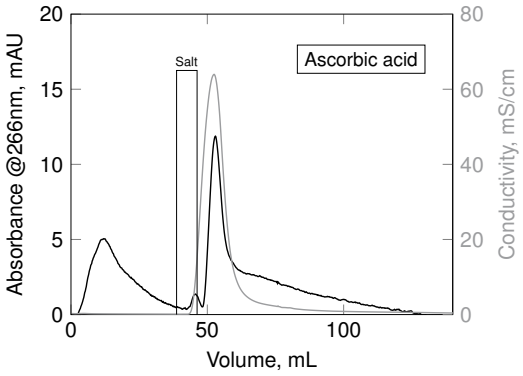

(a) 5 g/L Ascorbic acid.

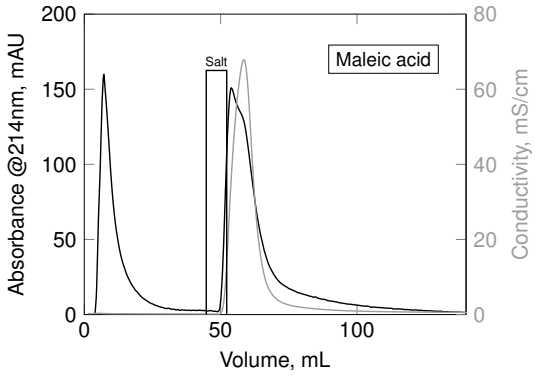

(b) 5 g/L Maleic acid.

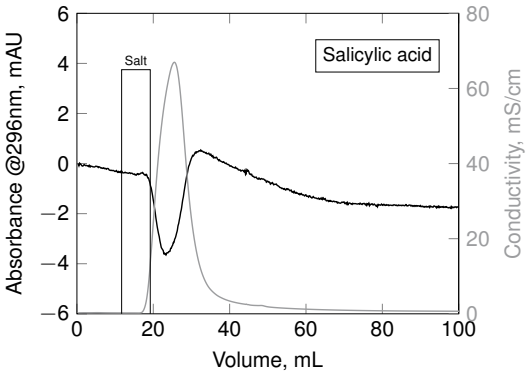

(c) 1 g/L Salicylic acid.

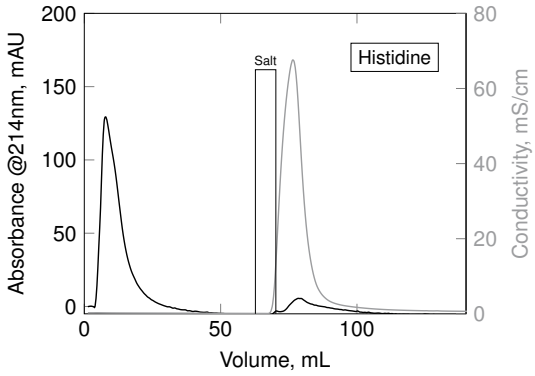

(d) 5 g/L Histidine.

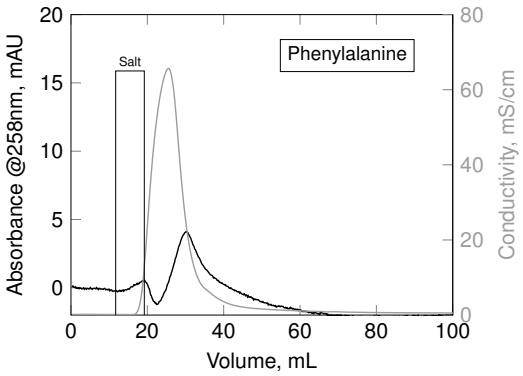

(e) 5 g/L Phenylalanine.

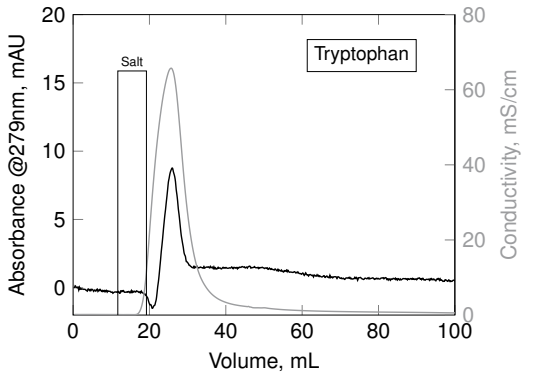

(f) 5 g/L Tryptophan.

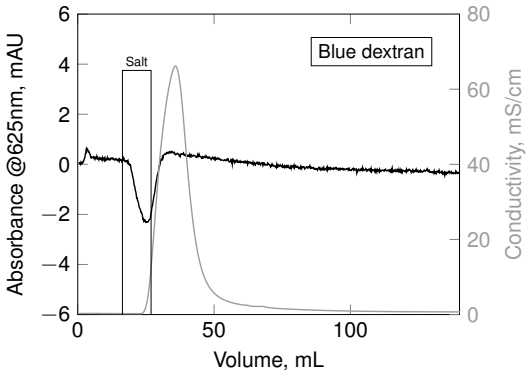

(g) 10 mM Blue dextrane.

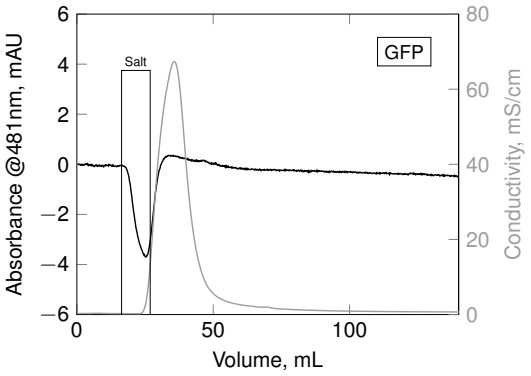

(h) 0.5 g/L GFP.

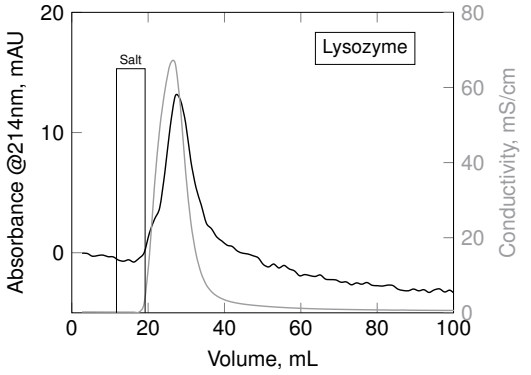

(i) 5 g/L Lysozyme.

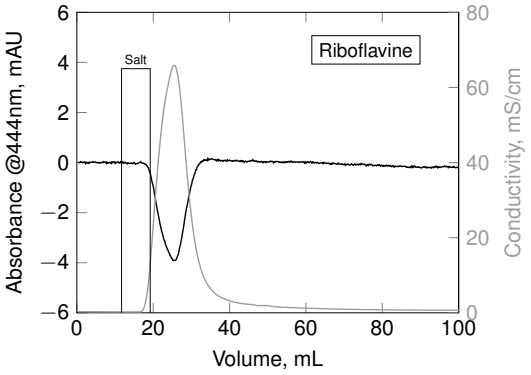

(j) 0.05 g/L Rivoflavin.

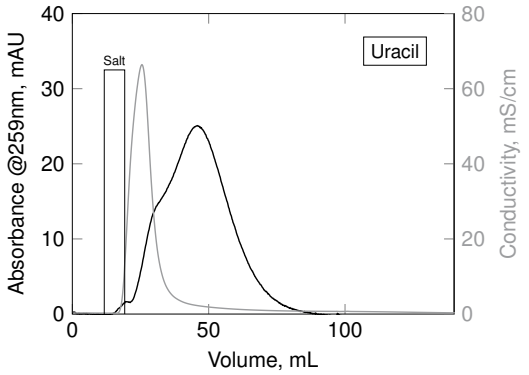

(k) 1 g/L Uracil.

Figure A.62: Interaction study to identify the native binding affinity of different organic molecules to the MWCNT. No potential applied, CNT-K matrix, DI-water, Adsorption phase: 0.5 mL/min, Salt elution: 1.5 mL/min, 1 M NaCl, 7.5 mL, Analyte injection: 50 µL, various concentrations. Cf. balance in Figure 5.25.

Table A.11: Summary of the injected amount C_{in}, the breakthrough amount C_{break} and the salt elution amount C_{salt} to exemplify irreversible binding behavior of organic molecules when impulse experiments are performed at OCP. Besides, the sum of the detection amount is related to the injection amount.

Molecule	C_{in}, g/L	C_{break}, g/L	C_{salt}, g/L	**Detection amount**, –
Ascorbic acid	5.00	0.12	0.22	0.07
Maleic acid	5.00	1.75	3.58	1.07
Salicylic acid	1.00	0.00	0.11	0.11
Histidine	5.00	2.99	0.53	0.70
Phenylalanine	5.00	0.00	4.31	0.86
Tryptophan	5.00	0.00	0.39	0.08
GFP	0.50	0.00	1.00	2.02
Lysozyme	5.00	0.00	0.66	0.13
Riboflavine	0.05	0.00	0.03	0.52
Uracil	1.00	0.00	0.90	0.90

Supplements of the potential-step experiment with maleic acid are illustrated in Figure A.64 (cf. capacities in Table 5.7). Besides, the potential-dependent adsorption behavior of maleic acid on IoLiTec-CNT is visualized in Figure A.65. Table A.12 lists the specific data for different MWCNT species.

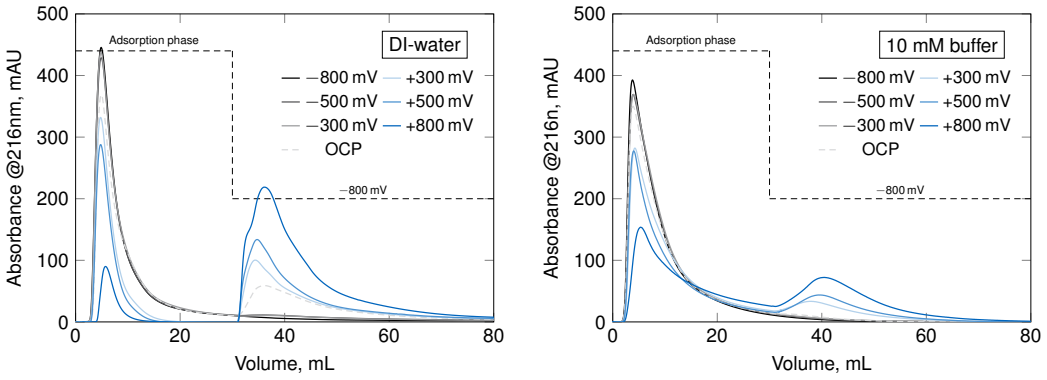

(a) Mobile phase DI-water. **(b)** Mobile phase 10 mM phosphate buffer.

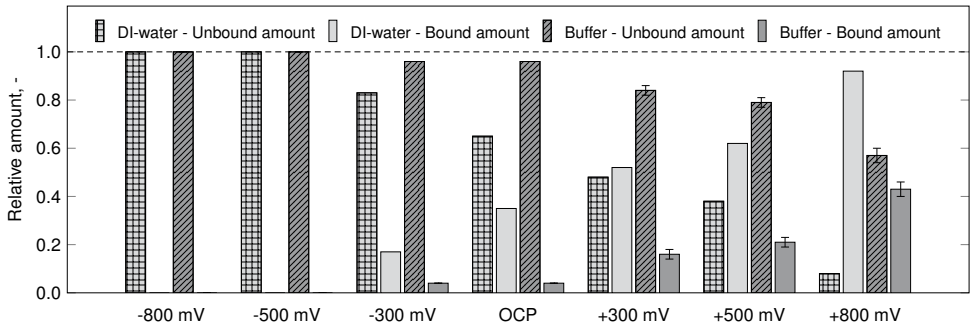

(c) Balance of the relative amount of maleic acid.

Figure A.63: Representative potential-step experiment to determine the potential influence on retention time and column capacity of maleic acid. CNT-K matrix, DI-water, 10 mM phosphate buffer, 1 mL/min, 50 µL, 5 g/L, 216 nm, pH 7. The adsorption was performed at various potentials (x-axis), the desorption potential was −800 mV. Adapted from Tunzer *et al.* [18].

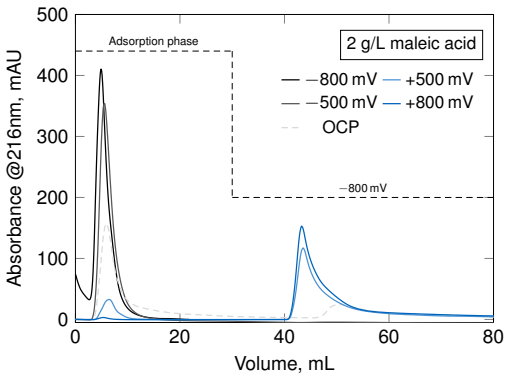

(a) 2 g/L MA, DI-water.

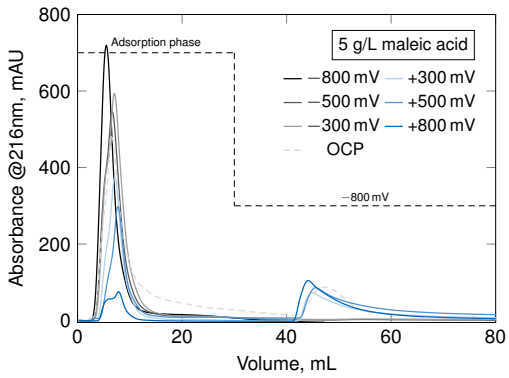

(b) 5 g/L MA, DI-water.

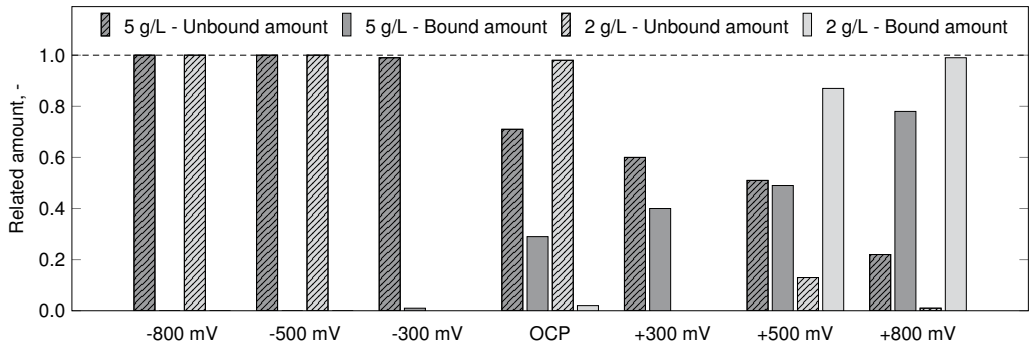

(c) Balance of the adsorption amount.

Figure A.64: Potential-step experiments to study the adsorption behavior of different maleic acid concentrations on CNT-K. The relative balance is calculated over the peak area. Adsorption phase: various potential, desorption phase: −800 mV. CNT-K matrix, DI-water, 1 mL/min, 50 µm, 2 g/L, 5 g/L, 216 nm, potential step at 40 mL Adapted from Trunzer *et al.* [18].

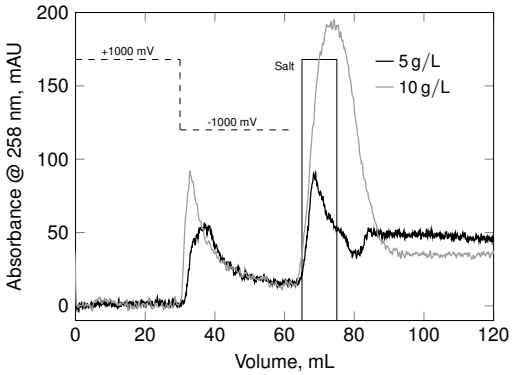

Figure A.65: Potential-step experiment with 5 g/L and 10 g/L maleic acid in DI-water. IoLiTec-CNT matrix, DI-water, 1 mL/min, 50 µm, 5 g/L, 10 g/L, 254 nm, pH 7, adsorption phase: +1000 mV, desorption phase: −1000 mV, elution phase: 10 mL, 1 M NaCl.

Table A.12: Comparison of Baytube C150P, CNT-K and IoLiTec-CNT.

MWCNT	**SSA,** m^2/g	**Bulk density,** g/cm^3	**Packed bed dry mass,** g
Baytubes C 150 P	220 [15]	0.13 [216]	1.42 [15]
CNT-K	200	2.1 [217]	0.5
IoLiTec-CNT	210	–	0.7

Figure 5.27 depicts the balance of the adsorption behavior of different amino acids.

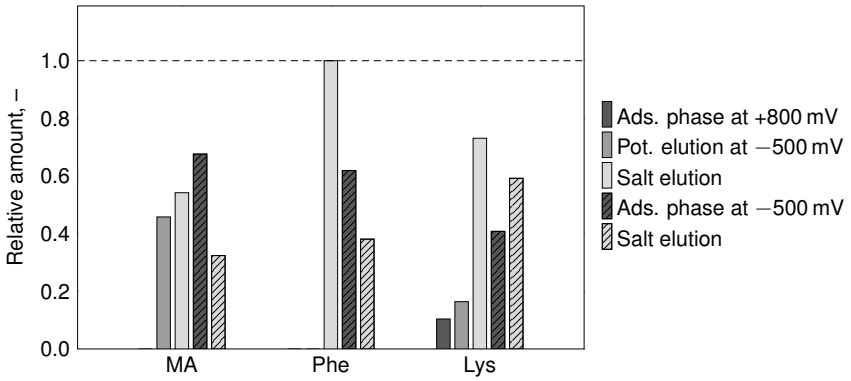

Figure A.66: Balance of the interaction study between different organic molecules and MWCNT at various potentials. CNT-K matrix, DI-water, Adsorption phase: 0.5 mL/min, Desorption phase 1.5 mL/min, Salt elution: 1.5 mL/min, 1 mM NaCl, 8 mL, Analyte injection: 150 µL, 25 mM, pH 7. The corresponding chromatograms are illustrated in Figure 5.27.